.

The Spatial and Temporal Distribution of Föhn Winds on the Larsen C Ice Shelf, Antarctica

Jenny Victoria Turton

Submitted in accordance with the requirements for the degree of

Doctor of Philosophy

University of Leeds

School of Earth and Environment

April 2017

The candidate confirms that the work submitted is her own, except where work which has formed part of jointly-authored publications has been included. The contribution of the candidate and the other authors to this work has been explicitly indicated below. The candidate confirms that appropriate credit has been given within the thesis where reference has been made to the work of others.

The work in Chapter 6 of the thesis has appeared in publication as follows: Turton, JV., Kirchgaessner, A., Ross,AN. and King, JC. (2017) Does high-resolution modelling improve the spatial analysis of föhn flow over the Larsen C ice shelf? *Weather*, 72(8), 192-196.

The article referenced above was written by Jenny Victoria Turton (first author). The work presented was completed by the first author, with guidance from her three supervisors (co-author). The model set-up and run, and the analysis were performed by the first author. The co-authors made suggestions on the structure and grammar of the article. The published work forms part of Chapter 6. More specifically the 'Autumn case study' has been published.

This copy has been supplied on the understanding that it is copyright material and that no quotation from the thesis may be published without proper acknowledgement.

2017, The University of Leeds and Jenny Victoria Turton.

Abstract

The Antarctic Peninsula (AP) was the fastest warming region on earth during the 20th century. The eastern side of the Peninsula is typically 5-10K colder than at equivalent latitudes on the western side. Despite this cooler climate, a number of ice shelves have collapsed in the last two decades. In 1995 Larsen A collapsed, shortly followed by Larsen B in 2002. Larsen C Ice Shelf (LCIS), the largest remaining ice shelf, is now showing evidence of potential destabilisation, including melt ponding and rift acceleration.

The 'hydrofracture mechanism suggests that percolation of melt water into crevasses allows them to deepen and extend to the ice shelf base, which leads to destabilisation. Advection of warm, dry air onto the ice shelf from föhn winds is partly responsible for the melt water. Investigating föhn winds over LCIS was one aim of the Orographic Flow and Climate of the Antarctic Peninsula (OFCAP) project. The aim of this research is to investigate the spatial distribution and frequency of the föhn winds, and assess their impact on the LCIS.

To investigate this, near-surface observational data at six locations is combined with archived regional model output at 5km horizontal-resolution from the Antarctic Mesoscale Prediction System (AMPS). A novel semi-automatic algorithm has been developed to detect föhn winds from near-surface observations. A relatively new algorithm has been adapted for use over the AP, to detect föhn conditions from the AMPS output. Föhn characteristics over the ice shelf have been identified to create a mini-climatology of the location and occurrence of föhn winds from 2009 to 2012.

Föhn conditions have been observed as far south as ∼68°S for the first time. Föhn events are most frequent in spring, when over 50% of days can experience the warm, dry winds. The average length of föhn events is approximately 12 hours, but they can occur in quick succession to have a longer-lasting effect.

Some of the spatial features within the föhn flow were investigated further using high-resolution (1.5km) Weather Research and Forecasting (WRF) model. Föhn jets, hydraulic jumps and localised föhn enhancement were simulated by WRF in four case studies. The presence of a statically-stable cold pool over the ice shelf appears to reduce the propagation of föhn air, and interrupt the near-surface signal.

When föhn winds occur in late spring they prompt earlier melt onset, increase the number of melt days and lengthen the melt season. Föhn-induced surface melting has been observed over 130km from the mountains. This research has highlighted the potential destabilising effect of föhn winds, which may provide an insight into the stability of the LCIS.

Acknowledgements

First and foremost, this thesis would not exist were it not for Amélie Kirchgaessner, Andrew Ross and John King. I would like to acknowledge and thank them for all of their guidance, advice and help. I would like to especially thank Amélie, for her advice on many aspects of my work during my time at the British Antarctic Survey (BAS). She has allowed me to pursue education and outreach activities, attend training courses to help start my career and encouraged me to attend conferences. A massive thanks must also go to Andrew, for reading every word of this thesis, and always making time to see me and support me on my monthly visits to Leeds. I have also benefited from advice and help from Alan Gadian, Daniel Bannister, Scott Hosking, Tony Phillips, Ralph Burton and many others at both BAS and the University of Leeds. I would also like to thank the Natural Environment Research Council (NERC) for providing the funding to make this research and this PhD possible. Thanks also to the Royal Meteorological Society for providing finance through the Legacies fund to support my attendance at the University Centre in Svalbard; it really was the trip of a lifetime.

Even on the hardest days, the Room 154 girls were there to provide support, laughter, friendship and chocolate. I really don't think I would have got this far without them, especially Michelle McCrystall. Massive thanks should also go to the netball girls, for providing me with sanity, weekend activities and years of fun. It was a pleasure to play with you for 3.5 years. Some of the best days were spent with the BAS students. Whether at the annual bonding day, the holidays in the Lakes and Majorca or sitting in Jesus Green. Some of the biggest laughs were with Will, the two Martins, Seb, Rich, Michelle, Vicky, Ian, Mike, Heather, Ashleigh and Jim. Thanks

also to Amy Wills and Emma Whybro, who provided much needed wine breaks on the weekends. You two have supported me for so many years now, and I am forever grateful.

To my mom, dad, sister, grandparents, Julie, Jean and Kerry. Thank you for giving me the opportunity to do this, and for your patience, support, cups of tea, advice, proof reading capabilities, stress-reducing gifts and for providing me with a place to escape. My parents will be pleased that I am now, finally, going into the working world; this thesis is for them. It is also for granddad Norman, who saw me finish this from afar.

Finally, a huge, gigantic thank you to my wonderful boyfriend, John. You moved your life down to Cambridge three years ago, and I'm so thankful and glad that you did. You were a source of happiness and stability in this roller coaster PhD life, and I will forever be grateful of the support, hugs and squeezes over the last seven years. You always believe in me. Massive love to all.

"One step beyond the pole, you see,
and the north wind becomes a south one."
-Robert Peary

Abbreviations

Table 1: The abbreviations used throughout the thesis.

Abbreviation	Description
BAS	British Antarctic Survey
AP	Antarctic Peninsula
LCIS	Larsen C Ice Shelf
WRF	Weather Research and Forecasting model
ASL	Amundsen- Bellingshausen Sea Low
SAM	Southern Annular Mode
DALR	Dry Adiabatic Lapse Rate
SALR	Saturated Adiabatic Lapse Rate
MAP	Mesoscale Alpine Programme
MDV	McMurdo Dry Valleys
MetUM	Met Office Unified Model
Fr	Froude Number
AMPS	Antarctic Mesoscale Prediction System
OFCAP	Orographic Flows and Climate of the Antarctic Peninsula
AWS	Automatic Weather Station
SEB	Surface Energy Balance
CIRES	Cooperative Institute for Research in Environmental Sciences
IMAU	Institute for Marine and Atmospheric research Utrecht
NOAA	National Oceanic and Atmospheric Administration
NCAR	National Center for Atmospheric Research
T	2m Air Temperature
RH	2m Relative Humidity
FF	Wind speed
DD	Wind direction
P	Air pressure
q	water vapour mixing ratio
SWin	Incoming shortwave radiation
LWin	Incoming longwave radiation
LWout	Outgoing longwave radiation
NetRad	Net Radiation
H	Distance between the surface and the sensor
CP	Cole Peninsula
RMSE	Root Mean Square Error
ECMWF	European Centre for Medium Range Weather Forecasts
Era-Interim	ECMWF Reanalysis Product
GFS	Global Forecasting System
BEDMAP2	Digital elevation model over the Antarctic
NCEP	National Centres for Environmental Prediction
WSM5	WRF Single Momentum 5-Class
RRTMG	Rapid Radiative Transfer Model for General circulation models
MYJ	Mellor-Yamada-Janjic scheme
MYNN	Mellor-Yamada-Nakanishi-Niino boundary layer scheme
RACMO2	Regional Atmospheric Climate Model v.2
TSK	Surface temperature

Table 2: The abbreviations used throughout the thesis (continued).

Abbreviation	Description
Eta	Janjic-Eta Monin Obukhov scheme
RH10P	RH at the 10th Percentile
RH15P	RH at the 15th Percentile
RH12hr	RH change over 12-Hours
NWP	Numerical Weather Prediction
a.s.l	Above sea level
T °0> C	Air temperatures above freezing
ENSO	El Nino Southern Oscillation
SW↓	Incoming shortwave radiation
SW↑	Outgoing shortwave radiation
LW↓	Incoming longwave radiation
LW↑	Outgoing longwave radiation
H_s	Sensible heat flux
H_l	Latent heat flux
G	Ground heat flux
M	Residual energy
Q	Shortwave radiation absorbed by the surface
E	Sum of Surface and subsurface melting
Q_*	Scaling mixing ratio
T_*	Scaling temperature
u_*	Friction velocity
C_P	Specific heat of air
ρ	Air density
τ	Surface stress
L	Monin-Obukhov length
$\phi_{M,T,Q}$	Functions of wind shear, temperature and scalar concentration gradients
κ	Von Karman Constant (0.4)
Pr	Prandtl constant (0.95)
Sc	Schmidt constant (0.95)
z_0	Surface roughness length
L_s	Latent heat of sublimation
α	Albedo
ϵ	Emissivity
σ	Stefan-Boltzmann constant (5.67×10^{-8} $Wm^{-2}K^{-4}$)
L_f	Latent heat of fusion
w.e	Water equivalent
PDD	Positive degree days
N	Number of PDD per year
k	Degree-day melt factor
E_{melt}	Energy for melting when TSK = 0°C
ρ_w	Density of water

Contents

List of Figures

Chapter 1

Introduction, Literature Review, Motivation and Aims

1.1 Introduction

The Antarctic Peninsula (AP) is a narrow, elongated mountain range with an average elevation of $\sim$ 1500m. Attached to the west and east coast of the AP are numerous ice shelves. In 1995 the Larsen A ice shelf collapsed, which was shortly followed by the collapse of its southern neighbour, Larsen B, in 2002. A direct effect of ice shelf collapse is the acceleration of glaciers into the embayments which once housed the ice shelves, consequently leading to indirect sea level rise (Holland *et al.*, 2011). Numerous theories have been proposed for the mechanism responsible for the destabilisation of these ice shelves. The leading theory is the 'hydrofracture mechanism' (Scambos *et al.*, 2003). Naturally-occurring crevasses in the ice shelf are widened and deepened by the percolation of surface melt water into the crevasses. Melt water ponds on the surface of the Larsen C Ice Shelf (LCIS) have recently been observed in satellite images (Luckman *et al.*, 2014).

The 'föhn hypothesis', originally coined by Marshall *et al.* (2006), links the cross-mountain advection of warm föhn-air onto the ice shelf, and the surface melt water available to contribute to the hydrofracture process. Föhn winds are warm and dry winds in the lee of mountains. Föhn air flows over ice shelves on the eastern side of the AP. It is believed that they can induce surface melting, which then ponds on

the surface and percolates into crevasses, and contributes to hydrofracturing of the ice shelf. In previous studies, föhn winds have been observed over the LCIS in aircraft and near-surface observations (King *et al.*, 2008; Kuipers Munneke *et al.*, 2012) and in regional modelling studies (Elvidge *et al.*, 2015, 2016).

Whilst föhn winds over the LCIS have been identified on a case-by-case basis prior to this study, the frequency and spatial distribution of föhn winds in this region is unknown. Without knowledge of their extent and dominance, only rough estimates are available for the impact of the föhn air on the ice shelf surface. In order to assess the frequency and spatial extent of the föhn winds, a novel föhn detection algorithm will be developed to identify föhn winds from near-surface observational data. A relatively new algorithm for detecting föhn conditions from model output will also be adapted and employed over the AP for the first time. To further investigate the spatial distribution of the winds, high-resolution simulations of föhn events using the Weather Research and Forecasting (WRF) model will be conducted. The impact of föhn winds from 2009 to 2012 is presented and it provides evidence that föhn winds may contribute to surface melting. The results from this study will lay the groundwork for assessing whether the frequency of föhn winds has increased over the last 50 years.

This chapter will outline the main research objective of this project; investigating the spatial and temporal distribution of föhn winds over the LCIS. The location of study, history of föhn research and the mechanisms responsible for the winds will be presented along with a more detailed description of why this work is necessary, and how it will expand the current understanding of föhn winds over the AP. The chapter will conclude with presenting the justification for research, and the five main aims which will be addressed throughout the thesis.

1.2 Location of Study

1.2.1 The Antarctic Peninsula

The Antarctic Peninsula (AP) mountain range stretches approximately 1300km from the Drake Passage in the north to Ellsworth Land in the south (Figure 1.1). The aver-

age elevation of the AP is 1500m, and Mount Jackson (71°23'S, 63°22'W), the highest mountain in the range, peaks at 3184m. The steep sided mountain range is less than 60km wide in some locations, and it has a complex topography. A number of islands neighbour the main mountain chain, including Adelaide Island to the west and James Ross Island to the north east. Approximately 80% of the AP is permanently ice covered, either by ice sheets or glaciers.

A key characteristic of the AP is the large number of ice shelves which are adjacent to both the east and west coasts (Figure 1.2). The ice shelves provide stability to the ice sheets and glaciers, and are an important aspect of the mass balance of the entire continent. Ice shelves are extensions of the ice sheet, ranging from 200-1000m in thickness (Van Den Broeke, 2005). The evolution and mass balance of ice shelves depends on the melt and accumulation above and below the ice. Mass is lost through basal and surface melting, and iceberg calving, whereas accumulation is mostly from snow and increased glacier influx (Pritchard *et al.*, 2012).

1.2.2 The Larsen Ice Shelf

One of the larger ice shelves along the eastern coast of the AP is the Larsen Ice Shelf (∼64° - 74°S, 61° - 65.5°W). This is a group of ice shelves that are divided into four separate ice shelves; Larsen A, B, C and D (north to south) (Figure 1.2). The topography of the ice shelves are characterised by slightly sloping surfaces which are mostly uniform, except for crevasses and small areas of surface melting (King *et al.*, 2008). This area is a stark contrast to the high altitude mountains that run along the western edge of the Larsen Ice Shelf.

The Larsen C Ice Shelf (LCIS) is the largest remaining ice shelf ($\sim$ 55,000km^2) and is the focus of this study. It is bounded by the AP to the west, Jason Peninsula (∼66.1°S) to the north, and Kenyon Peninsula (∼68.5°S) to the south, where the ice shelf meets the Larsen D ice shelf. The LCIS has twelve major 'flow units' where tributaries of glaciers feed into the ice shelf and contribute to its mass balance (Glasser *et al.*, 2009). At its widest, the ice edge is over 200km east of the AP mountains. The eastern edge is largely met by sea ice which is a permanent feature in the Weddell Sea. Polynyas

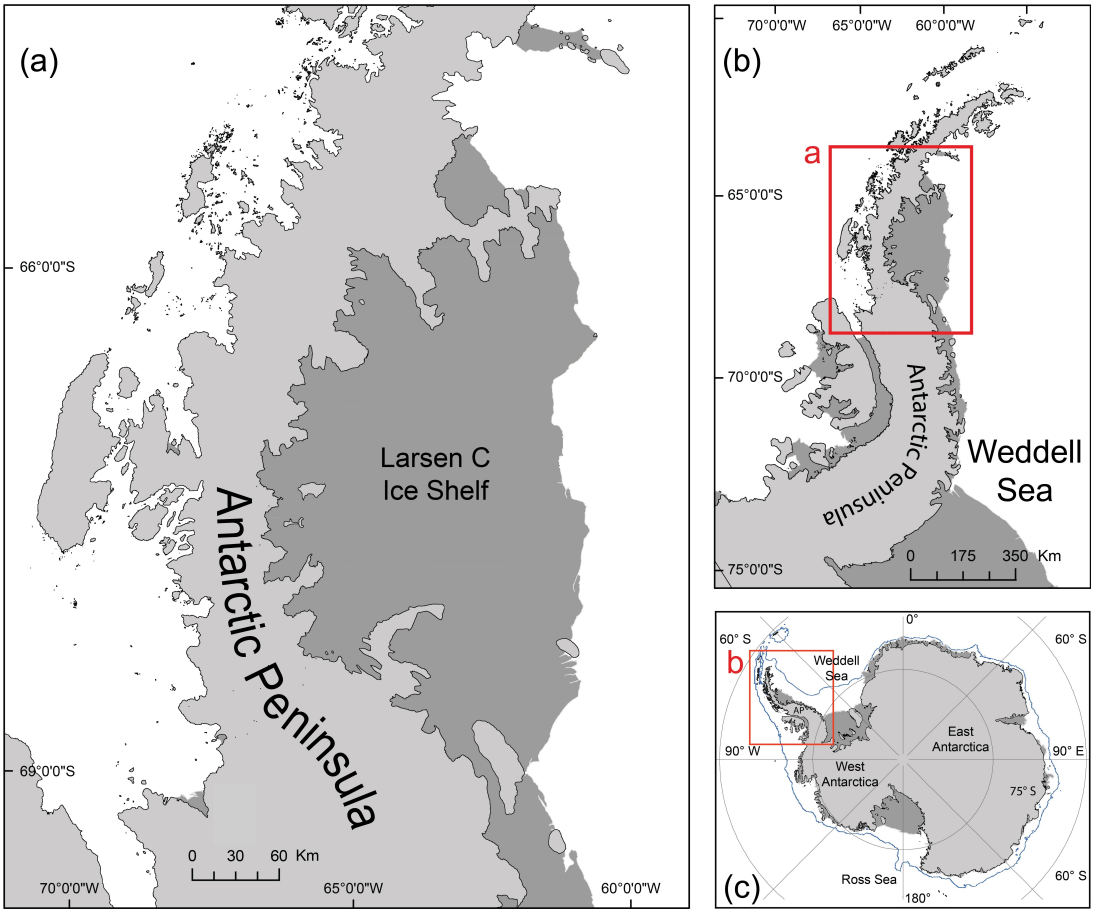

Figure 1.1: a) The Larsen C ice shelf and Scar Inlet; the remnants of Larsen B. Light grey are the mountains of the Antarctic Peninsula. Dark grey areas are ice shelves. b) The Antarctic Peninsula and adjacent islands. The red box outlines figure a. c) The Antarctic continent and surrounding southern ocean (white). The thin blue line is the annual average sea ice extent from . The red box outlines figure b. Figure credit: W. Dickens, British Antarctic Survey.

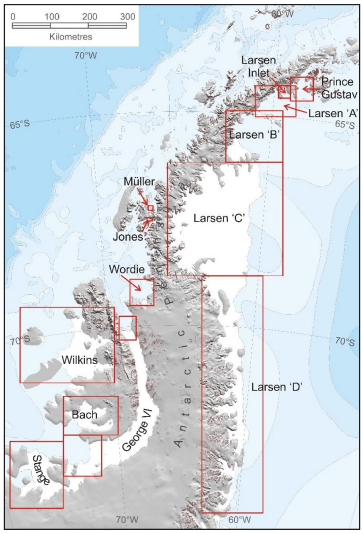

Figure 1.2: Until 2002, twelve ice shelves surrounded the Antarctic Peninsula, however a number of these have now collapsed and many have drastically retreated since the first observations in the 1960s. The Larsen C and remnants of Larsen B are the geographical focus of this study. From Cook & Vaughan (2010).

and leads, semi-permanent openings in the sea ice due to ice drift and localised wind forcing, can separate the ice shelf edge and the sea ice throughout the year (Haid, 2013).

A stable boundary layer and cool pools frequently form on the surface of LCIS due to its homogeneous, relatively flat surface. Cold, continental air flows onto the ice shelf during southerly winds. The low sloping gradient promotes the accumulation of the cold air, and during winter, the stable boundary layer can persist throughout the season (King *et al.*, 2008). During summer, the average air temperature over the ice shelf is approximately -4°C, and surface melt ponds form in the northwest section of the ice shelf (Luckman *et al.*, 2014).

1.2.3 Regional Climate of the Antarctic Peninsula

The climate of the AP is complex and influenced by a number of factors including the oceans, atmosphere and sea ice. The AP is the northernmost part of the Antarctic, and subsequently it has a relatively mild climate. Its climate categorisation is complex, as the western AP is 'maritime Antarctic', whereas the eastern side, and many northern

AP islands are 'Antarctic Tundra' (Maria, 2010).

The mean atmospheric circulation pattern in the southern hemisphere is dictated by the 'Polar' vortex. The central position, strength and shape of the vortex varies on monthly, seasonal and annual time scales. It develops during autumn, and becomes strongest during midwinter (Sheshadri *et al.*, 2014). The Polar vortex produces predominantly westerly winds (the circumpolar westerlies) (Thompson & Solomon, 2002). The AP intersects this predominant air flow almost perpendicularly. This has a strong influence on the climate of the AP. The AP region can be separated into two sectors, the warm west and cold east. With airflow from the Pacific segment of the Southern Ocean, the western slope experiences humid winds, strong storms and cloud formation. Despite the impact of passing depressions, the western side is much milder than the east (Ding & Steig, 2013; Turner *et al.*, 2002). The east has a much cooler continental climate. The orographic blocking of the maritime air by the mountains facilitates the northwards flow of continental air over the eastern AP (**?**). The annual mean temperature is 5-10K cooler on the east side, than that at the same latitude on the west coast (Morris & Vaughan, 2003). This blocking of flow by the AP also influences the mass balance of the region. The western AP experiences a relatively large mass accumulation of approximately 3000mm of water equivalent (w.e) precipitation per year. In contrast, the east side is much drier and experiences 500mm w.e yr^{-1} precipitation (van Wessem *et al.*, 2016).

At the end of austral winter, sea ice covers the vast majority of coastline surrounding the Antarctic (Figure 1.3). At the end of austral summer, when sea ice is at its minimum, only the Weddell Sea and other small pockets of ocean are covered by sea ice. The localised sea ice extent is controlled largely by the prevailing wind direction, rather than the air or water temperature. A year with frequent southerly winds leads to a vast sea ice extent, whereas northerly winds inhibit the growth of sea ice (Turner *et al.*, 2005). The air temperature on the northwest coast of the AP is closely correlated to the Bellingshausen sea ice extent (west of the AP) (King, 1994). The temperature is lower in years with a large sea ice extent.

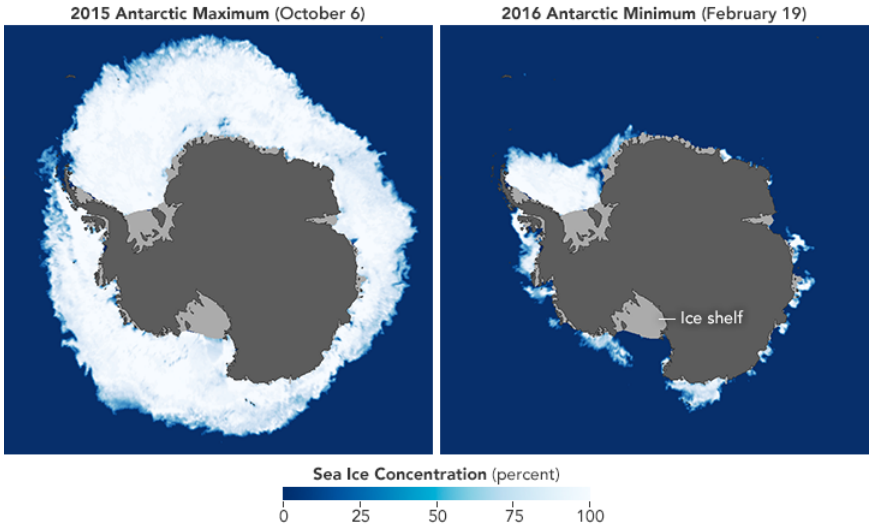

Figure 1.3: The absolute maximum (left) and minimum (right) sea ice concentration on October 6th 2015 and February 19th 2016 (respectively). Figure: NASA Earth Observatory (www.earthobservatory.nasa.gov, last accessed 20th February 2017).

The location and strength of the Amundsen Sea Low (ASL), a persistent low pressure system in the Bellingshausen Sea (to the west of the AP), also influences the climate of the AP. The number of days with precipitation has increased on the northwestern tip of the AP since the late 1950s due to more frequent northwesterly air masses arriving at the west coast of the AP (Turner *et al.*, 2005). Due to its influence over northerly flow, the depth and location of the ASL also affect the sea ice extent (Turner *et al.*, 2013). The ASL circulation is highly variable on a monthly, seasonal and decadal timescale, which makes it difficult to assess its links to other phenomena (Turner *et al.*, 2013). Figure 1.4 displays the average seasonal location and depth of the ASL. The ASL is deepest in Spring (SON) when it transports moist, northwesterly air to the west AP (Raphael *et al.*, 2016).

Due to the complexity and variability of the climate in the region, identifying long-term trends and changes, particularly related to anthropogenic climate change, is difficult. However, the regional air temperature warming during the late 20th century dominated the signal.

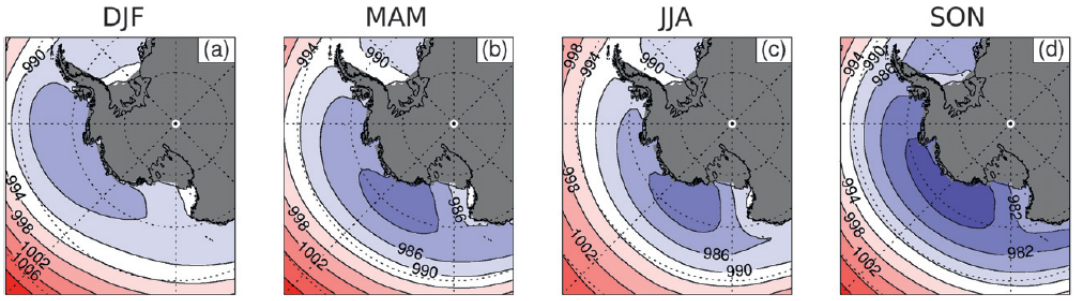

Figure 1.4: The seasonal average location and depth of the Amundsen Sea Low (ASL) pressure system from ERA-Interim data for 1979-2011. It is deepest in spring, which prompts northwesterly flow over the AP. Figure courtesy of Hosking *et al.* (2013).

1.3 Regional Climate Change

During the latter half of the 20th century the AP region experienced significant and accelerated warming, far exceeding the global average. Observations on the west of the AP revealed the annual mean air temperatures had increased by 2.8K from 1951 to 2000 (Turner *et al.*, 2016). This was the largest temperature increase observed over the whole Antarctic continent. The glaciological response to this warming has been highlighted by ice shelf disintegration and accelerated loss of land ice. The relatively short observational period over the AP (many observations only began in 1957), makes it difficult to interpret this 50-year warming trend in a longer context. However, analyses from marine sediments and ice cores suggest that a warming rate of this magnitude is unlikely to have occurred within the last 1800 years (Vaughan *et al.*, 2003).

The 20th century warming can partially be attributed to changes in the hemispheric wind circulation. The location and strength of the polar vortex is influenced by the Southern Annular Mode (SAM); the southern hemisphere's large-scale variability forcing (Marshall, 2003). It shifts between a positive and negative index (Figure 1.5), defined by pressure differences between the Antarctic and the mid-latitudes. Since approximately 1965 onwards, SAM has mostly been in a positive mode (Figure 1.6), when pressure around the Antarctic is lower than in the mid-latitudes (Marshall, 2003). A consequence of this is strengthening and contraction of the circumpolar westerlies

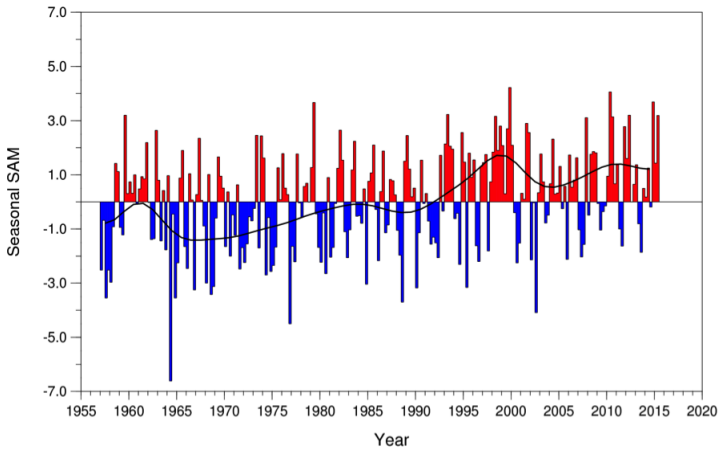

Figure 1.5: Seasonal values of the Southern Annular Mode (SAM) Index. The smooth black curve is the decadal variation. Since the mid 1960s the index has been predominantly positive (red). Figure from Marshall & National Center for Atmospheric Research (2016).

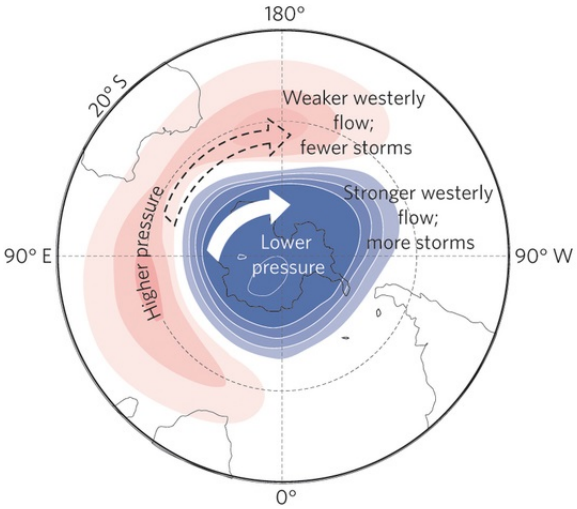

Figure 1.6: SAM is defined by the difference in atmospheric pressure between the mid and high southern latitudes. Under positive SAM index, displayed here, the pressure over the Antarctic is lower than at the mid latitudes. Figure adapted from Jones (2012).

towards the continent. This causes a more perpendicular interaction between the air flow and the AP, which brings more warm air over the AP (Carrasco, 2013).

Steig *et al.* (2009) suggest that the AP was not alone in its extensive warming, and that it was part of a larger trend seen over West Antarctica. This larger scale warming was attributed to a change in the atmospheric circulation which has increased the transport of warm air from northerly origin to West Antarctica (Steig *et al.*, 2009). The annual mean velocity of the westerlies at low levels (850 hPa) has increased by 15-20% in the last 50 years of the 20th century (Orr *et al.*, 2004). This can account for approximately 50% of the observed surface air warming (Thompson & Solomon, 2002), therefore displaying the strong influence of SAM on the air temperature in the region of the AP.

In the most recent decade, a hiatus in warming has been observed in the 21st century (Carrasco, 2013; Turner *et al.*, 2016) (Figure 1.7). The hiatus, and even cooling in some observations, does not suggest that the large scale atmospheric warming has stopped, but has mostly been attributed to extreme natural variability of the AP region (Turner *et al.*, 2016). The sea ice concentration and extent have shown a similar switch in trends, moving from a decreasing sea ice trend during the 20th century, to a sea ice increase in recent years. Interestingly, the 2016/2017 summer season experienced exceptionally low sea ice concentration and volume. The lowest ever recorded Antarctic sea ice volume was observed on the 20th February 2017 (2.191million km^2) (Turner, personal communication, 24th February 2017). Stronger east and southeast winds have brought colder, continental air to the eastern AP (Turner *et al.*, 2016). The hiatus in AP air temperature coincides with the onset of the 'global warming hiatus', however, it is believed that the local climatology has a greater influence on the AP than global trends (Turner *et al.*, 2016).

The exposure of ice shelves to the ocean and the atmosphere makes them sensitive to change. Of the 12 ice shelves which once adjoined to the AP (Figure 1.2), seven have either been lost entirely or have largely retreated (Cook & Vaughan, 2010). In total, the overall ice shelf area of the AP has reduced by over 28000km^2 since the late 1940s. Jones, Larsen B and Prince Gustav ice shelves all suffered a reduction in ice area since

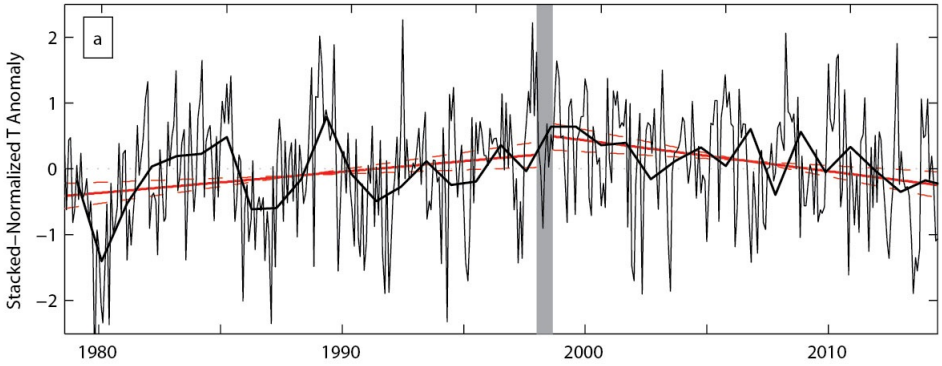

Figure 1.7: The air temperature anomalies from observations of the northern AP from 1979 to 2014 (thin black lines) and the annual average (thick black lines). The solid red lines highlight the linear trend for warming from 1979-1998 and cooling from 2000-2014, with the 95% confidence intervals (dashed red lines). The year 1999 is considered the transition year (grey shade). From Turner *et al.* (2016).

the beginning of the regional warming hiatus. Despite the cold, continental climate of the eastern AP, four ice shelves have disintegrated on this side. Two of these are from the Larsen ice shelves group.

1.4 Larsen Ice Shelf Collapse

The Larsen ice shelf gained notoriety in the late 20th to early 21st century due to the collapse of its two northernmost sections, Larsen A and Larsen B. Geological evidence suggested that the ice shelves were stable for several millennia prior to their collapse (Scambos *et al.*, 2003). The northern section of the Larsen ice shelf has consistently retreated since the mid 1940s (Rott *et al.*, 1996), and the rate of loss accelerated in 1975. In 1995 Larsen A deposited approximately 2100km^2 of ice into the Weddell Sea, and now has less than 10% of its original (1950s) volume remaining (Cook & Vaughan, 2010). In 2002, Larsen B ice shelf collapsed (Figure 1.8), losing 3200km^2 of ice, following an accelerated rate of loss since the 1980s (Cook & Vaughan, 2010). This was the first collapse of this scale in the last 10000 years (Hodgson *et al.*, 2006). Approximately 21% of Larsen B is remaining, with the majority located in Scar Inlet, and being sep-

arated from the LCIS by Jason Peninsula (∼66.5°S) .

The collapse of ice shelves is of global importance. Although sea level rise is not related directly to ice shelf collapse, the acceleration of glacial retreat following collapse does contribute to sea level rise (Holland *et al.*, 2011). After the collapse of Larsen A, glacial flow feeding into the area accelerated by a factor of three (De Angelis & Skvarca, 2003). Similarly, Hektoria glacier (which drained onto Larsen B) lowered by 38m after the break up in 2002 (Scambos, 2004).

Larsen C is the largest remaining ice shelf attached to the AP (∼51000km^2), and is the southerly neighbour of Larsen B. Over 90% of its original (1960s) volume is still remaining. Jansen *et al.* (2010) found that a slight reduction in marine ice production could prompt the ice shelf to become unstable. The northernmost section of the LCIS was considered to be most at risk due to its exposure to the mean annual -9°C isotherm. This is believed to dominate the stable limit of ice shelves (Morris & Vaughan, 2003), and any ice shelves north of this isotherm have the potential to become unstable. The presence of melt ponds on the northwest LCIS further suggests that the stability of northern part of the ice shelf may have been weakening (Luckman *et al.*, 2014). However, until 2013, it was widely believed that LCIS was stable.

Since 2013, the stability of the ice shelf has been brought into question, and it is now believed that approximately 10% of the ice shelf may collapse in a large calving event by the end of 2017. Conversely to the expected pattern, the destabilisation is being driven from the south of the ice shelf. A northward-propagating rift, starting at the Gipps Ice Rise (68.46°S, 60.56°W) is now over halfway along the ice shelf (Jansen *et al.*, 2015) (Figure 1.9). To start with, the rift propagated slowly northwards. However, in 2015 the rift accelerated, and as of February 2017, only 20km remain between the rift and the ice shelf edge (Project MIDAS, www.projectmidas.org, last accessed 20th February 2017). When the partial collapse occurs, further loss of ice and complete destabilisation is possible (Jansen *et al.*, 2015). Consequently, this would be a minimum in ice shelf area since the last interglacial period (Hodgson *et al.*, 2006). Once the calving event occurs, it is thought that further calving events are likely to happen.

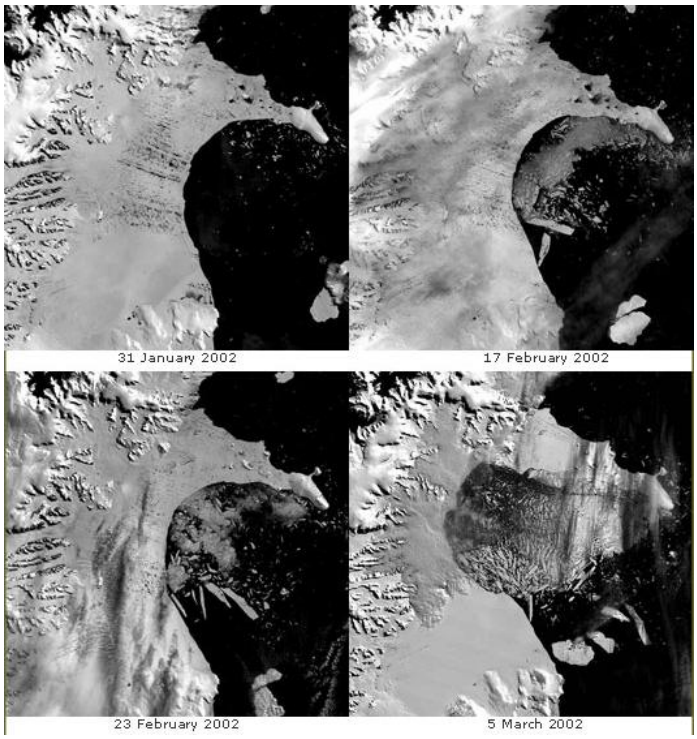

Figure 1.8: Collapse of Larsen B ice shelf over a three month period from January to March 2002 captured by NASA's Moderate Resolution Imaging Spectroradiometer onboard the Terra Satellite. Courtesy of National Research Council (2008).

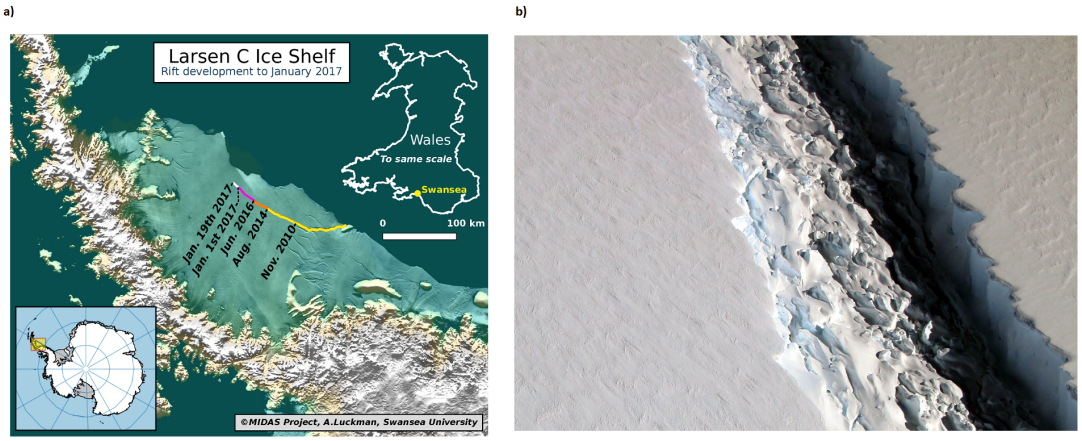

Figure 1.9: The growing rift on Larsen C ice shelf. a) The location and length of the rift on LCIS, with approximate dates of expansion. Figure credit: Project MIDAS, www.projectmidas.org, last accessed 20th February 2017. b) A photograph of part of the rift on the LCIS. Photo credit: NASA/John Sonntag, www.nasa.gov, last accessed 6th January 2017.

Calving of ice shelves is a natural process, however the scale and speed of the Larsen A and B (and possibly Larsen C) calving events is unprecedented, and has led to increased research into the mechanisms responsible for the instability. There have been numerous proposed theories for the break up of the ice shelves on the eastern AP. These include: basal melting as a consequence of changes to the ocean circulation in the Weddell Sea (Pritchard *et al.*, 2012; Robertson *et al.*, 2002), a reduction in snowfall and therefore changes to the surface mass balance (Monaghan *et al.*, 2006), and increased number of melt ponds on the ice surface (Scambos *et al.*, 2000). The leading theory is that the process responsible for the collapse of Larsen A and B is 'hydrofracturing' (Scambos *et al.*, 2000). This is a chain reaction of events whereby crevasses on the ice shelf are deepened, and propagate to the base, as a result of increased pressure from percolating melt water (Scambos *et al.*, 2003, 2009, 2000).

The hydrofracture mechanism relies on the intrusion of liquid water into the crevasses from melt ponds. The meltwater ponds can not form new crevasses, but can penetrate into existing cracks in the ice (Scambos *et al.*, 2000). The melt ponds were observed

in satellite images of Larsen B, and other disintegrated ice shelves (e.g Wilkins Ice ShelfScambos *et al.* 2009). They have also been observed recently on the northwestern side of LCIS (Luckman *et al.*, 2014). The formation of melt ponds on the surface of ice shelves can partially be attributed to the transport of warm, dry air over the AP from föhn winds.

1.5 The History of Föhn Research

In the most general sense, a föhn wind is a warm and dry downslope wind occurring on the leeside of a barrier such as a mountain chain (WMO in Drechsel and Meyr, 2008). Föhn events occur in numerous locations across the globe. The earliest observed, and most well studied location is the Alps in Europe. As early as 1835 Espy hypothesised the descent of air as the true cause of the warmth. However, the credit for föhn theory often goes to Hann (1866).

1.5.1 The Origins of Föhn Winds

Hann (1866) hypothesised that the air temperature increased during föhn events due to adiabatic heating of air descending in the lee of mountains. This hypothesis is still the main reference point for the 'thermodynamic föhn theory', which provides the basis for modern föhn understanding. The thermodynamic theory describes how air from lower altitudes rises up the windward side of an obstacle and cools at the saturated adiabatic lapse rate ($\sim$5K km^{-1}). This air parcel must possess enough momentum to ascend the obstacle, rather than being deflected. The condensation and precipitation of moisture on the windward side releases latent heat. Once the air overcomes the obstacle, it descends down the lee slope and warms at the dry adiabatic lapse rate (10K km^{-1}).

The irreversible release of latent heat associated with condensation and precipitation is partially responsible for the föhn warming and drying, and the thermodynamic mechanism often goes by another name; 'latent heating and precipitation' (Elvidge & Renfrew, 2016). This is often seen as the 'textbook' explanation for föhn development despite warming contributions from other mechanisms (see Section 1.5.2) (Richner &

Gutermann, 2007).

The thermodynamic mechanism for föhn development was generally accepted as the only explanation for the warm and dry conditions for nearly 60 years (Seibert, 2005). The 'isentropic drawdown' mechanism for warming was developed by Ficker (1920). Isentropic drawdown describes the process whereby low level air is blocked from passing over the barrier or mountain, so föhn air is drawn down from altitudes with higher potential temperature (Elvidge *et al.*, 2015; Ficker, 1920). For a while it was assumed that there were only two responsible mechanisms for föhn heating. However by the 1980s, the 'mechanical mixing' and 'radiative heating' mechanisms for warming were discovered (Elvidge & Renfrew, 2016).

1.5.2 Föhn warming mechanisms

Thermodynamic Mechanism

Thermodynamic warming, the most documented and 'original' föhn mechanism, suggests that the warming occurs when an air parcel ascends a mountain (Hann, 1866). Under low wind speed conditions, an air parcel approaching a barrier will be deflected to the right (in the Southern hemisphere due to the coriolis force) by the barrier. However, under higher momentum conditions (faster wind speed) the air parcel rises and ascends the windward side of the mountain. As the moist air rises, it will adiabatically cool at the Dry Adiabatic Lapse Rate (DALR) of 10K km^{-1}, until the dew-point temperature is reached and condensation occurs. The latent heat which is subsequently released from the condensation process provides additional energy for the air parcel to continue rising, and therefore cooling, but now at the Saturated Adiabatic Lapse Rate ($\sim$5K km^{-1}) (Figure 1.10a). If the condensed moisture evaporates in the lee of the mountain, the air mass cools and the process is reversed. Precipitation often occurs on the windward side, which reduces the moisture contained in the air parcel, and prevents the processes from reversing as the moisture is removed up-slope. Once the air has overcome the obstacle, it descends down the leeward slope, and warms by adiabatic compression at the DALR (10K km^{-1}) (Elvidge & Renfrew, 2016; Hann, 1866). This process produces a temperature gradient across the barrier, whereby the air in the lee of

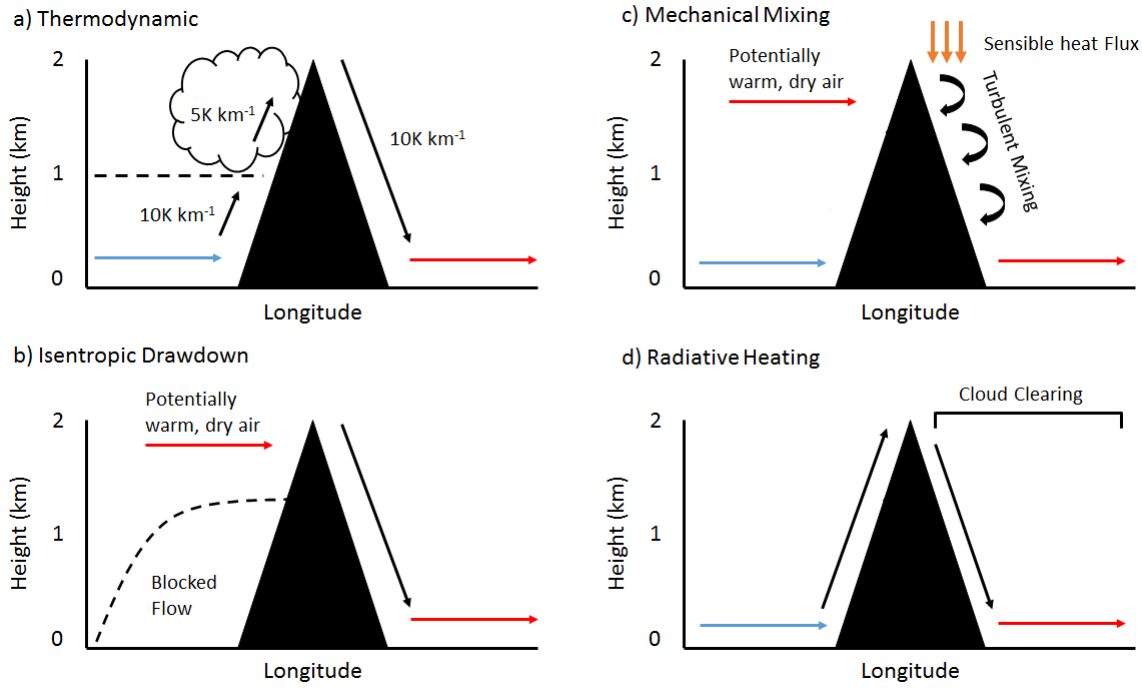

Figure 1.10: The four proposed mechanisms for föhn warming and drying. a) The thermodynamic or 'classical' theory for föhn warming, b) the isentropic drawdown mechanism, c) the mechanical mixing of sensible heat through turbulence, d) radiative heating through the 'föhn clearing' of clouds on the leeside of the AP.

the mountain is warmer and drier than air at the equivalent altitude on the windward side.

Isentropic Drawdown

This mechanism is viewed as the secondary, dynamic method for föhn warming. With this mechanism, the air parcel originates from higher up, rather than ascending the mountain side (Figure 1.10b). This is usually due to a low-level blockage of air on the windward side, or due to barrier-parallel wind at lower levels. In a stably stratified atmosphere, the upper level air is potentially warmer (and often drier). The interaction of the upper level air flow with the mountain advects warmer air towards the leeside surface, and when descending the lee slope, the air mass will warm further at

the DALR. This mechanism still requires the air flow to interact with the mountain (westerly in the AP case) so that the air can flow over to the lee side. However, there is no release of latent heat on the windward side, as is required by the thermodynamic approach. Isentropic drawdown and thermodynamic heating mechanisms were found to be dominant for föhn warming over the AP (Elvidge & Renfrew, 2016; Elvidge *et al.*, 2015).

Turbulent Mechanical Mixing

The third mechanism, mechanical mixing, was largely overlooked until a recent study by Elvidge & Renfrew (2016) demonstrated the contribution to föhn warming and drying by this process. Above complex or rough terrain, in a stably stratified atmosphere, turbulent sensible heating can occur (Figure 1.10c). As cool, moist air from lower levels passes over the obstacle, it mixes with the potentially warmer and drier air from above. This creates a downward (into the föhn air) flux of sensible heat, and an outward (out of the föhn air) flux of moisture (Elvidge & Renfrew, 2016). From 15 cases analysed by Elvidge *et al.* (2016), mechanical mixing dominated the warming mechanism for three of the cases and contributed over 20% of the warming in seven of the cases. Therefore, this mechanism can not be neglected when assessing the föhn warming processes over the AP.

Radiative Heating

The final, and often assumed negligible, heating process is radiative heating. This process does not cause the föhn warming, but can provide additional warming. A direct effect of the föhn winds is 'cloud-clearing' or 'föhn clearing'. The subsiding air in the leeside of the mountain prohibits the formation of clouds (Hoinka, 1985). Consequently, the near-surface air over the LCIS is heated by solar radiation (Figure 1.10d). This mechanism is often excluded as a föhn mechanism, and rather thought of as a secondary effect of the föhn winds, associated with the above three mechanisms (Elvidge & Renfrew, 2016).

1.5.3 Previous Föhn Research

The most documented location in terms of föhn research is the Alps, however they are not the only location to experience föhn winds. Theoretically, any mountain range which is relatively high, and runs perpendicular to strong wind can produce föhn winds. Föhn winds are experienced in many mountainous regions including the Rocky mountains and the Appalachian mountains of the USA where they are termed 'Chinook' (Turner, 1966). They are called 'Santa Ana' in California, 'Zonda' in the Andes and 'North Wester' in New Zealand (Brinkmann, 1971). In 1929, föhn winds were first observed in the Arctic. Schneider (1930) observed the link between föhn events and up to 25K temperature rise during January 1929 in Greenland. However it took another 50 years for föhn research to reach the Antarctic.

The first intensive campaign to address the lack of regional modelling of föhn winds was the Mesoscale Alpine Programme (MAP) in 1999. A number of föhn events from the MAP intensive observational period in 1999 were simulated as case studies (e.g Jaubert & Stein 2003; Zängl *et al.* 2004). Idealised and realistic modelling revealed new information including the interaction between gravity waves and turbulent mixing (Zängl *et al.*, 2004), the formation of gap jets (Jaubert & Stein, 2003), and the complex formation of orographic precipitation (Pradier *et al.*, 2002).

The small amount of literature focusing on Antarctic föhn events is likely due to the continent's vast extent and limited permanent observations. General climatological observations were the first papers to comment on the wind regimes and föhn events in Antarctica. The earliest mention of föhn over the AP was by Schwerdtfeger (1975) who observed föhn on Snow Hill island (64.3°S, 57.1°W) on the northeastern AP. However, further föhn studies were lacking until the 21st century.

The majority of the föhn studies in the Antarctic have focused on the McMurdo Dry Valleys (MDVs) (e.g Monaghan *et al.* 2005; Nylen *et al.* 2004; Speirs *et al.* 2010; Steinhoff *et al.* 2013 and Zawar-Reza *et al.* 2013). They are one of the few ice free locations on the continent, and the US Antarctic Programme have a base situated nearby, therefore observations are more common. Föhn winds have also been observed at Lake Hoare and Taylor Valley (Clow *et al.*, 1988), Lake Vanda (Bromley, 1985) and the Ross

Ice Shelf (Bromwich, 1991). Detailed föhn studies over the AP are restricted to the recent decade.

One of the earliest studies to simulate airflow over the AP was by Orr *et al.* (2004) using the Met Office Unified Model (MetUM). It was found that the westerlies had become stronger since the 1960s, consistent with changes in the SAM, which increased the possibility of air flowing over the AP (Orr *et al.*, 2004). The first study to directly model föhn winds using the MetUM over the AP was Elvidge *et al.* (2015). Elvidge *et al.* (2015, 2016) used the Met Office UM model at 1.5km horizontal resolution to simulate three föhn events over the Larsen ice shelf. 'Föhn jets', cooler, moister bands of air formed by gap flows, were visible from the model output, which had never been identified in this region before.

The WRF model has been used to successfully simulate föhn conditions in numerous studies including Speirs *et al.* (2010, 2013); Steinhoff *et al.* (2013, 2014) over the MDVs, Bannister & King (2015) over South Georgia and Grosvenor *et al.* (2014) over the LCIS. The föhn jets, initially discovered on the LCIS by Elvidge *et al.* (2015), were well resolved by WRF during a case study (6th - 7th January 2011) (Grosvenor *et al.*, 2014). In that study, WRF was able to capture the spatial evolution of wide and narrow jets.

The majority of föhn-modelling studies have simulated the conditions during individual case studies. These have provided insights into the mechanisms responsible for föhn winds, the near-surface characteristics, and features such as föhn jets. The impact of the föhn air on the ice shelf surface has also been assessed during the case studies, and it has been found that föhn winds are responsible for short-lived surface melting (Elvidge *et al.*, 2015; Grosvenor *et al.*, 2014). As far as the author is aware, no study has used model output to identify föhn winds over a longer period, over the AP. Grosvenor *et al.* (2014) highlighted the need for a climatological, or long-term assessment of the impact of föhn winds on the LCIS, such as the one over South Georgia by Bannister (2015).

1.5.4 The Föhn Hypothesis

The collapse of Larsen A and B ice shelves prompted both oceanic and atmospheric research surrounding the AP to determine the cause of the collapse. As part of this research, it was hypothesised that föhn winds could be responsible for surface melting and therefore for the destabilisation of the ice shelves. The föhn hypothesis, originally coined by Marshall *et al.* (2006), and developed further by Elvidge *et al.* (2015, 2016) theorises that the increasing strength of the westerly winds associated with the positive phase of SAM causes an increase in föhn conditions. A positive SAM index prompts a contraction of the winds towards the continent resulting in more frequent airflow over the AP. SAM has mostly been in the positive phase since 1965 (Marshall, 2003).

A laboratory study by (Orr *et al.*, 2008) discovered that air flow over the AP is dynamically possible, and that downslope winds and a hydraulic jump are present in the lee during these times. The idealised laboratory conditions were followed up with 12km horizontal resolution model runs using the MetUM. This detected determined the presence of föhn winds over the LCIS, and found that significant upper-level warming was only present on days with föhn winds present. However, this warming was not identified at the surface due to strong cold pooling over the LCIS. The lack of surface warming was likely due to the coarse resolution of the model and an exaggeration of sea ice to the north east of the LCIS (Orr *et al.*, 2008). Therefore further studies were required to investigate whether the föhn air can penetrate to the surface.

After the earliest observations of föhn winds over the AP by Schwerdtfeger (1975), the next observations were during summer 2006. Aircraft observations demonstrated that warm air advection from a föhn episode prompted the development of a strong, stable boundary layer. During the föhn event, the relative humidity in the lee was significantly drier, and the potential temperature higher than on the windward side (King *et al.*, 2008). Model output from the Antarctic Mesoscale Prediction System (AMPS) also reproduced the föhn air over the LCIS.

The Orographic Flow and Climate of the Antarctic Peninsula (OFCAP) project was devised to investigate the various interactions of the air with the AP, including gap jets and föhn winds, using observations and numerical weather prediction tools at

a high horizontal resolution. A field campaign was conducted in January and February 2011. As part of this, an Automatic Weather Station (AWS) was deployed at the foot of the AP mountains. Aircraft-based instruments and radiosonde releases also measured the near-surface and upper-air characteristics during the field campaign. Observations from the deployed AWS were used in this project.

1.5.5 Föhn Winds on the LCIS

It has been found that föhn winds originate over the AP and propagate across the LCIS. Two features control the spread of the föhn air over the LCIS. The first is the occurrence of föhn jets. These are narrow, elongated flows of air that are propelled through passes in the topography of the AP. Whilst these jets are cooler and moister than the surrounding föhn flow, they are still warmer and drier than the stagnant air they replace, and therefore the potential surface impacts are greater, as these jets can occur under relatively weak föhn events (Elvidge *et al.*, 2015). Föhn jets were identified from three case studies by Elvidge *et al.* (2015) using observations and the MetUM model and by Grosvenor *et al.* (2014) in the Polar WRF model.

The second control over the propagation of föhn air is the flow regime. The upwind flow regime is described by the Froude number (Fr):

$$Fr = \frac{u}{Nh} \tag{1.1}$$

where u is the mean flow, h is the height of the obstacle (2000m in the case of the AP) and N is the Brunt-Väisälä frequency given by:

$$N^2 = \frac{-g}{\rho}\frac{d\rho}{dz} \tag{1.2}$$

where ρ is the fluid density, g is the acceleration due to gravity and z is the vertical coordinate. N is usually given as 0.012s^{-1}, which is typical for approaching flow. The Brunt-Väisälä frequency describes the static stability of an air mass. The Froude number is the ratio of the kinetic energy of the upwind flow, to the potential energy needed to flow over the mountain. When the Froude number is large (Fr > 1), the flow is supercritical or linear, and flow over the AP is likely. In Bannister (2015), a Froude

value equal to or greater than 1.0 was used as a criterion for föhn winds in the lee of the mountains of South Georgia. When the Froude number is small (Fr < 1), the flow is subcritical, or non-linear, and the air flow is more likely to flow around the mountain due to blocked flow at lower levels (Durran, 1990; Elvidge *et al.*, 2016).

According to Elvidge *et al.* (2015) föhn winds in the lee of the AP are possible under both linear and non-linear upstream flow. The linear regime was associated with föhn winds generated by the thermodynamic mechanism. Low-level blocking during non-linear (Fr < 1) flow leads to upper-level air interacting with the AP, and the isentropic drawdown mechanism dominating Elvidge *et al.* (2016). It was found that during non-linear flow the warming was greatest at the foot of the mountains, but the warming was spatially restricted, and the föhn effect diminished with distance from the AP. Largely, this was due to the presence of a hydraulic jump, forcing the warm, dry air to flow upwards in the immediate lee of the AP (Elvidge *et al.*, 2016). Under a linear flow regime, the föhn flow remains subcritical and hydraulic jumps are absent. The föhn effect propagated further under linear flow, but was weaker.

The use of case studies for investigating föhn winds has both advantages and disadvantages. Field campaigns generate a large number of observations, but they can not be sustained over a longer period due to the labour intensive fieldwork. High-resolution modelling of the case studies provides further spatial and vertical representation of the föhn winds, but these are computationally expensive for long-term runs.

Further investigation of AP föhn winds may not be possible with case studies alone. Observations of föhn events have been restricted to a handful of cases, during field campaigns in summer. Making assumptions of the impact of föhn winds over the whole LCIS currently relies on these case studies. Therefore, these assumptions are skewed towards summer föhn events in particular years. Case studies provide no information about the frequency of föhn, their longer-term spatial distribution, any temporal patterns, or the impact they have during the other seasons. Case studies may highlight only very strong föhn winds which had a significant impact on the LCIS, or showcase very weak föhn winds, and assume they have little influence on the surface conditions.

The only study (that the author is aware of) in which föhn conditions are analysed over a sustained period of time is Cape *et al.* (2015). This study includes a climatology of föhn conditions by using the Matienzo AWS (located on the northeast of the AP between Larsen A and Larsen B ice shelves) which was active from 1962 to 2010. The other observations used were located over the northern AP, where Larsen A and B were located. It was determined that the frequency of föhn winds is linked to larger scale variability, mostly the SAM and ENSO. Shorter timescale patterns were also determined, including a seasonal cycle, with föhn frequency peaking in spring (SON).

Cape *et al.* (2015) provides additional support for the föhn hypothesis, as it was found that the years 1999, 2000 and 2001 experienced more föhn periods per month than other years. These years precede the breakup of Larsen B in 2002. This study was confined to the northern AP. Due to the more southerly location of the LCIS, it was suggested that föhn are less prevalent there as storm tracks are often further north (Cape *et al.*, 2015).

With föhn winds being a common feature of mountains regions across the globe, it is likely that research will continue. Current research efforts in the Alps region are focusing on optimising forecasts. Whilst forecasting föhn is also useful within the Antarctic for aircraft operation and safety, understanding the characteristics of föhn, and their impact on the ice shelf stability is of greater importance currently. A particular föhn event in March 2015 became international news due to its strength and links to potential climate change over the AP. Temperatures exceeding 17°C were observed by one AWS on the northern Peninsula (Skansi *et al.*, 2017).

1.6 Surface Energy Balance of the Antarctic Peninsula

The Surface Energy Balance (SEB) describes the interaction between the atmosphere and surface in terms of energy and momentum. Changes in wind speed, temperature, humidity and cloud cover all influence the transport of energy to and from the surface, and therefore influence the SEB. The synoptic conditions largely control the SEB. Air masses travel over oceans and land surfaces, resulting in different temperature and

humidity regimes (Braun *et al.*, 2001). The SEB comprises of the radiation terms (shortwave and longwave radiation), the turbulent fluxes (sensible and latent heat) and the ground heat flux. Over an ice shelf (or other snow and ice covered land), the residual energy remaining in the system is used to heat or melt the snow surface.

Understanding the SEB of ice- and snow-covered locations is necessary for predicting the consequences of a changing climate, and to estimate melting and the potential retreat of glaciers. Observing components of the SEB is crucial, as they are often parameterised in general circulation and region models. The SEB of the Antarctic is quite different to that in most other locations. The surface albedo is high (80-90%), and there are large seasonal variations in incoming solar radiation (Van As *et al.*, 2005). During the winter season, and darkness, a stable boundary layer often forms due to the cooling from net longwave radiation, and a lack of convection. During summer and daylight, convection is possible, developing an unstable (although thin) boundary layer (Van As *et al.*, 2005).

Several studies have focused on the SEB of the AP region, including Braun *et al.* (2001); King & Anderson (1994); King *et al.* (1996); Kuipers Munneke *et al.* (2012); Välisuo *et al.* (2014); Vaughan (2006) and King *et al.* (2015). Early SEB studies focused on calculating turbulent fluxes and appropriate parameters such as the surface roughness value (King & Anderson, 1994). SEB observations and mass balance estimates were conducted on the Brunt ice shelf by King *et al.* (1996). The influence of large scale circulation on the SEB has also been assessed on King George Island (Braun *et al.*, 2001). A number of SEB studies have focused on the LCIS. The reduction in solar radiation during austral winter (JJA) and near continuous exposure to solar radiation during austral summer (DJF) provide opposing conditions to investigate. The ice shelf was termed a 'natural laboratory' by Elvidge *et al.* (2015, 2016). King *et al.* (2015) validated three regional models to assess their success at simulating near-surface variables and SEB components over LCIS. Many of these studies were limited to the summer season, due to accessibility and field campaigns. However, Kuipers Munneke *et al.* (2009) and Kuipers Munneke *et al.* (2012) developed a SEB model, and analysed the SEB from the model output for a number of years.

Prior to the collapse of Larsen A and B ice shelves in 1995 and 2002 respectively, high surface melting rates were observed (e.g Sergienko & Macayeal 2005; Trusel *et al.* 2015; Van Den Broeke 2005). Van Den Broeke (2005) identified that surface melting prior to the collapse of Larsen B (Dec 2001 - Feb 2002) was three times greater than the average of the previous five years. The number of melt days, number of melt hours, melt duration and melt rate were all higher than average during the 2001/2002 austral summer season (Van Den Broeke, 2005). According to Trusel *et al.* (2015), melt water production on both Larsen A and B peaked just prior to each collapse, and was significantly higher than on surrounding, stable ice shelves.

Melt episodes are largely related to high incoming solar radiation and high sensible heat fluxes. Föhn winds can cause larger than average sensible heat flux and net shortwave radiation. As the sensible heat flux is dependent on the wind speed and temperature, it is often significantly higher (more downward fluxes) during föhn events (Elvidge *et al.*, 2015). Incoming solar radiation also increases as the dry air gives rise to cloudless skies.

1.6.1 Surface Energy Balance and Föhn Events

Melting of the surface ice and snow can be initiated by the advection of warm air, such as during föhn conditions. The radiation terms dominate the SEB during föhn (and non-föhn conditions). Increased downward shortwave radiation is often observed during summer föhn events, due to the föhn clearance of the clouds (Elvidge *et al.*, 2016). The majority of studies investigating the impact of föhn winds on the SEB have focused on the Antarctic. Only a few studies on locations outside of the Antarctic have been conducted. Melting of snow and subsequent evaporation during föhn conditions has been observed in mountainous regions of both the USA and Japan (Hayashi *et al.*, 2005; Hood *et al.*, 1999). Other studies have focused on the impact of föhn on agriculture through changes to the soil moisture (e.g Golding 1978; Grace 1990).

Inside the Antarctic, a number of studies have addressed the influence of individual föhn events on the SEB (Elvidge *et al.*, 2016; Hayashi *et al.*, 2005; Hood *et al.*, 1999; King *et al.*; Kuipers Munneke *et al.*, 2012; Van Den Broeke, 2005). Van Den Broeke

(2005), Kuipers Munneke *et al.* (2012) and Välisuo *et al.* (2014) linked the advection of warm air from the föhn winds to the surface melting on LCIS. The summer of 1992/1993 was characterised by predominant north-westerly winds which prompted anomalously high surface fluxes, leading to considerable surface melting (Välisuo *et al.*, 2014). The north-westerly winds advected warm air towards the surface, thus linking the influence of föhn air to the high heat fluxes.

Van Den Broeke (2005) identified that maximum melt rates over Larsen B ice shelf occurred during days of northwesterly air flow, when warm air advection from the föhn effect was present. Kuipers Munneke *et al.* (2012) analysed the föhn impact on the SEB during November 2010. During the föhn period, there was low net longwave and high net shortwave radiation and a significant positive sensible heat flux (Kuipers Munneke *et al.*, 2012). Elvidge *et al.* (2016) analysed the SEB response to three separate föhn events over the northern LCIS during summer 2010/2011. Two different flow regimes influence the extent and amount of melting over the LCIS. During linear föhn events, the melting is more widespread but less intense, whereas during nonlinear flow, the melting is more localised to the foot of the AP, but more intense (Elvidge *et al.*, 2016). Surface melting and ponding has been observed over the LCIS from satellite images (Figure 1.11). The increased melt days and observations of melt ponds near the AP are believed to be caused by (the occurrence of) föhn winds (Luckman *et al.*, 2014).

Most recently, King *et al.* has shown that föhn events during November 2010 can increase the frequency and duration of melting episodes over the LCIS. As only one season is analysed, it is difficult to say whether this result is true of all years, or whether spring 2010 was significant due to a larger number of föhn conditions, or a clustering of föhn events which amplified the effect. All of the current published work investigates the impact of individual or a small number of föhn events on the SEB of the ice shelf. The combined influence of year-round föhn winds on the SEB of the LCIS is presented in this thesis.

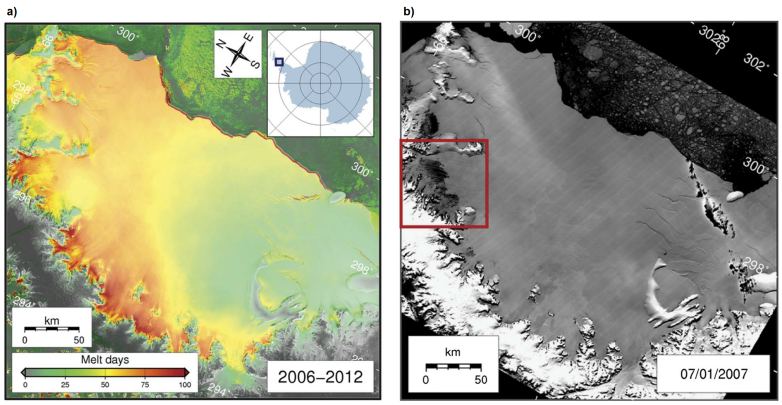

Figure 1.11: a) The annual surface melt duration (days) from 2006-2012 calculated from synthetic aperture radar, over the LCIS. Figure taken from Luckman *et al.* (2014) Figure 1. The red and yellow colours near the AP reveal a higher number of melt days. b) Near-infrared image of LCIS from MODIS channel 2 satellite on the 7th January 2007. The red box highlights areas of dark patches which are interpreted as water on the surface. Figure from Luckman *et al.* (2014) Figure 4.

1.7 Justification of Research

The examination of the impact of föhn winds on the LCIS is a relatively new research area. Until the International Geophysical Year (1957-1958), there were no regular near-surface observations of meteorological conditions on the ice shelf. In 1985 the 'Larsen Ice' AWS (67.01°S, 61.5°W) was installed, providing a near-continuous record of near-surface meteorological conditions (Van Den Broeke, 2005). The collapse of Larsen A and Larsen B ice shelves in 1995 and 2002 respectively prompted an increase in atmospheric research of the AP and LCIS region. The removal of ice shelves leads to significant glacier acceleration and hence loss of land ice into the ocean. The collapse of eastern AP ice shelves is interesting, as the east side can be up to 10K colder than on the west coast (Morris & Vaughan, 2003). In an attempt to determine the mechanisms responsible for the collapse of the large ice shelves, numerous field campaigns were launched, and the föhn hypothesis was developed.

The föhn hypothesis suggests that significant surface warming of the north-east region of the AP is due to increased frequency of föhn winds advecting warm, dry air

onto the ice shelves (Marshall *et al.*, 2006). A study by Van Den Broeke (2005) alluded to the presence of föhn air being responsible for high rates of surface melting on the Larsen ice shelf during the 2001/2002 summer season in which Larsen B collapsed. The first aircraft-based observations of föhn winds over the AP were during summer 2006 (King *et al.*, 2008).

Flow over the AP leading to adiabatic heating on leeside descent, was successfully reproduced in laboratory experiments by Orr *et al.* (2008). Furthermore, upper-atmosphere observations suggested that there had been a change in the upwind flow regime to a 'flow-over' regime, indicative of frequent föhn events, between 1965 and 1997 (Orr *et al.*, 2008). The installation of numerous, permanent AWSs from 2008 to 2011 has allowed the near-surface conditions of the LCIS to be monitored and analysed. The OFCAP project was devised to investigate the various interactions between the AP and airflow, including gap jets and föhn winds, using observations and numerical weather prediction tools at a high horizontal resolution. Aircraft and radiosonde observations from the OFCAP project were compiled and analysis has been presented in recent papers by Elvidge & Renfrew (2016); Elvidge *et al.* (2015); Grosvenor *et al.* (2014); King *et al.* (2015) and Elvidge *et al.* (2016).

In studies by Grosvenor *et al.* (2014); Kuipers Munneke *et al.* (2012) and Elvidge *et al.* (2016), the potential impacts of individual föhn events were presented. It was concluded by all three studies that föhn winds can cause melting of the ice shelf surface, but that the spatial extent of the melt can be limited. Northern sections of LCIS had similar melt rates to those identified on Larsen B prior to collapse. However, melt rates on the southern section of the ice shelf were much lower (Grosvenor *et al.*, 2014). Kuipers Munneke *et al.* (2012) and Elvidge *et al.* (2015) found that during föhn events, surface melt was observed over 100km from the foot of the AP.

Case studies of föhn winds have revealed crucial information about their dynamics and their melting potential over the LCIS. However, as the majority of föhn case studies have been during austral summer, the temporal persistence and patterns of föhn conditions throughout the year was not previously investigated. Similarly, many of the studies focused on the northern section of the LCIS, as evidence has shown this

area to be most at risk from destabilisation prompted by föhn-induced surface melting. The acceleration of the northwards propagating rift on the LCIS has now exposed the sensitivity of the southern section of the ice shelf as far south as 68.5°S, although no study has assessed the impact of föhn winds south of 67°S.

Spatially vast studies of föhn conditions over the LCIS are sparse. Luckman *et al.* (2014) used satellite images and Synthetic Aperture Radar to study the surface melting over the whole LCIS from 2006 to 2012. The melt duration had increased during the study period, and earlier melt onset and later re-freezing from east to west were also discovered (Luckman *et al.*, 2014). These melt patterns were explained by the föhn warming effect, and it was concluded that föhn conditions enhance surface melt close to the foot of the AP. This study did not however directly observe the föhn events, or analyse their spatial or temporal extent. The only spatially and temporally extensive study of föhn winds within the AP region is that by Cape *et al.* (2015). They analysed a number of AWSs over the northern AP, from Scar Inlet to the tip of the AP. No observations or analysis of föhn events on the LCIS were presented, however assumptions of the LCIS föhn events were discussed. Therefore, as far as the author is aware, no spatially-comprehensive, temporally-extensive study of föhn winds and their impacts on the LCIS is available.

In this thesis observations from four years, at six locations on the LCIS, will be used to provide a greater understanding of the potential impact of föhn over the LCIS. Archived model runs are available for the AP, which cover a wider spatial scale than observations alone. Föhn conditions will be identified from observations and archived model output using two föhn detection algorithms. One algorithm is novel, and was developed as part of this study. The other is yet to be applied to the LCIS. Identifying föhn conditions will build a picture of the spatial distribution and temporal patterns of föhn winds. The impact of the föhn winds on the surface energy balance of the ice shelf can then be quantified.

1.8 Research Aims

The overarching aim of the research presented here is to investigate the spatial distribution and frequency of föhn winds over the Larsen C ice shelf, and assess their impact on the surface of the ice. As föhn events are responsible for initiating short-lived surface melting episodes (Elvidge *et al.*, 2016; Grosvenor *et al.*, 2014), it is crucial to assess their spatial extent and temporal patterns. Current estimates of the föhn impact are reliant on case studies during summer field campaigns. This could lead to an over- or under estimation of their impact due to spatially and temporally limited cases. From the spatial and temporal analysis, the impact of the föhn conditions over the four years, and over the whole ice shelf will be investigated and presented in this thesis.

The project is split into a number of smaller, defined aims, in particular: to identify föhn winds over the ice shelf; to provide a mini-climatology of the near-surface conditions during föhn events; to assess the impact on the surface of the ice shelf. They are described in more detail below. The data and methods used to fulfil these aims are described in Chapter 2 and 3, and the results are presented in Chapters 4, 5 and 6. The research aims are as follows:

- ***Develop and employ a föhn detection algorithm for both near-surface observations and archived model output.*** There is currently no process, specific to the LCIS, to detect föhn conditions from observational data. Therefore an algorithm will be developed to identify föhn winds from AWS data at six locations across the ice shelf. To detect föhn conditions from the archived model output, a relatively new method used over South Georgia by Bannister & King (2015) will be adapted for the LCIS. The development of the thresholds, and the final algorithms are presented in Chapter 3. Based on the identified föhn events, further analysis will follow, outlined below.

- ***What is the spatial distribution of föhn conditions across the LCIS?*** Previous studies have revealed that the föhn effect can be widespread or limited to the foot of the AP (Elvidge *et al.*, 2016) depending on the mechanism. The dominant distribution of föhn conditions is yet to be known. Observations of föhn

conditions have so far been limited to north of ∼67°S. The analysis of the spatial distribution presented here will span from 65.9°S to 68.1°S, and from the foot of the AP, almost to the edge of the ice shelf. The results are presented in Chapter 4.

- ***How frequent are föhn events over the LCIS?*** Thus far, föhn studies over the LCIS have been restricted to relatively short case studies, often during summer. The föhn hypothesis suggests that the frequency of föhn events has increased since the 1960s, however the current frequency of föhn conditions is unknown. The frequency of föhn conditions from 2009 to 2012 is assessed. The frequency of föhn conditions is also crucial for understanding their influence on surface melt. If föhn conditions are persistent, especially during the austral summer, then surface melting is more likely to occur than if föhn conditions are infrequent or limited to the austral winter. These results are presented along with the spatial distribution of föhn winds in Chapter 4.

- ***What is the impact of föhn conditions on the ice shelf, and in particular do föhn winds initiate surface melting?*** Output from a SEB model will be analysed during föhn and non-föhn conditions to assess the long-term impact of föhn winds on components of the SEB. The amount of surface melt induced by föhn winds is estimated from observations and archived model output. Chapter 5 presents the impact of föhn events on the surface energy balance.

- ***Can high-resolution modelling of individual föhn events reveal additional information about the horizontal and vertical structure of the föhn winds?*** High-resolution simulation of individual föhn events can provide additional, detailed spatial information. The WRF model at 1.5km horizontal resolution and with 70 vertical levels will be used. High horizontal resolution will resolve the topography and small-scale features with more accuracy than the lower-resolution archived model output. The large number of vertical levels will accurately resolve the boundary layer processes and vertical structure of the föhn winds. Three case studies are presented in Chapter 6

The next chapter of the thesis is the data description chapter. Following that, the outline of the thesis follows the research questions presented above. The thesis will

conclude with a synthesis of the main findings and a discussion of the wider implications and potential future work.

Chapter 2

Data Description

2.1 Introduction

Geographically, this study covers a large and complex region. The AP is a long, narrow mountain range, which intersects the predominant air flow. More specifically, the LCIS is the focus of this project. This is the largest remaining ice shelf on the AP with an ice area over 51,000km^2 (Cook & Vaughan, 2010). The network of point-measurement observations is comparatively small, due to the poor accessibility of the region, and the harsh climate. Regional modelling has improved our understanding of the climate and meteorology of the region. Following on from the aims provided in Chapter 1, two main datasets were used to answer the research questions. This study made use of a network of six observational weather stations on or around the LCIS; one of the larger networks within Antarctica. To complement these point measurement data, model output covering the larger geographical region were used. This chapter will begin with a description of the observational data and pre-processing. Following this, the Weather Research and Forecasting (WRF) model is introduced. The model usage is split into two sections; coarser resolution archived output and higher resolution runs of particular case studies. More information on the case studies is given in Chapter 6.

2.2 Observational Data

Automatic Weather Stations (AWS) on the western side of the AP have been observing near-surface meteorological conditions prior to the International Geophysical Year

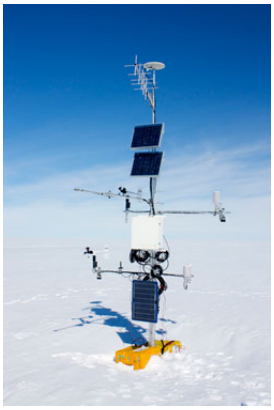

Figure 2.1: Photograph of a CIRES AWS deployed on the Larsen C ice shelf. Photo credit: cires.colorado.edu.

(1957-1958) at a number of locations (King & Anderson, 1994). However, deploying instruments on the ice shelves was more difficult due to their more inaccessible location. Therefore, the near-surface of the LCIS was largely unobserved until the 21st Century. The observational period used within this study runs from 1st January 2009 to 31st December 2012. A number of AWSs were deployed in December 2008 (Figure 2.1), however from 2009 to 2012, a larger number of stations were available. Some of the AWSs are still operational (at the time of writing in January 2017), however the densest observational network was during 2009-2012, providing a long enough timescale to make inferences about the temporal and spatial patterns.

Near-surface meteorological records from six AWSs provide the observational data for this study. These stations observed various near surface meteorological variables including temperature, humidity and wind speed. Four AWS were located on the surface of the LCIS, one located on Cole Peninsula, and one located on Scar Inlet. A further station was available (referred to as AWS4), but was only operational for 35 days, therefore this was not used within the project. The AWSs can be separated into three groups as follows.

The first group includes one AWS, referred to as 'Cole Peninsula AWS' (shortened to CP on some figures) throughout this thesis. This AWS was deployed as part of

the OFCAP field campaign (see Chapter 1) in January 2011 by BAS personnel. The second group is referred to as the IMAU group; so called as the three AWSs within it are owned by the Institute for Marine and Atmospheric research Utrecht (IMAU) in the Netherlands. These AWSs are referred to as AWS1, AWS2 and AWS3 in a north to south order (Figure 2.2). Group three is referred to as CIRES group as the three AWSs within it were deployed and owned by the Cooperative Institute for Research in Environmental Science (CIRES), a joint institute of the National Oceanic and Atmospheric Administration (NOAA) and the University of Colorado at Boulder, USA. These AWSs are referred to as AWS4, AWS5 and AWS6 in a north to south order.

All AWSs provided measurements of temperature, pressure, wind speed, wind direction, relative or specific humidity (which was then used to calculate relative humidity). Some also measured variables such as incoming or net radiation or the distance from the surface to sensor (which can be interpreted as changes in snow height). Details of the specific variables observed by each AWS are given in Table 2.1. Further information on the three groups is as follows.

2.2.1 Cole Peninsula AWS

The Cole Peninsula AWS (CP in Figure 2.2) was in operation from January 21st 2011 to January 8th 2012. It was roughly 420m a.s.l, located on an elongated, ice/snow covered feature at the base of the eastern side of the AP called Cole Peninsula. This station was well located to capture the onset and cessation of föhn events as they descend down the leeside of the AP. Data were logged every 10 seconds, and recorded as 10 minute averages (see Table 2.1). The air pressure was observed using the SPC1000 sensor, with an accuracy of 0.1hPa. Air temperature and relative humidity measurements were made using Vaisala HMP45D temperature and humidity probes. The accuracy of the temperature probe was 0.3°C. For relative humidity, the accuracy was 2% for up to 90% relative humidity, and 3% for values ranging from 90-100%. Wind speed and direction were measured using the Young 05103 sensor, and the accuracy was 0.3ms^{-1} for wind speed and 3° for direction.

Table 2.1: AWS Metadata for the seven stations available. BAS stands for British Antarctic Survey, IMAU is the Institute of Marine and Atmospheric research, Utrecht, University of Utrecht and CIRES is the Cooperative Institute for Research in Environmental Sciences, University of Colorado. T - air temperature, RH- relative humidity, FF- wind speed, DD- wind direction, P- pressure, SW- shortwave radiation, LW- longwave radiation, NetRad- net radiation (SWnet + LWnet), H- snow height, q - specific humidity, *- observations at two levels, $^{+}$- data from this AWS is not used.

AWS # (Ownership)	Location	Height meters	Frequency (Stored Avs)	Parameters Observed (calculated)	Dates Available
Cole Peninsula (BAS)	66.85S 63.8W	420m	10secs (10mins)	T, RH, FF, DD, P	22.01.2011- 08.01.2012
AWS1 (IMAU)	65.93S 61.85W	50m	6mins (60mins)	T, RH, FF, DD, P, SWin, SWout, LWin, LWout, (q), (H)	19.02.2011- 11.03.2014
AWS2 (IMAU)	67.02S 61.5W	50m	6mins (60mins)	T, RH, FF, DD, P, SWin, SWout, LWin, LWout, (q), (H)	22.01.2009- 11.03.2014
AWS3 (IMAU)	67.57S 62.15W	50m	6mins (60mins)	T, RH, FF, DD, P, SWin, SWout, LWin, LWout, (q), (H)	21.01.2009- 11.03.2014
AWS4^{+} (CIRES)	67.43S 62.88W	42m	10secs (60mins)	T, RH, FF, DD, P (H)	06.01.2011- 09.02.2011
AWS5 (CIRES)	67.57S 63.26W	42m	10secs (60mins)	T*, RH*, FF*, DD*, P, H*, Swin, SWout, NetRad	22.12.2008- 15.11.2011
AWS6 (CIRES)	68.14S 63.95W	53m	10secs (60mins)	T*, RH*, FF, DD, P H*	24.12.2008- 26.12.2012

Data from the Cole Peninsula AWS was used from the 06UTC 22nd January 2011 to 18UTC 31st December 2011.

2.2.2 IMAU AWSs

These stations are located furthest east on the LCIS. All three AWS are still in operation, however data are only used up until 31st December 2012 for consistency with other locations. AWS 1 is the northernmost station and is located on Scar Inlet, the remnants of Larsen B ice shelf, 50m a.s.l. AWS 1 is the most recent addition to the IMAU AWS group, commencing on the 19th February 2011. AWS2 and AWS3 are roughly 50m asl, and 70km apart in a north-south direction. These provide the longest continuous data sets for this study. Measurements at AWS3 started on 21st January 2009, and AWS2 started on 22nd January 2009. The frequency of observations is 6 minutes, and data are stored as hourly averages in a logger, or transmitted via an argos satellite system approximately hourly (Tijm-Reijmer C., personal communication, March 11th 2014). An exception to this, the air pressure, is observed and stored as hourly instantaneous data.

The air temperature and relative humidity instruments were the Vaisala HMP35AC, which has the same accuracy as the HMP45D used at Cole Peninsula. Air pressure was measured to an accuracy of 0.5hPa using the Vaisala PTB101B sensor. The same wind speed sensor was used as at Cole Peninsula. Young 05104 was used to measure wind direction (3° accuracy). The shortwave incoming and outgoing radiation was observed using the Kipp en Zonen CNR1 and CNR2 pyranometers (respectively), both with 2% accuracy. Similarly, the incoming and outgoing longwave radiation was measured using the Kipp en Zonen CNR1 pyradiometer with a $15\mathrm{Wm}^{-2}$ accuracy.

Data from 00UTC 19th February 2011 to 18UTC 31st December 2012. Data from AWS2 and AWS3 was used from 06UTC 22nd January 2009 to 18UTC 31st December 2012.

2.2.3 CIRES AWSs

The three AWSs in this group were not all operational at the same time. The AWS with the shortest operational period was AWS4 which was active for 35 days from 6th January 2011 to 9th February 2011. AWS5 was operational from 22nd December 2008 to 15th November 2011. The longest running station is AWS6; operational from 24th December 2008 to present. Observations were logged every 10 seconds and stored as hourly averages. The data were transmitted hourly via a GOES satellite. AWS6 was located 53m asl, and AWS4 and AWS5 were 42m a.s.l (Steffen K., personal communication, throughout 2014). AWS4 was discarded from further use within this study due to its short observational period.

The CIRES AWS sensors included the Vaisala PTB101B sensor to measure air pressure (0.5hPa accuracy) and the Young 05103 and 05104 sensors for wind speed and direction (respectively) were used (see above for accuracy). The same shortwave incoming and outgoing sensors were used (at AWS5) as the IMAU AWSs. The distance between the surface and the sensor, to infer snow accumulation, was measured by Campbell SR50 with a 0.01m accuracy.

Data from 00UTC January 1st 2009 to 12UTC November 15th 2011 was used from AWS5. Data from 00UTC January 1st 2009 to 18UTC 25th December 2012 was used for AWS6.

2.2.4 Observational Data Pre-Processing

In many circumstances errors within data are known and calculations can be made to correct the data, for example, adjusting for sensor height change due to snow accumulation. In other cases the errors are unknown or unquantifiable and the limitations must then be stated when making assumptions about the results. For the CIRES and IMAU AWSs, the data were quality controlled and pre-processed before being made available to this project. Outliers still remained in the IMAU data from frozen sensors and transmission problems. Occasionally the argos data transmission failed, and data were then interpolated from measurements either side of the hour (Tijm-Reijmer C.,

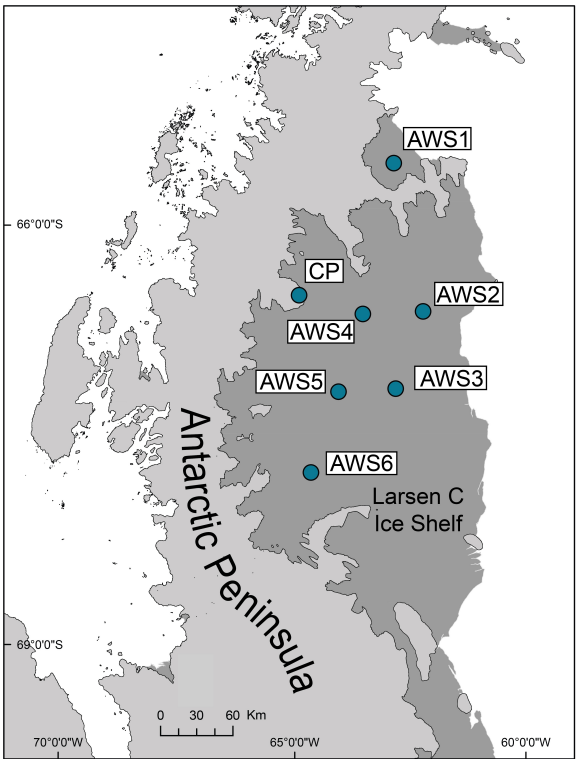

Figure 2.2: Map of the Larsen C ice shelf with AWS locations and names. The Cole Peninsula AWS has been abbreviated to CP for this figure. Data from AWS4 is not used in this project. Figure credit: W. Dickens, British Antarctic Survey.

personal communication, March 11th 2014). Quality control and pre-processing of the Cole Peninsula AWS data was carried out in the framework of the OFCAP project prior to this study.

There were specific data errors or outliers in the observations related to the climate of the Polar Regions. For example, riming occurs where ice particles form on instruments when relative humidity is at 100% and the temperature is below freezing (Makkonen & Laakso, 2005). This is particularly common with sonic wind anemometers, which are used at the IMAU AWSs. The ice particles block the sonic wave receivers and no wind speed is recorded. In that case, a reading of 0° wind direction and 0ms^{-1} wind speed were recorded. In a study of the surface energy balance over the LCIS by (Kuipers Munneke *et al.*, 2012), any gap in the wind speed at AWS2 or AWS3 were filled by data from the other station. That approach was not applied during this study, due to the importance of assessing spatial variations in meteorological conditions. Instead, erroneous data were flagged and removed from analysis.

The relative humidity values were corrected for two common issues in cold climates. Firstly, when temperatures are below 0°C, there are two definitions of relative humidity; being measured with respect to water, or with respect to ice (Anderson, 1994). The saturated vapour pressure over ice is lower than over water at the same temperature. The relative humidity values that were observed when the air temperature was below 0°C were converted to relative humidity with respect to ice. The observations were multiplied by a ratio of the saturated vapour pressure over ice to that over water. Figure 2.3a and 2.3b display the effect of the correction technique on observations of relative humidity used byAnderson (1994).

The second adjustment made for relative humidity observations was to correct the data for observations outside of the instruments calibrated range, using the technique detailed in Anderson (1994). The calibrated temperature range of the humidity sensor (HMP35A) was from -20°C to +65°C. Figure 2.3b shows that there is a maximum value of humidity that can be measured depending on the air temperature. In very cold temperatures ($<$ -35°C), the sensor accumulates moisture which, when frozen, coats the sensor in ice. This prevents the sensor from observing supersaturated conditions

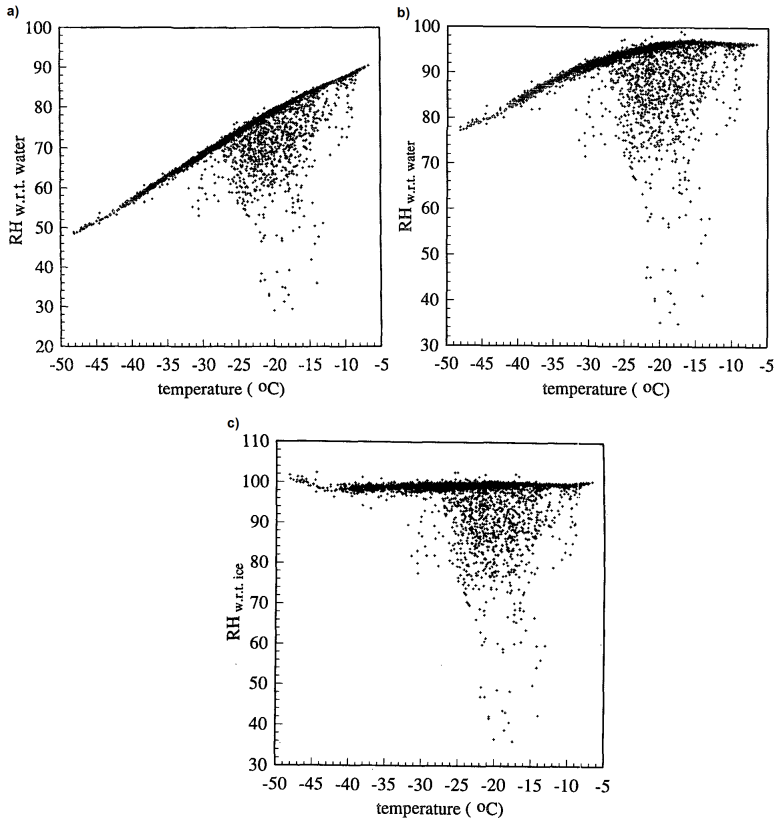

Figure 2.3: Plots from Anderson (1994) outlining the effect of the methods to correct the relative humidity with respect to ice, and to correct for observations outside of the instrument calibrated range. a) The relative humidity values observed on the Brunt Ice Shelf with respect to water. b) The recalculated (with respect to ice) values from Figure a. c) The relative humidities of Figure b, once the data have been rescaled for temperatures outside of the calibrated range.

when the air diffuses through the ice layer. The relative humidity values were rescaled for the full temperature range of the data to correct for the maximum relative humidity during very cold temperatures. The rescaling method is described in Anderson (1994), and the results of such are presented in Figure 2.3c.

Whilst the sample rate at each station is relatively frequent, the data have been averaged into six-hourly intervals, centre averaged around 00, 06, 12, and 18UTC. This temporal resolution was chosen to allow enough time for the onset and cessation of a föhn to be observed, and ensure that the föhn event lasted long enough to have an impact on the surface of the ice shelf. Similarly, the time interval was short enough to observe the transient nature of the föhn, and short lived events. The averages were centred around the above mentioned times to complement the six-hour archived model output (Section 2.3). Throughout the remainder of the thesis, six-hour averaged timesteps were used for the observational data reported, unless otherwise stated.

2.2.5 ERA-Interim

In 2011 the European Centre for Medium Range Weather Forecasts (ECMWF) released ERA-Interim, a reanalysis product. ERA-Interim covers the period from 1979 onwards, and is extended in near-real time (Dee *et al.*, 2011). Reanalysis products combine recorded observations, forecasts and model output through data assimilation and are often referred to as observations. The use of ERA-Interim in this project is two-fold.

Firstly, ERA-Interim data are used to assess the synoptic conditions prior, during and after the föhn events analysed in the case studies in Chapter 6. Due to the relatively sparse observational network, ERA-Interim is considered the best dataset to use when assessing the synoptic conditions in the Antarctic (Bracegirdle & Marshall, 2012). Secondly, ERA-Interim can be used to force the lateral and initial boundary conditions in the WRF model. Although ERA-Interim was not used to initialise WRF in this project, it was tested during the Summer case study (see Chapter 6).

2.3 Model Data

The second data set used within this study was model output from the Weather Research and Forecasting (WRF) model. WRF has primarily been used to provide more information on the spatial distribution and frequency of föhn winds. Comparing the WRF model with the observations also allows the model to be validated over the LCIS.

The WRF data used here can be split into two subcategories; 5km WRF archived output within the Antarctic Mesoscale Prediction System (referred to throughout as AMPS), and WRF case studies, run at 1.5km horizontal resolution. This section of the chapter will provide a description of WRF including the default options for physics and dynamics, the domain configuration and many other specifications, for both the AMPS archived output, and the case studies.

2.3.1 The Weather Research and Forecasting Model

The WRF model is a numerical weather prediction and atmospheric research tool used for both operational and research purposes. The original and continued development of WRF was an American based, multi-institute production between the National Center for Atmospheric Research (NCAR), NOAA, various defence and Air Force agencies and the University of Oklahoma to name a few (Skamarock & Klemp, 2008). A large user base has been built over the last decade, largely due to its supportive user-groups, multi-scale applications and flexible set-up allowing the use of WRF on smaller computers as well as supercomupters.

The Advanced Research-WRF model (used within this project) uses an advanced research dynamics solver. The dynamical core uses physics and dynamics options to produce the simulation, along with initial and boundary conditions. WRF is a non-hydrostatic, fully compressible model with terrain-following vertical coordinates and an Arakawa C-grid staggering system. The non-hydrostatic element means it uses the entire vertical momentum equation, and can be solved elastically to solve the Euler equations. Being fully compressible, the governing equations for atmospheric motion (compressible Navier stokes equations) are solved, allowing the volume of air to change

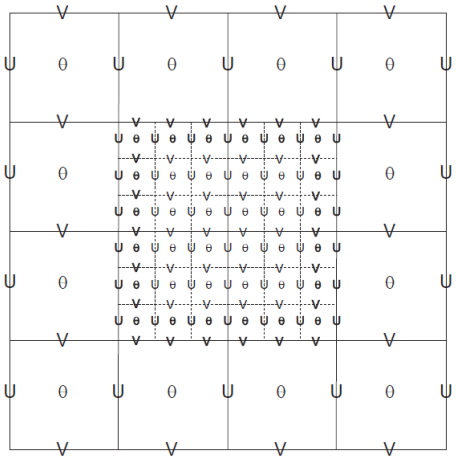

Figure 2.4: The Arakawa-C grid staggering for two domains, one child domain nested within the parent. The solid lines are the grid cell boundaries for the parent domain. The dashed lines are the grids cells for the inner domain. U and V (horizontal velocity components) are defined along the grid sides. The thermodynamic variables (denoted θ) are calculated at the centre of the grid. The bold variables are where the lateral boundaries are required at the interface of the nests. Figure from Skamarock & Klemp (2008) Pg. 59.

over time. The horizontal grid is an Arakawa C-grid (Figure. 2.4), whereby the U and V velocity components are evaluated on the grid sides, rather than in the centre of the grid cell. In the vertical, a terrain-following, pressure co-ordinate system is in place, denoted as η (Figure 2.5). A data assimilation package (WRF-Var), and chemistry attachment (WRF-Chem) are not used within this study, but can also be input into the dynamics solver.

WRF uses either ERA-interim data or Global Forecast System (GFS) data to force the lateral boundaries and initial conditions. For both AMPS and WRF used for the case studies, the GFS data were used for initialisation. This is a global weather forecast model developed by the National Centers for Environmental Prediction (NCEP), with a horizontal resolution of 28km between grid points at the lowest levels.

The WRF model allows nesting of domains to increase horizontal resolution over

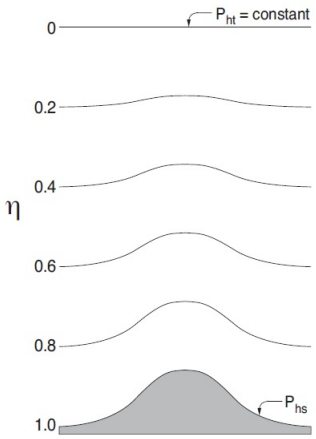

Figure 2.5: WRF uses terrain-following hydrostatic-pressure vertical coordinates. P_{ht} is the hydrostatic value of pressure at the top of the model. $P_{hs}$is the hydrostatic value of pressure at the surface. Figure from Skamarock & Klemp (2008) Pg. 7.

specific regions. The outer, coarser domain is the parent, whilst inner, finer domains are children. These nests may be one-way or two-way in their communication. The child grid receives lateral boundary conditions from the parent, similar to how the parent domain receives information from the GFS data. This allows a higher horizontal resolution over a smaller area (such as the AP), and scaling down of the initial and boundary conditions through temporal interpolation (Skamarock & Klemp, 2008). The vertical resolution of all domains must be the same. A 3:1 or 5:1 ratio for increasing horizontal resolution is suggested by the WRF developers as it allows data to transfer between the domains (http://www2.mmm.ucar.edu/wrf/, last accessed 09/02/2017). This allows two-way nesting, whereby the children domains can give information back to the parent domains.

WRF is frequently used within the atmospheric research community. Largely this is due to it being freely available and relatively easy to set-up and run. A lot of options within WRF can be manually set, which is an additional benefit to the research communities. WRF has been extensively tested for many regions, including the Antarctic, and has been shown to resolve a range of features including föhn winds (Grosvenor *et al.*, 2014, 2012; Steinhoff *et al.*, 2014). There is also an extensive list of parameter-

isation schemes, including radiation and microphysics, which can be set by the user, and combined in numerous ways. These schemes parameterise complex calculations to represent processes which are crucial for the accurate model output, but are not fully resolved due to their sub-grid scale. A number of options-combinations have been tested, and are therefore suggested for particular scenarios.

Polar WRF is a modified version of WRF that allows for better representation and improved model performance of both the Antarctic and the Arctic (Wilson *et al.*, 2012). It was developed by the Polar Meteorology Group at Ohio State University, USA. Many of the modifications are to the Noah land surface model. Noah has now been separated into additional modules for land ice, sea ice and glacier-free land (Hines *et al.*, 2015). Some of the modifications implemented in Polar WRF include fractional sea-ice parameters, thermal conductivity of ice and snow covered land, modified long-wave surface fluxes and enhanced cloud radiative properties (Hines *et al.*, 2015; Wilson *et al.*, 2012). Polar WRF has been extensively tested over both Polar regions (Bromwich *et al.*, 2009, 2013; Hines & Bromwich, 2008; Wilson *et al.*, 2012).

Polar WRF is used within this project for both the AMPS archived outputs, and the WRF case studies. The use of the abbreviation 'WRF' is used to represent Polar WRF for the remainder of this thesis.

2.3.2 AMPS

The first configuration of WRF used for this study was in the Antarctic Mesoscale Prediction System (AMPS). AMPS is a mesoscale numerical weather prediction system for the Antarctic, using the Polar WRF model. Originally developed 16 years ago for operational support to the US Antarctic Programme, it is now used by many international Antarctic research and operations programmes (Powers, 2007). AMPS has been run by members of NCAR in Boulder, Colorado for over a decade. The archived output is available for research, and was used in this study. AMPS has been shown to successfully identify and simulate föhn winds over the McMurdo Dry Valleys, Antarctic (Speirs *et al.*, 2010, 2013).

From the development in 2000 up to January 2011, AMPS was implemented using the standard versions of the advanced WRF atmospheric model. From January 2011 onwards Polar WRF was used within AMPS. For this research, archived AMPS outputs from 2009-2012 were used, using WRF version 3.2.1. The specific setup of AMPS and the options used from this period are described within this chapter, however, updated versions with higher resolutions are now available (see polarmet.osu.edu).

AMPS forecasts over six two-way nested domains. The outer domain covers the entire Antarctic continent and the Southern ocean at 45km horizontal resolution. Nested within this are domains covering the Antarctic continent, Ross ice shelf, and Ross island. Domain six is located over the Antarctic Peninsula at 5km horizontal resolution, and 44 vertical levels. Archived outputs from 2009-2012, from this domain were used in this research.

The 'namelist' file provides information to the model on the physics, boundary layer, radiation and surface options (amongst many more) to be read by the model. The AMPS physics options include the WRF Single Momentum 5-class (WSM5) cloud microphysics scheme (Hong *et al.*, 2004), the Noah land surface model (Chen & Dudhia, 2001), the Rapid Radiative Transfer Model for General circulation models (RRTMG) for the longwave radiation scheme, and the Goddard shortwave radiation scheme. The boundary layer scheme was the Mellor-Yamada-Janjic (MYJ) which was combined with the Janjic-Eta Monin Obukhov (Eta) surface layer scheme. Both the AMPS and WRF Case Study namelist options are provided in Table 2.2.

Extraction of data from AMPS

AMPS stores over 40 meteorological and radiation variables including potential temperature, U and V wind components and surface latent heat flux. Further to these, other variables (such as relative humidity) can be calculated from the output parameters. These values were extracted to create a six-hourly time series by combining data from the 12UTC and 18UTC forecasts. The time series were extracted continuously from the model output from January 1st 2009 to December 31st 2012 (except for 18th June 2010, when model runs were not available) at specific point locations within the model

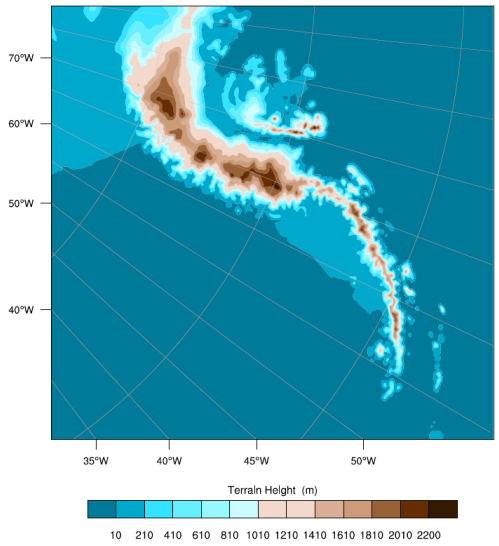

Figure 2.6: Domain 6 of the AMPS archived model runs. The terrain height is shown with the colour contours.

domain. For all locations except Cole Peninsula, the model data were extracted at the same co-ordinates as the AWS. The Cole Peninsula location in the model domain was unrepresentative of its altitude in reality, as the topography was not well resolved due to relatively coarse-resolution. As the altitude influences the air temperature (amongst other variables), it was crucial to extract the data at the right altitude. Therefore, a 'pseudo-location' for Cole Peninsula was used. Data were extracted from 66.8°S, 64.1°W in AMPS.

2.3.3 1.5km WRF Model Case Studies

The second configuration of WRF was used to run high-resolution, individual case studies. The version of Polar WRF used for these model runs was V3.5.1. This version had additional sea ice specifications from parameterisation of sea ice thickness and snow cover on sea ice (Hines, personal communication, 5th October 2014). Due to the added computational cost, the higher resolution model was not run for the full time period. Instead, specific short periods were selected and run as case studies. The data and

outputs from the 1.5km Polar WRF model are presented in Chapter 6.

The purpose of higher-resolution runs using WRF was to investigate whether increasing the horizontal resolution allowed better representation of the spatial distribution of föhn winds over the LCIS. The coarser-resolution of AMPS may have prohibited the accurate representation of some smaller features. To address this aim, the horizontal resolution of the WRF case study runs was increased to 1.5km. The majority of the manually-set options in WRF were set to match the AMPS set-up. This ensured that any differences in the representation of föhn winds from the AMPS to WRF case studies was due to the increased resolution, and not due to differing physics options for example. However, a number of namelist options needed to be altered for the case study runs (Figure 2.2). The differences are discussed below.

The first difference between the two set-ups is the size and position of the domains. As AMPS is used for operational purposes for the US Antarctic Programme, the outer domains focus over the South Pole and the Ross ice shelf. As this was not the area of interest for this study, no domains centred over these locations for the WRF runs. Instead, three domains, focused on the AP region were used (Figure 2.7). The outer domain (domain 1) covered the whole AP and surrounding oceans (60° -72°S, 85° -55°W) at 13.5km horizontal resolution. The second domain was nested within this and covers the Peninsula from approximately 71° -62°S, at 4.5km resolution. The third domain was nested within the second, and was located over the LCIS and Scar Inlet (64° -69°S, 70° -59°W).

Increasing the horizontal resolution without enhancing the topographic resolution can reduce the effectiveness of modelling in higher resolution. For AMPS, the topographic resolution was two minute arc-seconds (2min). For the WRF Case Studies, the topographic resolution was enhanced to 30 arc-seconds (30sec) over the whole AP, by employing the BEDMAP2 digital elevation model topographic information (Fretwell *et al.*, 2013). With the highly complex topography of the region, representing small scale features is important for potentially influencing the spatial distribution of the föhn winds. The vertical resolution was also increased to 70 vertical levels. Due to increased computational power in recent years, many regional climate models used for

Table 2.2: The AMPS and WRF Case Study namelist options to control the simulation. The variables which differ are highlighted in peach.

	AMPS Namelist	**WRF Case Study Namelist**
Initial and Lateral Boundary Conditions	Global Forecasting System	Global Forecasting System
Topography Resolution	2 minute arc-seconds (RAMP2)	30 arc-seconds (BEDMAP2)
Land Surface Physics	NOAH Land surface model	NOAH Land surface model
Horizontal Resolution	D01: 45km D02: 15km D03: 5km D04: 5km D05: 1.6km D06: 5km	D01:13.5km D02: 4.5km D03: 1.5km
Vertical Resolution	44 vertical levels	70 vertical levels
Model Top	1000pa	1000pa
Microphysics Options	WRF Single-Moment 5-class scheme (WSM5) (option 4)	WRF Single-Moment 5-class scheme (WSM5) (option 4)
Longwave physics	Rapid Radiative Transfer Model (RRTM) (option 4)	Rapid Radiative Transfer Model (RRTM) (option 4)
Shortwave physics	Goddard Scheme (option 2)	Goddard Scheme (option 2)
Surface layer physics	Monin-Obukhov similarity theory (option 2)	Monin-Obukhov similarity theory (option 2)
Planetary Boundary Layer scheme	Mellor-Yamada-Janjic (MYJ) scheme (option 2)	Mellor-Yamada-Janjic (MYJ) scheme (option 2)
Base Temperature	268K	290K
Slope and shading	Slope and topographic shading switched off	Slope and topographic shading switched off

research and operational purposes are run at 70+ vertical levels. In AMPS, 44 vertical levels were used. Increasing the vertical resolution provides better representation of features such as föhn winds, which have a vertical component to them, and lower level features such as the surface layer. To allow the WRF Case Studies to be comparable to other models (such as the MetUM used by Elvidge *et al.* 2015),the vertical resolution was increased. The lowest model level was 5.6m a.s.l, and there were 12 levels in the lowest 1km. This compares to 13.2m a.s.l as the lowest model level, and 10 levels in the lowest 1km in AMPS.

The base temperature has different vales in the two configurations. This is the base state potential temperature, and is often set to the International Standard Atmosphere value for the average surface temperature (288K). The AMPS namelist had this option set to 268K due to its positioning over the South Pole, where the elevation is higher, and temperatures lower (Powers J., personal communication, 25th August 2016). This value was not representative of the warmer average surface temperature over the LCIS, therefore the WRF default value of 290K was used.

The final difference is the initialisation frequency in AMPS and WRF. AMPS is initialised twice daily (00UTC and 12UTC) using GFS data, whereas for the case studies, WRF was only initialised at the start of the model run. Reinitialising the data regularly, as in AMPS, nudges the data back towards observations every 12 hours, and means that the longest forecast hour is 18 hours. In WRF however, the model is not nudged back towards observations, and the forecasts are over 10 days. This difference will be addressed in greater detail in Chapter 6.

The identification of föhn events in observations and AMPS data provided a variety of föhn conditions from which case studies were chosen. The case studies were chosen to represent a number of föhn events with varying characteristics, within each of the seasons. Due to the computational cost of running high resolution over a large region such as the LCIS, these case studies were limited to four simulations, to cover a föhn event in each season. The length of the case studies was roughly 10-15 days. This allowed the full föhn cycle to be simulated, from onset to cessation, and to allow the model to spin up beforehand. Forty-eight hours was allocated to 'spin-up' time, to

allow the model to function fully and incorporate the initial and boundary conditions. This is a relatively long spin up time, which may allow model output to drift from 'reality', however the reasons for this spin up length are provided in Chapter 6.

The case studies were selected to simulate a range of features such as the interaction of the boundary layer and föhn winds. The specific aims of each case study are presented in the Chapter 6. The 'Summer' case study was from the 15th to 31st January 2011. The 'Winter' case study spans the 1st to 15th August 2011. The 'Spring' case study simulates a föhn event from 3rd to 15th of October 2011, and the 'Autumn' case study was selected to cover a föhn event during the period from 10th to 22nd May. Chapter 6 is dedicated to the WRF case study output and the results of the high-resolution runs.

2.3.4 Model Limitations

There are limitations to every model and it is important to take them into account when interpreting the model output. This section of the chapter will focus on model limitations and errors specific to Polar WRF. Firstly, GFS data were used to provide the initial and boundary conditions to both AMPS and WRF Case Study runs. The GFS model has its own limitations, that were ingested into the WRF model prior to simulation. ERA-Interim reanalysis data can also be used to provide the initial and boundary conditions to WRF. Bracegirdle & Marshall (2012), evaluated numerous re-analysis data sets and concluded that ERA-Interim was considered the better and more reliable dataset for the Antarctic. However, as AMPS used GFS data to initialise the model, the WRF case ctudy runs also used GFS data to facilitate comparison with AMPS output.

A large contributor to the limitations of the WRF model is the approximations of the physics parameters (National Center for Atmospheric Research, 2014). This uncertainty is seen, for example, in the cloud parameterisations which are largely based on observational data of clouds in low to mid latitudes, with very few observations from the Antarctic (Lachlan-Cope, 2010). Similarly the radiation parameterisation introduces limitations into the model. A cold-summer, warm-winter surface temperature bias

is documented within a number of studies, largely driven by the model radiation difficulties (Bromwich *et al.*, 2013) and the land surface model set up (Wilson *et al.*, 2012).

Complex and steep topography can create instabilities in solving the model equations, and cause the model to crash. Due to the APs large surface area, it was difficult to place a domain edge away from the mountainous terrain, as is suggested by the WRF developers (National Center for Atmospheric Research, 2014). The edge of the inner WRF domain was placed across the southern AP Mountains to focus on the LCIS. This caused some instabilities when the model was running. Using an adaptive time step reduced the instabilities, and allowed the model to complete. The timestep (in seconds) determines how often the key equations are integrated. However, reducing the timestep leads to a slower model run and increases the computational cost. The adaptive time step provides a way of maximising the time step, and increasing run time whilst retaining model stability. Instead of prescribing the time step, the model chooses the appropriate timestep at every interval. The WRF case studies were run with an adaptive timestep. This is unlikely to produce any differences between the simulations from AMPS and WRF.

Regional models struggle to resolve all of the features and characteristics of the AP region. Most parameterisation schemes are tuned to lower latitudes, where more field campaigns have been performed and there are more observations. The problems caused by the lack of long-term, spatially vast observations in the Antarctic is two-fold. Firstly, there are relatively few observations for input data. Reanalysis datasets help to fill the gap in observations, and these are then used for initialisation in the regional models. However, using reanalysis products ingests some errors into the models. Secondly, the limited observations means model validation and testing of parameterisation schemes is restricted. The AMPS model has been operational for over a decade, and it has been thoroughly tested. Whilst the WRF model has also been tested, the exact set-up used for the case studies has not. This is taken into account when analysing the case study output.

2.4 Conclusion

This chapter has outlined the two datasets used in this research; observations from six automatic weather stations on the surface of the LCIS and the surrounding area, and the WRF model. The WRF model has been used in two configurations; archived 5km horizontal resolution output from the AMPS, and specifically run case studies using 1.5km horizontal resolution WRF. Föhn winds were identified from both the observations and AMPS output from 2009 to 2012. The next chapter will discuss the development of the algorithms used to detect föhn winds, and present the final, used algorithms. The föhn winds identified from the observations and archived AMPS output were analysed to investigate the spatial and temporal distribution of the föhn air across the ice shelf, and these findings are presented in Chapter 4. The high-resolution WRF model was run specifically for case studies, and the results of these simulations are presented in Chapter 6.

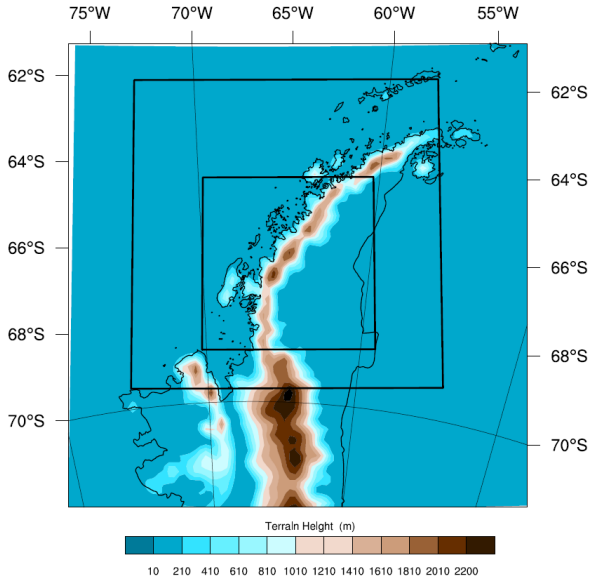

Figure 2.7: The location of the three domains for the 1.5km WRF case studies. Domain 1 (13.5km horizontal resolution) covers the AP and the surrounding oceans. Domain 2 (4.5km horizontal resolution) covers a large proportion of the middle AP, whilst domain 3 (1.5km horizontal resolution) is located over the LCIS.

Chapter 3

Development of the Föhn Identification Algorithms

3.1 Introduction

Föhn conditions have only been observed over the AP and LCIS within the last decade (Elvidge & Renfrew, 2016; Elvidge *et al.*, 2015, 2016; King *et al.*, 2008; Kuipers Munneke *et al.*, 2012), and often on a case-by-case basis. Föhn winds have not previously been objectively identified over the LCIS via a procedure or classification scheme. Semi-automatic detection algorithms to identify föhn winds do exist for a number of locations including the MDVs in the Antarctic and the Wipp Valley in the Austrian Alps. However, there was no identification procedure for the AP or the LCIS.

With multiple observation sites and a relatively long timeseries, semi-automation is necessary to identify föhn conditions quickly and easily. Föhn-detection algorithms have been used in the Antarctic previously (Cape *et al.*, 2015; Speirs *et al.*, 2010; Steinhoff *et al.*, 2014), however these algorithms were not applied to the data for this research. It was not deemed feasible to apply a previous föhn detection algorithm to these data, as the location-specific characteristics of the föhn winds would not be taken into account.

A novel föhn-detection algorithm has been developed for the LCIS for observational data. The algorithm can be applied to identify föhn conditions from all AWSs on the

LCIS. A second föhn-detection algorithm, originally developed by Bannister & King (2015), is adapted and used to identify föhn conditions from the AMPS model data. Bannister & King (2015) implemented the algorithm to identify föhn conditions over South Georgia, a sub-Antarctic island north of the AP. The algorithm was altered for use in this project, and it is the first application of this algorithm over the AP. The algorithms are not specific to an individual AWS or model grid cell. The thresholds used in the AWS algorithm take into account the climatological conditions of a location, and may therefore be applied to other locations on the ice shelf.

This chapter is split into two sections; the observational algorithm (referred to as the AWS föhn identification algorithm) (Section 3.2.3) and model algorithm (referred to as the AMPS föhn identification algorithm) (Section 3.3.2). Both sections start with a brief overview of previously used algorithms and their applications across the world, before moving onto the new algorithms developed for this thesis. They have been applied to data from January 1st 2009 to December 31st 2012, at six different locations.

3.2 AWS Föhn Identification Algorithm

3.2.1 Observational Classification Schemes

The process of identifying föhn conditions from observational data has progressed relatively little from early methods, such as those used in the Alps in the 1930s. Isolating the föhn conditions often relies on highlighting the phenomenological characteristics by applying arbitrary thresholds to the wind speed, wind direction, air temperature and humidity (Vergeiner, 2004). Although subjective, this approach is often relatively successful, as föhn winds have distinctive features, often very different to any other downslope wind storm or air mass. Even now, many föhn studies rely on such arbitrary thresholds to separate föhn air from any other.

Detecting föhn winds often relies on a critical threshold, such as wind speed above $5 ms^{-1}$, or a rate of change, such as a 5% decrease in relative humidity per hour (as used by Speirs *et al.* 2010). To ensure that föhn are identified, and to discriminate them from other air masses, these thresholds are often combined to create algorithms.

Early usage of these subjective algorithms was by Conrad (1936), Osmond (1941) and Obenland (1956) and is today termed the 'three-point method' (Drechsel & Mayr, 2008). An automatic algorithm previously used over the MDVs is discussed in Speirs *et al.* (2010), and was developed from a criterion used in the northern hemisphere by Gutermann (1970), Richner *et al.* (2005) and Gaffin (2007). The Speirs *et al.* (2010) algorithm includes a wind speed threshold and wind direction criterion as well as an increase in temperature and a decrease in relative humidity. This algorithm was used in Speirs *et al.* (2013), Steinhoff *et al.* (2013) and Cape *et al.* (2015). A slight adjustment was made in Steinhoff *et al.* (2014) to include an additional relative humidity threshold.

In cases where an additional AWS is available on the windward ridge, a less subjective method may be applied to identify föhn, as used by Dürr (2003) and Vergeiner (2004). In this method, the potential temperature is tracked from the ridge-top AWS to the valley-bottom AWS during adiabatically warmed föhn episodes. As potential temperature is conserved, the valley-bottom potential temperature will be equal to or higher than the ridge-top potential temperature during föhn winds (Vergeiner, 2004). As part of the OFCAP field campaign, attempts were made to deploy a ridge-top AWS on the AP. However, due to high accumulation rates and high wind speeds, data collection was unsuccessful (Elvidge A., personal communication, February 2017).

Due to the complexity of the location and the sparse number of observations, specifically the lack of (a) ridge-top AWS(s), the identification algorithm developed here was limited to a threshold approach. A number of measures were taken to reduce the subjectivity of the algorithm, as outlined below. The observational föhn detection algorithm is now presented.

3.2.2 AWS Algorithm Development

The AWS föhn identification algorithm is based on detecting key features or changes in the near-surface conditions observed by the AWS. To select thresholds that were appropriate for isolating key föhn characteristics over the LCIS, the climatology of each location was assessed, and a number of previously studied föhn events were assessed.

Initially, the relative humidity and temperature values were plotted, and clear deviations from the average conditions were identified (Figure 3.1).

Föhn onset over the AP is clearly identified by a significant decrease in relative humidity, as dry air replaces ambient, more moist air. This relative humidity decrease is observed at all six locations, and is the key identifier for föhn onset over the LCIS. Over the AP, the temperature signal is less pronounced during föhn onset. The amplitude of the seasonal air temperature cycle is considerable, and this influences the magnitude of the temperature change during föhn periods. During summer, the average conditions are close to freezing point, and air temperature increases are more modulated than during the colder periods. The seasonal relative humidity cycle is less pronounced (Figure 3.1). The cessation of the föhn effect was identified by an increase in relative humidity and a decrease of air temperature.

Climatological analysis of the AWS data allowed the thresholds to be specified. As Cole Peninsula data were only available for a year, the thresholds were set based on analysis of that year. Ideally, this would have been tested against other years of data to ensure that the thresholds were representative of föhn conditions at this location. For AWS2, AWS3 and AWS6, four years of data were available for this climatological analysis, and therefore the thresholds were more robust than at Cole Peninsula.

To highlight the origin of the thresholds and criteria, Figure 3.2 presents the near-surface characteristics during a föhn event at two locations. Cole Peninsula and AWS2 are presented. Cole Peninsula was closest to the foot of the AP, and experienced the most defined (strongest) föhn signal, whereas AWS2 was over 100km away from the AP, and experienced a weaker föhn effect.

This particular föhn event started on 11th November at 06UTC at Cole Peninsula and six hours later at AWS2. At Cole Peninsula, the föhn onset was marked by a 29.5% decrease in relative humidity, and a 6.3K increase in air temperature. At AWS2 the onset was characterised by 15.7% decrease in relative humidity and a 5.4K change in temperature. At its peak, the minimum relative humidity was 45.9% at Cole Peninsula and 71.5% at AWS2. The temperature maxima were similar at both, -0.5°C at Cole

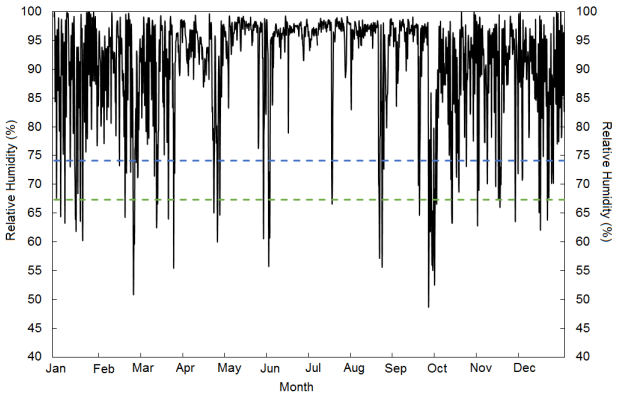

Figure 3.1: The relative humidity values observed at AWS1 during 2012. The green dashed line is at 67.3%, and the blue dashed line is at 74.1%. These are the two relative humidity thresholds for identifying föhn conditions at AWS1.

Peninsula and -0.7°C at AWS2 (Figure 3.2).

Westerly winds were present at both locations preceding and during the föhn period. The wind speed at both locations peaked 12-18 hours prior to the onset of the föhn event. During the föhn event, the winds were moderate at both locations ($\sim$ 4ms^{-1}). The decrease in relative humidity, increase in air temperature and predominantly westerly winds observed during the föhn event in Figure 3.2 are representative for all föhn conditions observed over the LCIS. The increased wind speed was not always replicated during every föhn event, or at every location.

The magnitude of the relative humidity decrease varied by location, as displayed in Figure 3.2. It is hypothesised that with increasing distance from the AP, the föhn signal weakens. The föhn air mixes with ambient conditions as it propagates away from the AP. This theory is explored in the Chapter 4. The air temperature change associated with föhn onset and cessation was less influenced by location. It was therefore necessary for the algorithm to capture the variable relative humidity signal and the more spatially homogeneous air temperature change.

For the warm, dry air mass to be of föhn origin, it must have crossed the AP, and therefore have originated from the west. As can be seen from Figure 3.2, the wind

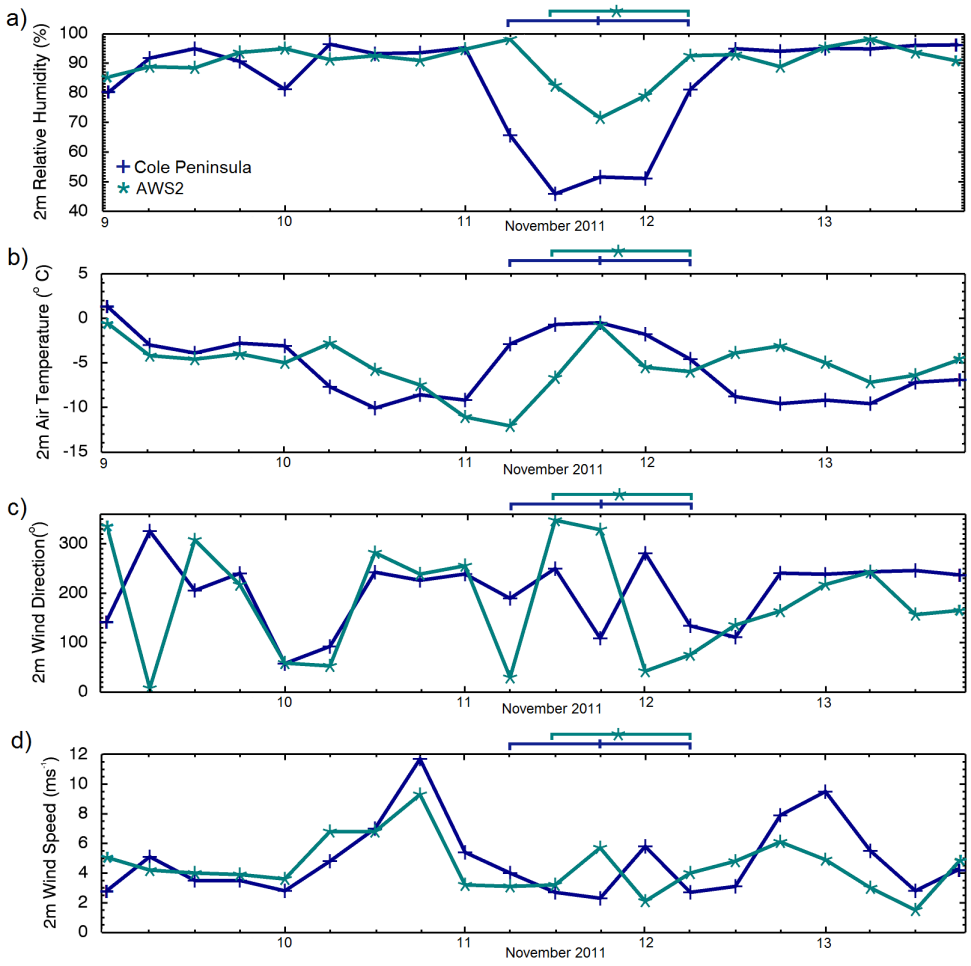

Figure 3.2: The near-surface meteorological conditions from 9th to 14th November 2011 observed at Cole Peninsula (dark blue) and AWS2 (teal). The relative humidity (a), air temperature (b) exhibit clear changes during föhn events. However the wind direction (c) and wind speed (d) exhibit lesser changes. The dark blue (Cole Peninsula) and teal (AWS2) lines above each plot indicate the identification of a föhn event from the AWS identification algorithm.

direction signal was highly variable, however during the föhn event, it did rotate to a westerly direction. Therefore, the wind direction was taken into account by the algorithm. Cole Peninsula was exempt however, as due to its position at the foot of the AP, it was exposed to winds directed by valleys and troughs on the AP leeside, which affected the wind direction signal.

3.2.3 AWS Föhn Identification Algorithm

A generic föhn identification algorithm, which can be tailored to individual locations on the LCIS has been developed. The thresholds are based on statistical, not absolute values, and can therefore be applied to numerous datasets. The generic algorithm is presented first. Then a description of how the algorithm was tailored to each AWS location is presented.

A time point was flagged as 'föhn' if criteria 1 was fulfilled and *at least one* of the thresholds in group 2 was met:

1. Wind direction was from 181-359° (i.e from the direction of the AP). For air to be of föhn origin, it must have descended the lee of the AP mountains, and therefore have had a westerly wind component. This criterion was not subjective, as föhn winds are a consequence of westerly winds across the AP. Cole Peninsula data were exempt from the wind direction criterion, as outlined above (Section 3.2.2).

2. At least one of the following must have been met:

- 2*a* A decrease in relative humidity of at least X% within 12 hours (RH12hr). X varied depending on the location of the AWS (see Table 3.1). Values of X were based on the climatology of the location to identify low frequency, extreme dry conditions. The use of a short time frame removed the possibility of incorporating slower, synoptic changes into the algorithm.
- 2*b* A relative humidity value below the 10th percentile (RH10P). This ensured that the dry signature of the föhn air was detected. Using percentiles rather

than absolute values allowed this algorithm to be adaptable for other locations on the LCIS. For example, the 10th percentile at Cole Peninsula was much lower than at other locations as the average conditions here were drier (see Table 3.1).

2*c* A relative humidity value below the 15th percentile combined with an air temperature increase of $\geq$ 3.0K over 12 hours (RH15P). An increase in temperature often accompanied föhn onset, however this signal could be masked by other processes. During summer, the increased surface temperatures due to incoming solar radiation weakened the temperature response to föhn onset (Cape *et al.*, 2015). Accompanying a temperature rise with a relative humidity decrease removed the bias caused by the seasonal temperature fluctuations. A 3K temperature rise was often observed coinciding with changes in relative humidity during initial assessment. This criterion was not met by synoptic changes over such a short time frame. The algorithm presented here removed any potential bias caused by the seasonal air temperature cycle by decreasing the influence of air temperature within the algorithm.

Thresholds for relative humidity dominated the algorithm presented here. A relative humidity decrease was a mandatory criterion for föhn identification, as this was the most pronounced föhn onset signal over the LCIS (Figure 3.2). Although continental air is relatively dry compared to ambient conditions, it is not as dry as the föhn air. Periods characterised by southerly wind (120° -200°) in the observational data experienced an average relative humidity of 94.5%, compared to an average of 65.3% during föhn conditions identified using the algorithm presented here. Combining a number of thresholds or criteria ensured that only föhn air was identified as such.

3.2.4 AWS Algorithm Limitations

Whilst this is a semi-automatic process, the initial thresholds were set arbitrarily after assessing average and extreme conditions at each location. Therefore, this process was somewhat subjective, and it is possible that a number of periods were falsely classified as föhn, or that some weak föhn conditions were missed. More conditions may have been missed in winter, when strong stable boundary layers develop and persist over the

Table 3.1: Summary thresholds for the AWS föhn identification algorithm.

AWS	RH10P	RH15P	RH12hr
Cole Peninsula	51.84%	58.53%	>17.5%
AWS 1	67.27%	74.09%	>15%
AWS 2	72.63%	78.66%	>15%
AWS 3	76.88%	81.34%	>15%
AWS 5	75.16%	80.05%	>15%
AWS 6	77.4%	82.41%	>10%

ice shelf. Föhn air can ride over the top of the stable layer and therefore lack a near-surface föhn signal (Drobinski *et al.*, 2007). Similarly, if the föhn air erodes the stable boundary layer, the föhn signal may weaken and therefore may not be detected by the algorithm. Another limitation is the possibility for the AWS algorithm to incorporate katabatic winds into the results, as these have a relatively dry signature.

One aim of this research was to investigate what impact the föhn conditions have on the surface of the ice shelf. If the föhn air was too weak to be detected by the algorithm, or the near-surface signal was absent completely, then these föhn conditions were unlikely to have had an impact on the ice shelf. Assessing the impact of föhn winds on the ice surface is a key aim of this research, therefore it is essential that the algorithm detects föhn events with a well-defined near-surface signal. Conversely, if weak föhn conditions are not detected, then the temporal analysis may be seasonally biased. The AWS algorithm detects only the near-surface signal. Föhn winds have an upper-air signal as well as a near-surface signal. The AMPS algorithm detects the upper-air signal by isolating the drawdown of potentially warmer air from aloft.

3.3 AMPS Identification Algorithm

3.3.1 Model Identification Schemes

There are two leading methods for identifying föhn winds from model data. The first is analogous to the observational algorithms discussed in Section 3.2.3. The second is a relatively new method, which isolates the isentropic drawdown of warm air from above

the AP.

In Steinhoff *et al.* (2014), föhn conditions were identified from the WRF output by applying the observational algorithm to near-surface model output at specific locations in the domain. The algorithm was adjusted to take into account the possible temporal offset and coarse resolution of the model. Using this method, WRF overestimated the number of föhn periods by 58% (Steinhoff *et al.*, 2014). This was largely due to incorrect wind speed and direction simulated by the model. Variations of the AWS algorithm were applied to near-surface output from WRF over South Georgia by Bannister (2015). It was concluded that this method was inefficient at identifying föhn winds, and had a poor correlation with the föhn identified from the observations. Applying an AWS algorithm to model data assumes that the model can successfully resolve the near-surface conditions prior to and during the föhn periods.

To assess whether AMPS accurately represents the near-surface conditions, a number of variables have been validated against observations (Tables 3.2 and 3.3). The pressure at most locations is well represented in AMPS (low mean bias, small standard deviation, high correlation). The standard deviation is much larger at Cole Peninsula than elsewhere (12.6hPa). There was a positive air temperature bias in AMPS (too warm), by as much as 2.9K at AWS5. The standard deviation at some locations was also relatively large (7.7K). The water vapour mixing ratio was overestimated by AMPS, leading to a moist bias compared to observations. Due to the positive biases in air temperature and humidity, using the near-surface AMPS output for detecting föhn air was not used as basis of the föhn identification algorithm.

The second known method for identifying föhn winds from model output is by identifying the upper-air signal created by the interaction of the mountain with the airflow. The isentropic drawdown in the leeside of the AP is isolated. This method was first (to the best of the author's knowledge) developed and implemented by Bannister (2015) and Bannister & King (2015). The potential temperature on the windward side of the barrier, at mountain height, is tracked across the barrier. If the isentrope decreases in altitude on the leeside, compared to its up-barrier height, this is evidence of warm air being advected towards the surface due to the interaction between the mountain and

Table 3.2: The AWS mean values and mean bias (AMPS-AWS) for the near-surface variables for each location for 2009-2012 (2011 only for Cole Peninsula).

	AWS Mean Values						Mean Bias					
	CP	AWS1	AWS2	AWS3	AWS5	AWS6	CP	AWS1	AWS2	AWS3	AWS5	AWS6
T (°C)	-12.3	-15.1	-15.9	-16.0	-14.7	-14.3	0.5	2.0	2.5	2.0	2.9	2.3
P (hPa)	942.7	988.4	985.9	986.4	984.1	984.2	-1.8	-3.4	-1.9	-3.2	-2.1	-3.1
FF (ms^{-1})	4.1	4.3	3.71	3.76	3.0	3.2	2.4	1.7	1.6	1.5	2.3	2.0
q (gkg^{-1})	1.5	1.1	1.3	1.3	1.5	1.5	0.1	0.3	0.3	0.3	0.3	0.3

Table 3.3: The standard deviation of the mean bias and the correlation of the observations and model output for near-surface variables for each location from 2009-2012 (2011 only for Cole Peninsula).

	Standard Deviation						Correlation Coefficient					
	CP	AWS1	AWS2	AWS3	AWS5	AWS6	CP	AWS1	AWS2	AWS3	AWS5	AWS6
T (°C)	3.9	4.6	5.13	4.5	7.7	5.4	0.9	0.9	0.9	0.9	0.7	0.9
P (hPa)	12.6	1.9	2.3	2.0	3.8	5.0	0.4	1.0	1.0	1.0	0.9	0.9
FF (ms^{-1})	4.5	2.5	2.4	4.9	2.8	2.9	0.4	0.8	0.6	0.4	0.6	0.6
q (gkg^{-1})	0.4	0.5	0.4	0.4	0.5	0.5	0.9	0.9	0.9	0.9	0.9	0.9

airflow. The required isentrope descent over South Georgia was 1000m (Bannister & King, 2015). Whilst this method still applies a potentially subjective threshold, it ensures that the dynamics responsible for föhn conditions are identified, rather than just the near-surface response. This method performed well over South Georgia, although it overestimated the number of föhn periods compared to observations (Bannister & King, 2015).

3.3.2 AMPS Föhn Identification Algorithm

The AMPS algorithm is similar to the AWS algorithm in that it is a generic algorithm that was applied to multiple locations across the LCIS. The same algorithm was applied to every location, however the specific thresholds varied depending on the location. The algorithm used is similar to the one implemented by Bannister & King (2015) discussed above.

Six west to east transects across the AP were taken at various latitudes to correspond with the AWS locations. The westerly start of the transects was at approximately 70°W. This location was upwind of the AP, and in undisturbed flow. A potential temperature isentrope is tracked along the transect, and it is crucial that the isentrope is extracted from undisturbed flow, and not already influenced by the AP. The distance required to ensure that flow is undisturbed is defined by the Rossby Radius of deformation (Gill, 1982; Orr *et al.*, 2008).

$$\lambda_R = \frac{Nh}{f} \tag{3.1}$$

where N is the Brunt-Väisälä frequency, a measure of the atmosphere's stability (typically in the order of $0.01 s^{-1}$), h is the mountain height (2000m for the AP), and f is the Coriolis parameter (-1.34 x $10^{-4} s^{-1}$ at 67°S). At 67°S, λ_R is approximately 150km. From the main ridge of the AP, the distance to 70°W is approximately 160km, and therefore far enough away from the AP to be in undisturbed flow. λ_R varies by latitude, and the upstream locations are given in Table 3.4.

For each west-to-east transect, the potential temperature at the upstream location, and at the height of the AP (see Table 3.4) was extracted. The height of the AP changes

along its length, and the isentrope was therefore extracted at heights between 1500m and 2000m depending on the location of interest. This isentrope was followed east along the transect, across the AP and to the leeside. At this point, if föhn development has occurred, the isentrope will have decreased in altitude on the leeside compared to the up-barrier height, as a wave-like motion in the air flow occurs with the interaction of the airflow with the mountain. If the isentrope descended, it implies that potentially warmer (and drier) air from above was being advected down towards the surface. The change in altitude of the isentrope (up-barrier - leeside) was defined. The decrease of the isentrope elevation must have been significantly large to approach the surface.

To assess the impact of föhn winds on the surface of the LCIS, the drawdown must be large enough for the föhn winds to be observed at the surface. A large parcel of potentially warmer and drier air is advected down towards the surface, not just one particular isentrope. The isentrope at the height of the AP was used as the threshold in the algorithm, however, the air just beneath this isentrope was also potentially warmer and drier than the air at the surface. After performing a number of sensitivity experiments altering the threshold of the isentrope descent (not shown), it was found that 500m descent of the isentrope provided the best agreement between the föhn periods identified from the AWS algorithm and the AMPS algorithm. The height at which the isentrope was located upsteam (θ_{up}) was not tested.

The transect along which the potential temperature was tracked across the AP was positioned directly west to east. The orientation of the transect allowed changes in the height of the isentrope to be identified under winds with a westerly component. Isentropic drawdown associated with föhn events with northwesterly or southwesterly winds were also captured by the west-east transect. 99.5% of the föhn periods identified by the AMPS algorithm were characterised by wind with a westerly component (positive u values at the height of the AP). The other 0.5% of periods were characterised by easterly winds (negative u values at the height of the AP), and were then reclassified as non-föhn periods, as air must have originated from the west of the AP to be of föhn origin. Due to the large percentage of föhn periods identified from the west-east transects, it was deemed unnecessary to include transects which were orientated northwest

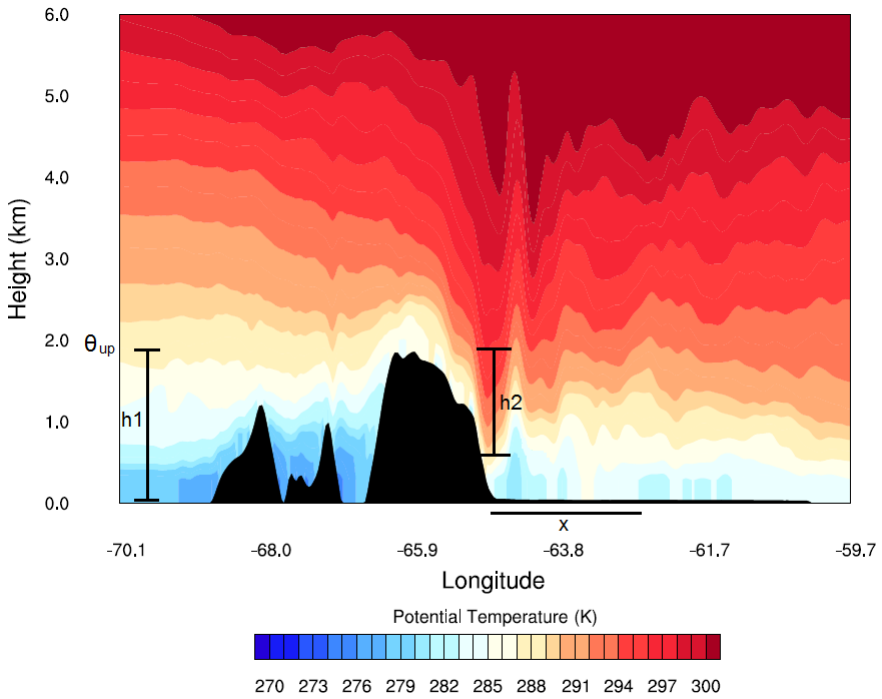

Figure 3.3: Cross section of the modelled potential temperature at 67°S during a typical föhn period. θ_{up} is the upwind potential temperature at the height of the AP (h1) in undisturbed flow (∼70°W). The decrease in altitude of the isentrope from upwind to leeside, h2, must exceed 500m and must be located within the vicinity of interest (x) to be classified as a föhn signal. The model topography along the cross-section is shaded black. Potential temperature values are displayed in coloured contours.

to southeast, or any other orientation.

For the föhn warming to be detected at specific locations (corresponding to the AWS locations), the minimum elevation of the descending isentrope must occur between the leeside of the AP and approximately 2° longitude onto the LCIS. Due to the curvature of the AP, the specific longitudes vary, and these are presented in Table 3.4. For example, when identifying föhn at the Cole Peninsula location, the 500m decrease must have occurred between 65°W and 63°W. This ensured that the warming signal from the isentropic drawdown was identified at the respective location.

Table 3.4: The location specific thresholds used to identify föhn conditions at each location within the AMPS output.

AWS	Upstream Latitude of θ_{up}	Latitude of θ_{up}	h1	x
CP	70°W	66.8°S	2000m	65-63°W
AWS 1	68°W	65.93°S	1700m	63-61°W
AWS 2	70°W	67.02°S	2000m	65-63°W
AWS 3	70°W	67.57°S	1500m	66-64°W
AWS 5	70°W	67.58°S	1500m	66-64°W
AWS 6	69°W	68.14°S	1500m	66-64°W

Figure 3.3 highlights the steps for identifying föhn, and they are summarised below. For each six-hour model output the following occurred:

- Isolate the potential temperature (θ_{up}) at an elevation just above the height of the AP (h1), and in undisturbed, upwind flow (∼70°W), at the latitude of interest (corresponds to the latitude of the AWS).
- Isolate θ_{up} again, due east of the up-barrier location, in the leeside of the AP, within a 2° longitude range of the AP (x).
- Determine the minimum elevation of θ_{up} within this longitude range.

The time point was flagged as 'föhn' when both the following criteria were satisfied:

1. The elevation of θ_{up} from up-barrier to leeside descends by at least 500m (h2).
2. The minimum elevation of θ_{up} is located within the 2° vicinity of the location of interest (x).

As a number of variables within the algorithm were specific to each location, Table 3.4 displays the various thresholds and criteria based on the AWS locations.

3.3.3 AMPS Algorithm Limitations

As the algorithm relies on the presence of the isentropic drawdown signature, it is possible that the algorithm does not identify all föhn conditions. If föhn conditions were

generated by mechanical mixing or radiative heating (Chapter 1), which have been observed over the AP (Elvidge & Renfrew, 2016), then they will not have been identified by the algorithm. However, it is assumed that these two additional heating mechanisms contribute less to the föhn heating than isentropic drawdown and thermodynamic processes (Elvidge & Renfrew, 2016).

Similarly, the AMPS algorithm may have overestimated the number of föhn periods, as the upper air disturbance may have been caused by frontal air masses moving across the region. An overestimation in the number of föhn periods simulated within WRF was found by both Steinhoff *et al.* (2014) and Bannister (2015). On the other hand, the relatively coarse-resolution of the AMPS domain may have lead to a number of cases when föhns were not identified, as weaker small-scale föhn flows were not resolved.

3.4 Algorithm Combination

From applying both the AWS and AMPS algorithms to the available data, a large number of times have been flagged as potential föhn conditions through meeting the criteria. In total 4009 times were flagged as föhn using the AMPS algorithm and 1695 using the AWS algorithm.

The AWS algorithm identifies the near-surface response to the föhn conditions, whilst the AMPS algorithm determines the upper air signal. Assessing the impact of föhn conditions on the surface of the ice shelf was a main aim of this research, and therefore, the AWS algorithm had a higher priority than the AMPS algorithm. However, in order to ascertain that the near-surface conditions were in response to föhn winds, and not due to advection of other warm or dry air sources, results from the two algorithms were combined. This ensured that there was an isentropic drawdown feature present in the lee of the AP, concurrent with the near-surface signal. Combining the algorithms in this manor reduced the possibility of including incorrectly categorised non-föhn periods into the analysis. From combining the two algorithms the following features must have been present :

- Near-surface wind from a westerly direction (except at Cole Peninsula), and westerly wind at the height of the AP,
- a relative humidity value, or a decrease in relative humidity over 12 hours, to meet the AWS algorithm,
- an increase in temperature (if the air is not dry enough to be identified by a single criterion) to meet the AWS algorithm,
- a decrease in altitude of the AP-height isentrope by at least 500m, as defined by the AMPS algorithm

Only six-hour periods indicated by both the AWS and AMPS algorithms as possessing föhn characteristics were taken further for analysis and categorised as 'föhn conditions. Therefore, both a near-surface *and* upper-air signal must have been identified simultaneously for a föhn to be classified as such.

To investigate the agreement between the two algorithms, a 'hit test was conducted (Figure 3.4). As the AWS algorithm is more discerning than the AMPS algorithm, the föhn conditions identified by the AWS algorithm were taken as the 'true föhn conditions. If the AMPS algorithm identified a föhn period at the same time as the AWS algorithm, this was considered a 'hit', and was categorised as a föhn condition. If the AMPS algorithm identified isentropic drawdown, but the AWS algorithm did not identify a corresponding near-surface signal, then this was classed as a 'false positive'. Similarly, if a föhn period was only identified by the AWS algorithm, and the AMPS algorithm did not detect one, then this was classified as 'false negative'. Neither false negatives, nor false positives were classified as föhn periods, these then became non-föhn periods. Only the föhn periods identified by both algorithms (hit), were classified as 'föhn conditions', and taken further for analysis. This hit test was also performed by Bannister (2015), to assist on selecting the best method for föhn identification over South Georgia.

Of the 4009 six-hour föhn conditions identified from the AMPS algorithm, and 1695 identified from the AWS algorithm, 878 were hits. Table 3.5 summarises the number

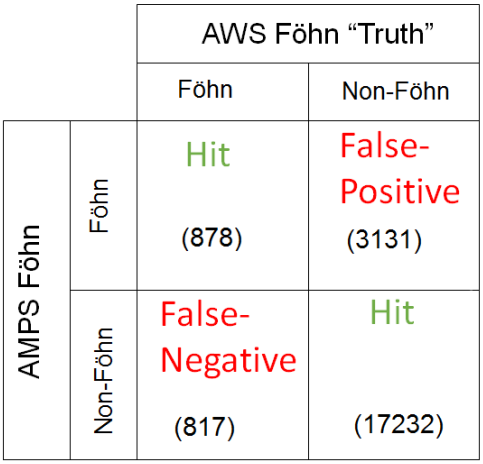

Figure 3.4: Schematic describing the number of föhn conditions identified in both AWS and AMPS algorithms (hit). A time is categorised as false negatives if the föhn condition was only identified by the AWS algorithm. A false positive is if the föhn conditions was only identified by the AMPS algorithm. Only 'hits' were categorised as föhn conditions and used for further analysis. In brackets are the number of six-hour periods classified in each group.

of hits, false negatives and false positives for the AWS and AMPS algorithms.

It should be noted, that a perfect, or very high number of hits was unlikely, as the two algorithms identify different processes. The hits were the total number of classified föhn periods, which have been used in further analysis. The AMPS algorithm over-estimated the number of föhn conditions, as highlighted by the large number of false positives at all locations.

There was often a lag between föhn periods identified by the AWS algorithm and the AMPS algorithm. For 13% of the false positive cases (AMPS only föhn), and 35% of the false negative cases (AWS only föhn), there was up to 12-hours offset between the identification by the AWS and AMPS algorithms. This could be due to the isentropic drawdown being identified first by the AMPS algorithm, and it taking a number of hours before the föhn air was observed at the surface. It may also be due to poor timing of the synoptic situation which generated the westerly flow in AMPS. The lag was neither consistent throughout the period of interest, nor by location, and therefore

Table 3.5: The annual average agreement between the AWS and AMPS algorithms. 'Hit' is the number of föhn periods identified by both the AWS and AMPS algorithms simultaneously. A time is classified as 'False negative' if the föhn period was only identified by the AWS algorithm. 'False positive' is the number of föhn periods identified by the AMPS algorithm only.

Location	AWS Föhn	Hit	False Negative	False Positive
Cole Peninsula	331	192	139	192
AWS1	88	63	25.5	294
AWS2	79	31	48.3	181
AWS3	90	43	47.3	199
AWS5	69	34	35.3	138
AWS6	86	42	44	129

it was not corrected.

In Bannister (2015), the timing offset was taken into consideration in the föhn identification process. If a föhn period was identified by one algorithm within ± 12 hours of the other algorithm, then this was considered to be the same föhn event. Including a time-lag between the two algorithms in the current study was considered and tested. The time-lag made it difficult to determine whether two separate föhn events had occurred within quick succession. It also introduced a further element of subjectivity, as the 12-hour offset had been selected arbitrarily. Therefore, if the AWS and AMPS algorithms did not agree on how to classify a time point, it was not considered a föhn condition, and a time lag was not included in the föhn identification process.

The time lag was not responsible for all the disagreements between the algorithms. For 67.5% of the false positives, there was clearly no föhn signal at the surface in observations, as the relative humidity was above 90% at the corresponding location. In only 1% of the false positive cases (only the AMPS algorithm detected föhn), the observed near-surface signal was close to, but did not meet the thresholds of the AWS algorithm. Therefore, the föhn effect would only be weak, and was not strong enough to be detected by the AWS algorithm. Positively, this was a very small number of cases, therefore, it is likely that the AWS algorithm thresholds are set to achieve the

best results for detecting the föhn events which will have an impact on the surface.

For 25% of the false negatives (AWS only föhn), the AMPS output did not simulate cross-barrier westerly winds, therefore isentropic drawdown in the lee of the AP was not possible. In those times, the synoptic situation may not have been accurately represented within AMPS. For approximately 11% of the false negatives, the isentropic drawdown was simulated in AMPS, but the change in isentrope elevation was not large enough to meet the threshold ($\sim$ 400m descent). Therefore, the föhn event was likely present over the ice shelf, but it was not clear enough to be detected by the algorithm. As this was a relatively small proportion of times, the AMPS algorithm was able to capture the majority of föhn conditions.

The hit test did not quantify the number of times that the algorithms agreed on non-föhn periods, but only the times when the two algorithms both detected föhn conditions. When accounting for both the föhn hits, and the non-föhn hits, the two algorithms agreed over 80% of the time. This is a relatively good agreement between the two algorithms, despite relying on different properties and föhn mechanisms. Therefore, two conclusions can be drawn. Firstly, that the algorithms identified a large number of föhn conditions, and could be considered successful. Subsequently they have been used to identify föhn periods throughout this research. Secondly, that the isentropic drawdown mechanism accounted for a large number of föhn conditions. As an objective of this research was to assess the impact of föhn on the surface of the ice shelf, a near-surface response to the föhn was essential, which provided the main reason for combining the algorithms, and discarding the time points that were not identified as föhn by both algorithms.

A number of known, previously researched föhn events over the LCIS have been selected to test the algorithms. These are föhn events on the 15th-16th November 2010, 26th-28th January 2011 and 4th-5th February 2011, as presented in Elvidge *et al.* (2015) and Elvidge *et al.* (2016). All three of the periods were identified by the AWS and AMPS algorithms.

For the remainder of this thesis, the terms 'föhn conditions', 'föhn events' and other use of the word 'föhn', refer only to the periods which were identified by both algorithms (unless otherwise stated as being 'AWS only' or 'AMPS only' föhn periods). The two algorithms were applied to all AWS locations from 2009-2012. The identified föhn conditions were analysed to investigate the spatial and temporal distribution of the föhn effect on the LCIS. The results of these analyses are presented in the following chapter.

Chapter 4

The Spatial and Temporal Distribution of Föhn Winds

4.1 Introduction

Föhn winds have been identified from near-surface observational data using the 'AWS föhn identification algorithm', and from archived 5km model output using the 'AMPS föhn identification algorithm' (see Chapter 3). When a particular time was identified as experiencing föhn characteristics by both algorithms simultaneously, this was categorised as 'föhn'. The spatial and temporal analyses of the föhn periods are presented in this chapter.

Four specific terms are used to describe the föhn winds. Firstly, 'föhn conditions' are six-hour averaged times when föhn characteristics were identified. Secondly, 'föhn events' refer to continuous periods of föhn conditions. The duration of föhn events increases in six-hour intervals due to the averaging used for the observations (see Chapter 2). Föhn events are not shorter than six hours for the same reason. A föhn event is terminated by the identification of non-föhn conditions. Even one non-föhn period will terminate a föhn event, and a second föhn event will then begin when föhn conditions resume. This allows the length of föhn events to be analysed, and to assess whether the duration of föhn events varies by location or over time. 'Föhn days' are 24-hour periods, from 0000UTC to 2359UTC, dufing which föhn conditions have been identified at least once. Within a föhn day, föhn conditions may have been identified once, or up

to four times. This term is used in numerous föhn studies (e.g Bannister & King 2015; Speirs *et al.* 2010, 2013). It is a useful measure for analysing the dominance of föhn winds over a number of days as föhn conditions can often be intermittent. The final term used is 'multi-location föhn conditions'. These are föhn conditions which were identified at more than one location at the same time. This is used to assess the spatial extent of föhn air over the LCIS.

The analysis presented in this chapter intends to answer two of the research questions stated in Chapter 1. The research questions focus on investigating the spatial and temporal distribution of föhn conditions over the LCIS. In order to do this, a number of more specific hypotheses are suggested. The first hypothesis is that föhn conditions are identified most frequently close to the AP, and decreases in frequency with increasing distance from the AP (further east). Secondly, it is hypothesised that there is a west to east gradient in decreasing föhn strength over the LCIS, with relatively weaker (higher relative humidity, lower air temperature) föhn conditions to the east of the ice shelf, and the strongest föhn signal close to the mountains. These hypotheses were formed based on previous studies by Elvidge *et al.* (2016). From a number of individual case studies, it was found that föhn conditions were strongest close to the AP. Similarly, in studies by Luckman *et al.* (2014), surface melting has been observed in satellite images close to the foot of the mountains on the northwest section of the LCIS. It is suggested that föhn-induced melting is strongest in this region due to the high number of föhn conditions.

The third hypothesis is that a north-south gradient in föhn frequency and strength (more frequent and stronger further north) is present over the ice shelf. This is based on the study by Cape *et al.* (2015) which found that föhn conditions were more frequent further north on the AP, and that this increased frequency prompted the destabilisation of Larsen A and B ice shelves. The spatial and temporal distribution of the föhn conditions are presented in this chapter and the hypotheses are addressed.

The chapter is split into three main results sections; temporal distribution, spatial distribution and the near-surface characteristics of the föhn conditions over the LCIS. In some cases, föhn conditions from one individual location will be assessed, in which

case the location name (e.g AWS2) will be stated. At other times, föhn conditions from all locations will be assessed together, for example when looking at the total number of föhn conditions over the whole ice shelf. In this case, föhn conditions identified from all locations will be summed up or averaged, and this will be referred to as the 'whole ice shelf'. The chapter will continue with a presentation of the temporal distribution and spatial distribution of föhn conditions. The near-surface characteristics during föhn conditions will then be presented. The three main sections will then be discussed, and a conclusion will highlight the key findings.

4.2 Temporal Patterns

This is the first study to assess the temporal distribution of föhn conditions over the LCIS over a period of more than one year. Prior to this study, föhn conditions were mostly assessed as part of a case study. Without knowing how often föhn conditions occur, especially during the months with higher than average air temperatures and increased incoming solar radiation, the impact of föhn conditions on the surface of the LCIS can only be estimated over a short time scale, and these may under- or over estimate the impact. Four AWSs were active in 2009 (AWS2, AWS3, AWS5, AWS6), 2010 (AWS2, AWS3, AWS5, AWS6) and 2012 (AWS1, AWS2, AWS3, AWS6). In 2011, all six AWSs were active, and therefore more föhn conditions were identified.

From 2009 to 2012, 878 föhn conditions were identified in total. This equates to 5268 hours of föhn conditions, or 219.5 consecutive days, accounting for approximately 15% of the four year period. There were 422 föhn events, and 504 föhn days. Of the 878 föhn conditions, 24% of them were multi-location föhn conditions and 37 were identified by all active AWSs simultaneously. Figure 4.1 is the 'barcode' of föhn conditions. It indicates when and where all of the föhn conditions were identified throughout the four year period. It highlights the temporal and spatial variability of föhn conditions, as well as showing gaps in the observational data.

The location with the largest number of identified föhn conditions, events and days was Cole Peninsula. With its proximity to the AP, and higher elevation (420m a.s.l)

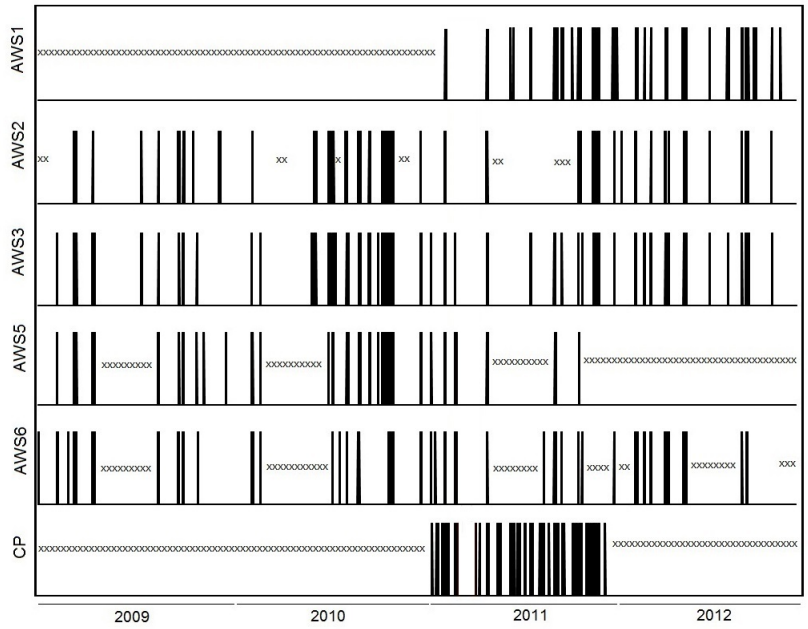

Figure 4.1: The föhn condition barcode. The number of föhn conditions at each location, as identified by the AWS and AMPS algorithms, from 2009-2012. The black bars are the föhn conditions. × displays periods where at least 72 consecutive hours of data are missing.

than the other AWSs, almost all descending föhn air, even weak föhn conditions, were identified at this location. The location which experienced the fewest föhn conditions was AWS2. Conversely to Cole Peninsula, this AWS is located at a distance of over 130km from the foot of the AP Mountains, and only strong föhn winds are able to propagate this far across the ice shelf. The spatial distribution of föhn winds will be assessed in more detail in Section 4.3.

4.2.1 Inter-annual Distribution

The number of föhn conditions varied per each year. The least number of föhn conditions were identified in 2009 (Figure 4.2). 134 föhn conditions, 65 föhn events and 87 föhn days were identified over the whole ice shelf (i.e the total of all locations). This was statistically significantly less than the number identified in 2010 and 2012 (significance level from students t-test (α) = 0.05). 194 föhn conditions were identified in both 2010

and 2012.

The year with the largest number of identified föhn conditions was 2011 (356 föhn conditions) (Figure 4.2). This year also experienced the most multi-location föhn conditions compared to other years (82 multi-location conditions). However, there were six operational AWSs during this year, including Cole Peninsula, which experienced significantly more föhn conditions than any of the other AWSs. The large number of föhn conditions at Cole Peninsula compared to other locations is evident in Figure 4.1. When excluding Cole Peninsula data, a total of 165 föhn conditions were identified in 2011, which is comparable to the other years.

Not only were there more AWSs in 2011, but the spatial distribution of the AWSs was more homogeneous than in other years. This led to more föhn conditions being identified in 2011. In an attempt to normalise the data, the total number of föhn conditions in a year have been averaged by the number of active locations. An average of 34 föhn conditions were identified at each location in 2009, and 49 were identified at each location in 2010 and 2012. In 2011, an average of 59 föhn conditions were identified from each location. Therefore, after removing the effect of a larger number of locations, there were still more föhn conditions identified in 2011 due to the inclusion of Cole Peninsula data. When Cole Peninsula was excluded, and just five locations were taken into account, the average number of föhn conditions identified at each location was 33; fewer than in 2009. Therefore, it is likely that the impact of föhn conditions was smaller in 2011 than in other years, even though a higher number of föhn conditions were identified in total.

To assess the inter-annual variability further, only föhn conditions identified at AWS2, AWS3 and AWS6 were analysed. These three AWSs observed near-surface conditions for the full four-year period. At these three locations, fewer föhn conditions were identified in 2011 (87) than in any other year (Figure 4.2). There were only 22 multi-location föhn conditions identified at AWS2, AWS3 and AWS6 combined, less than in other years. When analysing all six locations in 2011, there were 82 multi-location föhn conditions (Figure 4.2). This increase is due to the large number of föhn conditions at Cole Peninsula, which were simultaneously identified at one or more of the other

locations. Finally, the average duration of föhn events in 2011 was also (marginally) shorter than in other years. It is therefore likely that föhn conditions were less frequent and shorter in 2011, but the inclusion of Cole Peninsula data masks this finding.

4.2.2 Intra-annual Distribution

Föhn conditions were identified all year round, as can be seen in Figure 4.1, however there was a seasonal cycle in the number of föhn conditions identified over the ice shelf. There were significantly more ($\alpha = 0.05$) föhn conditions identified during spring (September, October, November) than during autumn (March, April, May), winter (June, July, August) and summer (December, January, February) (Figure 4.3). In total, 338 föhn conditions were identified in spring, 187 in autumn, 185 in summer and 168 in winter (June, July, August). Over 38% of the total number of föhn conditions were identified in spring.

On average, 54% of the days in spring were föhn days. The seasonal cycle was evident in 2010, 2011 and 2012, but it diverged in 2009. In 2009, more föhn conditions were identified in autumn than in any other season (46%). The spring peak was strongest in 2010. Over 65% of the f öhn conditions in 2010 were identified during spring. This had an impact on the average air temperatures during spring 2010. Excluding Cole Peninsula due to its higher altitude, the average near-surface air temperature over the ice shelf in spring was -15.3°C. However the average near-surface air temperature during spring 2010 was -11.3°C, i.e statistically significantly higher than the average spring air temperature ($\alpha = 0.05$).

The seasonal cycle in the number of föhn conditions was evident at AWS1, AWS2, AWS3 and AWS5. The highest seasonal number of föhn conditions was found in spring (Figure 4.3). There was also significantly more föhn conditions identified during spring than during summer or autumn at Cole Peninsula, however föhn conditions were more common in winter. As Cole Peninsula data were only available for one year, it is impossible to say whether this pattern is representative of the average conditions at this location. At AWS6, föhn conditions were identified most often during autumn. The number of föhn conditions in each season and at each location are displayed in Figure

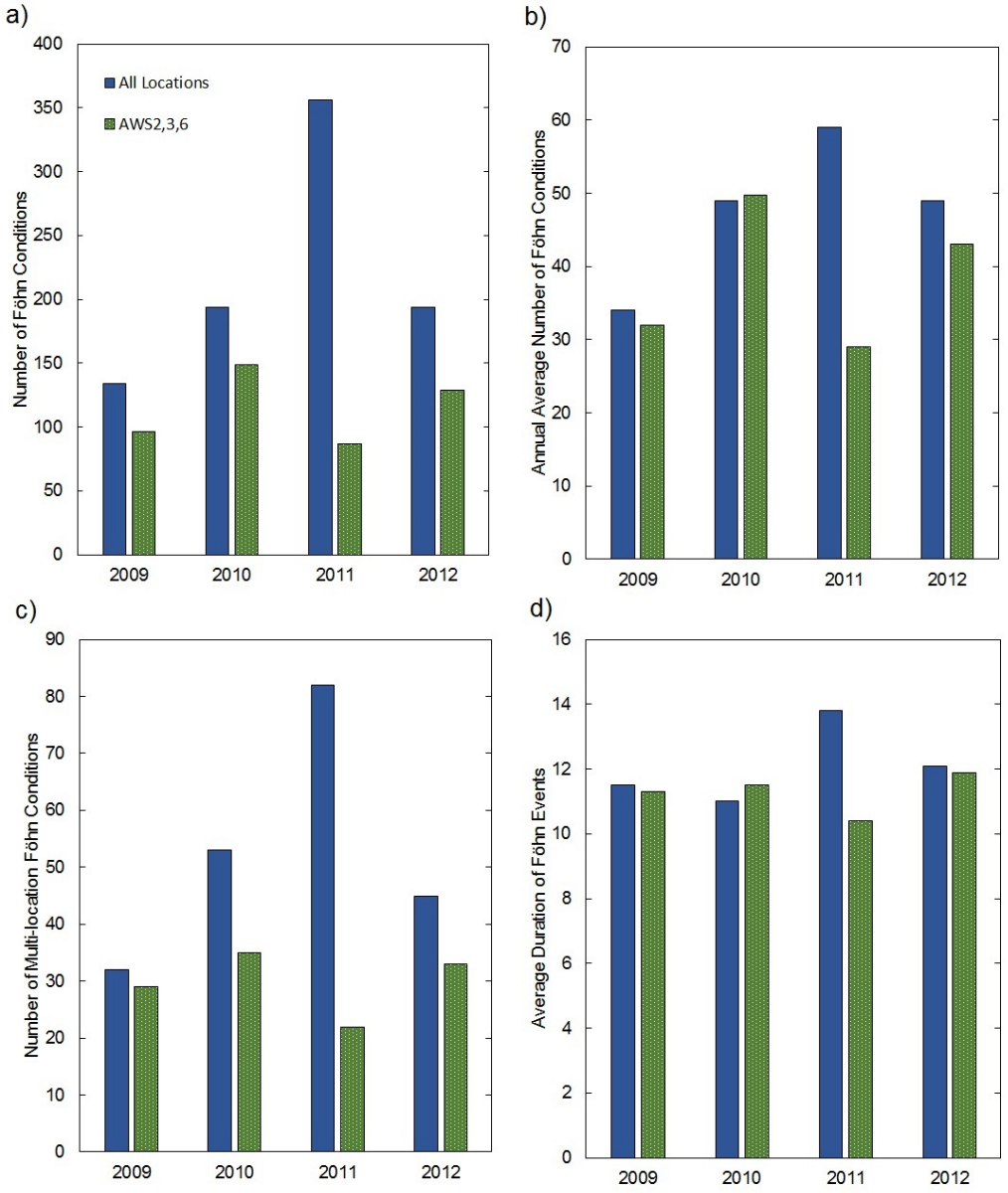

Figure 4.2: a) The total number of föhn conditions identified in each year. b) The average number of föhn conditions at each active AWS location, in each year. c) The number of multi-location föhn conditions in each year. d) The average duration of föhn events in each year (hours). Blue bars include data taken from all locations in the year. Green bars include data only from AWS2, AWS3 and AWS6 locations, as these were the only locations to have consistent observations throughout all four years.

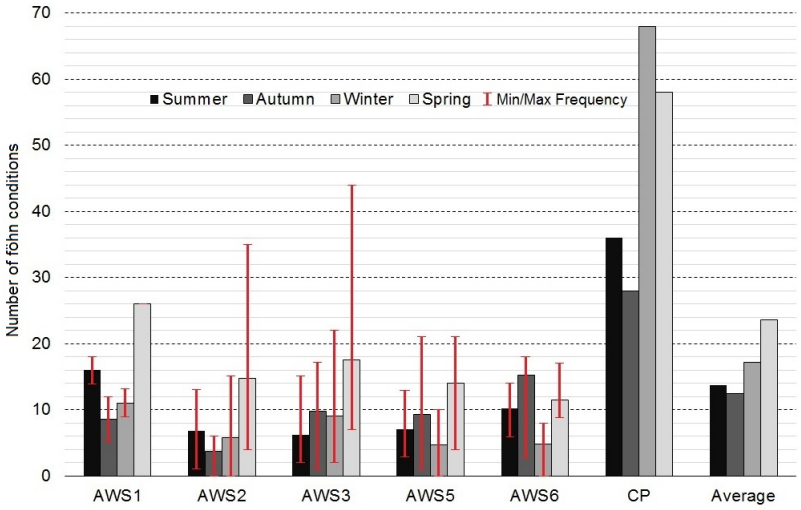

Figure 4.3: The average number of föhn conditions during each season (bars), at each location and average of all locations. The red lines depict the maximum and minimum seasonal föhn count at each location during any of the four years of data. No range is displayed on the Cole Peninsula (CP) frequencies as there was only one year of data. AWS1 has no red lines for spring as the same number of föhn conditions were identified in both years for which data are available at this location.

4.3.

The month to month variability in the number of föhn conditions is large(Figure 4.4). Föhn conditions peaked in September, and were at a minimum in June. On average, 37 föhn conditions were identified during September in each year, equating to more than one a day. In June, an average of 11 föhn conditions were identified per year. In a number of months, no föhn conditions were identified at particular locations. For example, May and June in 2009, and April and May in 2010.

4.2.3 Duration Analysis

The length of föhn events ranged from six to 72 hours. The average duration of a föhn event was 12.5 hours. Six-hour föhn events were most common, accounting for 48% of the 422 identified föhn events. The two longest föhn events (72 hours) were both

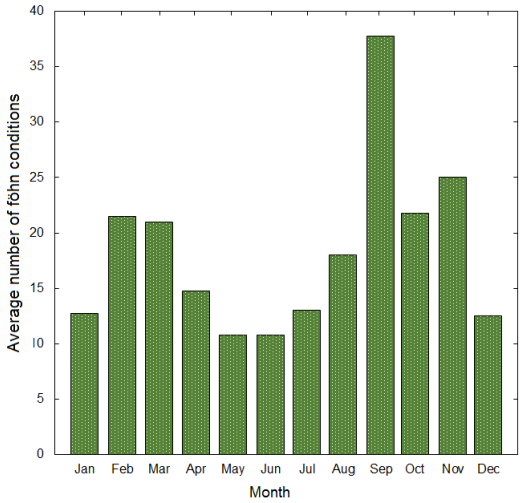

Figure 4.4: The average number of föhn conditions identified at all locations in each month, for 2009-2012.

identified at Cole Peninsula. The majority of the föhn events with a duration greater than 36 hours were identified at Cole Peninsula.

From year to year, the average duration of föhn conditions varied very little (Figure 4.2). Although not statistically significant, föhn events were longer in winter (13.0 hours) than during any other season (12.1 hours on average). This may be due to the higher number of föhn events with a duration greater than 24 hours during winter. Over 40% of the föhn events identified in June had a duration of 24 hours or more. The longest two föhn events (72 hours) though, both took place in spring.

Despite the relatively short duration of most föhn events, they are often grouped together, with more than one föhn event in a day, and/or multiple föhn days in a week. A 7-day (28 six-hour averaged time points) moving total of föhn conditions was calculated for the whole ice shelf to assess the frequency of föhn conditions. On two separate occasions (from 18UTC on the 20th to 18UTC on the 27th of September 2011, and from 00UTC on the 26th of September to 00UTC on the 3rd of October 2012) 23 föhn conditions were identified within 7 days. That equates to 138 hours or 5.75 days of föhn conditions within 7 days. The combined duration of all individual

föhn conditions within this one week was longer than the longest continuous föhn event.

There were over 280 7-day moving average periods (in four years) with 72 and more hours of föhn conditions within the 7 days. In comparison, the longest föhn event lasted for 72 hours. An event of that duration was only observed twice. Therefore, there are a great number of week-long periods for which many föhn conditions were identified, and the frequency of föhn conditions was high. The grouping of föhn conditions throughout the four years is visible in Figure 4.1.

The longest period of consecutive föhn days was eight days long. In 2011 back-to-back föhn days were identified from the 26th of August to the 2nd of September and from the 21st to the 28th of September. In 2012 an 8 day föhn period occurred from the 22nd to the 29th of April. Six and seven consecutive föhn days were also often identified throughout the four years. The majority of these occurred in spring and summer, when föhn days can have larger impacts on the surface due to higher average temperatures with the increased incoming solar radiation. This will be discussed in greater detail in the SEB chapter.

4.3 Spatial Distribution

Föhn conditions were identified at all six locations across the LCIS (Table 4.1). They varied in number, strength and near-surface characteristics by location.

The AWSs were distributed relatively evenly across the ice shelf (see Chapter 2 for a map), and were in useful locations to assess the spatial distribution of the föhn winds. As Cole Peninsula was closest to the AP, it was expected that more föhn conditions would be identified at this location. It is unfortunate that observations from this AWS are only available for 2011, as it was in the perfect position to identify föhn conditions. In 2011 alone, more föhn conditions were identified at Cole Peninsula than at AWS2 in four years. However, even one year of data are useful, to identify which föhn events had a strong enough signal to be able to propagate across the ice shelf, and which were

Table 4.1: The number of föhn conditions identified at each AWS for each year of available data. 'ND' indicates that no data were available for this year.

Location	2009	2010	2011	2012	Location Average
CP	ND	ND	191	ND	191
AWS 1	ND	ND	58	65	62
AWS 2	22	51	21	30	31
AWS 3	32	69	32	37	43
AWS 5	38	45	20	ND	34
AWS 6	42	29	34	62	42
Total	134	194	356	194	-
Average	34	49	59	49	-

only identified at Cole Peninsula.

AWS1 is located on the remnants of Scar Inlet, and was therefore ideally located to capture föhn events to the north of the ice shelf. It was also closer to the AP than any other AWS (except Cole Peninsula). AWS5 is located almost in the centre of the ice shelf, and is ideal for investigating the propagation of föhn air across the ice shelf from the AP to AWS3, which is located at the same latitude as AWS5, but 47km further east. AWS6 is the most southerly AWS, and is well located to capture föhn events generated by southwesterly winds.

This is the first study to present observations of föhn conditions as far south as 68.14 °S, 63.95°W) AWS6. In total 167 föhn conditions were identified here. This is probably an underestimation of the true number of föhn conditions, as no data are available during winter. In 2009, more föhn conditions were identified at AWS6 than at any other AWS (Table 4.1). In 2012, only at AWS1 were more föhn conditions identified than at this AWS. Many previous studies suggest that föhn conditions are infrequent over the south of LCIS. This would explain the lack of observations of föhn conditions at AWS6. However, it is now clear that föhn conditions are as frequent in the south of the LCIS than at locations further north.

Of the 191 föhn conditions identified at Cole Peninsula in 2011 (Table 4.1), 37% were multi-location föhn conditions (Figure 4.5). For 15% of the föhn conditions that

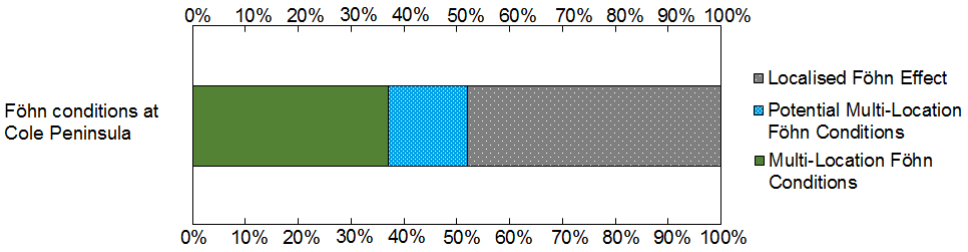

Figure 4.5: The percentage of föhn conditions identified at Cole Peninsula that were: 1) also identified elsewhere simultaneously (multi-location föhn conditions, dark green), 2) had a weak föhn signal but it did not meet the requirements of the AWS algorithm at other locations (potential multi-location föhn conditions, spotted blue), and 3) were not identified elsewhere (localised föhn effect, spotted grey).

were only identified at Cole Peninsula, the föh air may have stretched further across the ice shelf but the signal was not detected by the AWS algorithm (Figure 4.5). This is inferred from the fact that the relative humidity of these föhn periods was close to the identification threshold at other locations (within 5% of the RH15 threshold). 48% of the föhn conditions only identified at Cole Peninsula are thought to have been very localised and/or relatively weak, and were therefore unable to propagate further (Figure 4.5). In these cases, the relative humidity at the other locations was well above 90%, and therefore no föhn signature was detected at the near-surface level. Cole Peninsula is therefore well positioned to identify both strong and weak föhn conditions, and localised and spatially-extensive föhn conditions.

From 2009 to 2012, 103 multi-location föhn conditions were identified from at a minimum of two of the following locations: AWS2, AWS3, AWS5 and Cole Peninsula. That means that approximately 11% of all föhn conditions were identified over a large, central portion of the ice shelf. Twelve föhn conditions were identified at all four of the above mentioned locations at the same time. For this to be the case, the föhn air must have propagated across the ice shelf from approximately west to east. 45% of the föhn conditions identified at AWS6 were also identified at AWS3, highlighting the propagation of föhn air from southwest to northeast. Similarly, multi-location föhn conditions were also identified at AWS1 and AWS2, displaying a northwest to southeast propagation of föhn air. The multi-location föhn conditions reveal that the föhn air

propagated across the ice shelf not only in a strict west to east direction.

One six-hour föhn condition was identified at all locations simultaneously. This was part of a long föhn event. The föhn event was intermittent at some locations, but over the whole two day period, it displayed a west to east propagation of the föhn air. The föhn event began at 00UTC on the 23rd of February 2011 at Cole Peninsula. It was then identified 12 hours later at AWS5. By 18UTC on the 23rd of February, it was identified at AWS2, AWS3 and AWS6. For the following 12 hours it was only identified close to the AP, at AWS1 and Cole Peninsula, as the near-surface föhn signal diminished further east. The föhn wind strengthened again at 18UTC on the 24th of February and föhn conditions were identified at all six locations simultaneously, before retreating from the whole ice shelf. Although this was only one individual period, many föhn events appear to display a propagation of the föhn air, by being identified first at Cole Peninsula, and six or 12 hours later at locations further east.

In section 4.1 it was hypothesised that more föhn conditions would be identified on the west of the ice shelf, and that the number of föhn conditions would decrease further east. If that was the case, AWS3 would have identified the fewest number föhn conditions, and the most would have been identified at Cole Peninsula. More föhn conditions were identified at Cole Peninsula, and in general, fewer föhn conditions were identified east of this location, however there was no gradient. On average, more föhn conditions were identified at AWS3 (furthest away from the AP) than at AWS2, AWS5 and AWS6 (Table 4.1).

It was also hypothesised that more föhn conditions would be identified further north, and that the number of föhn conditions would decrease further south. However, despite more föhn conditions being identified at AWS1 than at locations further south, there was no evidence of a north to south gradient in the number of föhn conditions. On average, there were more föhn conditions identified at AWS6 than at AWS5, which is ∼70km further north, and at AWS2 which is more than 150km further north.

The duration of föhn events displayed a spatial variability. At Cole Peninsula, föhn events were longer than elsewhere, with an average duration of 18 hours. Further east,

the föhn events were significantly shorter ($\alpha = 0.05$). At AWS5, the average duration was 11 hours, at AWS2 and AWS3, the average duration of föhn events was 10 hours. This is likely due to distance from the AP. It takes time for the föhn air to propagate across the ice shelf, but as it does, it mixes with cooler, more moist ambient air, which erodes the signal and interrupts the föhn event. Six-hour föhn events were most common at all locations. Föhn events with a duration of more than 36 hours were rare at AWS2 and AWS3.

4.4 Near-Surface Characteristics

Unless otherwise stated, the near-surface characteristics presented in this chapter are taken from the observational data only. When simulated near-surface conditions are discussed, this will be explicitly stated.

4.4.1 Relative Humidity Changes

Changes in near-surface conditions associated with föhn onset were detected by the AWS algorithm. Wind direction and relative humidity changes were the primary criteria, followed by the air temperature change. As mentioned in Chapter 3, the relative humidity change was the largest signal associated with föhn onset.

From 2009 to 2012 the average relative humidity over the ice shelf was 89.6%. This value includes the relative humidity values during föhn events. When föhn conditions were excluded, the average relative humidity was 94.2%. During föhn conditions only, the average relative humidity was 66.1%. The föhn conditions influenced not only the near-surface conditions during the föhn periods, but also influenced the average conditions over the ice shelf.

The magnitude of the relative humidity change during föhn conditions varied by location. The largest relative humidity decrease from non-föhn to föhn conditions was observed at Cole Peninsula (δRH = 40.8%). AWS1 also experienced a large magnitude of change (δRH = 27.5%). The least pronounced change was observed at AWS3, where

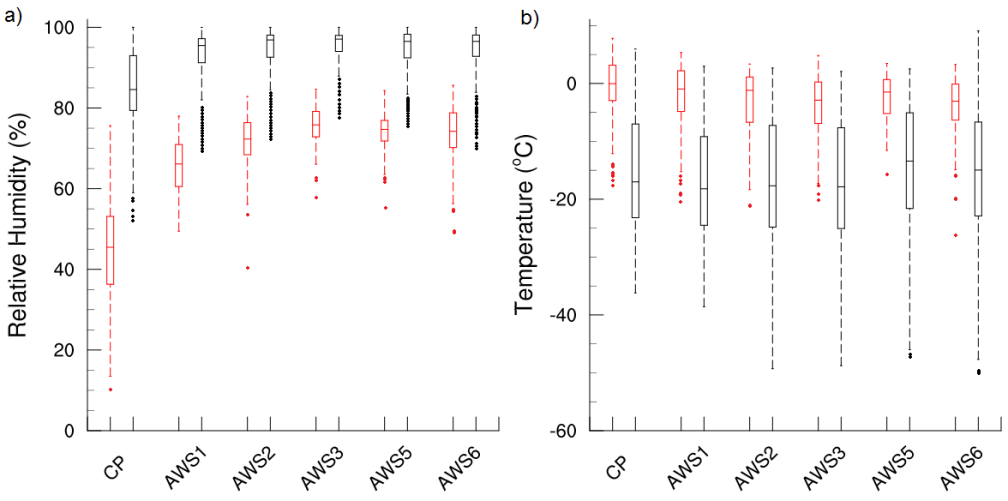

Figure 4.6: Average relative humidity (a) and air temperature (b) during föhn (red) and non-föhn (black) conditions observed at each location from 2009-2012. The box presents the 25th, 50th and 75th quartile values. The whiskers extend to the minimum and maximum values (dashed lines). Outliers are circles.

relative humidity decreased by an average of 19% during föhn conditions. A comparison of föhn and non-föhn composites of near-surface relative humidity is presented in Figure 4.6a.

The lowest observed relative humidity during any föhn condition was observed at Cole Peninsula at 12UTC on the 6th of October 2011 (10.0%). Excluding Cole Peninsula, the driest observed föhn condition was recorded at AWS2 at 18UTC on the 25th of February 2012 (39.7%). The lowest relative humidity during a föhn event was observed from 18UTC on the 26th - 06UTC on the 27th of August 2011 (15.5%). The lowest relative humidity during a föhn day was observed on the 8th of June at Cole Peninsula (daily average of 17.5%).

Despite the absence of a west to east gradient in the number of föhn conditions, there was a west-east gradient in the near-surface föhn signal. As the air propagated eastwards, away from the AP, the relative humidity signal weakened due to the mixing with ambient, moist air. This signal was most defined when analysing the multi-location föhn conditions. As these periods displayed the propagation of the föhn air across the

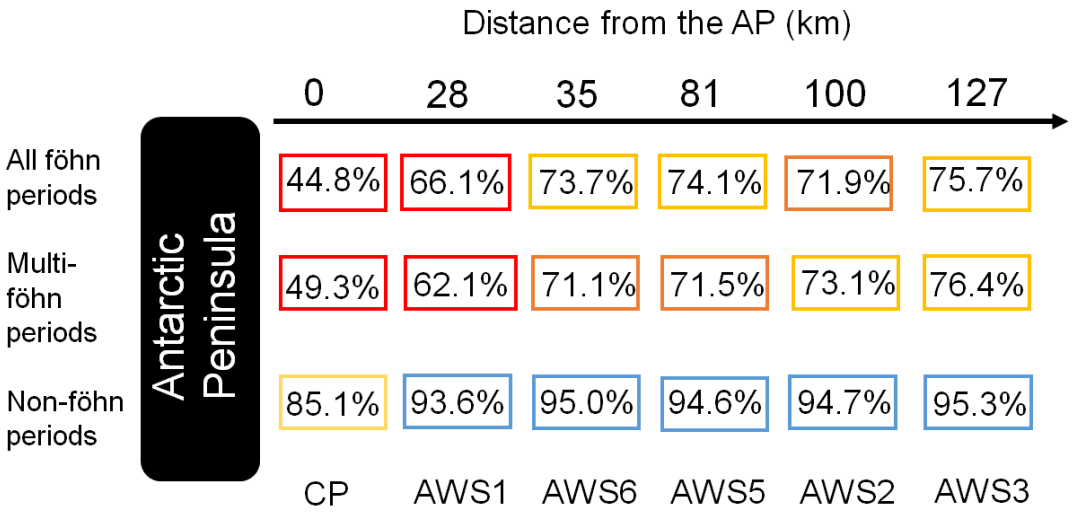

Figure 4.7: A west to east gradient in decreasing föhn signal (increasing relative humidity) was identified when assessing the average relative humidity during multi-location föhn conditions (middle line) and all föhn conditions (top line). 'CP' is Cole Peninsula AWS. The average relative humidity at each location is colour coded to show the decreasing föhn signal (increasing relative humidity) with distance from the AP.

ice shelf, they had the clearest west to east gradient in relative humidity.

The average relative humidity values during multi-location föhn periods, with increasing distance from the AP are presented graphically in Figure 4.7. A similar signal was also found when assessing all föhn events, as opposed to multi-location föhn events. However, this signal was less pronounced, as AWS2 did not follow the west to east gradient. AWS2 is exposed to a localised föhn effect from Jason Peninsula (see Chapter 2). Under north to northwesterly winds, the interaction between the airflow and Jason Peninsula can induce a localised föhn signal, which was occasionally observed at AWS2. Assessing the spatial distribution of föhn events over this wide scale has revealed locations where a small-scale or localised föhn effect was present. This potentially contribute to the drier conditions identified at AWS2 and it may have gone unnoticed in previous case studies. The air temperature values during all föhn events, and multi-location föhn events did not show a similar west-east gradient, as displayed in Figure 4.8.

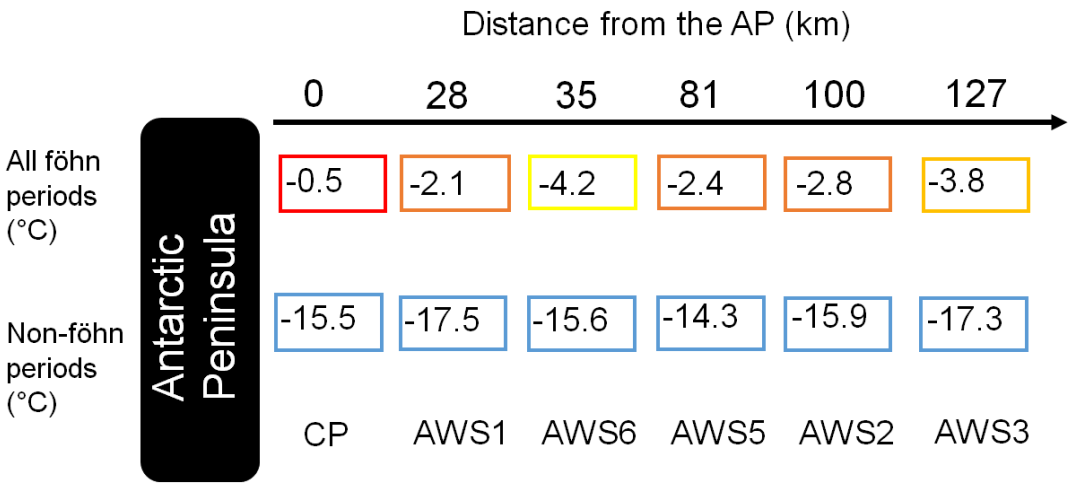

Figure 4.8: A west to east gradient in decreasing föhn signal (decreasing air temperature) was identified when assessing and all föhn conditions (top line). No significant change was identified when assessing only the multi-location föhn conditions as was found with the relative humidity values. 'CP' is Cole Peninsula AWS. The average relative humidity at each location is colour coded to show the decreasing föhn signal (decreasing temperature) with distance from the AP.

A north-south gradient was identified, with strongest föhn conditions furthest north, and weaker conditions further south. The north-south gradient was not as pronounced or defined as the west to east gradient. Largely, this was due to the dominance of the west-east signal. To asses only the north-south pattern, the AWSs would need to be located equidistant from the AP, so as not to include the west-east gradient (due to föhn propagation) in the signal. However, that is not the case here. In an attempt to combat that issue, Cole Peninsula data were not included in the analysis due to its proximity to the AP.

Firstly, a group of locations was assessed, this included AWS1, AWS2 and AWS3. All three locations are located approximately along the same line of longitude, and AWS2 and AWS3 are both over 100km distance from the foot of the AP, to reduce the influence of the west-east gradient. From north to south, the average relative humidity during all föhn conditions (not just multi-location föhn events) was: 65.5% at AWS1 (65.93°S), 72.8% at AWS2 (67.02°S) and 76.2% at AWS3 (67.57°S). A decreasing gradient in average föhn air temperature was also discovered; -2.1°C (AWS1), -3.2°C (AWS2) and -3.9°C (AWS3).

When assessing all locations (except Cole Peninsula), a gradient in air temperature and relative humidity was also identified (Figure 4.9). It should be noted that AWS5 and AWS3 are located at the same latitude, and their average föhn conditions were combined for this analysis. The gradient in relative humidity was not observed at AWS6, as it recorded lower average relative humidity values than AWS5 and AWS3. At AWS1 the average air temperature recorded during föhn conditions was -2.1°C, at AWS2 it was -3.2°C, at AWS3+AWS5 it was -3.3°C, and at AWS6 it was -3.9°C. The average relative humidity value during föhn conditions was (in north to south order): 65.5% (AWS1), 72.8% (AWS2), 74.4% (AWS5+AWS3) and 73.7% (AWS6). AWS6 is closer to the AP than some of the other locations, which may explain why drier föhn conditions were observed here, and why it does not fit the north-south pattern.

Composites of simulated near-surface conditions from AMPS during föhn and non-föhn periods were analysed from 2009-2012, and are presented in Figures 4.10 and 4.11.

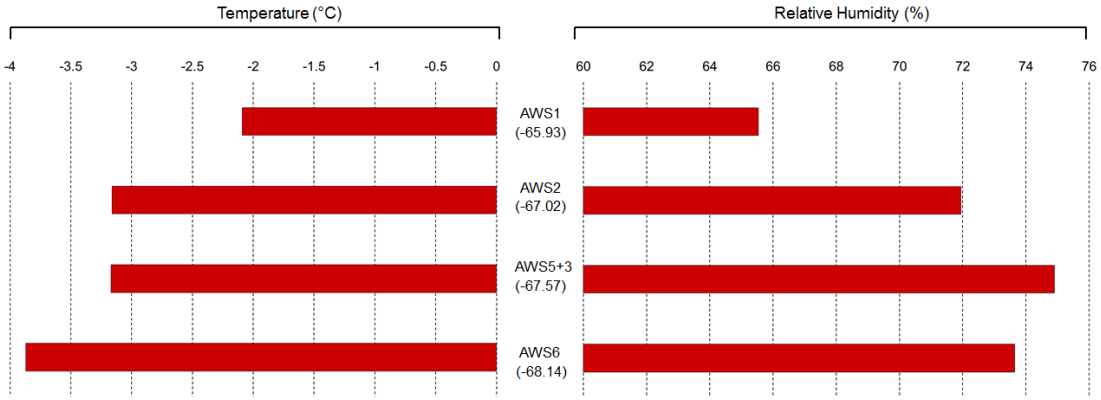

Figure 4.9: The average relative humidity and air temperature during föhn conditions from north to south. AWS5 and AWS3 were located at the same latitude, and therefore their conditions have been averaged together. In general, the relative humidity increases and temperature decreases (weaker föhn signal) further south.

From assessing these composites the most dominant spatial distribution appears to be a combination of the west-east propagation and the north-south gradient. The average föhn conditions were strongest on the northwest of the ice shelf and decreased towards the southeast. This spatial pattern was not evident during non-föhn conditions, suggesting that the northwest-southeast spatial distribution is due to the propagation of föhn air.

4.4.2 Air Temperature Changes

The rise in air temperature associated with föhn onset was secondary to the relative humidity change. As discussed in Chapter 3, the air temperature threshold used to identify föhn conditions was the same for all locations. The spatial variability in average air temperature during föhn conditions was much smaller than the relative humidity variability. This is highlighted in Figure 4.6b.

The 2009 to 2012 average air temperature over the ice shelf (all locations) was -14.8°C. This includes the air temperature during föhn conditions. When removing the föhn effect, the average air temperature over the ice shelf was -15.7°C. During föhn

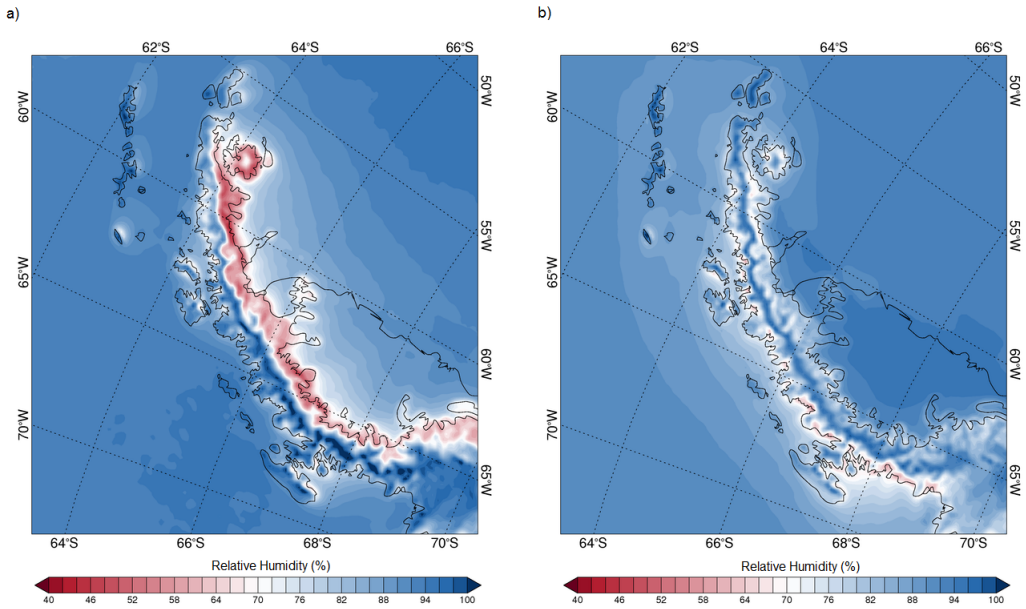

Figure 4.10: Composites of the near-surface relative humidity during föhn conditions (a) and non-föhn periods (b). The propagation of föhn air is visible in the föhn-composites as the driest conditions occur along the foot of the AP, and the humidity increases towards the edge of the ice shelf. Almost the opposite spatial pattern is visible in the non-föhn composite, with the driest areas being on the western side of the AP.

conditions the ice shelf experienced an average air temperature of -4.5°C. The location which experienced the largest temperature difference between non-föhn and föhn conditions was AWS1 (17.3K). At both AWS3 and AWS5 the average temperature difference was 11.9K. These two latter locations experienced the smallest change in air temperature with föhn onset. Therefore, the change in air temperature during föhn conditions was significantly larger than the threshold of 3K used in the AWS algorithm, and the majority of the föhn conditions should have been detected.

The warmest individual föhn condition was observed at Cole Peninsula (7.8°C). However, an air temperature of 9.1°C was observed at AWS6 during a non-föhn period (8th December 2012). This was detected by the AWS algorithm, however it was not identified by AMPS and was therefore categorised as a non-föhn period. The wind direction simulated by AMPS at the height of the AP was from a northeasterly direction, and therefore isentropic drawdown due to westerly winds was not possible. AWS2, AWS5 and AWS6 all observed temperature maximum between 3.3°C and 3.5°C during föhn conditions.

At all locations föhn events raised the air temperature above freezing (T> 0°C) on more than one occasion. At Cole Peninsula 85% of all temperature values above freezing were observed during föhn conditions. Further east at AWS3, and also further south (AWS6), the influence of föhn conditions was similar. Although there were fewer observations of T> 0°C, 64% of these times were during föhn events at AWS3. At AWS6, 76% of the observations of T> 0°C corresponded to föhn conditions. At every location, at least 60% of the observations of T> 0°C were associated with föhn events.

Near-surface air temperatures values above freezing are often used as a proxy for ice melt when surface temperature observations are unavailable. Therefore, if T> 0°C was used as a proxy for melt, it may be inferred that föhn conditions are responsible for 85% of the melting episodes at Cole Peninsula. This will be addressed further in the Chapter 5.

Out of the total 878 föhn conditions, 37% experienced air temperatures above 0°C. This adds up to 1950 hours, or 81.3 days of potential melt in four years. This varied

by location, and by season. At Cole Peninsula, over 51% of the identified föhn events observed T> 0°C. Over 81% of the summer föhn conditions were characterised by T> 0°C, and even during winter over 41% of the föhn conditions led to observations of T> 0°C at Cole Peninsula. The location with the fewest föhn conditions with T> 0°C was at AWS6 (23.4%). At AWS6, the AWS furthest south, the majority of the föhn conditions experiencing T> 0°C occurred during the summer months.

The longest period above freezing was a 66-hour föhn event identified at Cole Peninsula between the 23rd and the 25th of February 2011. This was a multi-location föhn event, which was also identified at all other locations, but for a shorter duration. Episodes of T> 0°C were observed at three of the locations, including at AWS3, 130km distance from the AP. The average air temperature over the whole ice shelf during this period was 3.8°C, and the maximum six-hour averaged air temperature was 6.0°C.

The west-east gradient in the föhn signal was not evident in the observed near-surface air temperature. However, when analysing the simulated near-surface temperature from the AMPS output, an approximate northwest-southeast gradient is visible in the composite of föhn conditions. (Figure 4.11). As a composite of all föhn conditions, the air temperature was highest close to the AP and decreased further east. The lowest air temperature was found in the southeast section of the LCIS.

4.4.3 Wind Speed and Direction

As the wind direction was used as a criterion in the AWS algorithm (see Chapter 3), all föhn conditions must coincide with westerly wind. Over 63% of the föhn conditions identified over the whole ice shelf observed wind from a northwesterly direction (300-360°). This varied by location, as displayed in Figure 4.12. At all locations (except Cole Peninsula), northwesterly winds dominated during föhn conditions.

At Cole Peninsula, no wind direction criteria was used in the algorithm due to its proximity to valleys which influenced the localised wind direction, hence some of the föhn conditions were characterised by winds with an easterly component in Figure 4.12f.

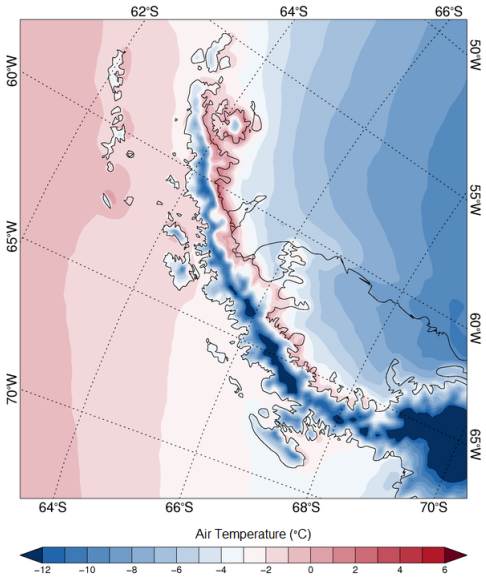

Figure 4.11: The simulated near-surface air temperature from AMPS as a composite of all föhn conditions.

Here, 26% of the föhn conditions experienced northwesterly flow and 42% experienced southwesterly flow.

The wind speed was not taken into account when identifying föhn conditions. In some previous studies, an increase in wind speed was used as a criterion (e.g Speirs *et al.* 2010). However, over the LCIS, an increase in wind speed did not accompany all föhn conditions. That being said, the average wind speed over the whole ice shelf (average of all locations) was higher during föhn conditions (4.9ms^{-1}) than during non-föhn conditions (3.8ms^{-1}).

The location with the highest average wind speed during föhn conditions was AWS3 (5.5ms^{-1}), while the lowest (average) was observed at Cole Peninsula (4.4ms^{-1}). During non-föhn conditions, this pattern was almost reversed, as wind speed was highest at Cole Peninsula (4.1ms^{-1}). The largest difference between the average wind speed during föhn and non-föhn conditions was observed at AWS3 (1.7ms^{-1}).

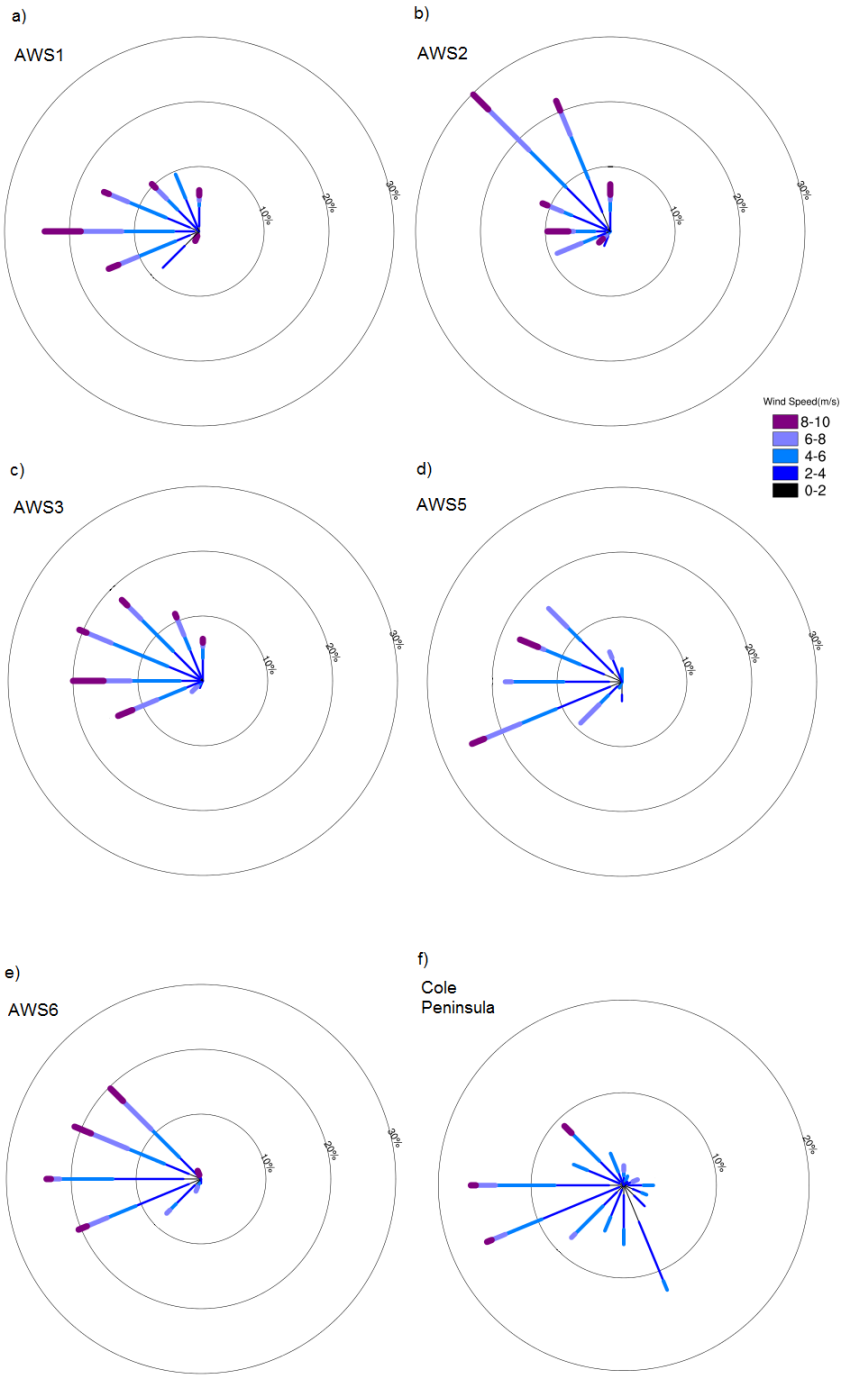

Figure 4.12: Wind roses displaying the wind direction (vector) and wind speed (colour) during föhn conditions at AWS1 (a), AWS2 (b), AWS3 (c), AWS5 (d), AWS6 (e), and Cole Peninsula (f). The frequency circles are set at 10% intervals.

4.5 Discussion

Dry warm föhn conditions have been observed over the whole of LCIS, stretching ∼260km in north-south direction and up to ∼130km east of the AP. The föhn winds were identified in near-surface AWS observations and in archived 5km resolution AMPS data.

This is the first study to investigate the spatial distribution and temporal features of föhn winds over the whole LCIS. Previous studies over the LCIS have focused on individual föhn events in order to gain an insight into the dynamics and mechanisms of föhn winds (Elvidge *et al.*, 2015, 2016). Kuipers Munneke *et al.* (2012) highlighted the need to investigate the frequency and spatial distribution of föhn conditions in a bid to understand the large-scale impact they can have on longer timescales. However, further south (AWS6), no study has investigated föhn winds.

The clearest temporal signature was the peak in the number of föhn conditions identified during spring (SON). In some years, over 50% of the föhn events were identified during spring. In 2010, 34% of the spring days were characterised by föhn conditions. This result is consistent with a study conducted over the northern AP by. Cape *et al.* (2015) who assessed the frequency of föhn winds over the AP below 64.8°S and 66°S from observations. They found that föhn conditions accounted for 5-25% of the time during spring months. The föhn identification algorithm used in the current project was different to the one used in Cape *et al.* (2015). Therefore, the peak in spring föhn conditions is robust regardless of the data used, the period assessed and the algorithm used to define föhn conditions.

There are numerous local and large-scale forcings known to influence the frequency of föhn events and the associated increased air temperatures on the northeastern AP. There are also relationships between these local and large scale forcings, which complicate the signal. The Southern Annular Mode (SAM) has a strong positive correlation with the frequency of föhn events and the associated northeast AP temperature. The link between SAM and föhn conditions has been known for over a decade, and it forms the basis of the föhn hypothesis (Marshall *et al.*, 2006). When the SAM index is positive,

positive zonal wind anomalies are observed over the northeast AP (during all seasons), which leads to more frequent föhn events due to the increased flow over the AP (Clem *et al.*, 2016). Positive air temperature anomalies on the northeast AP (called 'warm years' by Clem *et al.* 2016) were strongly, positively correlated to significant westerly flow over the AP (Clem *et al.*, 2016). A positive phase of the SAM index is positively correlated to the frequency of föhn conditions over the northern AP (Cape *et al.*, 2015).

From AWS observations at Esperanza and Marambio stations on the AP, Clem *et al.* (2016) found that air flow was primarily westerly during summer and autumn, which prompts föhn events over the northeastern AP. In winter and spring, air flow was primarily northwesterly which led to föhn formation further south on the AP. This may account for the increased frequency of föhn events during spring (and winter at Cole Peninsula) over the LCIS, which is further south than the above mentioned AWS locations. The relationship between SAM and the development of föhn events was significant for the 'entire northern two thirds of the AP' in summer, spring and autumn (Clem *et al.*, 2016). This area was not well defined, however it includes the area north of Rothera (67.57°S, 68.13°W), and therefore includes the northern section of the LCIS.

The SAM is closely linked to the synoptic situation in the Amundsen-Bellingshausen Seas, especially to the location and strength of the Amundsen Sea Low (ASL) (Hosking *et al.*, 2013). The ASL dominates the interannual variability of the eastern AP air temperature and the frequency of föhn conditions. The spring time peak in the number of föhn conditions is closely correlated to the position and strength of the ASL (Cape *et al.*, 2015). The latitudinal and longitudinal position of the ASL, as well as the pressure minimum, are correlated to the number of föhn conditions over the northeastern AP (Cape *et al.*, 2015). During spring the ASL moves southwesterly (away from the AP), which directs more airflow over the AP, and this coincides with a peak in the number of föhn conditions (Cape *et al.*, 2015; Clem & Fogt, 2013; Hosking *et al.*, 2013). Cape *et al.* (2015) analysed observations north of, but including Scar Inlet. The spring peak in the number of föhn conditions has been identified over the LCIS in the present study, and therefore it is likely that the ASL has an influence over this too.

The El Niño Southern Oscillation (ENSO) is known to influence the climate of the AP (Clem & Fogt, 2013). It was found that there was a significant relationship between ENSO and the western AP air temperature during winter and spring. However, the relationship between ENSO and the eastern AP was significantly weaker. ENSO does not influence the flow of air over the AP (Clem *et al.*, 2016), therefore, it is unlikely that tropical teleconnections through ENSO had any influence on the frequency of föhn conditions on the LCIS.

The high number of föhn conditions in spring dominated the intra-annual variability of föhn events over the LCIS in the current study. This was also found to be the case for the region north of the LCIS by Cape *et al.* (2015). It is therefore inferred that the large-scale forcing over northeastern AP föhn events, identified by Cape *et al.* (2015) and Clem *et al.* (2016), also influences the number of föhn conditions over the LCIS.

SAM influences the longer-term (decadal to half century) climatic conditions over the AP, such as the increase in the frequency of föhn events since the 1960s found by Cape *et al.* (2015). Whereas the ASL influences the shorter-term frequency of conditions over the AP, for instance the peak in spring. The relationship between the large scale forcing, westerly winds and föhn events is complex, and therefore it is unlikely that all of the temporal variability can be attributed to the large scale forcing. The influence of local forcings, such as topography, boundary layer stability and upwind blocking further increase the complexity of the system.

Cold pools have previously been observed over Larsen B and C ice shelves (Scambos, T., personal communication, September 2016). The strong stability of the surface layer during winter, and the low sloping surface of the LCIS allow cold air to pool on the surface. A number of studies have investigated the relationship between cold pools and and the penetration of föhn winds (e.g Drobinski *et al.* 2007; Richner & Gutermann 2007). These studies have mostly focused on föhn winds in the Alps, where cold pool build up is often diurnal (due to the radiation cycle in mid latitudes) and cold pools can be difficult to erode due to the complex valley systems preventing the 'flushing' of cold air (Richner & Gutermann, 2007). However, some inferences can be made about cold pool build up in the Antarctic from these studies. According to Drobinski *et al.*

(2007), only particularly strong föhn winds in the Rhine Valley are able to penetrate to the surface, and cold pools often prevent the föhn air from reaching the ground during föhn events. This does not seem to be the case over the LCIS, as over 400 föhn events, of varying durations, were observed near the surface in just four years. The cold air build up over the LCIS can be persistent, but it may erode more easily as it can be flushed off the ice shelf due to the flat surface of the LCIS.

Richner & Gutermann (2007) found that over the Swiss Plateau in the Alps, cold pools of 100m depth can persist at the surface whilst the föhn air flows over it. It is possible that this can sometimes happen over the LCIS. The AMPS algorithm over-predicted the number of föhn conditions relative to the AWS algorithm (see Chapter 3 for more details). One explanation for this may be that there was no associated near-surface föhn signal to accompany the upper air signal detected by the AMPS algorithm, because the föhn air was overriding a cold pool. There are, however, other potential reasons for the disagreement between the AMPS and AWS algorithms (see Föhn Identification Algorithm). It is not possible to assess this further with the data available for this research as the AWSs only observed conditions within the lowest 2-3m of the boundary layer.

The interaction between wind and cold pools over Antarctic ice shelves has been discussed by Renfrew (2004) and Elvidge *et al.* (2015). Cold pools were responsible for reduced katabatic flow over the Brunt Ice Shelf, due to them acting as a 'dam' to the katabatic flow (Renfrew, 2004). Over the LCIS, aircraft observations and regional modelling revealed a steep near-surface, horizontal gradient of $\sim$10K over 60km formed by the interaction of föhn air and a cold pool (Elvidge *et al.*, 2015). Case studies of individual föhn events have shown that föhn air over the LCIS is generally able to penetrate to the surface, and either displace or mix the cold pool air (Elvidge *et al.*, 2015). The interaction of a cold pool and föhn winds is investigated in greater detail through simulations with a high-resolution model. This is part of the work presented in the Chapter 6.

The high number of föhn conditions in spring has implications for the ice shelf surface. The impact of föhn winds is potentially amplified in spring, compared to other

seasons. During spring, the average air temperature over the ice shelf is -14°C, and surface melt is unlikely. However, it has been shown that in seasons with a particularly large number of föhn conditions (e.g spring 2010), the seasonal air temperature was higher than average. Föhn winds were able to influence both the short term, immediate air temperature, and (during seasons with a high number of föhn events) the average seasonal temperature. Near surface air temperatures of higher than 0°C were recorded for a total of 103 föhn conditions in spring (2009-2012). In the absence of föhn conditions, only 41 six-hour periods experienced an air temperature above freezing during spring.

Preceding the collapse of Larsen B Ice Shelf, a large amount of surface melt was observed during the spring and summer, which was associated with northwesterly föhn winds (Van Den Broeke, 2005). A number of other studies also attribute surface melting to föhn winds. King *et al.* found that whilst a sequence of föhn events in a short space of time induced surface melt on the northwest LCIS, they had only a limited impact on the overall seasonal amount of melt (relative to the average melt season). However, in the current study, a considerable increase in seasonal air temperature was found in spring 2010, which is attributed to the large number of föhn events during that particular season. The impacts of föhn events on the surface melt and energy balance is discussed in greater detail in the Chapter 5.

The average duration of föhn events identified over the LCIS was shorter than observed elsewhere in the Antarctic (Bannister & King, 2015; Speirs *et al.*, 2010). Over South Georgia they were, on average, over 30 hours long. Cape *et al.* (2015) regularly observed föhn events lasting over a week, whereas over the LCIS they were 12.5 hours on average, and the longest event was 72 hours. This study is not directly comparable to the above mentioned ones, as different algorithms were used to define föhn conditions. Furthermore, the combination of the AWS and AMPS algorithms shortened the duration of some föhn events when the two algorithms did not agree on the onset or cessation of föhn conditions. If föhn events were only determined by the AMPS algorithm, föhn events would have regularly surpassed 48 hours duration. Similarly, one föhn event lasted 108 hours when identified by the AWS algorithm alone. However, without both the upper-air and near-surface signal present together, these were not

classified as föhn conditions in this thesis.

Theoretically, as cold pool stability is weaker in summer (weakly convective surface layers are often observed Kuipers Munneke *et al.* 2012), the duration of föhn events should perhaps be longer to reflect this. However, enhanced mixing during summer may cause the föhn air to mix more readily with the ambient air, thus leading to erosion of the föhn signal (Zängl *et al.*, 2004). In winter, cold pools may be more stable and more frequent, but they can be overwhelmed by other factors such as the synoptic conditions. Low pressure systems are more persistent during winter, and can direct airflow over the AP, unlike during high pressure systems which can lead to cold pool development. This may account for the marginally longer winter föhn events compared to other seasons.

Although individual föhn events may be short, they occur in rapid succession, which aggregates and prolongs their impact on the surface. It has previously been found that in the MDVs, multiple, consecutive föhn events had an impact on soil temperatures and surface melting that outlived the length of the föhn events themselves (Barrett *et al.*, 2008). A comparable effect has been observed over the LCIS. The repeated melting and refreezing of surface ice reduces the firn air space. This is air trapped in the pores within the semi-compacted firn snow. There is then less space available for melt water in the firn layer, forcing it to percolate deeper into the snow layer and then the ice shelf itself, or remain on the surface as melt ponds (Kuipers Munneke *et al.*, 2014). This loss of firn air and densification of the surface ice is considered to be a good indicator for ice shelf (in)stability and a precursor for the collapse of an ice shelf (Kuipers Munneke *et al.*, 2014). Repetitive föhn-induced melting from successive föhn events, especially during spring when föhn conditions are frequent, can lead to the loss of firn air over the LCIS. Melt ponds have been observed on the northwest section of the LCIS, close to the AP and Jason Peninsula, where föhn conditions are most frequent, and the föhn effect is stronger (Luckman *et al.*, 2014).

Föhn conditions were observed more frequently, and showed the strongest signal (lowest relative humidity, highest air temperature) at Cole Peninsula. 38% of these were multi-location föhn conditions, i.e the föhn air propagated across the ice shelf,

and was also identified at other AWSs. However, 48% of the föhn conditions were only identified at Cole Peninsula. The proximity of Cole Peninsula to the AP, and its altitude (420m a.s.l), mean it is well located to capture even weak or short-lived föhn conditions, which were not able to propagate further across the AP. The föhn signal was strongest here as the föhn air had yet to mix with ambient air on the ice shelf.

Two spatial patterns were identified over the LCIS. Firstly, a west to east signal of decreasing föhn strength (increasing relative humidity) was identified from observations during multi-location föhn events, and during all föhn events. The second hypothesised spatial pattern was a north to south gradient in föhn signal and föhn frequency. This was theorised largely due to the works of (Cape *et al.*, 2015) and (Bannister & King, 2015), who found longer and more frequent föhn episodes in the north of the AP and over South Georgia. Furthermore, due to the curvature of the AP, the westerly winds interact with the AP more perpendicularly further north of the LCIS, which increases the potential for föhn conditions. There was no evidence of a gradient in the number of föhn conditions over the LCIS. The strength of the föhn signal displayed a weak north-south spatial signal. In general the air during föhn events was warmer and drier further north, however a AWS6 did not fit this north-south gradient. As the AWSs were not equidistant from the AP, the effect of the diminishing föhn signal with increasing distance from the AP (west-east gradient) dominated over the north-south gradient.

Due to the relatively sparse network of observations, the observed spatial patterns were likely influenced by the location of the AWSs. Assessing the near-surface conditions simulated by AMPS provided more evidence for the spatial distribution of the föhn air. The composites of the relative humidity and air temperature output from AMPS revealed that the strength of the föhn signal decreased in a northwest to south-east orientation; a combination of the west-east and north-south patterns found also (to a lesser extent) in the observations. This gradient in föhn strength is attributed to the propagation of föhn air across the ice shelf. The dominant wind direction during föhn events at most of the locations was northwesterly, which determined the direction of föhn air propagation.

On average, föhn air propagated in a southeasterly direction. However, the analysis of individual föhn events shows that the spatial distribution of föhn air is highly variable. The direction of the föhn propagation depends on the direction of the prevailing winds, on the stability of the air overlying the ice shelf, and the mixing and turbulence over the ice shelf. Some of these aspects are investigated in more detail through high-resolution modelling of case studies. These results are presented in Chapter 6.

There are other factors that control the spatial distribution of föhn air, e.g the flow regime over the ice shelf (linear or non-linear) and the occurrence of cooler, more moist, föhn jets, both of which were described by Elvidge *et al.* (2015, 2016). The linearity of the flow regime may influence the west-east gradient of the föhn strength. Under linear flow, the föhn air spreads across the majority of the ice shelf, leading to more extensive warming, whereas under non-linear flow the föhn warming decreases more rapidly with distance from the AP (Elvidge *et al.*, 2016). A larger horizontal gradient in temperature and relative humidity was identified under non-linear flow by Elvidge *et al.* (2016). The large number of föhn conditions identified only at Cole Peninsula (92 föhn conditions in one year), suggests that these föhn conditions were present under a non-linear regime, whereby the föhn effect was localised but strong. This will be addressed in more detail in the Chapter 6.

The occurrence of föhn jets may have influenced the spatial distribution of föhn warming. In previous studies, föhn jets have been found to flow west to east, across the ice shelf, as they emanate out of gaps in the AP (Elvidge *et al.*, 2015). It is possible that one of the AWSs was located in the path of frequently occurring föhn jets, and therefore the föhn signal at this location was reduced. However, the föhn jets were not visible in the composite AMPS output due to the coarse horizontal and topography resolution. The interaction of föhn jets and flow linearity are discussed in greater detail in the Chapter 6.

4.6 Conclusions

Föhn conditions have been identified at all AWS locations on the LCIS and in all years. There are a number of months with a particularly low number of föhn conditions, however föhn conditions occur all year round. Föhn conditions were observed as far south as 68.14°S. This is the furthest south on the AP that föhn conditions have been observed. Therefore, föhn winds impact the surface of the ice shelf much further south than previously known.

The föhn signal was detected as far as 130km east of the AP, and over a distance of 260km in the north-south direction. Föhn winds therefore can be assumed to have a widespread impact on the near-surface conditions, and on the ice shelf surface. The direction and distance of the propagation of individual föhn conditions is determined by the wind direction, the strength of the föhn signal, and ambient conditions over the ice shelf. On average, there was a northwest to southeast propagation of föhn winds. Northwesterly wind direction was dominant during the majority of the föhn conditions, which likely influenced this signal.

The average air temperature values were highest, and the relative humidity values were lowest during föhn conditions in the north of the area under investigation. Therefore, on average, both the latitude and proximity to the AP determine the strength of the föhn signal that is observed near the surface. On a more local scale, föhn jets have previously been identified by Elvidge *et al.* (2015) on the LCIS. However, due to the limited observation locations, it was not possible to find a persistent pattern of the föhn jets, nor were they visible in the föhn composites simulated by AMPS due to the coarse-resolution of the model.

Föhn conditions have immediate, potentially large impacts on the near-surface conditions. They increase the air temperature and decrease the relative humidity for the duration of the föhn event, and for a numbers of hours afterwards. They can also influence the average conditions over the ice shelf, by increasing the seasonal temperature when a large number of föhn conditions occurred in quick succession. At all locations,

periods with air temperature higher than 0°C were observed. Over 50% of all observations of T> 0°C could be attributed to föhn conditions.

More föhn conditions were identified during spring than in any other season. This has important implications for the surface of the ice shelf, especially in years with an especially high number of föhn conditions during spring, such as in 2010. During spring, the incoming solar radiation begins to increase, which raises the average air and surface temperature. It has been found that föhn conditions occurring during spring can initiate earlier onset of melt, and increase the duration of the melt season (King *et al.*; Luckman *et al.*, 2014).

Previous research identified that surface melting on LCIS can be induced by föhn conditions. However, the frequency of föhn conditions, and the spatial distribution over the LCIS were unknown. This led to an estimation of the impacts of föhn conditions based on a number of case studies. With the current findings, the number of föhn conditions are better known. The identification of föhn conditions as far south as AWS6 has widened the previous understanding of the spatial distribution of föhn air. Even this far south, föhn conditions are able to raise temperatures above freezing and potentially initiate surface melt. The implications of föhn winds on the surface energy balance and surface melt of the LCIS are discussed in the following chapter.

Chapter 5

The Impacts of Föhn Winds on the Surface Energy Balance of the Larsen C Ice Shelf

5.1 Introduction

The interaction between the atmosphere and the surface in terms of energy is collectively termed the Surface Energy Budget (SEB). The components of the budget represent the energy and turbulent fluxes between the atmosphere and, in the case of this research, the ice shelf. Changes in temperature, wind speed, humidity and cloud cover all influence the SEB. If the SEB can not be closed (where it equates to $0\mathrm{Wm}^{-2}$), any energy remaining in the system can be used to heat or melt the snow surface.

The SEB comprises of the radiation terms (shortwave and longwave radiation), the turbulent fluxes (sensible and latent heat) and the ground heat flux. The calculation of the SEB varies by study, and often depends on the main interest of the authors. However, the main components are as follows:

$$SW\downarrow + SW\uparrow + LW\downarrow + LW\uparrow + H_s + H_l + G = M \tag{5.1}$$

Where SW is the shortwave downward and upward radiation and LW is the longwave downward and upward radiation. H_s is the sensible heat flux, H_l is the latent heat

flux, G is the conductive heat flux through the snowpack. This component is often neglected for SEB studies over the Antarctic due to small conductive heat fluxes (Välisuo *et al.*, 2014). M is the amount of residual energy, used for heating or melting the surface. For this chapter, the adopted sign convention is that fluxes of energy towards the surface are positive. This is the usual convention in the glaciological and snow physics community. Other communities (e.g hydrometeorology) define fluxes away from the surface as positive.

Investigating the SEB of ice shelves is crucial, especially in the AP region, where accelerated warming dominated in the late 20th century but has now temporarily ceased (Turner *et al.*, 2016). Numerous AP ice shelves have at least partially collapsed, and investigating the SEB can reveal the mechanisms responsible for this ice loss. Studies have shown that the creation of melt ponds through surface melting can lead to ice shelf destabilisation (Scambos *et al.*, 2003; Van Den Broeke, 2005). Other studies have counteracted this, and suggest that surface melting was not enough to destabilise ice shelves such as Larsen B (Sergienko & Macayeal, 2005). The interactions between the atmosphere, oceans and ice shelves further prompt the interest in, and increase the complexity of, understanding the SEB.

Prior the collapse of Larsen A and B ice shelves in 1995 and 2002 respectively, high surface melting rates were observed (e.g Sergienko & Macayeal 2005; Trusel *et al.* 2015; Van Den Broeke 2005). According to Trusel *et al.* (2015), melt water production on both Larsen A and B peaked just prior to each collapse, and was significantly higher than on surrounding, stable ice shelves. Therefore it is clear that strong surface melting could be a precursor for ice shelf collapse in this region. Melting episodes are largely related to high incoming solar radiation and high sensible heat fluxes. Föhn winds can prompt larger than average sensible heat and shortwave radiation. The winds are warmer than the surrounding air, and are often accompanied by gusts of wind, or stronger wind speed in some regions (e.g McMurdo Dry Valleys Speirs *et al.* 2010). As sensible heat flux is dependent on the wind speed and temperature, it is often significantly higher (more downward fluxes) during föhn events (Elvidge *et al.*, 2015). Incoming solar radiation also increases during föhn, as the dry air gives rise to

cloudless skies.

The current study expands on the temporal scale of the King *et al.* study, and adds SEB quantification and near-surface observations to the Luckman *et al.* (2014) paper. Furthermore, the current study assesses the impact of föhn on the intensity, duration and timing of melting during all seasons and at multiple locations, and the results are presented here.

The impact of föhn on the SEB over Larsen C has been studied, largely on a case-by-case basis (Elvidge *et al.*, 2016; King *et al.*; Kuipers Munneke *et al.*, 2012). Kuipers Munneke *et al.* (2012) analysed the föhn impact during November 2010. Elvidge *et al.* (2016) analysed the SEB response to three separate föhn events over the northern LCIS during summer 2010/2011. According to Välisuo *et al.* (2014), the summer of 1992/1993 was characterised by predominant north-westerly winds which prompted anomalously high surface fluxes, leading to considerable surface melting. The winter of 1991 had anonymously low heat fluxes, and was characterised by very little westerly advection of warm air across the AP, thus linking the influence of föhn air to the heat flux. The Van Den Broeke (2005) study identified that maximum melt rates over Larsen B ice shelf were during days of northwesterly air flow, when warm air advection from the föhn effect was present. Most recently, King *et al.* has shown that föhn observed during November 2010 can increase the frequency and duration of melting episodes over the LCIS, but that they have little impact on the intensity, due to negligible influence on the energy available for melt. This is one of very few studies to assess the impact of föhn during spring. As only one season is analysed, it is difficult to say whether this result is true of all years, or whether spring 2010 was significant due to a larger number of föhn conditions, or a clustering of föhn amplifying the effect.

The influence of föhn conditions on the SEB varies by location and by case. Wind speed, temperature and humidity of the air overlying the ice surface all dictate the turbulent flux components of the SEB, as does the indirect impact of föhn on the radiation components. Therefore, it is important to investigate the individual impacts of föhn conditions. The short case study periods allow the SEB before, during and after the event to be accurately assessed, with limited seasonal influence, to provide an insight

into the immediate influence of föhn winds.

The limitation of using case studies alone is that the impact of föhn on the LCIS surface may be deduced from just a handful of cases. If the SEB is only calculated for the short period over which the föhn case study occurs, the impact of föhn winds may be over or under estimated. For example, a föhn case study during winter may reveal little impact on the SEB due to the static stability of the boundary layer and the limited melt potential. Similarly, during summer, when surface melting is higher regardless of föhn, the additional impact on the SEB may be limited. Conversely, the föhn-induced melting during summer may extend the melt season, or intensify the melting by providing additional energy. Therefore, expanding the case study approach is advantageous to allow a full investigation of the year-round impact.

A greater spatial understanding of the surface melting over Larsen C, and the links to föhn were provided by Luckman *et al.* (2014). That study identified a stronger melting signal, earlier melt onset and longer melting duration closer to the foot of the AP mountains and around the inlets using satellite images. Melt ponds were visible on the ice shelf surface, and Luckman *et al.* (2014) concludes that föhn winds are the likely cause of these.

5.2 Data Description and Methods

The data used in this chapter come from three sources. Firstly, output from a SEB model at AWS2 and AWS3 was used. Secondly, turbulent fluxes were calculated at AWS5 and AWS6 from near-surface observations. Finally, AMPS data were used. These data were used to estimate the influence of föhn conditions on SEB components and the energy available for melt. A number of methods were employed to estimate the amount of melt and number of melt days. The SEB model and methods for calculating turbulent fluxes are described in this section.

5.2.1 A Surface Energy Balance Model- AWS2 and AWS3

Calculation and validation of the SEB at AWS2 and AWS3 using the SEB model was conducted by P. Kuipers Munneke. The output included all the SEB components, as well as melt energy, surface temperature, and the values of components driving the separate modules within the model. For AWS3 the data were provided as daily averages from 22nd January 2009 to 26th January 2011. For AWS2, daily averages were provided for the full length of the study period (1st January 2009- 31st December 2012), and 30-minute averages were provided from 0130UTC 22nd January 2009 to 00UTC 1st April 2011). From the 30-minute data, six-hourly averages have been calculated to allow comparison with AMPS output and to remain consistent with the near-surface meteorological variables used in earlier chapters.

A complete budget (see Equation 5.2) has been calculated from a SEB model at AWS2 and AWS3 by P. Kuipers Munneke (personal communication, 2016) and values were provided for this study. A SEB model is often required to estimate a number of the components, as not all are observed by a typical AWS. Observations of radiation fluxes were used to initiate the model. Both AWS2 and AWS3 observed the longwave and shortwave incoming and outgoing radiation every six minutes, from which hourly averages were calculated and stored. Surface and subsurface snow temperatures were also observed at depths to 1m below surface.

This SEB model (Kuipers Munneke *et al.* 2009; Van Den Broeke 2005 and (Kuipers Munneke *et al.*, 2012)) calculates the energy fluxes into and out of a skin layer. The equation used is an extension to the one provided in the introduction (equation 1).

$$SW\downarrow + SW\uparrow + LW\downarrow + LW\uparrow + H_s + H_l + G + Q = E \tag{5.2}$$

Where E is the sum of surface and subsurface melting, and Q is the amount of shortwave radiation absorbed by the subsurface due to penetration of the radiation into the snowpack. All fluxes are positive when directed towards the surface.

To define periods where melt is possible, the following condition is followed:

$$E_{melt} = \begin{cases} E, TSK = 0°C \\ 0, TSK < 0°C \end{cases} \tag{5.3}$$

The additional term E_{melt} states that melting is possible, and is equal to the residual of the SEB calculation (E), when the temperature of the surface is at the melting point. Otherwise, the additional energy is not used for melting.

In this model the sensible and latent heat fluxes are calculated using the bulk flux method (section 5.2.3). The ground heat flux is calculated using a snowpack module, which allows for multiple layers of melting, freezing and percolation of melt water (Kuipers Munneke *et al.*, 2012). Within the multi-layer snowpack module, the vertically-integrated temperature change is calculated to compute the ground heat flux (G). The temperature of the snowpack is initialised using the subsurface temperatures measured by the AWS. Penetration of radiation into the snowpack and the amount of absorbed shortwave radiation (Q) are calculated by another module based on Brandt & Warren (1993) and van den Broeke *et al.* (2008).

The surface skin temperature is calculated iteratively, until the SEB is closed (Kuipers Munneke *et al.*, 2012). This surface skin temperature provides a value of outgoing longwave radiation, which can be compared to observed longwave radiation for model validation. In Kuipers Munneke *et al.* (2009) further model validation was performed against observed sensible heat from an AWS on the Greenland summit. The SEB model was found to reproduce surface and subsurface temperatures successfully, but that the model was sensitive to surface roughness in the calculation of turbulent fluxes (Kuipers Munneke *et al.*, 2009).

As the SEB components at AWS2 and AWS3 were derived from a SEB model but based on measurements at the AWSs, they are referred to as 'observationally-derived' in this chapter, to avoid confusing the output with the AMPS model data. The sensitivity of the SEB model to slight changes in the input data (e.g air temperature) was conducted by Van As *et al.* (2005). It was found that there was a small change of between 0 and 4.7Wm^{-2} for individual components, but insignificant change in the

total SEB value. Therefore, the SEB model used here to estimate surface melting from föhn winds is robust. That being said, when stating the amount of melt from föhn winds in the sections of this chapter, a $\pm 4.7 Wm^{-2}$ error is used for the total SEB, to ensure that the values given lie within the maximum values identified by Van As *et al.* (2005).

5.2.2 Calculation of Turbulent Fluxes- AWS5 and AWS6

The sensible and latent heat fluxes were not observed by any AWS. At AWS5 and AWS6, the turbulent fluxes were calculated to facilitate their spatial analysis over the LCIS. AWS5 and AWS6 observed temperature, relative humidity and wind speed and direction at two levels, separated by 1.0m. The distance between the sensors and the snow surface was also observed by two separate sensors (snow height sensor). Instrument boom 1 (level 1) was located 20cm above the height sensor and instrument boom 2 (level 2) was 1.2m above the height sensor. This allowed the height above the snow surface to be inferred regardless of accumulation.

From the data observed at two levels, the sensible and latent heat fluxes were calculated using the bulk flux method. This method was also used within the SEB model for calculation of turbulent fluxes, and is very common in boundary layer research. Turbulent fluxes can also be calculated using ultrasonic anemometers, however these are badly affected by ice riming and blowing snow (King, 1990). Similarly, in very low or relatively high (>11m/s) wind speeds, the results are unreliable (King, 1990). The high energy consumption and large data storage can also be problematic. Therefore, these instruments are often not used, especially for long observational periods. The bulk method is well tested over the Antarctic (e.g King 1990; King *et al.* 1996, 2001) and is outlined in the following section.

5.2.3 Bulk Flux Method

The turbulent flux components can be inferred from temperature, humidity and wind speed observations. The Monin-Obukhov similarity theory describes the relationship of fluxes of momentum, water vapour and heat between the surface, and the profiles of momentum, water vapour and heat in the lower 10m of the atmospheric boundary layer.

The fluxes of water vapour and heat vary with stability, and are functions of a stability parameter (King & Anderson, 1994). The 'flux-profile' relationships allow estimation of fluxes using logarithmic profiles of mean temperature, wind speed and water vapour .

The relationships are expressed as:

$$\frac{\kappa z}{u_*}\frac{\partial u}{\partial z} = \phi_M\left(\frac{z}{L}\right) \tag{5.4}$$

$$\frac{\kappa z}{T_*}\frac{\partial T}{\partial z} = \phi_T\left(\frac{z}{L}\right) \tag{5.5}$$

$$\frac{\kappa z}{Q_*}\frac{\partial Q}{\partial z} = \phi_Q\left(\frac{z}{L}\right) \tag{5.6}$$

where u is the wind speed, T is the potential temperature and Q is the water vapour mixing ratio. The friction velocity, u_*, is defined as:

$$\tau = \rho u_*^2, \tag{5.7}$$

where τ is the surface stress. T_*, the scaling temperature is defined by:

$$T_* = \frac{H_s}{(\rho C_P u_*)}, \tag{5.8}$$

where H_s is the sensible heat flux (defined later), ρ is the air density (here taken as 1.25kg m^{-3}), C_P is the specific heat of air at constant pressure (1005 J Kg K^{-1}). The scaling mixing ratio, Q_*, is defined by:

$$Q_* = \frac{E}{(\rho u_*)} \tag{5.9}$$

where E is the water vapour flux. ϕ_M, ϕ_T, ϕ_Q in equations (5.4) to (5.6) are functions of wind shear, temperature and scalar concentration gradients (respectively), which were determined by field measurements (Högström, 1988) and depend on the stability parameter, $\frac{z}{L}$. The Monin-Obukhov length,

$$L = \frac{u_*^2 \bar{T}}{\kappa g T_*}, \tag{5.10}$$

is a ratio of the buoyancy and shear production of turbulence. It helps define the stability of the surface layer. It has been found that under low to moderately

stable conditions ($1 \gg \frac{z}{L} > 0$), there is a linear relationship between the ϕ functions and the stability ($\frac{z}{L}$) (King *et al.*, 1996). However, under high stability, the linear relationship breaks down, and the ϕ functions never exceed a value of 12 (King *et al.*, 1996). The limitation allows the calculations to converge under high stability, when the relationships start to break down. For stable conditions ($\frac{z}{L} > 0$), the ϕ functions are as follows:

$$\phi_i = \min \left\{ \left(A_i + \alpha_i \frac{z}{L} \right), \phi^{LIM_i} \right\} \tag{5.11}$$

where i is M, T, or Q and ϕ_i^{LIM} equals 12. There are many values suggested for the ϕ functions dating back to those by Dyer (1967) and by Dyer & Hicks (1970), and they are often termed the 'Businger-Dyer Relationships'. The ϕ functions for unstable conditions ($\frac{z}{L} < 0$) are different to the stable ones. The following forms of ϕ functions for unstable conditions are employed from Högström (1988):

$$\phi_M = (1 - \gamma_1 L)^{-\frac{1}{4}} \tag{5.12}$$

$$\phi_T = (1 - \gamma_2 L)^{-\frac{1}{2}} \tag{5.13}$$

where γ_1 has the value 19.0 and γ_2 has the value 11.6 (Högström, 1988). The fundamental flux profile relationships in equations (5.4), (5.5) and (5.6) are integrated using the appropriate ϕ functions (based on stability). The integrated forms relate fluxes to the gradient in wind speed, temperature and humidity between two levels. For humidity and temperature calculations, the measurements on two levels of the AWS were used. For wind speed, one sensor level and the surface, where $u = 0ms^{-1}$, were used.

The integrated versions of equations (5.4) to (5.6) are as follows:

$$\frac{\kappa}{u_*}(u(z_2) - u(z_1)) = \ln(\frac{z_2}{z_1}) - (\psi_M(\frac{z_2}{L}) - \psi_M(\frac{z_1}{L})) \tag{5.14}$$

$$\frac{\kappa}{T_*}(T(z_2) - T(z_1)) = Pr \times ln(\frac{z_2}{z_1}) - (\psi_T(\frac{z_2}{L}) - \psi_T(\frac{z_1}{L})) \tag{5.15}$$

$$\frac{\kappa}{Q_*}(Q(z_2) - Q(z_1)) = Sc \times ln(\frac{z_2}{z_1}) - (\psi_Q(\frac{z_2}{L}) - \psi_Q(\frac{z_1}{L})) \tag{5.16}$$

Pr and Sc are the Prandtl and Schmidt numbers, and are both set to 0.95, following from Högström (1988) and King *et al.* (1996). ψ are the vertically integrated forms of the ϕ functions, depending on stability. For equations 5.15 and 5.16, z_1 and z_2 are the height of the two sensor levels. For equation 5.14, z_2 is the sensor level height, whereas z_1 becomes equal to z_0; the surface roughness length, as the surface is used as z_1.

The surface roughness length (z_0) is the height above a surface at which the wind speed is theoretically zero, taken from the logarithmic wind profile. Using this simplifies the equations, as the windspeed at z_0 must be $0ms^{-1}$, therefore only one wind speed observation is required. The value of z_0 is dependent on the surface type. For this study $z_0 = 5.6 \pm 0.5 \times 10^{-5}$m, as suggested by King & Anderson (1994), based on the Brunt Ice Shelf. z_0 is a source of uncertainty in the calculations of turbulent fluxes, as small changes in its value can affect the calculations. For sensitivity analysis, the upper and lower value of z_0 was used in the calculations, and provides an error estimate for the values from section 5.4.1 onwards. The surface roughness is sensitive to changes in synoptic conditions and seasonal changes, which makes it difficult to estimate accurately, or assign one average value (Sicart *et al.*, 2014).

As the value of u_* is used in the calculation of L (equation 5.10), the process to calculate the fluxes is an iterative process. The process is as followed, using equations (5.14), (5.15) and (5.16).

Driving equation 5.14 with observed wind speed values at z_2, and u=$0ms^{-1}$ at z_0, a 'best guess' of u^* is derived, assuming neutral conditions ($\frac{z}{L} = 0$). To calculate T^* (equation 5.15), temperature observations from two levels, with the first estimate of u^* are used, again assuming neutral conditions. The first estimates of u^* and T^* are then used in equation 5.10 to estimate L.

The first estimate of L is then substituted back into equation 5.14 to calculate an improved estimate of u^*. This improved estimate of u^* is then used to recalculate T^*. The process of improving estimates of u^*, T^* and L were repeated until the successive iterations calculate a value of u^* which differs from its previous estimate by less than 1%. Sensible heat flux (equation 5.17) and latent heat flux (equation 5.18) are then

calculated.

The turbulent fluxes, sensible and latent heat, are expressed as:

$$H_s = \rho C_P (T_* u_*) \tag{5.17}$$

$$H_l = \rho L_s (Q_* u_*) \tag{5.18}$$

where the latent heat of sublimation is L_s = (28.34-0.00149 T)$\times 10^5$. This procedure was conducted using AWS5 and AWS6 hourly observations. There were no direct measurements of fluxes to validate the bulk flux method, however in previous studies by King *et al.* (1996), the correlation between calculation and observation of sensible heat flux was 0.87.

5.2.4 Shortwave Atmospheric Transmissivity

As the föhn and non-föhn conditions are not equally distributed throughout the year, comparing the incoming shortwave radiation will include the impact of the seasonal cycle. Therefore, comparing average values of the incoming shortwave radiation does not give a meaningful indication of the influence of föhn conditions over this component. The shortwave atmospheric transmissivity (SW_T) (sometimes referred to as the 'clearness index' (Okogbue *et al.*, 2009)) has been calculated:

$$SW_T = \frac{SW\downarrow}{SW\downarrow^{TOP}} \tag{5.19}$$

where $SW\downarrow^{TOP}$ is the incident shortwave radiation at the top of the atmosphere. This values allows the impact of föhn conditions on the SW↓ to be assessed without the seasonal bias. The downwelling longwave radiation is less dominated by a seasonal cycle and the föhn and non-föhn composites are less biased by seasonality.

5.2.5 AMPS Data

Due to the limited surface observations throughout the Antarctic, modelling the SEB can provide spatial and temporal simulation of SEB components, and can be used to assess previous events, such as the collapse of Larsen B.

However, calculations of the budget rely on realistic representation of a number of parameters including cloud cover, land use and near-surface meteorology. The turbulent fluxes are parameterised within models, using the near-surface meteorological conditions. King *et al.* (2015) validated three models (including AMPS) against summer SEB observations at AWS2 on the LCIS. AMPS is able to forecast the pressure, surface temperature and wind speed with a high degree of skill, and also provides a relatively good representation of air temperature and humidity. The albedo in AMPS is lower than in observations, and is a fixed value, which causes a positive bias in the net shortwave radiation component. However, this is partially offset by a negative bias in the net longwave radiation, likely due to the lower degree of skill in representing clouds within the model (King *et al.*, 2015). The turbulent fluxes were accurately simulated by AMPS, and the biases contributed insignificantly to the overall errors. The frequency of melting episodes and the melt rate were overpredicted by AMPS, and it was concluded by King *et al.* (2015) that interpretation of melt rates from models should be used cautiously.

This project uses output from AMPS to calculate the SEB from 2009-2012. The surface turbulent fluxes are calculated using an Eta similarity scheme, which is based on the Monin-Obukhov similarity theory as mentioned in section 5.2.3. The components of the SEB are directly output from AMPS.

This section of the chapter will focus on the impact of föhn conditions on various components of the SEB, and the surface melting. Firstly, the AMPS output will be validated against SEB components observed at multiple locations. Composites of mean föhn and non-föhn values will be compared to highlight the changes in the SEB due to föhn conditions. Numerous methods have been employed to estimate surface melting at locations without observations. The results of these will be compared here. Finally,

Table 5.1: The observed and calculated SEB components at each AWS location to compare with AMPS output. SW↑- SW outgoing, SW↓- SW incoming, LW↑- LW outgoing, LW↓- LW incoming, H_s- calculated sensible heat flux and H_L- calculated latent heat flux. As no SEB components were available at Cole Peninsula, this location is not included in the table.

Location	SEB Components (Wm^{-2})
AWS1	SW↑↓, LW↑↓
AWS2	SW↑↓, LW ↑↓, H_s, H_l
AWS3	SW↑, SW ↓, LW ↑, LW↓, H_s, H_l
AWS5	SW↑, SW ↓, H_s, H_l
AWS6	H_s, H_l

the spatial distribution of föhn-induced melting will be discussed.

5.3 AMPS Validation

The AMPS model was used to simulate the SEB and surface melting over the LCIS by King *et al.* (2015) at the AWS2 location. In the validation provided by that study, the AMPS model performed reasonably well at this location for representation of near-surface variables and the SEB components. As the King *et al.* (2015) study only validated AMPS for one location, during one summer season, it was considered crucial to assess the success of the AMPS model for more than one location and for a longer time period. As only a number of AWS locations provide observations of the SEB, the reliability of AMPS must be assessed before it is used to calculate SEB at the locations where observations are not available. The number of components validated depends on which observations were available. Table 5.1 provides a list of the components validated at each location.

The surface pressure, air temperature and humidity are well simulated by AMPS at the majority of locations as discussed in Chapter 3. This is comparable to the King *et al.* (2015) study at AWS2 during summer. From 2009-2012, the mean biases and standard deviation of biases are small, although AMPS is positively biased for air tem-

Table 5.2: The AWS mean values and mean bias (AMPS-AWS) of the SEB components for each location from 2009-2012. 'ND' refers to no data available for the comparison.

	AWS Means						Mean Bias					
Variable	CP	AWS1	AWS2	AWS3	AWS5	AWS6	CP	AWS1	AWS2	AWS3	AWS5	AWS6
SW↓	ND	126.1	122.7	125.1	147.8	ND	ND	20.4	26.5	2.9	32.6	ND
SW↑	ND	106.3	106.1	111.7	131.5	ND	ND	11.0	12.6	6.1	10.7	ND
LW↓	ND	231.8	234.2	233.7	ND	ND	ND	-18.9	-10.3	0.2	ND	ND
LW↑	ND	250.8	249.6	249.2	ND	ND	ND	-7.0	-3.2	-1.1	ND	ND
H_s	ND	ND	0.9	3.2	6.08	0.5	ND	ND	6.8	5.2	-2.8	2.4
H_l	ND	ND	-2.6	-1.5	-1.8	1.3	ND	ND	-0.3	-1.7	-1.5	-5.4

Table 5.3: The standard deviation and the correlation of the AWS observations and AMPS model output for the SEB components from 2009-2012. 'ND' refers to no data available for the comparison.

	Standard Deviation						Correlation Coefficient					
Variable	CP	AWS1	AWS2	AWS3	AWS5	AWS6	CP	AWS1	AWS2	AWS3	AWS5	AWS6
SW↓	ND	74.5	38.0	34.2	104.8	ND	ND	0.96	0.97	0.98	0.91	ND
SW↑	ND	102.1	27.0	23.1	81.1	ND	ND	0.84	0.97	0.98	0.9	ND
LW↓	ND	42.1	26.4	24.6	ND	ND	ND	0.6	0.77	0.81	ND	ND
LW↑	ND	17.1	15.1	14.2	ND	ND	ND	0.9	0.92	0.94	ND	ND
H_s	ND	ND	12.7	12.6	26.4	21.2	ND	ND	0.65	0.72	0.13	0.33
H_l	ND	ND	6.1	6.3	20.3	13.7	ND	ND	0.41	0.15	0.14	-0.14

perature and wind speed at all locations. The correlation coefficients for pressure and air temperature are relatively high (above 0.72 for all locations). The correlation is slightly poorer for wind speed, and was lowest (0.37) at AWS3.

The shortwave incoming and outgoing is well represented at all locations (Tables 5.2 and 5.3). The correlations show a good agreement between the observations and model output from 2009 to 2012, and the mean biases are relatively small. AMPS does overestimate the net shortwave radiation in all locations and this is relatively large at AWS5. The overestimation in net shortwave radiation may be attributed to the poor representation of cloud cover in AMPS, and to the unrealistically low albedo value, which affects the outgoing shortwave radiation. The longwave incoming and outgoing are both well represented by AMPS, although the incoming longwave radiation shows a lower positive correlation than outgoing longwave radiation. At most locations, the net longwave is negatively biased in AMPS due to the poor cloud cover representation.

The representation of turbulent fluxes in AMPS is highly variable. The correlation at each location is mostly low, except at AWS2 where it is higher (0.65 for H_s, 0.41 for H_l) and AWS3 for sensible heat (0.72). The latent heat correlation at AWS6 is negative, although weak, and there is a relatively large mean bias (-5.4Wm^{-2}), with AMPS underestimating latent heat fluxes. The latent heat was overestimated by AMPS at AWS2 (although only slightly), AWS3, AWS5 and AWS6, with some locations displaying an average bias of almost double the observed value (e.g AWS6 with a mean bias of 5.4Wm_{-2}).

The mean sensible heat flux was overestimated at AWS2, AWS3 and AWS6 which is likely due to the higher air temperatures in AMPS and the overestimation in wind speed (see AMPS near-surface parameters validation in Chapter 3). The mean bias and standard deviation of bias are relatively high at AWS5 and AWS6 (26.4Wm^{-2} at AWS5), which may be due to errors arising from the implementation of the bulk flux method to the AWS data. King *et al.* (2015) found similar correlations for turbulent fluxes at AWS2. Temporal variability in the modelled SEB was not used for validation, however in King *et al.* (2015), the AMPS model showed moderate skill in simulating

variations in shortwave radiation and turbulent fluxes for durations longer than daily.

The results from this validation were taken into account when using AMPS data to calculate the SEB and surface melting during föhn and non-föhn conditions. As the observations for surface melting were sparse, AMPS was used to estimate the spatial distribution of surface melting, and the amount of föhn-induced melting.

5.4 Impact of Föhn on the SEB of the LCIS

From previous studies (e.g Elvidge *et al.* 2016; King *et al.* 2015; Kuipers Munneke *et al.* 2012), the impact of individual föhn events on the various components of the SEB have been identified. These case studies were often in summer, and only a few days to one week long. The long term, year-round impact of föhn conditions on the SEB will be presented here. Primarily the results will focus on AWS2, AWS3 and AWS5 as these locations have observations of most, if not all, SEB components. To assess the impact of föhn, composites of föhn and non-föhn average conditions have been compiled. Föhn are not evenly distributed throughout the year, or even within a season, therefore isolating the impact of föhn on components with a large seasonal cycle is problematic. Any differences in the SEB components could reflect the seasonal cycle rather than the impact of föhn. However, due to the short timescale of this study, especially in a number of locations with only two years of data, the seasonal cycle can not be removed from the data prior to analysis. The seasonal signal will mostly influence the shortwave radiation, although other components may be affected, and this will be discussed in the relevant sections.

5.4.1 Year-Round Impact

Table 5.4 displays the annual average SEB components from AWS2 observations for composites of föhn and non-föhn conditions. The föhn conditions were identified using the algorithms outlined in Chapter 3, and the spatial and temporal characteristics of the föhn conditions are presented in Chapter 4. For all components except the latent heat flux the differences between non-föhn and föhn SEB conditions are significant at

the α=0.05 confidence level.

During föhn conditions, SW↓ is much larger due to the clearance of clouds in the lee of the AP mountains. However, due to the seasonal bias in SW↓, the shortwave transmissivity (SW_T) is a more reliable indication of the impact of föhn winds on the downwelling shortwave. There was a slight increase in the SW_T (0.01 increase) during föhn conditions, indicating an increase in the incoming shortwave, however this was not statistically significant (α =0.5).

The sensible heat was much larger during föhn conditions (Figure 5.1), and positive (downwards) due to the increased air temperature and often wind speed, providing heat for the surface. This is true for all available locations. The annual average sensible heat values for AWS2 and AWS3 (during föhn) are very similar (23.0Wm^{-2} and 23.6Wm^{-2} respectively). The annual impact on sensible heat is smallest at AWS6.

The positive residual energy associated with the föhn conditions was partially offset by a decrease (more negative) in latent heat flux. At AWS2 however, this is the only non-significant change during föhn conditions, and it was not large enough to remove the impact of the high sensible heat and net shortwave radiation. The negative latent heat flux was considerably larger at AWS5 which indicates more evaporation or sublimation. At AWS3 and AWS6, the annual average latent heat fluxes were positive during föhn, indicating accumulation at the surface.

There was a significantly larger amount of energy available for melt during föhn conditions than under non-föhn conditions at AWS2 (Table 5.4). Föhn days do not coincide with all times of melting, but high melt energy is observed during föhn days (Figure 5.2). At AWS3 (the only other location for which melt energy was available), the melt energy increased during föhn conditions, however this was not significant on an annual scale. The short data period at AWS3 may be influencing the data. As AWS2 and AWS3 are relatively close together (∼70km) and in a similar location, it is expected that they have similar SEB characteristics (Kuipers Munneke *et al.*, 2012). However, they did observe different föhn event characteristics, including frequency, which may

Table 5.4: Annual average values from 2009-2012 for SEB components and the surface temperature during composites of föhn and non-föhn conditions at AWS2 (observations). The asterisk indicates significance (α= 0.05).

Variable	Non-Föhn	Föhn
$SW_{net}(Wm^{-2})$	15.7	31.1*
SW_T	0.62	0.63
$LW_{net}(Wm^{-2})$	-13.9	-40.6*
$H_s(Wm^{-2})$	-0.5	23*
$H_l(Wm^{-2})$	-2.5	-3.6
$G(Wm^2)$	2.3	-3.8*
Melt Energy(Wm^{-2})	1.6	7.6*
Amount of melt (mm w.e day^{-1})	0.43	1.57*
Surface Temperature(°C)	-16.8	-8.3*

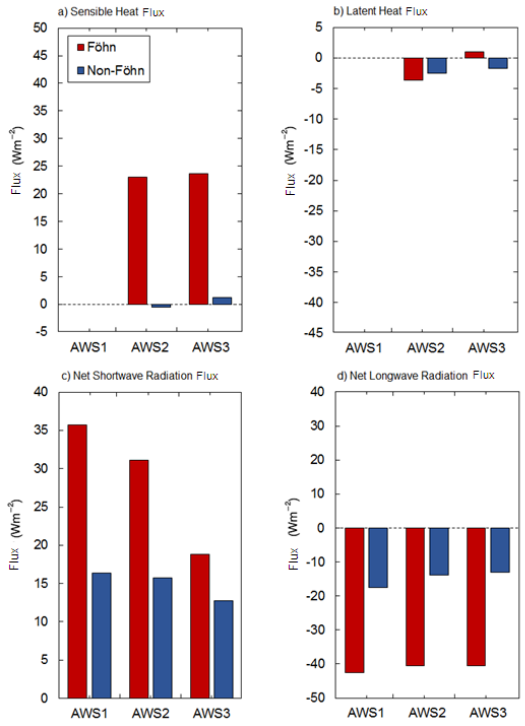

Figure 5.1: The 2009-2012 average föhn (red) and non-föhn (blue) composites of the observationally derived sensible (a) and latent heat (b) fluxes and net shortwave (c) and longwave (d) radiation for each available location. AWS5 and AWS6 are not included due to the lack of winter observations.

be responsible for the difference in föhn composite values.

Melt days are days with melt energy greater than zero. 14% of non-föhn days at AWS2 were melt days. The number of melt days more than doubles for föhn composites, with 31% of föhn days at AWS2 coinciding with melt days. A similar magnitude of increase was observed at AWS3, which increased from 12% during non-föhn conditions to 20% during föhn days. Therefore, over 130km from the foot of the mountains, föhn conditions increase the number of melt days.

The average daily water-equivalent melt amount for föhn and non-föhn conditions at AWS2 are provided in Table 5.4. The daily amount of melt more than tripled during föhn conditions compared to non-föhn conditions. Therefore, as well as additional melt days, the amount of melt on those days also increases in association with föhn conditions. The combination of these causes föhn-induced melting of the ice shelf.

The annual average amount of melt (föhn and non-föhn conditions) was 179.8mm w.e yr^{-1} at AWS2. The maximum annual melt was 263.0mm w.e yr^{-1} in 2011. To assess the influence of föhn conditions over this value of melting, they were removed from analysis. Without including föhn conditions identified at AWS2, the annual average melt amount reduced significantly to 146.1mm w.e $year^{-1}$ (a decrease of 33.7mm w.e $year^{-1}$). Therefore, föhn conditions contribute over 18% of the annual amount of melt at AWS2 alone.

The influence of föhn conditions on surface melting is largest in the years with a large number of föhn identified during the extended summer season (Oct-Mar). The highest number of föhn conditions during the extended summer were identified in 2010 when 26 föhn conditions were identified at AWS2 alone. The annual melt amount observationally-derived at AWS2 in 2010 was 258.2mm w.e. This annual total decreased by 76.4mm w.e to 181.8mm w.e when the melting associated with föhn conditions was removed. Conversely, in 2012 only 7 föhn conditions were identified at AWS2. The annual melt amount in 2012 was 83.4mm (significantly less than in 2010 at the 5% confidence level). When the föhn days were removed from analysis, the annual total melt only decreased by 0.1mm w.e, and therefore in years with relatively few föhn conditions

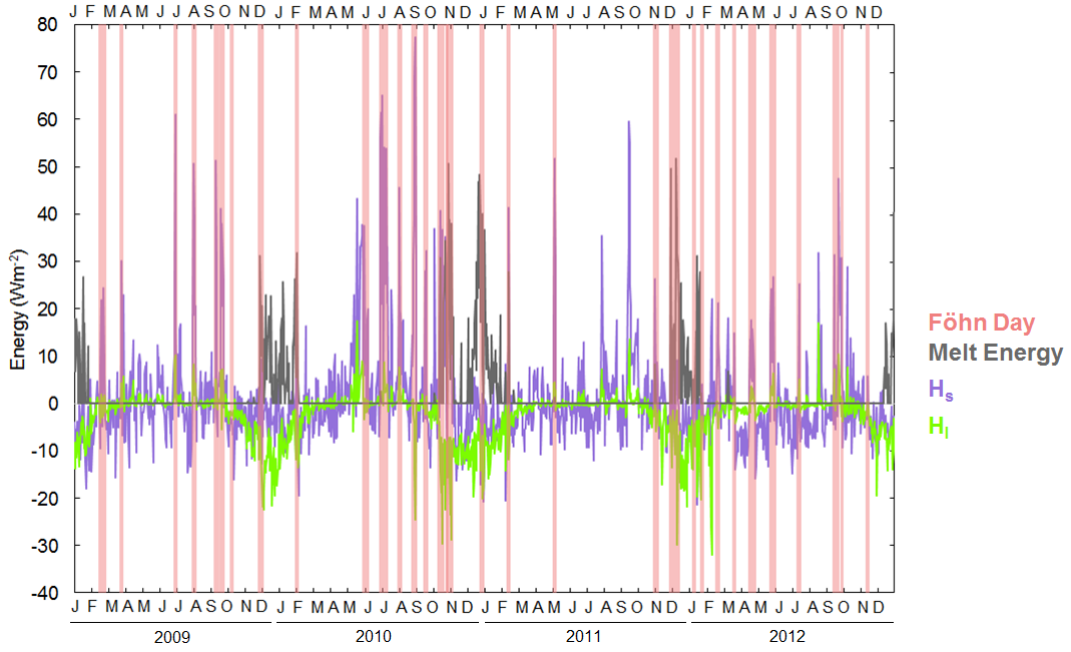

Figure 5.2: Daily values of sensible (purple) and latent heat (green) fluxes and melt energy (grey) from AWS2 SEB model for all years of data. The coral transparent lines over the plot indicate föhn days. The x-axis ticks are at monthly intervals.

present, there was little increase in annual melt totals.

The annual number of melt days, daily and annual energy available for melt and annual water equivalent melt amount all increased due to the occurrence of föhn winds, and especially in years when a large number of föhn conditions were identified during the extended summer period (Oct-Mar).

5.4.2 Winter

The smallest impact from föhn conditions was observed during winter. This is likely due to the lack of change in the net shortwave radiation, as very little is available. The very cold air and low surface temperatures mean that even with relatively warm air advection, the surface temperature does not encroach upon the melting point, and often does not rise above -15°C (Figure 5.3). However, the surface temperature was

statistically significantly ($\alpha = 0.05$) higher during föhn conditions than non-föhn conditions at AWS2 and AWS3. There were no melt days in either föhn or non-föhn periods during winter.

Sensible heat flux and latent heat flux both experience a significant change between föhn and non-föhn conditions. At AWS2 the average sensible heat flux increased significantly ($\alpha = 0.05$) from 3.4Wm^{-2} to 36.6Wm^{-2} during föhn conditions, and the latent heat increased from 0.57Wm^{-2} to 2.9Wm^{-2}. At AWS3 the sensible heat flux increased by 27.8Wm^{-2} and latent heat flux increased by 3.6Wm^{-2}, suggesting an absence of evaporation or sublimation. Similar values for sensible and latent heat flux were also observed at AWS6. At AWS5, the sensible heat flux during föhn conditions was much larger than at other locations, and the latent heat flux was negative, indicating that sublimation occurs during föhn conditions.

Although no föhn-induced surface melt was experienced during winter, there was a significant change to a number of the SEB components, and there was a slight decrease in the total SEB from -1.7Wm^{-2} during non-föhn periods to -1.9Wm^{-2} during föhn periods at AWS2. Figure 5.3 displays an example of a föhn and non-föhn week during winter. Part 'a' and 'c' of the figure also show the close relationship between air temperature and surface temperature. In this particular case, the sensible heat was negative during non-föhn, but positive (downward energy) during föhn conditions. Although the air temperature reaches the melting point, the surface temperature has a maximum of -4°C, so no melt was observed.

5.4.3 Autumn

The föhn conditions had a greater average impact during autumn than winter. Largely this can be attributed to the increased amount of incoming shortwave radiation. The atmospheric transmissivity was larger during föhn conditions, indicating an increase in incoming shortwave radiation observed at the surface (Figure 5.4). The net shortwave energy increased from 5.1Wm^{-2} (non-föhn) to 9.4Wm^{-2} (föhn) at AWS2, with increased downwelling shortwave contributing most to the net increase. The net longwave radiation was more negative during föhn conditions at AWS1, AWS2, AWS3 and

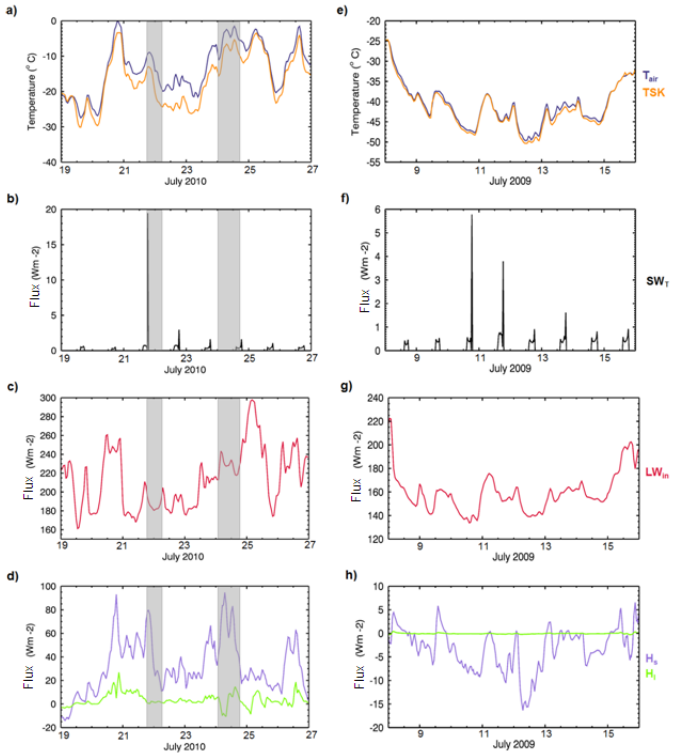

Figure 5.3: SEB components observationally-derived at AWS2 during a week in which föhn conditions were identified (a to d) and were not identified (non-föhn conditions) (e to h) during winter. a) Surface temperature (TSK) and air temperature (T_{air}), b) Shortwave atmospheric transmissivity (SW_T), c) longwave incoming radiation (LW_{in}) and d) sensible heat flux (H_s) and latent heat flux (H_l) during a week with föhn conditions from 19th to 27th July 2010. Figures e to h are the same as a to d, but during a week in which no föhn conditions were identified from the 8th to 16th July 2009. The shaded sections indicate the föhn conditions.

AWS5. The larger negative net longwave radiation counteracts the increased shortwave radiation, and contributes to an overall negative net SEB during föhn conditions.

The sensible heat flux was significantly larger (α=0.05) (more positive) during föhn conditions in all available observations. On average it increased from 0.01Wm^{-2} during non-föhn periods to 20.9Wm^{-2} during föhn conditions at AWS2. This increase in sensible heat flux is visible in Figure 5.4. The other locations observed a similar sensible heat flux during föhn conditions. Surface warming was also significant at AWS2 and AWS3 during föhn conditions, raising the surface temperature by 10.5K and 11.8K respectively.

Although the energy available for melt increased by only 0.08Wm^{-2} (at AWS2), the number of melt days during föhn conditions was larger than during non-föhn. Only 0.8% of days were melt days during non-föhn times, whereas during föhn conditions 8% of days experienced melti at AWS2. Therefore, föhn-induced melting is possible during autumn, although it has a minimal impact, and is likely short lived due to an average negative SEB.

5.4.4 Summer

The energy available for melt, and percentage of melt days during summer is relatively high, regardless of additional föhn induced melting. It is therefore more difficult to assess the contribution of surface melting from föhn alone. A day may already have experienced melting, and the presence of föhn winds was coincidental and did not cause the melting. However, from previous studies, it has been found that individual föhn events can increase or prologue melt when it occurs during summer (Elvidge *et al.*, 2016; Kuipers Munneke *et al.*, 2012).

There was a significant increase in the incoming shortwave and net shortwave radiation and a decrease in net longwave radiation during summer föhn periods, largely due to the cloud clearing during föhn conditions. The increase in atmospheric transmissivity during summer föhn composites also provides evidence for the cloud clearing impact. The average sensible heat flux increased by 12.1Wm^{-2} at AWS2, which

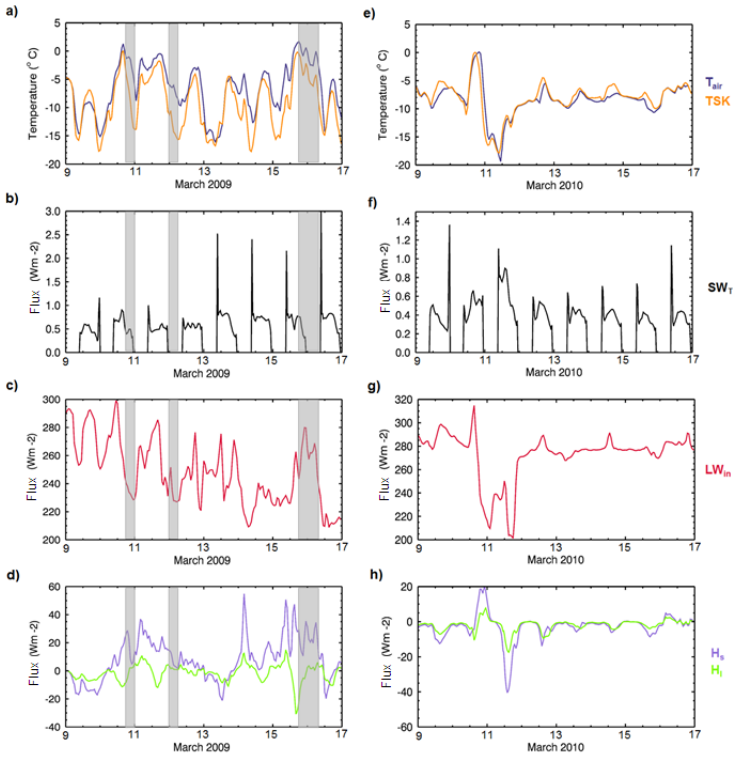

Figure 5.4: SEB components observationally-derived at AWS2 during a week in which föhn conditions were identified (a to d) and were not identified (non-föhn conditions) (e to h) during winter. a) Surface temperature (TSK) and air temperature (T_{air}), b) Shortwave atmospheric transmissivity (SW_T), c) longwave incoming radiation (LW_{in}) and d) sensible heat flux (H_s) and latent heat flux (H_l) during a week with föhn conditions from 9th to 17th March 2009. Figures e to h are the same as a to d, but during a week in which no föhn conditions were identified from the 9th to 17th March 2010. The shaded sections indicate the föhn conditions.

changed the direction of energy transport from negative (upwards) during non-föhn to positive (downwards) during föhn conditions. Negative sensible heat flux is common in the Antarctic during summer due to convection (Kuipers Munneke *et al.*, 2012), as is visible in Figure 5.5d. The same sign change and magnitude of sensible heat flux increase was observed at AWS3 and AWS6. Therefore the influence of föhn conditions on the SEB can be observed as far south as AWS6. A larger increase in sensible heat flux was observed at AWS5 ($25\mathrm{Wm}^{-2}$). At this location the non-föhn value was also positive, indicating little convection, unlike at the other locations.

The latent heat flux increased (less negative) from non-föhn to föhn conditions at AWS2 and AWS3. However the increase was not statistically significant. As a consequence of the higher surface temperatures, sublimation and evaporation are common in summer, leading to an average negative latent heat flux. At AWS5 the latent heat flux decreased (more negative) during föhn conditions, indicating stronger cooling at the surface through sublimation or evaporation. The föhn conditions observed at AWS5 had a larger impact on both turbulent fluxes than elsewhere. This may be due to the larger number of föhn conditions observed during summer at AWS5 than at AWS2 and AWS3 (see Chapter 4). At AWS6, there was very little change in latent heat flux between the composites, and for both conditions, the flux was positive.

The surface temperature increased by only 0.4K at AWS2 during föhn conditions (not significant). During summer, the surface temperature is already quite close to 0°C, and therefore it is unable to warm much higher during föhn conditions. At AWS3 the surface temperature increased by 1.8K during föhn conditions, which was significant (α =0.05). The average surface temperature during summer was already close to the melting point, and therefore any additional energy input had relatively little impact on raising the surface temperature further. However, a surface temperature of 0°C is an important tipping point in terms of ice shelf surface melt.

Despite small surface temperature changes at AWS2, the increase in energy available for melt during föhn conditions was statistically significant (α=0.05). During föhn conditions the energy available for melt ($18.3\mathrm{Wm}^{-2}$) more than doubled that of

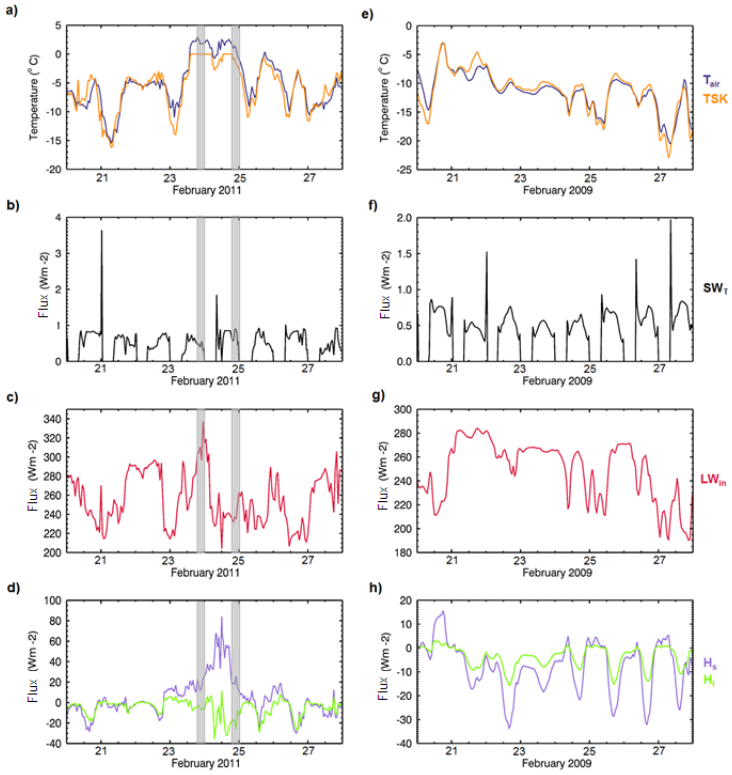

Figure 5.5: SEB components observationally-derived at AWS2 during a week in which föhn conditions were identified (a to d) and were not identified (non-föhn conditions) (e to h) during winter. a) Surface temperature (TSK) and air temperature (T_{air}), b) Shortwave atmospheric transmissivity (SW_T), c) longwave incoming radiation (LW_{in}) and d) sensible heat flux (H_s) and latent heat flux (H_l) during a week with föhn conditions from 20th to 28th February 2011. Figures e to h are the same as a to d, but during a week in which no föhn conditions were identified from the 20th to 28th February 2009. The shaded sections indicate the föhn conditions.

Table 5.5: Spring (SON) daily average values from 2009-2012 of SEB components and the surface temperature during composites of föhn and non-föhn conditions at AWS2 (observations). The asterisk indicated significance (α= 0.05).

Variable	Non-Föhn	Föhn
$SW_{net}(Wm^{-2})$	23.4	36.3
SW_T	0.58	0.64*
$LW_{net}(Wm^{-2})$	-22.6	-43.5*
$H_s(Wm^{-2})$	3.5	25.4*
$H_l(Wm^{-2})$	-2.5	-5.4*
$G(Wm^2)$	-0.9	-6.2*
Melt Energy(Wm^{-2})	1.2	7.7*
TSK(°C)	-16.4	-7.5*

non-föhn conditions ($7.0Wm^{-2}$) at AWS2. This leads to 73% to 78% of föhn days potentially producing surface melting, compared to just 46% to 54% of non-föhn summer days. The energy available for melt increased almost four-fold during föhn conditions at AWS3. The number of melt days and the melt energy increase in summer under föhn conditions. It is therefore possible that föhn conditions prolong the melt season and increase the intensity of melt during summer.

5.4.5 Spring

Arguably the largest impact of föhn winds was experienced during spring (SON). Although not all changes in mean values between non-föhn and föhn conditions were statistically significant, the impact on the melt energy indicates a large impact due to föhn winds. Table 5.5 displays the average spring values for composites of föhn and non-föhn periods.

The atmospheric transmissivity (SW_T) increased significantly ($\alpha = 0.05$) during föhn conditions indicating an increase in incoming shortwave radiation at the surface due to the föhn-induced cloud clearing. The net longwave radiation was significantly (α=0.05) lower during föhn conditions than during non-föhn conditions at AWS2 (-$43.5Wm^{-2}$), AWS3 and AWS5, providing further evidence of the impact of cloud clear-

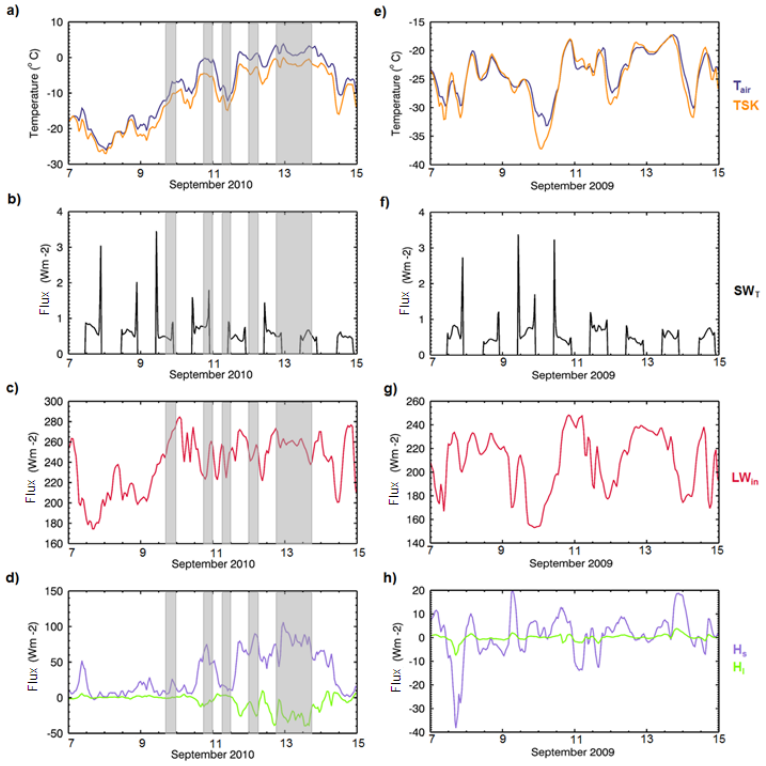

Figure 5.6: SEB components observationally-derived at AWS2 during a week in which föhn conditions were identified (a to d) and were not identified (non-föhn conditions) (e to h) during winter. a) Surface temperature (TSK) and air temperature (T_{air}), b) Shortwave atmospheric transmissivity (SW_T), c) longwave incoming radiation (LW_{in}) and d) sensible heat flux (H_s) and latent heat flux (H_l) during a week with föhn conditions from 7th to 15th September 2010. Figures e to h are the same as a to d, but during a week in which no föhn conditions were identified from the 7th to 15th September 2009. The shaded sections indicate the föhn conditions.

ing.

Both turbulent fluxes exhibited significant differences during non-föhn conditions compared to föhn conditions at AWS2. The sensible heat flux increased (more positive) by over 20Wm^{-2} during föhn conditions at AWS2 and at AWS3. The warmer air and higher wind speeds contributed significantly to increasing the fluxes over the ice shelf. The latent heat flux became more negative to -5.4Wm^{-2} (AWS2) during föhn conditions, indicative of sublimation and evaporation. The large increase in sensible heat flux and decrease in latent heat flux during föhn conditions is displayed in Figure 5.6. AWS5 also observed similar changes. However, AWS3 observed no significant change in latent heat flux. The cooling effect of the net longwave radiation and latent heat flux was not able to counteract the considerable heating processes, therefore, there was a large melt energy during föhn conditions, and an overall positive SEB at AWS2 during spring.

The percentage of melt days increased from 3% during non-föhn conditions, to 25% to 28% during föhn conditions at AWS2. The earliest annual melt day observed at AWS2 was the 27th October 2010. This was earlier melt onset than the typical December to February melt period observed in the other years. Between the 27th of October and the 16th of November 2010 melting was frequently observed at AWS2. During this 21 day period, 22 föhn conditions and 14 föhn days were observed at AWS2; far higher than identified during the same period in other years. Therefore, it is inferred that föhn conditions can extend the melt season by increasing the number of melt days outside of the usual summer melt period. This also increases the energy available for melt. King *et al.* studies this period in more detail and identifies that föhn conditions in November 2010 extended the duration and frequency of melting over the LCIS.

Föhn conditions were not only observed at AWS2, but also at AWS3, AWS5 and AWS6 during this period. At AWS5 16 föhn days were observed, with air temperatures and windspeeds comparable to those observed at AWS2. At AWS5 föhn winds are likely to have had a greater impact, as the strength of the föhn conditions is stronger, and the frequency of föhn conditions is higher at the foot of the AP (in Cole Peninsula observations). In satellite images presented by Luckman *et al.* (2014), the foot of the AP and inlets on the western ice shelf observed the highest number of melt ponds and

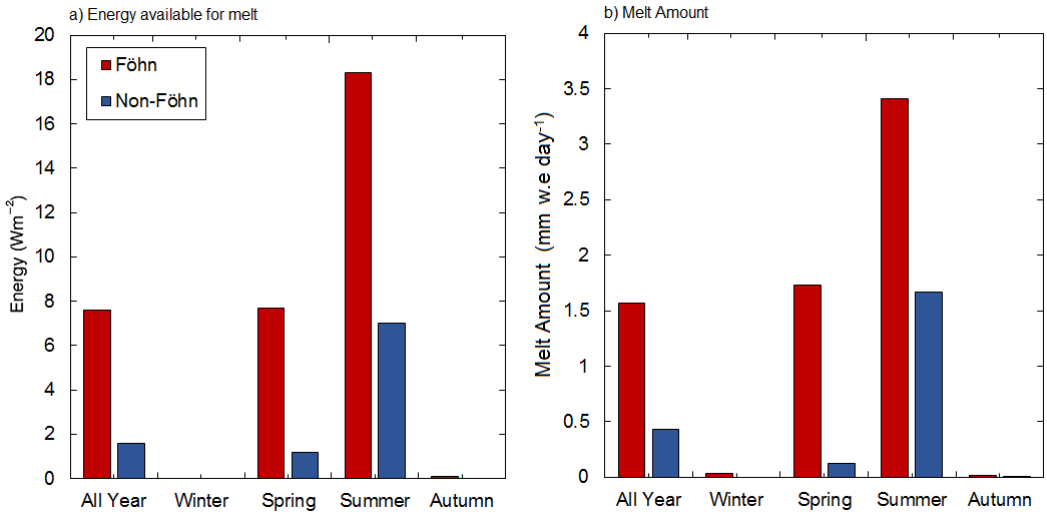

Figure 5.7: The average daily energy available for melt (a) and the amount of energy (b) from the AWS2 SEB model for all seasons, and an annual average from 2009-2012. Average föhn values are red, and average non-föhn values are blue.

sustained periods of melt.

At AWS2, the amount of energy available for melt during spring föhn conditions was 7.7Wm^{-2} (Figure 5.7). This was greater than the mean summer melt energy (7.0Wm^{-2}). Therefore, the melting potential during spring was increased significantly by the presence of föhn conditions, and föhn-induced melting alone contributed as much melting during spring, as non-föhn melting in summer (Figure 5.7).

The amount of water equivalent melting increased due to föhn conditions in spring (Figure 5.7), as well as in other seasons. A considerable amount of melting occurred during spring föhn conditions (1.73mm w.e day^{-1}), which was comparable to summer melting in the absence of föhn conditions (1.67mm w.e yr^{-1}). Therefore, föhn conditions increase the energy available for melt, increase the amount of melting, and increase the number of melt days, which prolongs the melt season and initiates melting earlier in the year (as early as October 27th).

5.4.6 Surface Melting

The only two locations for which melt energy estimates were available were AWS2 and AWS3. From results presented in previous sections, föhn-induced melting was evident during spring and summer at these locations. For the other locations, only air temperature was available. To assess the spatial distribution of föhn-induced melting, an estimate of the surface melting at other locations is required. A number of studies have developed air-temperature-based indices for melt (e.g Ohmura & Ohmura 2001; Trusel *et al.* 2015; Vaughan 2006). One of the earliest studies to use air temperature for measuring ablation of glaciers was Hann in 1908 (Ohmura & Ohmura, 2001) (recall that it was Hann who also developed the thermodynamic föhn theory). Using air temperature as a proxy for melt is useful due to the large availability of near-surface temperature observations compared with surface temperature measurements. Air temperature based methods are known to be accurate, despite the relative simplicity (Ohmura & Ohmura, 2001). Furthermore, several components of the SEB are closely related to, or depend on the air temperature, and therefore air temperatures above freezing are justified for analysing melt (Abram *et al.*, 2013). From Figures 5.3 to 5.6, the close relationship between air and surface temperatures is evident, as is the offset between the variables once the surface temperature approaches the melting point.

There are limitations with using temperature-based melt proxies however. Extrapolation of melting over a large area is not always accurate. Hock (2003) found that features such as topographic shading can alter the melt significantly over small areas. The accuracy of these simple proxies decreases with the temporal resolution. Using daily values of temperature can underestimate melt periods, as the daily temperature may be below freezing, but periods of warmer air caused melting during a short period of the day (Hock, 2003).

Due to the limited surface temperature observations available over the LCIS, a number of temperature-based melt proxies were used to locate potential melting. The methods were tested against the known melting values from AWS2.

Table 5.6: The annual average melt produced at each location, calculated from the summer air temperature values by Trusel *et al.* (2015). 'T_{DJF}' is the 2009-2012 annual summer air temperature values. '$Melt_{T_{DJF}}$' is the amount of melt estimated from the summer air temperatures. $T_{DJF_{non}}$ is the summer air temperature excluding the föhn conditions. '$Melt_{T_{DJF_{non}}}$' is the amount of melt estimated from '$T_{DJF_{non}}$' without including the föhn-induced melting.

Location	T_{DJF} (°C)	$Melt_{T_{DJF}}$ (mm w.e yr^{-1})	$T_{DJF_{non}}$ (°C)	$Melt_{T_{DJF_{non}}}$ (mm w.e yr^{-1})
CP	-2.5	379.3	-3.2	275.8
AWS1	-3.8	209.9	-4.2	175.0
AWS2	-3.9	200.6	-4.4	159.8
AWS3	-4.5	152.7	-4.6	145.9
AWS5	-4.5	152.7	-4.5	152.7
AWS6	-4.9	127.3	-5.4	101.4

Calculating melt from total summer air temperatures

One study has tested the links between the summer air temperature and surface meltwater production over Larsen B, and developed a relationship. As the majority of surface melting occurs during summer over Larsen C, this method has been employed here. The method presented by Trusel *et al.* (2015) uses mean summer (DJF) air temperature to estimate the amount of meltwater produced using the following equation:

$$Melt(mm\,yr^{-1}) = 1183e^{(0.455T)} \tag{5.20}$$

where T is the mean summer air temperature (°C) and melt is the amount of surface melting (mm w.e yr^{-1}).

The average summer air temperature at AWS2 was -3.9°C. Putting this into equation 5.20 results in a melt rate of 200.6mm w.e yr^{-1}. This value is relatively close to the observationally-derived value of 179.8mm w.e yr^{-1} at AWS2. Table 5.6 displays the calculated annual melt using the method proposed by Trusel *et al.* (2015) equation (5.20.

As this method produces a relatively accurate estimate of melting compared to observationally-derived values at AWS2, it has been used to estimate the influence of

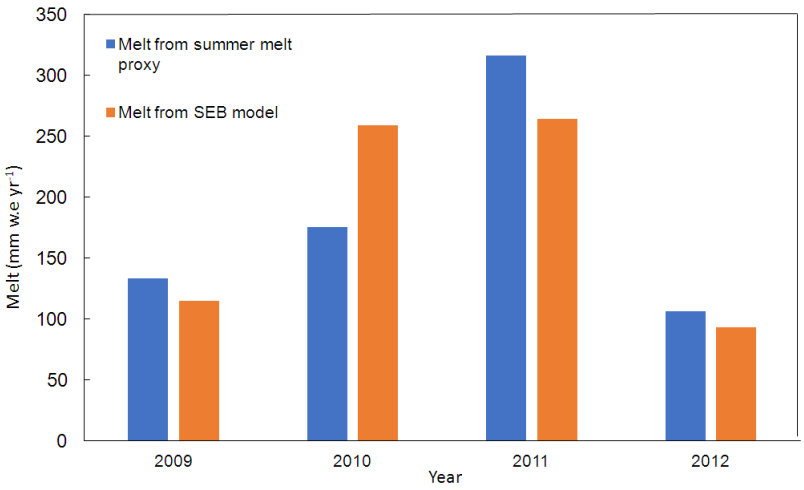

Figure 5.8: The annual amount of melt from the AWS2 SEB model (blue), and from the summer-temperature-melt proxy by Trusel *et al.* (2015) (orange).

föhn conditions at each location. The values in Table 5.6 use the average summer air temperature, which includes the föhn and non-föhn conditions, and therefore incorporates the higher temperatures. To assess the impact of the föhn air, the process has been repeated, but using summer average temperatures excluding föhn conditions. These are presented in Table 5.6 along with the estimated melt.

At all locations except AWS5, there was a decrease in melt rate when the effects of föhn conditions are removed from analysis. The largest impact was found at Cole Peninsula, where föhn conditions provide an additional 103.5mm w.e yr^{-1} of melting. At AWS2, the impact of the warm föhn air can contribute 40.8mm w.e yr^{-1}.

Compared to the melt amount estimated by the SEB model (Figure 5.8), the Trusel *et al.* (2015) method underestimates the amount of melting in each year. It does however capture the increase of melting in 2011, and is able to capture the general magnitude of melt in each year. The calculation used by Trusel *et al.* (2015) does not include melt during other seasons (including föhn-induced melt), which may be important as more föhn conditions are identified during spring, and they have a positive influence on the

amount of melt as shown earlier.

Melting in AMPS

It has been shown that in comparison to observations AMPS is relatively accurate at simulating near-surface variables and SEB components (Table 5.1). Although caution should still be taken when interpreting the estimates of melt, AMPS can give an idea of the spatial distribution of melt.

To estimate the accuracy of both the annual and summer air temperature methods for calculating surface melt AMPS data have been used to estimate föhn-induced surface melting. To calculate melt from AMPS data, the following equation was used:

$$E = SW\downarrow + SW\uparrow + LW\downarrow + LW\uparrow + H_s + H_l \tag{5.21}$$

where E is the net energy flux available for heating or melting the surface when positive. To define periods when melting may occur, the condition outlined in Equation 5.3 in Section 5.2.1 is used. The melt energy (E_{melt}) can be converted to water equivalent melt (mm w.e) using the following equation:

$$Melt\,amount = \frac{E_{melt}}{\rho_w \times L_f} \tag{5.22}$$

where L_f is the latent heat of fusion (334 kJ kg^{-1}) and ρ_w is the density of water (1000kg m^{-3}).

The AMPS data have been compared against observationally-derived values at AWS2 (Table 5.7), as these are the best representation of true surface melt on the LCIS. As the AWS2 SEB model does not use the same method to estimate melt energy, the amount of melting produced by both AWS and AMPS was unlikely to be the same.

The total number of melt days from 2009-2012 was 214 in AWS2 observations, and 289 in AMPS data. AMPS therefore overestimates the number of melt days compared to observations. This was not unexpected. As shown in Section 5.3, the downwelling

shortwave radiation is overestimated by AMPS. Combined with the low albedo and the poor representation of clouds in the model, the surface is much warmer in AMPS than it reality (mean bias of 1.8°C). This has also been found in many other studies using AMPS or Polar WRF model (e.g Grosvenor *et al.* 2014; King *et al.*, 2008, 2015).

AMPS estimated the percentage of föhn days experiencing melt with greater accuracy. Over 30% of the föhn days coincided with melt days in both observations and AMPS data, compared to less than 20% of non-föhn days (Table 5.7). The largest annual number of melt days was in 2010, when 85 and 73 melt days were identified from AMPS and AWS data respectively. This was influenced by the large number of föhn conditions during the melt season in 2010 (see Chapter 4).

Despite AMPS overestimating the number of melt days, the amount of melt during those days was similar to in observations. Figure 5.9 presents the daily melt amount from AMPS and AWS2. The average daily amount of melt was well represented in AMPS. The average daily amount of melt at AWS2 was 2.0mm w.e day^{-1} whereas in AMPS data it was 1.7mm w.e day^{-1}. However, as evident in Figure 5.9, AMPS fails to capture the amount of melt on days with a large magnitude of melt. The maximum daily amount of melt in AMPS was 21.4mm w.e on the 4th of January 2011. However, in AWS2 data, there were over 40 days which experienced melting greater than this.

During föhn days, the amount of melt increased significantly ($\alpha = 0.05$) in AWS observations to 7.6mm w.e day^{-1}. However, the increase was more modulated in AMPS, and during föhn days the amount of melt was 2.1mm w.e day^{-1}. Therefore, AMPS is able to capture the average daily amount of melt, but underestimates the amount of melt associated with föhn conditions, which was typically much larger.

Although AMPS was unable to capture the high amount of melt during föhn days, the daily average amount of melt at AWS2 was well captured. Therefore, to estimate the spatial distribution of melting, surface melt at all other locations has been assessed (Table 5.8).

Table 5.7: The representation of surface melt from observationally-derived data at AWS2 and AMPS data at the same location. The total number of melt days and percentage of melt days which coincide with föhn and non-föhn periods are for 2009-2012. The melt amount values are daily averages over the same period.

Parameter	AWS2 Values	AMPS Values
Total number of melt days	214	289
Percentage of föhn days with melt	31.4%	33.7%
Percentage of non-föhn days with melt	13.8%	19.2%
Average melt amount (mm w.e day^{-1})	2.0	1.7
Average melt amount during föhn days (mm w.e day^{-1})	7.6	2.1
Average melt amount during non-föhn days (mm w.e day^{-1})	1.6	1.4

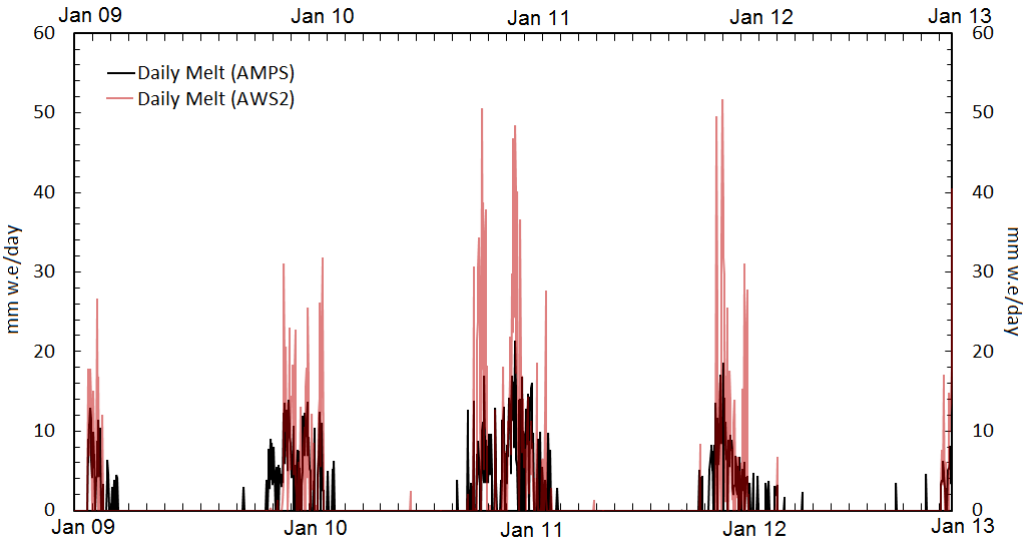

Figure 5.9: The daily amount of melt observationally-derived at AWS2, and calculated using Equation 5.3 from AMPS data for 2009-2012. Melt estimated by AMPS is black, and by AWS2 is transparent red.

Table 5.8: The representation of surface melt from AMPS data at all locations. The total number of melt days and percentage of melt days which coincide with föhn and non-föhn periods are for 2009-2012. The melt amount values are daily averages over the same period.

Location	Cole Peninsula	AWS1	AWS2	AWS3	AWS5	AWS6
Average Annual number of melt days	49	79	72	75	72	69
Percentage of föhn days with melt	11.6	38.4	33.7	24.6	39.3	31.9
Percentage of non-föhn days with melt	10.0	19.6	19.2	20.0	20.5	17.9
Average melt amount (mm w.e day^{-1})	0.8	1.2	2.0	1.6	1.6	1.2
Average melt amount during föhn days (mm w.e day^{-1})	1.1	2.6	2.1	1.4	1.8	1.5
Average melt amount during non-föhn days (mm w.e day^{-1})	0.7	1.1	1.4	1.6	1.4	1.2

The location with the highest number of melt days was AWS1, however the highest percentage of föhn days with surface melt was at AWS5. AWS5 and AWS6 locations may be biased due to the lack of föhn conditions identified during winter, leading to a higher percentage of föhn conditions during the warmer summer months. The location with the highest daily average melt amount during föhn days was AWS1 (2.6mm w.e day^{-1}). From assessing the estimated melt from AMPS, AWS1 experienced the highest amount of föhn induced melt, and the greatest number of melt days. This is not unexpected as more föhn conditions were identified at this location than any other, except for Cole Peninsula. Interestingly, Cole Peninsula experiences the shortest melt season duration in AMPS, and the lowest percentage of föhn days which coincide with melt days. This is likely an unrepresentative estimate for surface melt at Cole Peninsula, as will be discussed below.

5.5 Discussion

Investigating the impact of föhn winds on the SEB is critical in understanding the interaction between the warm winds and the surface, and to quantify the surface melting induced by föhn. Prolonged surface melting and ponding of the melt water on the surface is believed to be a precursor for the destabilisation of ice shelves (Luckman *et al.*,

2014). Numerous contemporary studies suggest, or discover links between föhn winds and surface melting induced by the warm air (Elvidge *et al.*, 2016; Grosvenor *et al.*, 2014; King *et al.*; Kuipers Munneke *et al.*, 2012; Van Den Broeke, 2005). Whilst many studies have investigated the influence of singular föhn events (often during summer) on the SEB, only very few have assessed the cumulative affect of numerous föhn events, and no studies (that the author is aware of) have assessed the climatological or more general impact of föhn on a larger timescale over the LCIS.

Föhn conditions have been identified frequently over the four year study period, with a peak in the number of föhn conditions during spring (see Chapter 4). The warm, dry signal of the föhn regularly propagates over 100km across the LCIS. AWS2 and AWS3 often observe surface temperatures above freezing during these föhn conditions and an associated increase in energy available for melt has also been observed at these locations (Kuipers Munneke *et al.*, 2012). Despite these observations, it is widely believed that the extent of the föhn impact, and specifically the föhn induced melting, is limited to the inlets at the foot of the AP, and does not stretch across the LCIS.

The current study focuses on the impact of föhn conditions on multiple components of the SEB as well as the melt energy and water equivalent melt amount. This relied on the observations of various components, and the calculation of others. One limitation of this study is the limited number of locations which observed the SEB components. The most reliable SEB dataset was obtained for AWS2 where a SEB model was run by Kuipers Munneke. Unfortunately, no SEB data were available for the Cole Peninsula location, where the largest melt rate and highest number of melt days have been previously observed in satellite images (Luckman *et al.*, 2014). However, investigating the impact of föhn at AWS2, over 100km from the AP, provides an insight into the extent and strength of the föhn induced melting.

The increase in energy available for melt due to föhn conditions was significant at both the annual and seasonal scale (spring and summer). This increased melt energy can be largely attributed to the increased shortwave radiation from the cloud clearing by föhn winds. This has also been found for individual föhn events in studies by Elvidge *et al.* (2016); Kuipers Munneke *et al.* (2012), during spring 2010 (King *et al.*) and over

the northern AP (Cape *et al.*, 2015). The increased shortwave radiation provides heating for the surface on an annual scale, as well as during spring, summer and autumn. The increase shortwave radiation was not observable during winter, however the increase in sensible heat flux during föhn conditions was largest in winter (33.2Wm^{-2} increase). The föhn air is significantly warmer than the ambient air during winter, which prompts the large increase in sensible heat flux. The increase in sensible heat flux was largest at AWS5. AWS5 was closer to the AP, and may have experienced greater turbulent heat fluxes due to stronger föhn conditions at this location than at AWS2 or AWS3. However, this location also experienced the largest cooling due to latent heat flux, which counteracts the warming from the sensible heat flux increase. Therefore, the energy available for melt was not as large as at other locations.

The large increase in melt energy, number of melt days and the water equivalent melt amount during spring föhn conditions is likely the biggest implication of föhn conditions on the surface of the LCIS. The large sensible heat flux during spring föhn conditions causes a positive SEB. This, combined with the more frequent periods of warm air and high surface temperature, creates a larger amount of residual energy. This föhn-induced melting during spring is comparable in energy and melt amount to that of non-föhn conditions in summer. In the absence of föhn conditions in spring, the melt amount is much smaller (1.2Wm^{-2} daily average) than that in summer, and likely insignificant. However, with the large melt energy in spring due to föhn conditions, the melt season is extended. Föhn induced melting in spring can cause early onset of the melt season, prolong individual periods of observable surface melt and extend the duration of the melt season. These results were also found during a spring 2010 föhn study by King *et al.*. However King *et al.* conclude that there was only a minimal impact of föhn on the intensity of the melt, as the reduced latent heat flux and incoming longwave radiation balanced the positive values of sensible heat and shortwave radiation, and the seasonal changes due to föhn conditions were not significant. The current study however does show that composites of föhn conditions increase the available energy for melt and increase the intensity of melt during spring and summer.

A number of methods for calculating surface melt were used at the locations without SEB observations. The relationship between summer air temperature and melt

estimated surface melt values comparable to the observations at AWS2, whereas the annual air temperature and melt relationship underestimated the amount of melt at AWS2. Over the LCIS, an extended summer (Oct-March) temperature relationship with melt may be more reliable due to the additional föhn induced melting in spring. From the summer air temperature-melt proxy (Trusel *et al.*, 2015), the largest melting was identified at Cole Peninsula. At AWS2, an additional 40.8mm w.e yr^{-1} was estimated during föhn conditions using the summer air temperature-melt proxy. In AWS2 observations (SEB model output), the additional melt due to föhn conditions was 33.6 mm w.e yr^{-1}. Therefore the relationship is relatively successful at estimating the additional melt generated by föhn conditions, and the results can be interpreted with confidence.

Interestingly, the additional melt due to föhn conditions at AWS1 and AWS2 was of similar magnitude. It is possible that additional föhn melting at AWS2 has occurred due to a localised föhn effect over Jason Peninsula. This localised föhn effect is evident in high-resolution model simulations, and this will be discussed in Chapter 6. The peak number of identified föhn conditions at AWS1 occurred during spring, with an average of 26 föhn conditions each spring. If the summer air temperature and melt relationship took spring temperatures into account, the increase in melt energy due to föhn would likely be much higher than at AWS2.

It was estimated by the summer air temperature-melt proxy that there was no additional föhn-induced melting at AWS5. There was no change in the summer air temperature when the föhn conditions were removed. Similarly, in assessment of the SEB components at AWS5, there was little net change in SEB due to föhn conditions, as the large sensible heat flux was counteracted by a large latent heat flux. Therefore, it is possible that the large amount of sublimation or evaporation (if liquid water was present) at this site was removing any melt potential. The increase in sensible and decrease in latent heat flux during föhn conditions was significant, and although melting did not occur, the impact of föhn conditions on the SEB should not be dismissed.

The melting estimated from the AMPS data exceeded the observationally-derived values at AWS2 and AWS3. The values are similar to those simulated by Grosvenor

et al. (2014) for a summer föhn case study, and by King *et al.* for a spring and summer study incorporating a number of föhn events. The melt overestimation stems from the positive bias in surface temperature. This is caused by the positive bias in incoming shortwave radiation, the poor representation of clouds in the model, and the low albedo value in AMPS. This has been discussed by Grosvenor *et al.* (2014); King *et al.* (2015) and King *et al.*. Therefore currently, the values of melt energy can not be trusted if used as an estimate of melting. However, as the overestimation is found at all locations, it can be used to infer the spatial patterns of melting, and show the increase in melt amount during föhn conditions.

5.6 Conclusion

The use of composites of föhn conditions to study the impact on surface melting and the SEB creates a robust understanding of the föhn impact, by assessing the more general response to föhn, as opposed to one or two studies of individual events. The limitation of assessing case studies is that the chosen event may be an anomaly, or not representative of the average föhn conditions, whereas assessing the average impact of föhn provides more confidence in the quantification of surface melt due to föhn. This study has similar findings to studies by King *et al.* (2015) and King *et al.*. The föhn conditions prolong the melt season due to the high frequency of föhn events in spring, and the higher average temperatures. However, this study also concludes that the intensity of melt increases during föhn conditions, even 100km from the AP. Using composites of föhn conditions has strengthened the föhn theory; that melting can be prompted by föhn and this causes additional melt.

This composite analysis has improved the understanding of föhn conditions in this region. Whilst some results differ slightly from those of other studies, the overall conclusions remain the same. Föhn conditions have the largest impact on the incoming shortwave radiation (during spring, summer and autumn), which, combined with a large sensible heat flux creates positive residual energy. This can induce melting when the surface temperature is at the melting point. Föhn conditions can generate melting over 100km away from the AP, and when this occurs during spring, the melt season

starts earlier, and becomes longer.

If the frequency of föhn conditions over the LCIS is increasing, as theorised by the föhn hypothesis, then this spring maximum could have implications for increased melt over the next few decades. If an increasing number of föhn conditions occur in spring, the amount of melt, length of the melt season and frequency of melt may increase, and push the ice shelf past a tipping point. Monitoring the surface melting, and föhn induced surface melting, may be crucial to monitoring the stability of the LCIS.

Chapter 6

High-Resolution Modelling of Föhn Events using the Weather Research and Forecasting Model

6.1 Introduction

Idealised and realistic modelling studies have long been conducted to investigate the interaction between airflow and mountain ranges. Idealised simulations usually generate conditions over simplified topography such as a 2-D bell-shaped hill, using an individual sounding (National Center for Atmospheric Research, 2014). Realistic simulations require pre-processing (WPS for WRF modelling) which inputs static fields such as topography, and atmospheric data (GFS or ERA-Interim reanalysis data for WRF), which is then scaled appropriately to the selected grid resolution (National Center for Atmospheric Research, 2014). Idealised modelling provides an insight into the key processes and parameters controlling the flow, whilst reducing the complexity of including realistic topography and varying meteorology data. The main aim of realistic modelling is to gain a 'real-world' insight into the interactions between the land, topography, atmosphere and oceans. Regional atmospheric models are often used to simulate small scale, localised features such as föhn winds (e.g Elvidge *et al.* 2015, 2016; Speirs *et al.* 2010, 2013; Steinhoff *et al.* 2014). The output from both idealised and realistic modelling provides information on features such as gap flows, channelling, mountain waves, spatial distribution of air flow. In remote locations such as the Antarctic, there is an

additional benefit of using regional models to fill the observational gaps, as observations are relatively sparse.

Elvidge *et al.* (2015, 2016) used MetUM at 1.5km horizontal resolution to simulate three föhn events over the Larsen ice shelf. Zängl (2002) used the MM5 model to gain a deeper understanding of shallow föhn conditions in the Alps. The WRF model has been used to successfully simulate föhn conditions in numerous studies including Bannister & King (2015); Grosvenor *et al.* (2014); Speirs *et al.* (2010, 2013); Steinhoff *et al.* (2013, 2014), and is the model used in the current study.

In Chapter 3 the AMPS output at 5km horizontal resolution was used to identify föhn conditions by isolating the leeside isentropic drawdown associated with their onset. Whilst AMPS successfully simulated the upper-air characteristics of föhn winds, the horizontal and vertical resolutions of the output may not be fine enough to resolve small-scale features within the föhn winds, or the boundary layer interactions with the föhn air. Resolving the smaller wakes and jets, and simulating the spatial distribution of föhn air with better accuracy is crucial for investigating the impacts associated with föhn winds.

Four föhn events have been simulated as case studies using the WRF model at 1.5km horizontal resolution and they are presented here. The main aim of this is to use a high-resolution model to gain more information about the spatial distribution of föhn winds than a 5km model and observations can provide. To assess the impact of increasing the resolution, much of the WRF configuration has been set to the same values in AMPS. This allows the AMPS and WRF output to be directly compared. Numerous studies have conducted sensitivity tests of WRF options to find the optimal set-up for resolving various features (e.g Cohen *et al.* 2015; Hines & Bromwich 2008; Hines *et al.* 2011). However, this was not necessary for this project, as the over-arching aim was to assess the impact of increasing only the horizontal and vertical resolution on the simulation of föhn events.

The four case studies centre on föhn events within each season, to gain an insight into the interaction between the föhn air and the seasonally varying near-surface condi-

tions. The summer case study was additionally used to test a number of set-up options (Section 6.2). Within this chapter, the main findings from simulating each case study are presented and discussed. A brief validation of the near-surface variables for WRF and AMPS is also presented. A comparison of the spatial distribution of the föhn winds in AMPS and WRF are also discussed.

The chapter continues with a brief overview of the WRF set-up before presenting the findings from the Spring case study. Autumn and winter case studies follow on from this. A discussion of the main themes and features which were present in all case studies is in section 6.7. The chapter concludes with a summary of the main findings, implications for future work and how these findings may influence the current knowledge of the impacts of föhn winds on the surface of the LCIS.

In this chapter, 'AMPS' or '5km' refers to the archived 5km horizontal resolution output, and 'WRF' or '1.5km' refers to the high-resolution, case study output.

Part of this chapter has been submitted as an article to Weather with the title 'Does high-resolution modelling improve the spatial analysis of föhn flow over the Larsen C ice shelf?'. On the 7th of April 2017 it was accepted. The specific text and figures used in the article are referenced.

6.2 WRF Model Description

A full description of the WRF model set-up is provided in Chapter 2. Only a brief overview of the main set-up options is presented here. The development of WRF, its core structure, topography, boundary and lateral inputs and main options were discussed in the Chapter 2. To assess only the advantage of increasing the horizontal and vertical resolution of the model, the other options remained as close to the AMPS set-up as possible. There are a few exceptions to this, as increasing the horizontal and vertical resolutions lead to some required changes. However, the main parameterisation schemes and options are the same in both model set-ups.

Table 6.1: The specifications and options for the set up of WRF for the case study simulations.

Option	Specifications for 1.5km WRF runs
Topographic resolution	30 arc-seconds (BEDMAP2) ($\sim$ 480m at 67°S)
Land Surface Physics	NOAH Land surface model
Model Top	10hPa
Microphysics Option	WRF Single-moment 5-class (WSM5)
Longwave Physics	Rapid radiative transfer model (RRTM)
Shortwave Physics	Goddard Scheme
Surface Layer Physics	Monin-Obukhov similarity theory
Planetary Boundary Layer Scheme	Mellor-Yamada-Janjic (MYJ) scheme

The differences between the set-up of AMPS and the WRF are described in Chapter 2. For the AMPS runs, WRF version 3.2.1 with Polar WRF modifications was used for the archived output between 2009 and 2012. For the WRF runs, WRF version 3.5.1 with Polar WRF modifications was used. The main changes and bug fixes between model versions are described on the WRF development website (http://www2.mmm.ucar.edu/wrf/, last accessed 09/02/2017). Briefly, the main differences include additional parameterisation schemes, different default options for sea-ice thickness and correcting soil moisture values. As the same parameterisation schemes and options are used in WRF as in AMPS, the model version differences are assumed to make little difference on the outputs. WRF has been used in this project primarily due to the ability of the model to represent complex topography and small-scale features in previous studies (e.g Grosvenor *et al.* 2014; Speirs *et al.* 2010, 2013; Steinhoff *et al.* 2013). The dynamical core and numerical schemes used within WRF allow for representation of orographically-forced processes (see Skamarock & Klemp (2008) for information on the numerics and dynamics). The WRF model was also used within AMPS for the 5km archived output, used to identify föhn conditions (Chapter 3). Therefore retaining the same model for the case studies (although a different version) will reduce the uncertainty when comparing the output. Table 6.1 summarises the main options used for the high-resolution case study runs.

In WRF, three domains have been used to nest the simulations down to 1.5km horizontal resolution in the inner domain (D03). The three domain locations are displayed in Chapter 2. Nesting the domains allows a smaller, inner grid to have higher horizontal resolution. It also allows the coarser, initial and boundary conditions to be scaled down to the inner, higher-resolution domain. The outermost (middle) domain has a horizontal resolution of 13.5km (4.5km) respectively. The innermost domain has a horizontal resolution of 1.5km, and data from this domain was analysed for the case studies. A 3:1 ratio for increasing resolution is suggested by the WRF developers and allows data to transfer between the domains. All three domains have 70 vertical levels in WRF, which has increased the vertical levels from 44 used in AMPS. Due to the higher resolution used in WRF, the topographic data used in the model was also of higher resolution than that used in AMPS. The BEDMAP2 topography was used in the WRF runs. This has increased the topography resolution from 2 minute arc-seconds in AMPS to 30 arc-seconds in WRF.

The lateral and boundary conditions for the outermost domain for both AMPS and WRF were provided by the Global Forecast System (GFS) analysis data from the National Centers for Environmental Prediction (NCEP) at the National Oceanic and Atmospheric Administration (NOAA). The analysis data, GFS, used for this project are at 0.5° resolution. AMPS is reinitialised with the GFS data every twelve hours, whereas WRF was initialised with GFS at the start of the case study only, but the lateral boundary conditions were updated every 24 hours. WRF can be initialised with data sources other than GFS data. In Bracegirdle & Marshall (2012) it was found that the ERA-Interim dataset was the most accurate reanalysis product at reproducing Mean Sea Level Pressure (MSLP) over the Antarctic. Over the Bellingshausen and Amundsen seas ERA-interim successfully reproduced independent MSLP observations (not ingested within ERA-interim), and captured individual synoptic systems (Bracegirdle, 2013). As the weather systems over these seas influence the airflow over the AP, using ERA-interim to force the lateral and boundary conditions in WRF was considered. Therefore, a number of WRF simulations were run using ERA-Interim data (WRF-ERA) to assess the representation of the near-surface variables when ingesting ERA-Interim.

Figure 6.1 presents the near-surface air temperature simulated by WRF forced with GFS (WRF-GFS) and with ERA-Interim (WRF-ERA). As is evident in the plot of WRF-ERA, there was a significant cold bias in the near-surface air temperature values. The mean bias between WRF-ERA and AWS2 was -13.5°C. The diurnal air temperature cycle was also exaggerated in the WRF-ERA simulation. The exaggerated diurnal temperature cycle in WRF-ERA was also evident in summer simulations over West Antarctica by Deb *et al.* (2016). When WRF was initialised with GFS however, the cold bias and magnitude of the diurnal cycle was reduced. The mean bias between WRF-GFS and AWS2 was -2.6°C. From the 23rd to 27th of January the mean bias between WRF-GFS and AWS2 was considerably smaller, and the diurnal temperature cycle was well simulated. Due to the large cold bias, and exaggerated diurnal cycle evident in the WRF-ERA simulation, and because AMPS is initialised with GFS, the WRF simulations in Chapter 6 were initialised and updated with GFS data.

The final difference between the two model set-ups was the base temperature. This value is used to calculate the potential temperature profile. As the parent domain used in AMPS focuses on the South Pole, which has a higher elevation and is colder than the AP, the base temperature was set to 268K. As the high-resolution WRF domains were located over the warmer region of the AP and the surrounding oceans, the AMPS base temperature value was too cold for case study simulations. The WRF base temperature was adjusted to 290K to take into account the warmer conditions and lower average elevation of the AP. This measure was suggested by WRF developer Dr Jordan Powers (Personal communication, August 2016). Using 290K instead of 268K for the base temperature reduced the cold bias in the WRF simulations. When using a base temperature of 268K the mean bias between near-surface observations and WRF was -6.0°C, however when using 290K, the mean bias was reduced to -3.4°C. For all case studies, the WRF set-up used a base temperature value of 290K. 290K is the default value used in WRF and it was therefore set to this value to avoid adding subjectivity into the configuration.

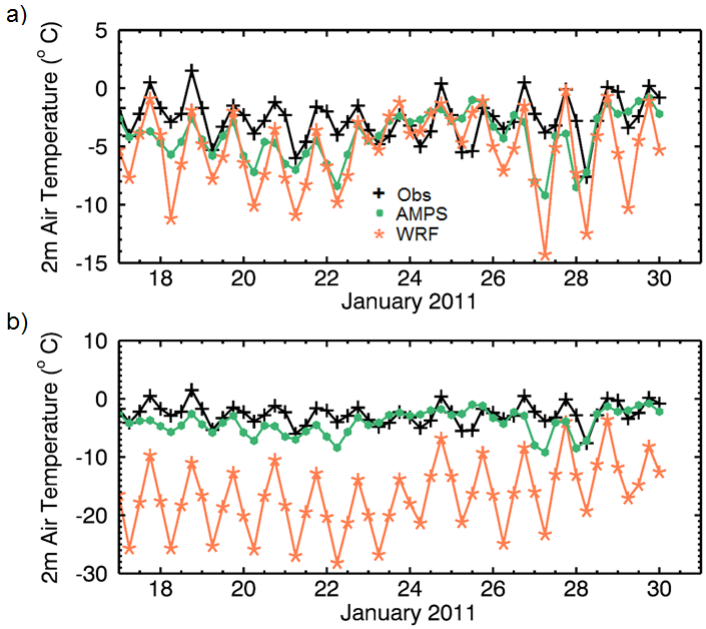

Figure 6.1: A timeseries of the near-surface air temperature at AWS2 from the 17th to 30th January 2011. AWS observational data are black crosses and data from the 5km AMPS output are green dots. Air temperature simulated by WRF forced with GFS data (WRF-GFS) are plotted by coral asterisks in a) and WRF forced with ERA-Interim data (WRF-ERA) are plotted by coral asterisks in b). Note the different y-axis scales to accommodate for the significantly cooler air temperatures in b).

6.2.1 Case Study Specifications

Four case studies have been run using the WRF set-up outlined above. They are centred on föhn events during 2011, as there were six operational AWSs (at least during part of the year), as opposed to a maximum of four in the other years. The dates of the case studies are as follows:

1. Spring: from 00UTC on the 3rd of October 2011 to 00UTC on the 15th of October 2011.

2. Autumn: from 00UTC on the 10th of May 2011 to 00UTC on the 22nd of May 2011.

3. Winter: from 00UTC on the 3rd of August 2011 to 00UTC on the 15th of August 2011.

4. Summer: from 00UTC on the 18th of January 2011 to 00UTC on the 31st of January 2011.

The first 48 hours of each model run were removed from the analysis to allow for model spin-up time and stabilisation. The length of spin-up time depends on the input fields and the topography of the region (Kleczek *et al.*, 2014). Skamarock & Klemp (2008) suggest that a minimum of 12 hours is required to allow the model to ingest the initial and boundary conditions, and produce realistic mesoscale and large-scale circulation. Increasing the spin-up time to 24 hours showed some improvement in simulating the radiation during a recent evaluation of WRF by Kleczek *et al.* (2014). Due to the complex topography of the AP, and to ensure at least one diurnal cycle was successfully simulated by WRF, the spin-up time allowed for the model was 48-hours.

Analysis of the case study periods begins with a discussion of the synoptic situation observed by ERA-Interim. This provides an independent data source to the WRF and AMPS runs, and gives a wider perspective than the near-surface observations alone.

6.3 Summer Case Study

'Föhn conditions' are the six-hourly averaged periods which were detected by both the AWS and AMPS algorithms. 'Föhn events' refers to the continuous period of föhn conditions, and provides information on the length and persistence of the föhn effect. Föhn days are days with at least one six-hourly averaged föhn condition present.

The summer case study period runs from the 17th to 31st of January 2011, after the first 48 hours were discarded from analysis to allow for spin-up time. This case study was used as the test period for the WRF set up, and was therefore run multiple times with varying options. As discussed in Section 6.2, both GFS and ERA-Interim data were used to initialise WRF during this case study. Similarly the decision to alter the base temperature from 268K to 290K (see Section 6.2) was made after running WRF with both values and assessing the output from this case study.

This period was also simulated using high-resolution WRF to assess the impact of föhn conditions during summer. Towards the beginning of the case study, a number of short periods were identified as föhn conditions by the AWS algorithm, but there was no corresponding föhn signal identified by the AMPS algorithm. Over a number of days, the AWS algorithm detected near-surface föhn conditions, whilst the AMPS algorithm did not. However, towards the end of the case study, both the AWS and AMPS algorithms agreed with each other, and therefore föhn events were identified over the LCIS. On further assessment, the near-surface conditions which prompted the detection by the AWS algorithm may be attributed to the diurnal temperature cycle. An aim of this case study was to investigate whether the diurnal temperature cycle influenced the AWS algorithm, or whether the AMPS algorithm failed to capture a number of föhn events.

The föhn events towards the end of the case study occurred during the OFCAP field campaign (January-February 2011). It was a relatively short föhn period, identified over just two days (27th and 28th of January 2011), at a number of the locations.

6.3.1 Summer Synoptic Situation

In the week prior to the onset of the föhn event (18th to 26th of January), low pressure systems were located either side of the AP. To the west, a large, broad low pressure system, spreading across much of the Bellingshausen-Amundsen sea was present. On the east, a relatively weak low pressure system sat to the northeast edge of the AP (Figure 6.2). On average, flow over the LCIS was weakly easterly. To the west of the AP, winds were predominantly southeasterly.

The föhn period was relatively short, so the synoptic conditions during this time are limited to the 27th and 28th of January. During these days the low pressure system to the west of the AP deepened to a minimum of 968hPa, and moved further north. This lead to relatively strong westerly winds over the AP ridge and across the LCIS. The winds over southern AP were strongest, and a föhn effect would have likely been present on both Larsen C and Larsen D ice shelves.

The development of föhn winds was likely halted by the development of a low pressure system close to the west coast of the AP on the 29th of January (Figure 6.2). This forced the winds to flow in a northeasterly direction over the LCIS. The northern tip of the AP experienced northwesterly flow, which may have caused a continuation of the föhn effect over the northeast coast of the AP.

6.3.2 Identified Föhn Events

Föhn conditions were identified on the 27th and 28th of January at Cole Peninsula, AWS3, AWS5 and AWS6. There was no AWS data available at AWS1 during this period. There was only one föhn event at each location but the length of them varied by location, as displayed in Figure 6.3. The longest föhn event was identified at Cole Peninsula (36 hours), from 06UTC on the 27th to 12UTC on the 28th of January. At AWS6 the event was 24 hours long and spanned over the 27th and 28th of January. The föhn event identified at AWS5 spanned 12 hours, and the event at AWS3 was only 6 hours long.

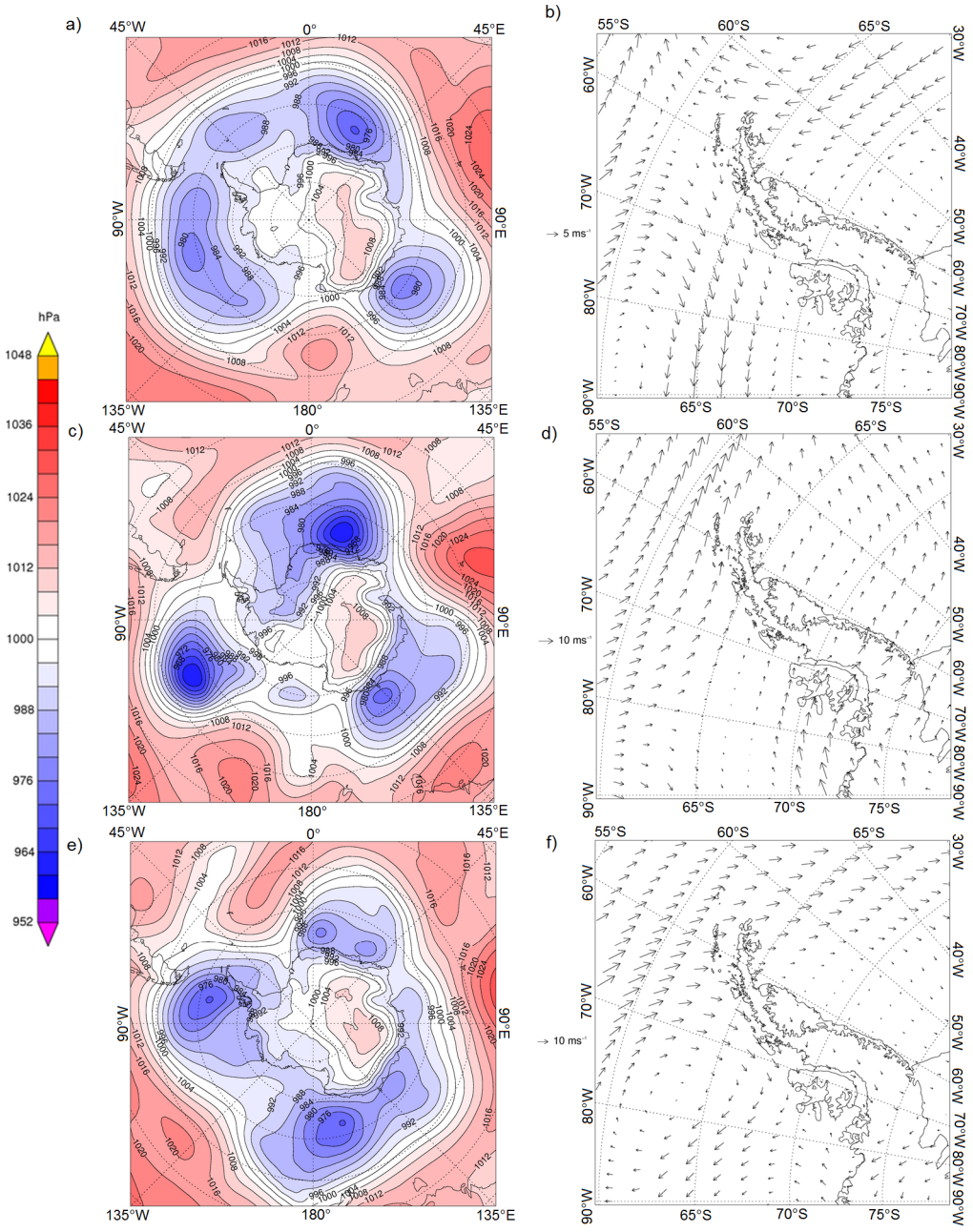

Figure 6.2: The mean sea level pressure (MSLP) over the whole Southern Ocean (left panels: a, c, e) and mean 850hPa wind vectors over the AP region (right panels: b, d, f) before, during and after the föhn events in the summer case study. a) and b) from 18th to 26th of January, the week prior to the föhn events. c) and d) during the föhn days (27th and 28th of January). e) and f) displays the synoptic situation for four days after the föhn events (29th to 31st of January).

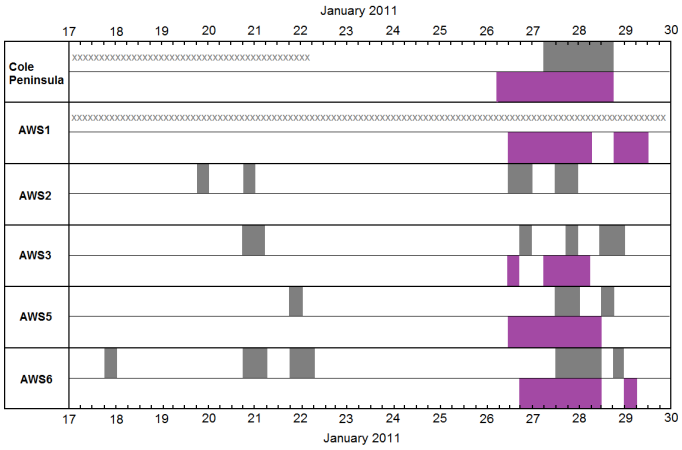

Figure 6.3: The timing of föhn events at each location during the summer case study. The grey bars are times when föhn conditions were identified by the AWS algorithm. Purple bars are times when föhn conditions were identified by the AMPS algorithm. When they overlap, and föhn conditions were identified by both algorithms, these periods were analysed and are presented in Chapter 4. × represents missing AWS data, and therefore no föhn conditions could be identified.

Föhn events were not identified at AWS2, as föhn conditions were only detected by the AWS algorithm, and not by the AMPS algorithm. Similarly, no föhn events were identified earlier in the case study, despite near-surface conditions being detected by the AWS algorithm at AWS2, AWS3, AWS5 and AWS6 between the 17th and 22nd of January.

6.3.3 Model Validation

Validation of both the WRF and AMPS output at AWS2 is presented first. This was the only available location which did not experience a föhn event during the case study. There was a well-defined diurnal cycle in the observations of both the air temperature and the relative humidity at AWS2 (and all other locations). Both WRF and AMPS failed to simulate the large magnitude of diurnal change in the relative humidity, and WRF overestimated the diurnal changes in the air temperatures (Figure 6.4). Throughout the majority of the case study, both models overestimated the relative humidity

Table 6.2: The mean bias and Root Mean Square Error (RMSE) between the two models and the observations for each near-surface variable assessed at Cole Peninsula, for the Summer case study period (17th - 31st of January 2011) at AWS2.

Variable	AMPS-AWS Mean Bias	AMPS-AWS RMSE	WRF-AWS Mean Bias	WRF-AWS RMSE
Relative Humidity (%)	7.1	11.8	4.5	8.2
Air Temperature (°C)	-1.3	2.6	-2.6	3.6
Wind Speed (ms^{-1})	0.4	1.4	-0.3	1.3

(moist bias) and underestimated the air temperature (cold bias). This led to large positive mean biases and RMSE for relative humidity, and relatively large negative biases in air temperature (Table 6.2). WRF performed better at representing the relative humidity than AMPS (4.5% mean bias compared with 7.1% in AMPS). However, the opposite was true for the air temperature.

The wind speed and wind direction were both successfully simulated by both WRF and AMPS (Figure 6.4). The mean biases and RMSEs of both models were small. The models captured the increased wind speeds from the 23rd to the 25th of January. The models did not overestimate the wind speeds as they did in other case studies (see Sections 6.4, 6.5 and 6.6). During the 26th to 28th of January, near-surface föhn conditions were identified by the AWS algorithm, but there was no corresponding föhn signal identified by the AMPS algorithm. Due to the low relative humidity values and peak air temperatures at 18UTC of each day, the near-surface föhn signal was not well defined. The wind direction did rotate from southeasterly (22nd to 25th of January) to northwesterly, however this was the only signal which provided evidence for the föhn event.

The second validation focuses on AWS6, however this is representative of the other locations which experienced the föhn event. Simulation of the near-surface air temperature by AMPS and WRF at AWS6 was similar to at the other locations, however, the relative humidity was simulated with greater accuracy by WRF (Figure 6.4). The mean bias between WRF and the observations was relatively small (-0.9%) (Table 6.3).

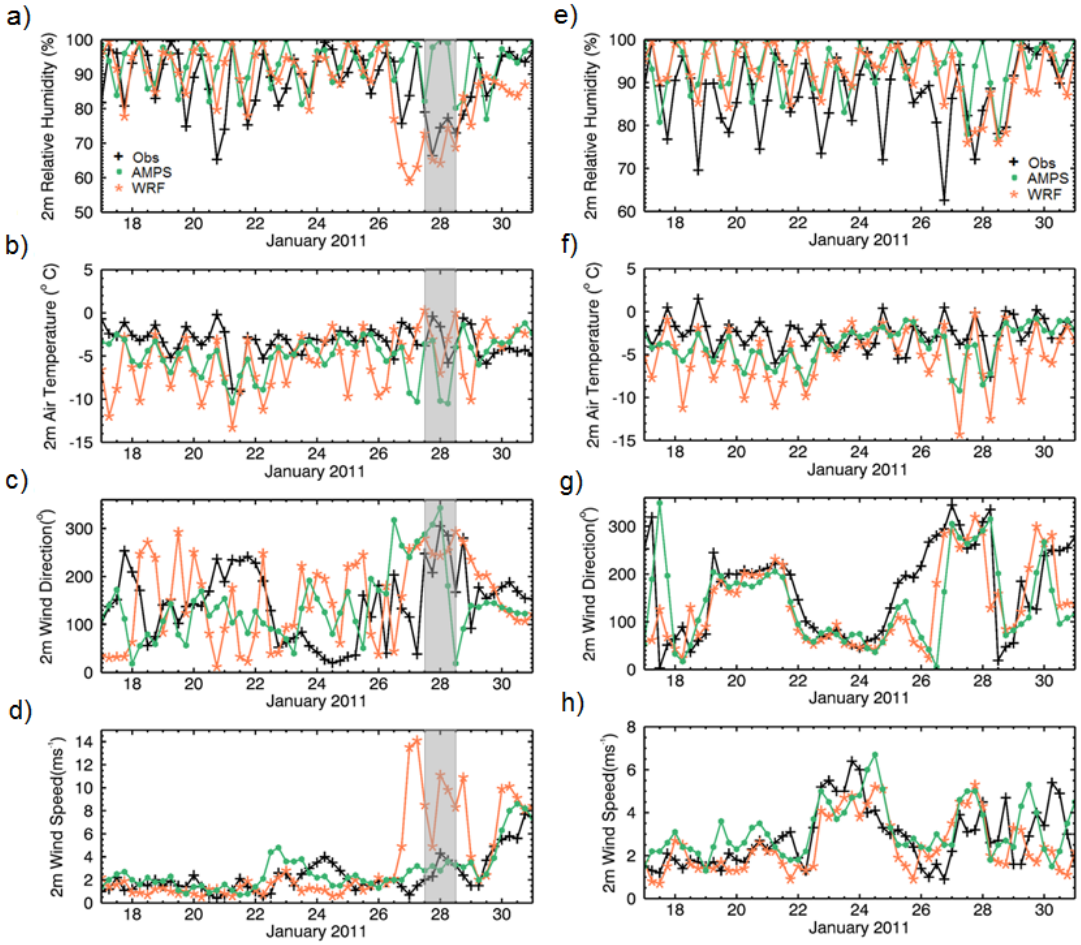

Figure 6.4: Timeseries of observational data from AWS6 (a-d) and AWS2 (e-h) during the summer case study (17th to 31st of January 2011). The 2m relative humidity (a,e), 2m air temperature (b,f), 2m wind speed (c,g) and wind direction (d,h). AWS observational data are black crosses, data from the 5km AMPS output are green dots and 1.5km WRF data are coral asterisks. Periods defined as föhn events are highlighted by grey boxes.

Table 6.3: The mean bias and Root Mean Square Error (RMSE) between the two models and the observations for each near-surface variable assessed at Cole Peninsula, for the Summer case study period (17th - 31st January 2011) at AWS6.

Variable	AMPS-AWS Mean Bias	AMPS-AWS RMSE	WRF-AWS Mean Bias	WRF-AWS RMSE
Relative Humidity (%)	5.9	13.3	-0.9	9.5
Air Temperature (°C)	-1.6	2.9	-2.2	3.6
Wind Speed (ms^{-1})	0.5	1.4	1.1	3.4

The mean bias between AMPS and the observations was also smaller at AWS6 than at AWS2, however, it still failed to simulate the minimum daily relative humidity values. WRF managed to simulate the near-surface response to the föhn event. The relative humidity decrease associated with the föhn onset was captured by WRF, however it was simulated 24-hours too early. AMPS did not capture the decreased relative humidity associated with the föhn event.

Similar to at AWS2, and during the spring case study (Section 6.4), the average air temperature was underestimated (cold bias) and an exaggerated diurnal cycle was simulated by both models, but to a greater extent by WRF (Figure 6.4). The peak value of air temperature at 18UTC each day was well simulated by WRF. When assessing the mean bias at 18UTC only, it was -0.05°C. The daily minimum air temperature values were underestimated by WRF, leading to a mean bias of -4.6°C when assessing values at 06UTC each day.

The wind speed was overestimated by WRF prior to and during the föhn event. This was also evident during other case studies. It is apparent that during föhn events, WRF overestimates the wind speed considerably. The large peak in windspeed on the 26th of January coincided with the large decrease in relative humidity marking the (early) onset of the föhn event in WRF. AMPS simulated the wind speed with greater accuracy, although the mean biases for both AMPS and WRF were relatively small (Table 6.3). The wind direction was simulated with greater variability by AMPS and WRF than was observed at AWS6. The observed winds changed direction more grad-

ually during the first nine days of the case study than simulated. The westerly winds during the föhn event were captured by both models.

The poor representation of the near-surface temperature and relative humidity by WRF provides further support for using an algorithm which detects the upper-air dynamics of the föhn winds (such as the AMPS algorithm) rather than an algorithm synonymous with the AWS algorithm which detects the near-surface response of the föhn air. However, it does also provide evidence for the need to develop better boundary layer and surface schemes for implementation in regional models.

6.3.4 Summer Simulation Results

This case study was largely used to test a number of options for setting up WRF. However, there were a number of interesting findings from this case study. The influence of the seasonal cycle in air temperature on the föhn characteristics is evident from the simulation. The difference in the near-surface air temperature during a non-föhn condition, and a föhn condition is displayed in Figure 6.5.

During föhn conditions, the relatively dry air spread across the majority of the ice shelf. There was a band of warmer air across the centre of the ice shelf at approximately 67.5°S. This feature was also simulated during the Autumn case study, and it will be discussed more in Section 6.5.5. Over the southern section of the ice shelf, the air flow was stronger and more westerly than further north. Over the north of the ice shelf, the air flow was predominantly north to northwesterly. WRF simulated a localised föhn effect on the north of the ice shelf due to the interaction between northerly winds and Jason Peninsula (Figure 6.5). This led to dry air conditions over the northwest portion of the ice shelf. At AWS2, the AWS algorithm identified near-surface conditions indicative of föhn winds, however there was no associated identification in AMPS, and therefore no periods were defined as föhn conditions at this location. The AMPS algorithm identifies isentropic drawdown over the AP, and requires cross-barrier flow at the height of the AP. Therefore, the AMPS algorithm is incapable of identifying föhn development over Jason Peninsula.

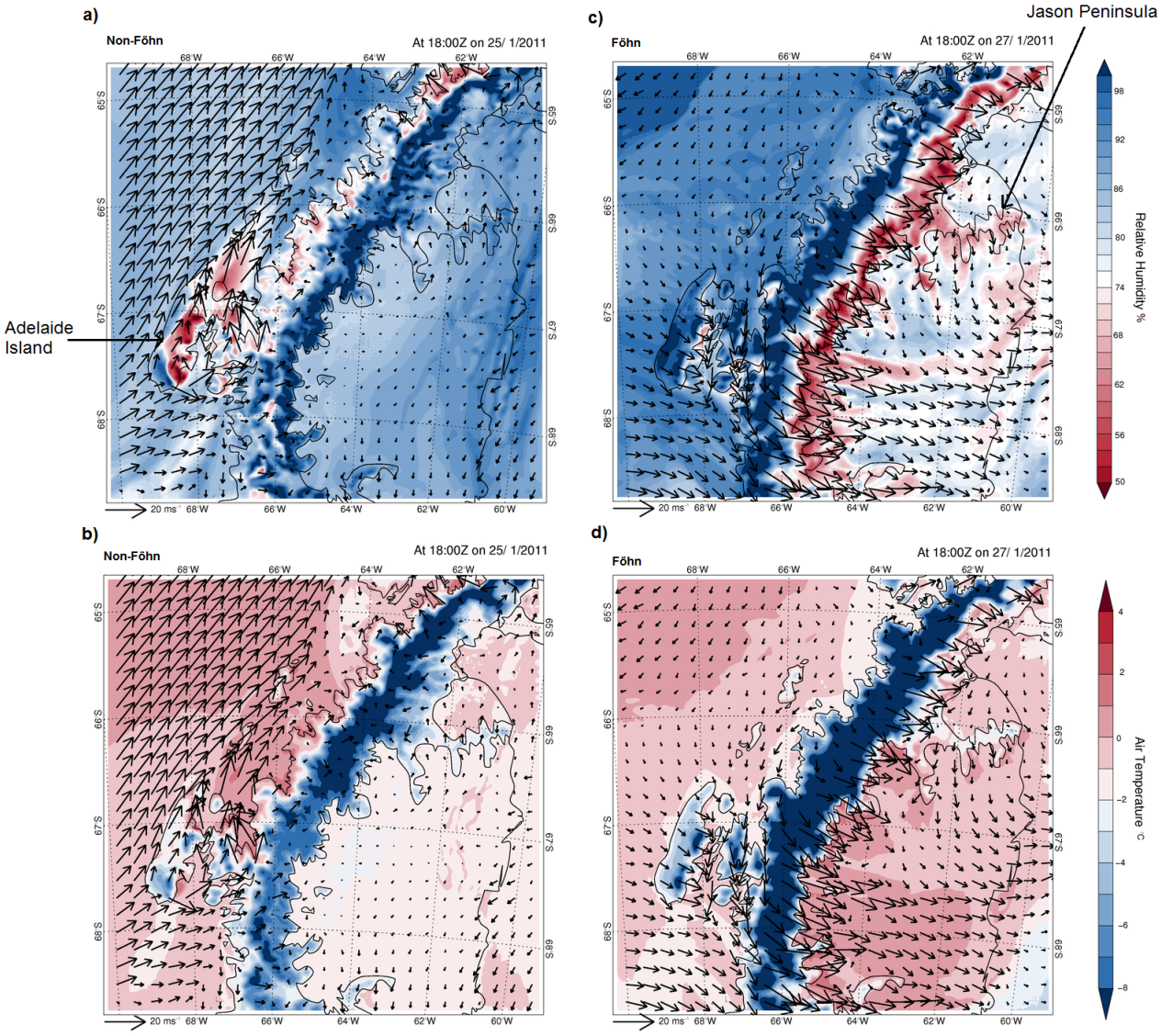

Figure 6.5: The simulated near-surface relative humidity (a and c) and air temperature (b and d) fields during a non-föhn period at 18UTC on the 25th of January 2011 (a and b) and a föhn period at 18UTC on the 27th of January 2011 (c and d).

The air temperature signal during the föhn period was difficult to isolate from the average conditions during this time of the year. As is presented in Figure 6.5, during both the föhn and non-föhn periods, the near-surface air temperature was above -2°C over all of the ice shelf. At 18UTC each day, the maximum air temperatures were observed and simulated due to the diurnal maximum in incoming shortwave radiation. Due to this, the increase in air temperature associated with the föhn winds was not discernible from the diurnal temperature cycle. The masking of the air temperature rise was taken into account in the development of the AWS algorithm. The air temperature criterion was secondary to the relative humidity criteria so that the seasonal changes in air temperature did not influence the outcome of the AWS algorithm.

The wind speed was overestimated by WRF just prior to, and during the föhn event at AWS6 but not during the same period at AWS2 (Figure 6.4). From assessing the simulated near-surface wind field, it is clear that this positive bias in wind speed was present over the southern section of the ice shelf. It was likely influenced by the stronger up-barrier flow south of 67.5°S.

During the non-föhn period on the 25th of January, there was a very localised föhn effect simulated over Adelaide Island, to the east of the main AP ridge (Figure 6.5). The predominant near-surface wind direction up-wind of the AP was northeasterly. To the north and east of Adelaide Island, the air was considerably drier than the southwest of the island, and drier than on the ice shelf. This near-surface signal was not as well defined in the AMPS simulation (not shown).

6.3.5 Summer Discussion

The summer case study was initially used as a test study for assessing a number of the WRF setup options. However, as a number of interesting features were identified during this process, it has been included as a separate case study. A number of the findings were more clearly defined in the other case studies, and therefore they are discussed in more detail in other sections.

There was a long period of non-föhn conditions in the first half of the case study, which allowed the non-föhn conditions during summer to be assessed. Despite the absence of föhn air over the ice shelf, the near-surface air temperatures were relatively warm, and the daily maximum temperature was frequently around 0°C. In a number of other studies, the föhn identification algorithms rely on changes in the air temperature as a major criterion for detecting near-surface föhn conditions (Speirs *et al.*, 2010, 2013; Steinhoff *et al.*, 2014). However, if that approach was applied over the LCIS, many more föhn conditions would have been (incorrectly) classified as such. Abrupt changes in the air temperature occurred daily during the summer case study due to the diurnal shortwave incoming radiation cycle. With increased air temperatures, the air mass was able to hold more water vapour, and the relative humidity subsequently decreased at 18UTC each day. As displayed in Figure 6.3, the AWS algorithm did identify a number of föhn conditions in the first half of the case study, often at 18UTC due to this diurnal relative humidity and air temperature cycle. However, as the AMPS algorithm was not influenced by the diurnal cycle, no föhn conditions were detected. The results from this case study provide evidence for the use of relative humidity as the main criterion within the AWS algorithm and for combining the AWS and AMPS algorithms to reduce the influence of the diurnal and seasonal temperature cycle on the results.

Two localised föhn-effect regions were identified from this case study. Föhn conditions were simulated on the leeside of Adelaide Island and Jason Peninsula, which were not evident in observations or in the lower-resolution AMPS output. The föhn effect generated over Jason Peninsula influenced the near-surface conditions at AWS2. The AWS algorithm detected these near-surface conditions, however the AMPS algorithm is incapable of detecting föhn events generated over Jason Peninsula, and therefore this period was classified as non-föhn at AWS2. To fully investigate the overall impact of föhn winds on the LCIS, it may be necessary to include the localised effects. For future development of this research, it may be necessary to include the isentropic drawdown and föhn effect over Jason Peninsula in the AMPS and AWS algorithms.

The diurnal cycle in air temperature was enhanced in the WRF simulation. The daily maximum air temperatures were simulated with higher accuracy than the daily

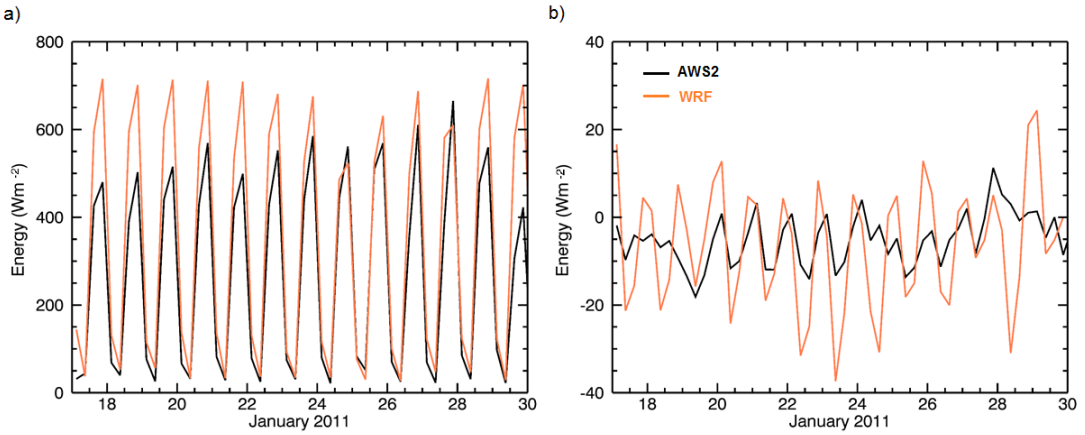

Figure 6.6: a) The incoming shortwave radiation and b) sensible heat flux observed at AWS2 (black) and simulated by WRF at the AWS2 location (orange) from the 17th to 30th of January 2011 (the Summer case study period).

minimum temperatures in both WRF and AMPS. The magnitude of change between the daily maximum and minimum values was overestimated. The near-surface air temperature in models is influenced by the surface temperature, the stability of the boundary layer, and the surface energy balance. Figure 6.6 presents the incoming shortwave radiation and sensible heat flux simulated by WRF and observationally-derived at AWS2. The shortwave incoming radiation was overestimated during the day, especially at 18UTC. This contributes to reducing the mean bias between the observed and simulated air temperatures during the day. However, even with the positive incoming shortwave radiation bias, the surface and air temperatures were too cold during the night. WRF overestimates the negative (outgoing) sensible heat flux during the night (Figure 6.6), most likely due to the strong static stability of the surface layer. The incorrect simulation of the surface fluxes leads to unrealistic cooling of the surface, and therefore the overlying air. This is a common issue in regional modelling during strong nocturnal stability (Sterk *et al.*, 2015). This characteristic was also evident in the Spring case study, and is discussed in greater detail in Section 6.4.5.

The simulation of near-surface characteristics was relatively poor during the summer case study. The mean bias between the simulation and the observations was greatest

for the air temperature. Some of the features simulated by WRF during this case study were also present during some others. Issues that were consistent throughout all four case studies are discussed in greater detail in Section 6.7.

6.4 Spring Case Study

The spring case study spans from the 1st to 15th October 2011. Removing the first 48 hours for spin-up, the analysis periods spans the 3rd to 15th October 2011. From the 6th to 9th October, numerous föhn events were identified at multiple locations. For a period to be classified as a föhn condition, it must have been identified as such by both the AWS and AMPS algorithms (Chapter 3 for more information).

Initially, this case study was selected due to its interesting spatial pattern. North of ∼67°S, föhn events were identified on four consecutive days, whereas south of this latitude, föhn events were only identified on one day. It has been hypothesised that locations further north on the AP experience more frequent föhn conditions (Chapter 4). A previous study by Cape *et al.* (2015) found föhn conditions over Larsen A and B were more frequent than those identified over Larsen C by the current study. However, on Larsen C alone, there was no latitudinal pattern in the frequency of föhn conditions. There was a north-south gradient found in the strength of the föhn signal however. The first aim of running this case study was to investigate the latitudinal gradient in föhn strength further, and assess what features influence the spatial pattern.

The second aim of simulating this case study was to gain insight into the disagreement between the AWS and AMPS algorithms at AWS2. At this location, föhn conditions were detected by the AWS algorithm, as the near-surface conditions met the requirements of the algorithm, however there was no associated identification by the AMPS algorithm (see Chapter 3). Due to this disagreement, this time-point was categorised as non-föhn. To address this issue, the AMPS algorithm will be applied to the WRF output to ascertain whether the AMPS horizontal and vertical resolution was too coarse to identify the upper-air signature of the föhn winds at all times, and

therefore was the cause of the disagreement between algorithms.

6.4.1 Synoptic Situation

The synoptic situation prior to, during and after the föhn events are inferred from the ERA-Interim re-analysis dataset. The timing of the onset and cessation of the föhn events may be inferred from assessing the synoptic situation during the case study. It will also provide an insight into the larger-scale situation.

Multiple f'ohn events were identified within the period from the 6th to 9th October. The week prior to the föhn events was characterised by a low pressure system to the east of the AP centred at approximately 67.5°S, 45°W (Figure 6.7a). There was a high-pressure region to the west of the AP, extending south from South America. The two opposing systems either side of the AP prompted southerly airflow over Larsen C (Figure 6.7b). The low pressure system weakened over the week prior to the earliest föhn observation. By the 5th October the low pressure centre had separated into multiple, weaker centres and travelled further east, away from the AP. The high pressure to the west became stronger throughout the week, reaching a maximum daily pressure of 1024hPa on the 4th October. The southerly airflow continued until the 6th October due to the persistence of the high pressure system.

The earliest föhn onset was at 00UTC on October 6th at Cole Peninsula and AWS6. Further, intermittent föhn events were identified over the LCIS from the 6th to 9th of October. Throughout this period, the high pressure system moved northwards towards the Falkland islands, and an expansive low pressure zone moved towards the west of the AP. The low pressure system was wide spread around the whole West Antarctic region, with two centres (Figure 6.7b). To the east of the AP, air flow was dominated by a low pressure system, which stretched from the AP to the Kong Haakon VII sea, near the East Antarctic coast. This created westerly airflow over the northern AP, and northwesterly flow over the LCIS (Figure 6.7c). This airflow direction was perfect for the development of föhn winds over Scar Inlet and LCIS. For a 12-hour period from the 06UTC to 18UTC on October 8th, the wind direction briefly turned northerly over the LCIS, and some air was deflected by the AP. This likely lead to a break in

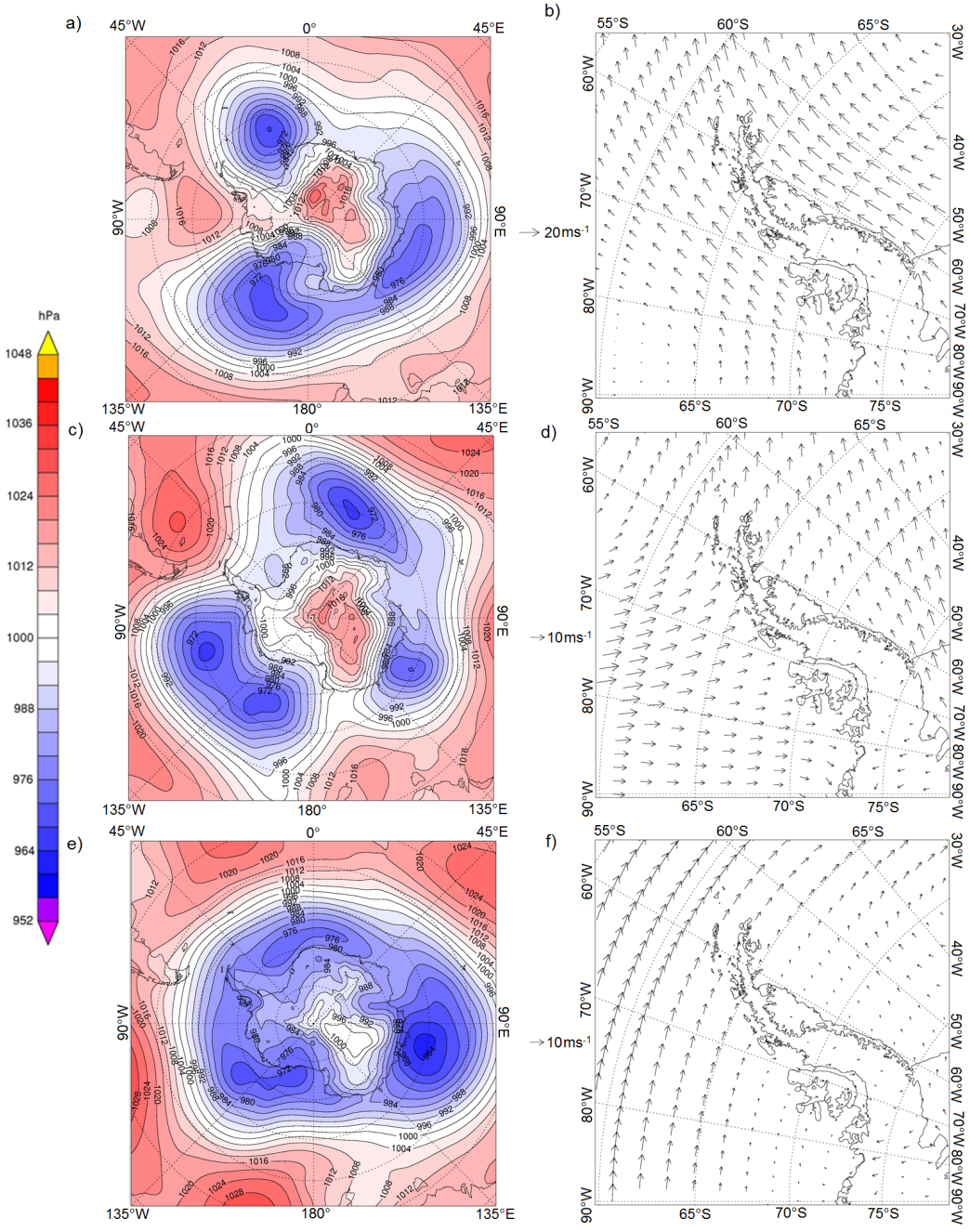

Figure 6.7: The mean sea level pressure over the Southern Ocean (MSLP) (left panels: a, c, e) and mean 850hPa wind vectors over the AP region (right panels: b, d, f) before, during and after the föhn events from ERA-Interim. a) and b) cover the period from 27th September to 5th October, the week prior to the föhn events. c) and d) are during the föhn days (6th to 9th October). e) and f) display the synoptic situation for five days after the föhn events (10th to 15th October).

föhn conditions in some locations, before a second föhn event began on the 9th October.

From 10th to 15th October, after the föhn events, very weak westerly winds characterised the flow over the LCIS. Three expansive, widespread low pressure centres surrounded the continent (Figure 6.7e). Further north, high pressure dominated, leading to strong, westerly winds further north of the AP, but relatively weak flow across the AP. Low-level winds were deflected south by the AP on the west side of the mountains.

6.4.2 Identified Föhn Events

At Cole Peninsula and AWS1, the 6th, 7th, 8th and 9th of October were föhn days (Figure 6.8). At AWS3 and AWS6, only the 6th of October was a föhn day. During this period, föhn days were more frequently identified to the north of the ice shelf (Cole Peninsula and AWS1) than further south (AWS3 and AWS6). At AWS2 and AWS5, föhn conditions were not present, as they were only detected by the AWS algorithm, and not by the AMPS algorithm. When including the AWS-only detected föhn conditions, four föhn days were observed at AWS2 and only one was observed at AWS6. This provides more evidence for a north-south split in the number of föhn days identified on the LCIS.

Although there were four föhn days identified at the northern locations, the number of föhn events varied. At AWS1, there were four föhn events, on four separate days. At Cole Peninsula there were two föhn events which stretched over four föhn days, as shown by Figure 6.8.

6.4.3 Model Validation

A pseudo-timeseries from the AMPS (5km) and WRF (1.5km) output has been created for each location during the case study period. This provides a way of validating the near-surface model output against the observations at the same location. Validation is used to assess the success of the models at representing reality, assuming that the observations are a true representation of reality themselves. Validation results will only

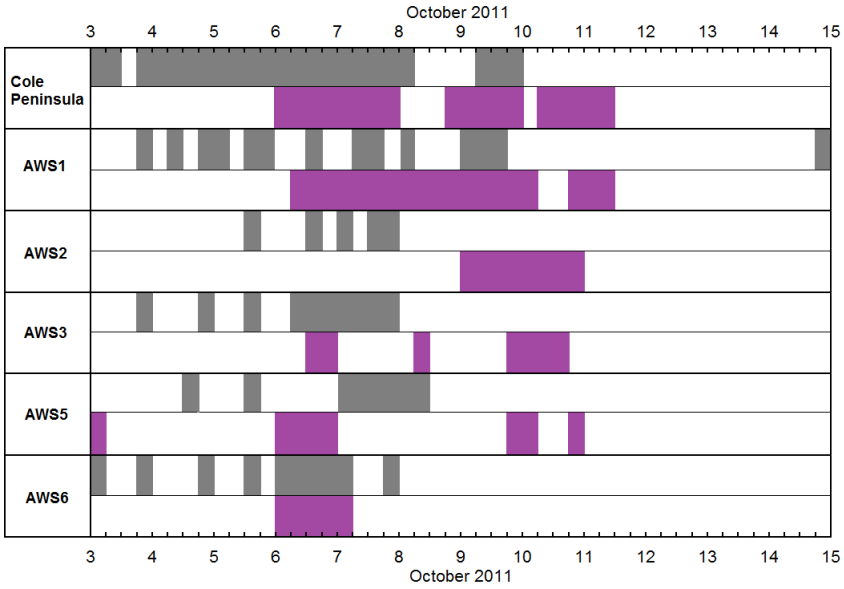

Figure 6.8: The timing of föhn events at each location during the spring case study. The grey bars are times when föhn conditions were identified by the AWS algorithm. Purple bars are times when föhn conditions were identified by the AMPS algorithm. When they overlap, and föhn conditions were identified by both algorithms, and these periods were analysed in Chapter 4.

Table 6.4: The mean bias and Root Mean Square Error (RMSE) between the two model runs and the observations for each near-surface variable assessed at AWS1 during the case study.

Variable	AMPS-AWS Mean Bias	AMPS-AWS RMSE	WRF-AWS Mean Bias	WRF-AWS RMSE
Relative Humidity (%)	6.4	14.0	0.3	12.7
Air Temperature (°C)	2.5	4.1	3.1	4.6
Wind Speed (ms^{-1})	2.3	3.9	1.0	3.2

be presented for two locations as the results are similar at all other locations.

Validation of both the WRF and AMPS runs at AWS1 is presented first. The near-surface air temperature was well simulated by both the AMPS and WRF runs at AWS1 (Figure 6.9). The mean bias and Root Mean Square Error (RMSE) were slightly larger in the WRF run (Table 6.4). The general increase in air temperature from the 6th to 8th of October was well resolved by the model runs. Similarly the sharp drop in air temperature on the 10th of October was also simulated well. The largest discrepancy between the observations and the models for air temperature was the exaggerated diurnal cycle simulated by both WRF and AMPS.

The average daily difference between the maximum and minimum temperature values in WRF was 6.8K, whereas in observations the difference was only 2.8K. The exaggerated diurnal cycle is clearly visible in Figure 6.9. The daily maximum temperature values (six-hourly averaged) were on average 4.1K higher in WRF than in observations. During the föhn events the diurnal signal was dampened. This lead to greater agreement between the WRF run and the observations during the 7th to 10th of October.

The near-surface relative humidity at AWS1 was better simulated (lower mean bias and RMSE) by the WRF run than by the AMPS run. AMPS overestimated the relative humidity during the case study (Table 6.4). The relative humidity decrease on the 6th October was relatively well resolved by both models, although a little better by WRF (Figure 6.9). There was a humidity decrease of 53% over 18 hours observed by AWS1.

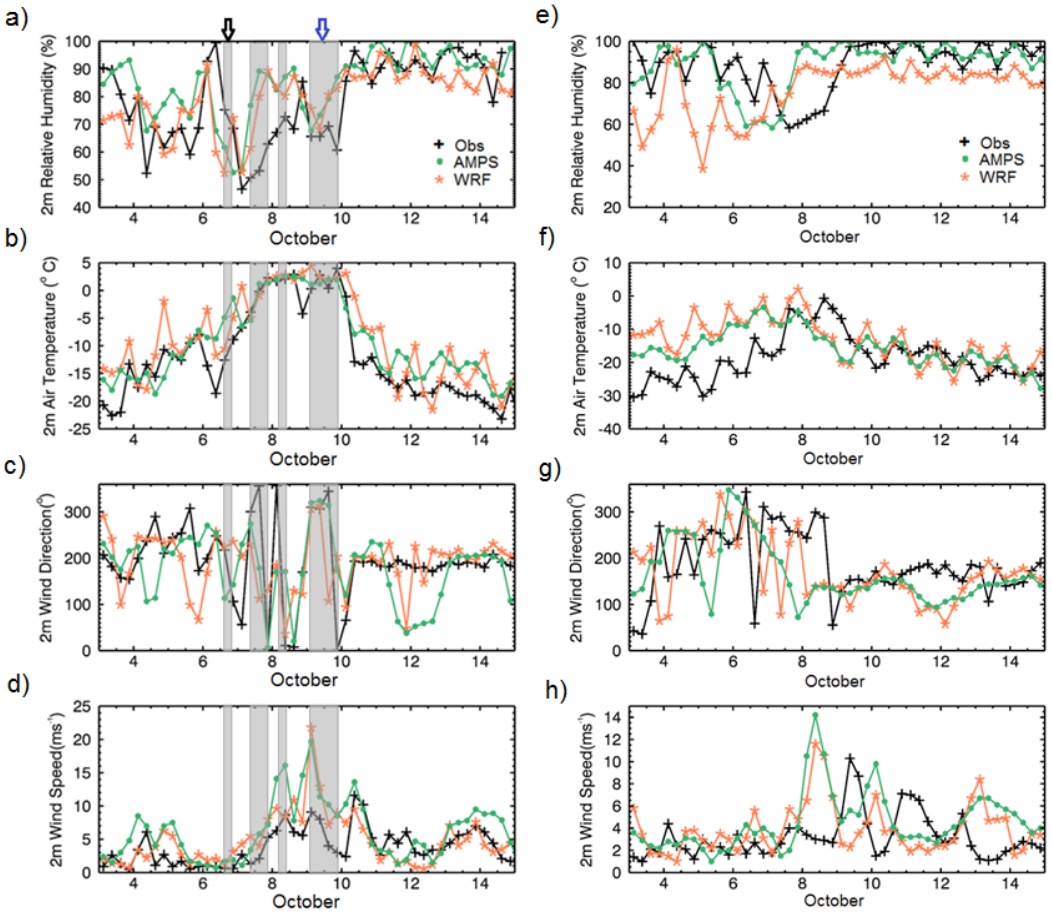

Figure 6.9: Timeseries of observational data from AWS1 (a-d) and AWS5 (e-h) during the Spring case study (3rd to 15th of October 2011). The 2m relative humidity (a,e), 2m air temperature (b,f), 2m wind speed (c,g) and wind direction (d,h). AWS observational data are black crosses, data from the 5km AMPS output are green dots and 1.5km WRF data are coral asterisks. Periods defined as föhn events are highlighted by grey boxes.

AMPS shows a decrease of 36.5%, whilst the WRF run estimated a 44.8% decrease. The time of the decrease was simulated six hours too early by both model runs. On a number of occasions throughout the study there was a lag between what was observed and what was simulated. For example, the observed increase in relative humidity at the end of the fourth föhn event (10th of October) was simulated 24-hours too early by both datasets (Figure 6.9). The timing issue was not systematic, as the offsets between the observations and the model outputs were varied in sign and duration.

The wind direction at AWS1 during the four föhn days rotated between northwesterly and northeasterly, and this was simulated with varying degrees of success. The two model runs successfully simulated the wind direction during the fourth föhn event, but were less successful at simulating the changes in wind direction during the first three events (Figure 6.9c). The persistent southwesterly winds from the 10th-15th of October were simulated better by WRF than AMPS.

The wind speed was overestimated by both WRF and AMPS at AWS1, especially between the 8th and 10th October (Figure 6.9d). The mean bias and RMSE were smaller in the 1.5km WRF run than in AMPS. The timing of the peaks in wind speed was well captured by both AMPS and WRF. The magnitude of the two largest peaks during the third and fourth föhn events was considerably overestimated by both. The observed wind speed at 00UTC on October 9th was 9.1ms^{-1}. AMPS simulated a wind speed of 19.7ms^{-1} and WRF simulated a value of 21.8ms^{-1}.

Overall, the WRF run performed better than AMPS when simulating relative humidity, wind direction and wind speed, but it did slightly worse in the simulation of the air temperature at AWS1. During föhn events, the temperature and wind direction estimations improved in both models, whereas for the wind speed, the agreement with observations became worse. The magnitude of the changes in relative humidity were well resolved by WRF, however there was an offset between the timing of the changes in the observations and the models, which lead to a poorer agreement during föhn conditions.

Table 6.5: The mean bias and Root Mean Square Error (RMSE) between the two model runs and the observations for each near-surface variable assessed at AWS5 during the Spring case study.

Variable	AMPS-AWS Mean Bias	AMPS-AWS RMSE	WRF-AWS Mean Bias	WRF-AWS RMSE
Relative Humidity (%)	0.9	13.2	-11.5	20.4
Air Temperature (°C)	3.1	3.5	5.3	10.0
Wind Speed (ms^{-1})	1.4	3.5	0.7	3.3

Contrary to at AWS1, the models performed relatively badly at representing the near-surface conditions at AWS5 (Figure 6.9), AWS2, AWS3 and AWS6. Relative humidity was underestimated and the air temperature was overestimated prior to the 8th October. From the 9th to 15th of October, the representation of these variables improved.

Validation of the simulations at AWS5 will be presented now. No föhn event was identified at AWS5, although there was a near-surface signal detected by the AWS algorithm. Between the 3rd and 8th of October, WRF and AMPS both underestimated the relative humidity and overestimated the air temperature. WRF had a warm, dry bias which was more exaggerated than that in AMPS (Figure 6.9). It is likely that the amount of water vapour simulated by WRF was accurate, but the higher simulated temperatures led to a low relative humidity simulation, as warmer air can 'hold' more water vapour. After approximately the 9th of October, the biases between the observations and the model output decreased. The WRF run continued to underestimate the relative humidity throughout the case study, but the dry bias was considerably smaller than in the beginning. Near-surface föhn conditions were simulated by WRF on the 5th October. A relative humidity of 38.6% was simulated by WRF which was not simulated by AMPS or observed at AWS5. This contributed to the large negative mean bias of -11.5% in the WRF model (Table 6.5).

The relative humidity decrease observed by AWS5 on the 7th of October was captured by the two models, however it was simulated too early. The amplitude of the decrease was well resolved by AMPS, however the dry bias in WRF made it harder to

isolate the relative humidity change. AMPS performed well at representing the relative humidity at this location, as shown by the smaller mean bias and RMSE than that of the WRF run.

The gradual air temperature increase over the first five days was well resolved by the models at AWS5, however the amplitude of the increase was underestimated due to the warm bias in both WRF and AMPS. The observed diurnal temperature cycle was simulated with greater accuracy for the AWS5 location than at AWS1. The average difference between the daily maximum and minimum temperature values simulated by WRF was 8.3K; in observations it was 5.2K. After the 9th of October, there was a better agreement between the simulations and the observations, as the magnitude of the warm bias decreased.

The observed wind direction at the start of the case study was westerly to north-westerly. From the 9th of October onwards, this shifted to a southerly wind direction, which the models captured relatively well. Similar to the temperature and humidity fields, the simulations became more accurate after the 9th October. Similar to results at AWS1, the wind speed was overestimated by the models during the middle section of the case study. Both models simulated a peak in wind speed on the 8th of October which was not observed (Figure 6.9). This was possibly an early simulation of the peak observed on the 9th of October. The agreement between the model output and the observations was better at the start of the case study period, which is opposite to the other three variables. However, during this period, the wind speeds were calmer, and no föhn conditions were present. The positive wind speed bias in both AMPS and WRF was present at AWS1 and AWS5, however it was not simulated at any other location.

There appears to be a consistent timing error in the WRF and AMPS simulations compared to observations at AWS5. Both models simulate the changes in relative humidity and air temperature associated with föhn onset and cessation, however the changes occur approximately 24 hours too early. This increased the mean bias between the models and the observations.

6.4.4 Spring Simulation Results

The first aim of this case study was to investigate the north-south split in the number of föhn days during the spring case study. More föhn days were identified at AWS1 and Cole Peninsula (and at AWS2 in observations alone) than were identified further south on the ice shelf. Spatially assessing the near-surface conditions from the WRF model reveals why this split was present. The majority of the results presented here focus on the WRF simulations. When either the observations or the AMPS simulations are being compared to WRF, it will explicitly say which data are being presented.

The first föhn event discussed here is marked with a black arrow on Figure 6.9. The föhn event was identified at Cole Peninsula, AWS1, AWS3 and AWS6. The AWS algorithm also identified near-surface föhn characteristics at AWS2. At the beginning of the first föhn event at AWS1 (12UTC 6th of October), dry and warm conditions were simulated across much of the ice shelf, suggesting a widespread föhn event (Figure 6.10). The warmest (above-freezing) conditions were limited to close to the AP and surrounding Jason Peninsula and Kenyon Peninsula. Lower amplitude, localised föhn effects generated over the two smaller Peninsulas bounding the north and south of the ice shelf may have caused additional föhn warming and drying, and increased the spatial distribution of the föhn air. The wind direction over the ice shelf was predominantly westerly. The simulated spatial distribution of the föhn air at the start of this föhn event agrees with the observations.

The duration of the first föhn event varied by location. At AWS1 it lasted just six hours, whereas at Cole Peninsula it lasted 54 hours. The föhn air retreated relatively quickly over much of the ice shelf, but it remained close to the Peninsula, leading to a prolonged föhn effect at Cole Peninsula. WRF simulated a stronger föhn event (lower relative humidity, warmer air temperatures) over the ice shelf than was observed. The large mean bias in relative humidity at AWS5 (Table 6.5) was largely due to this widespread simulated föhn effect.

The next föhn event discussed is the fourth event, marked by a blue arrow on Figure 6.9. A very different near-surface pattern marked the onset of the föhn event at AWS1. This föhn event was identified at 00UTC on the 9th of October at AWS1 and

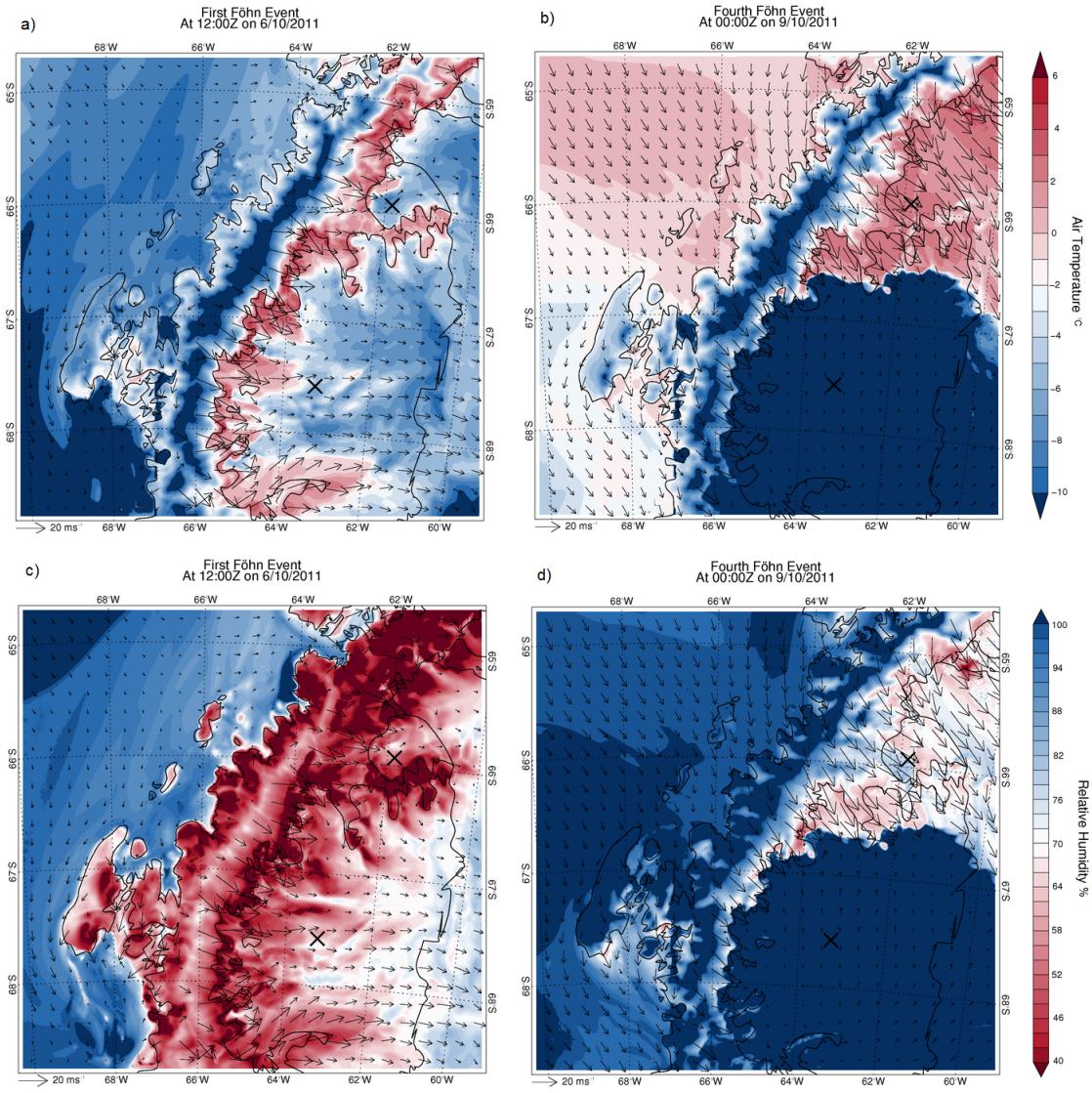

Figure 6.10: The air temperature (top panel) and relative humidity (bottom panel) output from WRF during the first and fourth föhn events identified at AWS1. a) and c) are the temperature and relative humidity (respectively) at 12UTC on October 6th 2011; the first föhn event. b) and d) are the temperature and relative humidity (respectively) at 00UTC on October 9th 2011, the fourth identified föhn event, as shown in Figure 6.9. The föhn air during the two events had considerably different spatial distributions.

six hours later at Cole Peninsula. There was no near-surface föhn signal identified further south. Very cold (< -14°C) and moist (∼ 90%) air was present over the ice shelf from approximately 67°S southwards (Figure 6.10). No föhn conditions were subsequently identified south of this location. On the very northern section of the LCIS and over Scar Inlet, the air temperature was significantly warmer (∼2°C) and drier (∼60%). The föhn event over Scar Inlet was generated by relatively strong (∼9ms^{-1} observed, 21ms^{-1} modelled by WRF), northwesterly winds. However, over the southern section of the LCIS, the winds were southerly, pushing cold, continental air northwards.

At 06UTC on the 9th of October, the southerly winds weakened, and turned southeasterly, which allowed more of the northwesterly föhn air to push into the cold, stable air, and disperse the föhn effect wider. An interesting spatial pattern in the föhn air developed between 12UTC and 18UTC on the 9th of October (Figure 6.11b). This spatial signature provides an explanation for the observed near-surface föhn conditions detected by the AWS algorithm at AWS2. The northwesterly wind over the northern AP and Scar Inlet pushed the föhn air over the AWS2 location. At the same time southeasterly flow over the south of the ice shelf pushed the cold continental air over the west side of the ice shelf. In the simulated air temperature field, the föhn air and continental air appear to 'curl' around each other, and AWS2 was located within the warm, föhn air. There were no strong cross-barrier winds at the AWS2 latitude which would have lead to the AMPS algorithm detecting the isentropic drawdown. Therefore there was a disagreement between the result of the AWS and AMPS algorithms.

This spatial pattern was not simulated by the AMPS model. AMPS successfully simulated the north-south division in air temperature over the LCIS. However, the southeast propagation of the föhn air and the 'wind curl' feature was not simulated (Figure 6.11a) by AMPS. Over the AWS2 location, AMPS simulated southeasterly winds, and air temperatures of approximately -6°C, whereas in observations at 10UTC on the 9th of October, the wind was from the north and the air temperature was -1.7°C.

Over the next six to twelve hours, the southeasterly wind strengthened and pushed colder air into the föhn air. Simultaneously the northwesterly wind which generated the föhn event, diminished, and easterly flow was present over Scar Inlet. By 06UTC

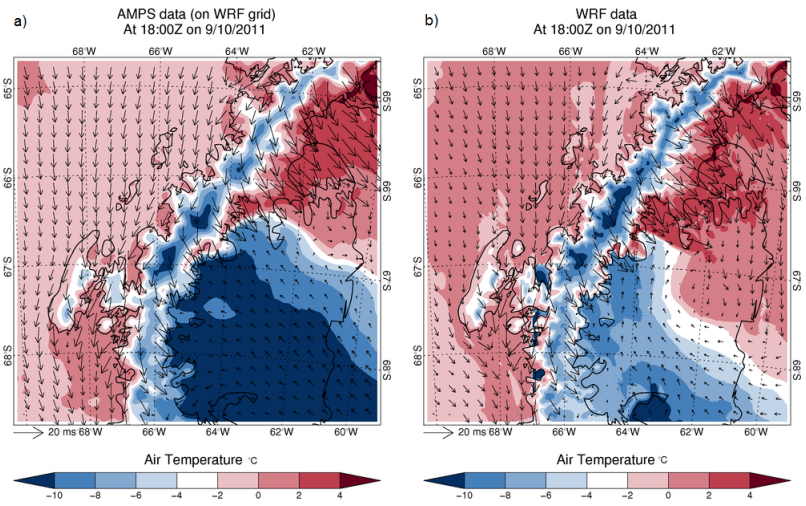

Figure 6.11: The 2m air temperature field at 18UTC on the 9th of October 2011 simulated by AMPS (a) and by WRF (b). AMPS was able to simulate the north-south split in föhn air distribution, however it did not capture the southeasterly spread of the föhn air which was observed at AWS2, and simulated by WRF.

10th October, the cold continental air had encompassed the whole ice shelf, including Scar Inlet, and the föhn ended. The timing of the föhn cessation was well represented by both WRF and AMPS.

The first föhn event identified at AWS1 (black arrow on Figure 6.9) was spatially vast, and was characterised by a strong föhn signal, especially in the relative humidity field. The widespread propagation was likely due to the westerly wind, leading to a fairly uniform föhn effect along the full length of the AP. The final föhn event identified at AWS1 (blue arrow) was only identified at locations in the north of the LCIS, and had a moderate relative humidity signal but higher air temperatures on the north of the ice shelf (compared to the first föhn event). The north-south divide in the föhn signal was controlled by the two opposing wind regimes controlling the interaction of the föhn air and the pre-existing cold stable air. The second discussed föhn event provided an insight into the localised, small-scale, near-surface patterns which influenced the disagreement between the detection algorithms.

The apparent absence of föhn events at AWS2 during the case study was due to this disagreement between algorithms. Periods were only categorised as föhn events when both algorithms detected föhn conditions. The AMPS algorithm did not detect föhn conditions, because, although isentropic drawdown was simulated by AMPS at the AWS2 location, the change in height of the isentrope from upwind of the AP to the lee-side was not large enough to meet the threshold for föhn detection. When applying the AMPS algorithm to the WRF output, the isentropic drawdown was present at AWS2, but the change in height of the potential temperature was still not large enough to be identified as föhn. Therefore, in this instance, increasing the horizontal and vertical resolution of the model did not alter the number of identified föhn events, or the spatial distribution of the föhn wind. The better representation of the cold-air feature in the higher-resolution run is attributed to differing initialisation between the two models, rather than due to increased resolution, as the feature is large enough to be resolved in the 5km run. This may also explain the differences in the spatial distribution of the cold air in Figure 6.11.

6.4.5 Spring Discussion

The spring case study was chosen to simulate two main features. The first aim was to investigate the north-south divide in the number of föhn events over the LCIS. The second was to assess why there was a disagreement between the AWS and AMPS algorithms at AWS2. Whilst investigating these aims, other interesting spatial features came to light, which will be discussed below.

In the Cape *et al.* (2015) study, the number of föhn conditions further north of the AP (over the Larsen B region) was found to be higher than those over the LCIS. Weaker correlations between surface melting and föhn frequency were identified over Larsen C compared to those identified over Larsen A and B (further north) (Cape *et al.*, 2015), leading to the conclusion that föhn events may be less frequent over Larsen C. The föhn hypothesis also suggests that the frequency of föhn events may be greater further north of the LCIS, due to the perpendicular interaction of the predominately westerly winds and the AP. Figure 6.12 presents the average 850hPa wind vectors from January 2009 to December 2012. North of Jason Peninsula, the westerly winds interact with the AP

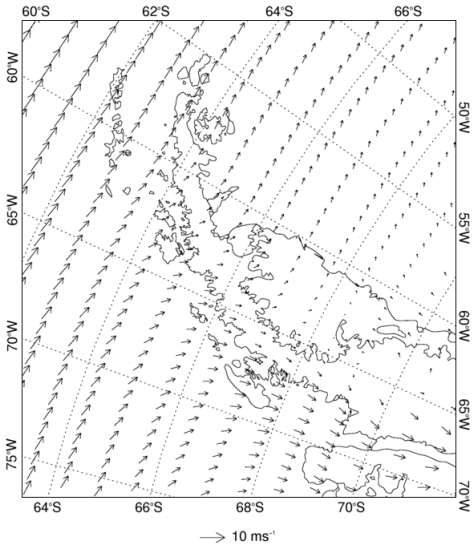

Figure 6.12: The 2009-2012 average 850hPa wind vectors for the LCIS and northern AP region. North of LCIS, the wind interacts almost perpendicularly with the AP, whereas further south the wind is deflected south, possibly leading to fewer föhn events.

more directly. Further south however, the average wind direction was northerly, and there was less flow over the mountains. This is likely from the formation of a barrier jet. Barrier jets typically occur when statically stable, cold, low-level air is blocked, and the air is deflected to the right (under westerly flow) (Parish, 1983). Blocked flow occurs when the Froude number is small ($Fr < 1$). This may explain the larger number of föhn events and stronger föhn effect identified further north of the LCIS, and the occurrence of melt ponds over the northwest section of the LCIS (Luckman *et al.*, 2014).

Simulating just one case study can not provide evidence for a north-south gradient in föhn frequency or strength, however it can provide an insight into the potential drivers for a north-south gradient should there be one. The föhn event at AWS1 (10th October) displayed a north-south gradient in föhn air propagation. Föhn conditions were identified at AWS1 and Cole Peninsula, and there was a near-surface föhn signal detected by the AWS algorithm at AWS2. This was a sharp north-south split, rather than a gradual change in relative humidity and temperature.

The main control over this north-south split was the wind direction. Over the north of the ice shelf (Scar Inlet and north of ∼67°S) the wind direction was northwesterly, generating föhn winds. Over the majority of the LCIS (south of ∼67°S) the wind direction was southerly, pushing cold continental air onto the ice shelf. There was a very sharp near-surface temperature gradient between the föhn air and the continental air. The air temperature over the majority of Scar Inlet and the northern LCIS was approximately 2-4°C, whilst over the rest of the ice shelf it was ∼-15°C.

Simulating this föhn event in WRF revealed the small-scale spatial distribution of the föhn air which was not captured by the 5km AMPS simulation. The AWS algorithm detected near-surface föhn conditions at AWS2 at 18UTC 9th October, however there was no corresponding identification in the AMPS output. This was due to the 'curl' of the föhn air as it pushed into the continental air on the northeast side of the ice shelf (Figure 6.11). However, when taking a cross section through the AP and LCIS at the latitude of AWS2, the isentropic drawdown was too shallow to be detected by the AMPS algorithm, due to the lack of northwesterly flow over the AP at this latitude.

This finding brings into question whether the AMPS algorithm is appropriate for identifying föhn conditions over an area as large as the LCIS. When applying the isentropic drawdown algorithm to the WRF output, föhn conditions were still not identified at the AWS2 location. Therefore, the lack of föhn detection within AMPS was not due to the (relatively) coarse vertical and horizontal resolution of the model, but due to the near-surface spatial distribution of the föhn air.

In a number of studies, a method similar to the AWS algorithm was used to identify föhn conditions in WRF by using the simulated near-surface characteristics (e.g Steinhoff *et al.* 2013, 2014). However, this relies on the good representation of near-surface characteristics in the model, and was found to simulate 58% more föhn events than were observed over 15 summer seasons by (Steinhoff *et al.*, 2014). As can be seen from Figure 6.9 WRF had a near-surface, warm and dry bias, which would lead to identification of a greater number of (erroneous) föhn events if the AWS algorithm was applied. Therefore, as the current AMPS algorithm used to identify föhn conditions agreed with the AWS algorithm 80% of the time (see Chapter 3), and the spatial distribution of

the föhn air during this case study may be unique to the specific föhn event, this is still the preferred method.

The first föhn event identified at AWS1 (12UTC on October 6th) had a remarkably different near-surface spatial pattern than the fourth föhn event identified (00UTC on October 9th). The föhn event on the 6th October was identified at AWS1, Cole Peninsula, AWS3 and AWS6, and, in AWS observations only, at AWS2. This föhn event had a widespread influence over the near-surface conditions, and displayed an eastward propagation of the föhn air.

Closer to the AP, the föhn signal was strongest, and this diminished with distance from the AP. This pattern mimics the west-east gradient in föhn strength that was identified by analysing all föhn conditions from 2009-2012 (see Chapter 4). As can be seen from Figure 6.10, this was not a simple linear decrease in föhn strength across the LCIS though, due to the complex topography of the AP.

Surrounding the smaller topographic features such as Jason Peninsula and Kenyon Peninsula, locally-enhanced föhn conditions were simulated by WRF. This extended the strong föhn signal further east than in regions without these elongated peninsulas. The localised, enhanced föhn effect at the foot of these smaller peninsulas could have implications for the surface energy balance of the ice shelf. Melt ponds have been observed in satellite images on the northwest part of LCIS (Luckman *et al.*, 2014). The enhanced föhn effect surrounding Jason Peninsula could have contributed to the surface melting and formation of melt ponds in this area. Therefore, the estimation of surface melting based on coarse-resolution regional modelling or sparse observations may be underestimating the surface melt induced by föhn winds. High-resolution modelling is crucial for understanding this sort of small-scale spatial information.

A trait that was present in the WRF simulations, but was not replicated to the same extent by AMPS, was an enhanced diurnal air temperature cycle. A diurnal temperature cycle was observed at AWS1, with an average difference of 2.8K between the daily maximum and minimum (six-hourly averaged) temperatures. In WRF, this average difference was 6.8K. The largest bias between observations and the WRF output was

during the nighttime (minimum daily temperatures) when the mean bias (WRF-AWS) was 8.2K. On one occasion, the nighttime bias was 18.8K at AWS5. However, the daytime bias was also considerable, with a mean bias of 7.5K at AWS5.

An enhanced diurnal air temperature cycle in Polar WRF has been previously noted in numerous publications. Over the West Antarctic, Deb *et al.* (2016) found an exaggerated diurnal cycle with a bias of up to 10K during January (summer) simulations. It was found that the exaggeration in the model was likely due to the poor simulation of clouds, leading to a problematic representation of the radiative fluxes. The pronounced cold-nocturnal and warm-daytime biases presented by Deb *et al.* (2016) were consistent with a negative bias in incoming longwave radiation and a positive bias in incoming solar radiation respectively. This may not be the case in the present case study, as both the modelled daytime and nighttime values were considerably warmer than the observations at AWS5 for the first six days of the case study.

In Wyszogrodzki *et al.* (2013) it was found that an enhanced diurnal cycle was present in the WRF model over the United States, and biases between observations and WRF were greatest near mountainous terrain. A number of possible explanations for this overestimation were suggested, including an inaccurate simulation of clouds over mountainous regions and uncertainty in the surface-snow process parameterisation (Wyszogrodzki *et al.*, 2013). Over the Arctic, WRF simulated an exaggerated diurnal near-surface temperature cycle (Wilson *et al.*, 2011). The largest errors were during times and at locations with the highest and lowest solar angles. During this case study, the approximate solar zenith angle was 79° (taken from the AWS2 surface energy balance model, see Chapter 5). (Wilson *et al.*, 2011) attributed the exaggerated diurnal cycle to the misrepresentation of stratus clouds, and the interaction with the incident solar radiation during the daytime, especially under the low solar zenith angle (Wilson *et al.*, 2011). Figure 6.6 is evidence of the overestimated incoming shortwave radiation during the summer case study which contributes to the exaggerated diurnal cycle.

The representation of clouds in WRF is sensitive to the choices of boundary layer, radiation and microphysics schemes chosen. The same microphysics and radiation

schemes were used in AMPS and WRF. Therefore, the exaggerated diurnal cycle simulated by WRF, but not as enhanced in AMPS, cannot be attributed to using different schemes. Deb *et al.* (2016) found that using the Mellor-Yamada-Janjic (MYJ) boundary layer scheme instead of the Mellor-Yamada-Nakanishi-Niino (MYNN) scheme in the set-up of WRF improved the representation of the diurnal air temperature cycle. Both MYJ and MYNN are local closure schemes, whereby simulated turbulent fluxes of a conserved variable (moisture, heat and momentum) at any vertical level are calculated based on the gradient of the variables between the levels above and below (Milovac *et al.*, 2016). The MYJ scheme is the default scheme used in AMPS, and was used in the WRF runs also. Therefore, changing the boundary layer scheme would not have introduced this problem.

The difficulty in the representation of high-latitude clouds in regional models is a well-known, and ongoing issue in the atmospheric research field. The microphysical properties of clouds and their parameterisations in models are often based on observations at lower latitudes, and are therefore not necessarily representative of Antarctic clouds (Lachlan-Cope, 2010). Cloud measurements over the LCIS performed in February 2010 by Grosvenor *et al.* (2012) revealed that the observed clouds were mostly mixed-phased (water and ice crystals) with a low ice concentration, whereas AMPS (and therefore the WRF runs here, as the same default settings are used) simulated predominantly ice-phase clouds with little water content in the King *et al.* (2015) study during summer. Therefore, the properties of the clouds are not well represented in the WRF model, most likely due to the erroneous microphysics.

The differences between the WRF and AMPS output are highlighted within the diurnal cycle. A smaller diurnal temperature cycle in AMPS may be due to the higher average wind speeds, which allow more mixing of air masses, and reduced stability of the air overlying the ice shelf. At 1.5km resolution (WRF), smaller eddies and grid-scale fluxes can be resolved, which are parameterised in AMPS at 5km resolution. This may lead to an overestimated cooling of the ice surface under strongly stable conditions. As the AMPS model is used for operational forecasting, the model is re-initialised every 24 hours and updated with input data every six hours. The WRF runs here were initialised only at the start of the model run, and therefore you may expect the model and

observations to diverge as the run continues. This may have lead to further differences between the two models.

6.5 Autumn Case Study

This period was simulated due to the intermittent nature of the föhn conditions. Föhn conditions were observed at all but one location (AWS5, due to a lack of observational data during this period), but at different times. The AMPS algorithm detected a continuous, 108-hour föhn event at Cole Peninsula whereas the AWS algorithm detected multiple, shorter föhn events at this location during the same time period. This suggests that the föhn air was being interrupted, or halted by something at the surface, as there were intermittent, near-surface, föhn signals. The main aim of this case study was to investigate what was interrupting the föhn flow at the surface of Larsen C.

6.5.1 Synoptic Situation

The week prior to the first identification of föhn conditions (6th to 12th of May 2011) was characterised by relatively weak winds, and two low pressure zones were present either side of the AP (Figure 6.13). The west coast low pressure system generated weak, northerly flow over the AP and LCIS. The pressure system deepened and expanded towards the end of the week, to reach a minimum of 944hPa on the 12th May. The pressure centre moved eastwards towards the AP throughout the week.

Föhn events were identified from the 13th to 17th of May. During this time the low pressure system to the west of the AP moved eastwards, towards the AP. A high pressure system to the north of the AP influenced air flow over the north of the AP (Figure 6.13). The combination of the low pressure near the west coast, and the high pressure to the northeast of the AP, forced the wind to flow northwest over most of the ice shelf. Towards the south of the AP the wind was more northerly. Therefore, föhn conditions likely affected the northern section of the LCIS more than the south.

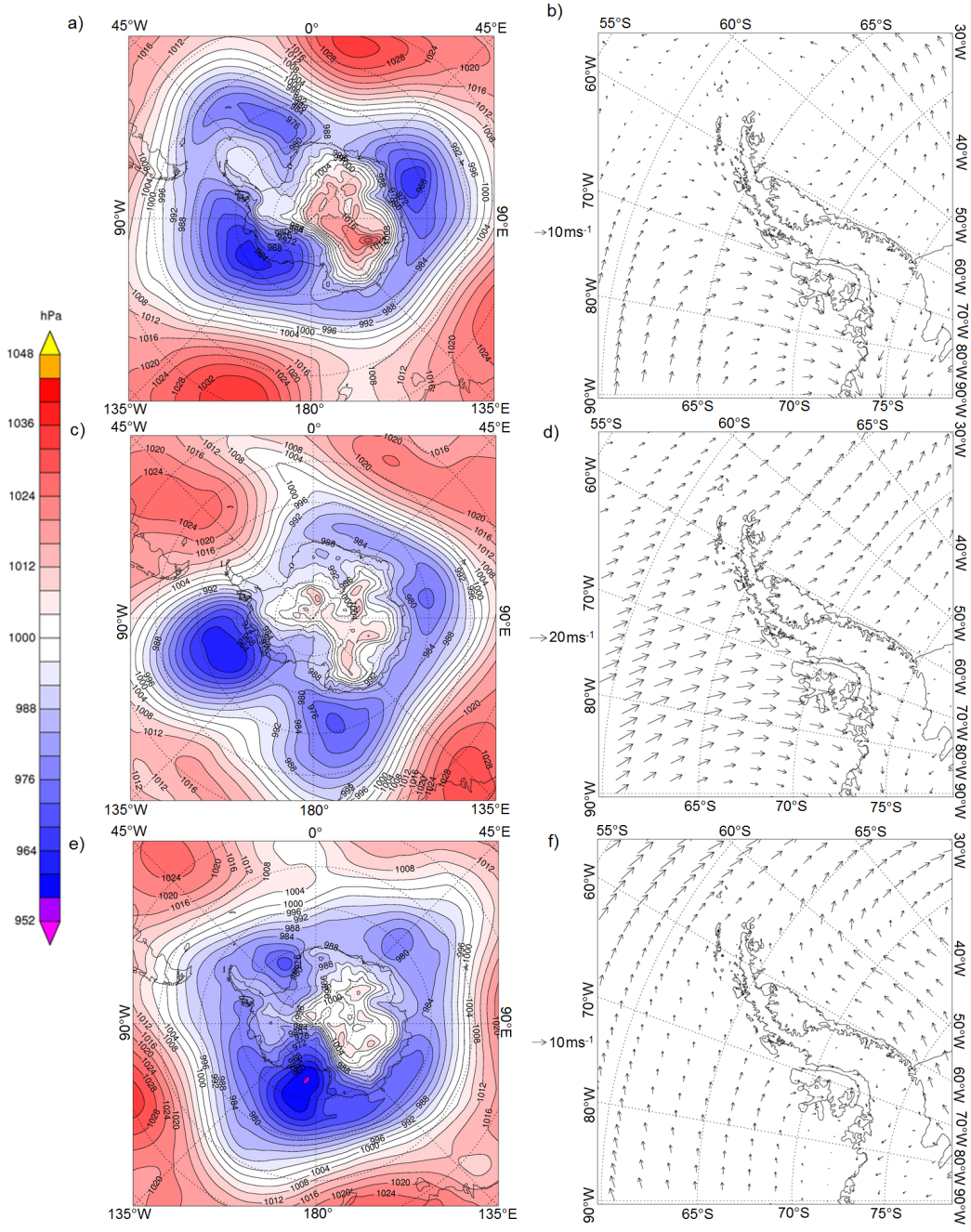

Figure 6.13: The mean sea level pressure (MSLP) for the Southern Ocean (left panels: a, c, e) and mean 850hPa wind vectors over the AP region (right panels: b, d, f) before, during and after the föhn events. a) and b) cover the period from 6th to 12th May, the week prior to the föhn events. c) and d) are during the föhn days (13th to 17th May). e) and f) display the synoptic situation for five days after the föhn events (18th to 22nd May).

Between May 13th and May 17th, the wind direction varied between north and northwesterly, which likely caused intermittent föhn conditions over the north LCIS. Some airflow over the mountains was observed on the northern section of the AP throughout this period.

From the 18th to 22nd May the low pressure centre to the west of the AP moved away from the AP. The shape of the pressure system became more elongated, still influencing the airflow over the AP. To the west, and along the spine of the mountains, the air flow turned towards the south (Figure 6.13). Over Larsen C, the airflow was much weaker and became southerly due to the increasing influence of a developing low pressure system to the east of the AP, marking the end of the föhn event. Compared to the surrounding region, the airflow over Larsen C was relatively quiet.

6.5.2 Identified Föhn Events

Föhn conditions were identified at five locations between the 13th and 17th May. AWS5 was not operational during this period, therefore five out of five available locations experienced föhn conditions (Figure 6.14). The intermittent occurrence of föhn events during this case study was largely due to the AWS algorithm. The AMPS algorithm identified long, continuous föhn events, lasting between 30 hours at AWS3 and 120 hours (5 days) at AWS1 (Figure 6.14). Whereas the AWS algorithm identified two or three, short föhn events, with breaks in between. This suggests that the föhn signal was interrupted at the surface.

The observations propose that the break in föhn conditions coincided with a change in wind direction. During föhn events, the wind was predominately westerly or northwesterly, but changed to north or northeasterly during the breaks in föhn conditions. Often coinciding with the direction change, the wind speed decreased and the relative humidity increased.

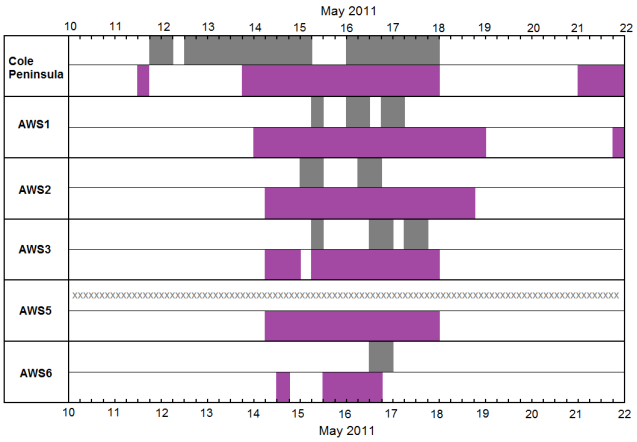

Figure 6.14: The timing of föhn events at each location during the autumn case study. The grey bars are times when föhn conditions were identified by the AWS algorithm. Purple bars are times when föhn conditions were identified by the AMPS algorithm. When they overlap, and föhn conditions were identified by both algorithms, and these periods were analysed and are presented in Chapter 4.

6.5.3 Model Validation

The model validation results will be presented for Cole Peninsula and AWS2. A better agreement between both models and observations was present at Cole Peninsula than at any other location. The validation at AWS2 is representative for the other locations.

The first location to be discussed is Cole Peninsula. The near-surface air temperature values throughout the case study were simulated very well by both AMPS and WRF. The sharp increase in temperature on the 11th and 12th May, and the large decrease in temperature on the 18th May were well represented by the models in terms of timing and magnitude of change (Figure 6.15). Temperatures during the two föhn events were slightly underestimated by both AMPS and WRF, although the average bias over the full period was smaller for the WRF run (Table 6.6). The very low relative humidity and simultaneous increase in temperature on the 13th May were not resolved by either model resolution. This period was detected as a föhn event by the AWS algorithm, but not by the AMPS algorithm.

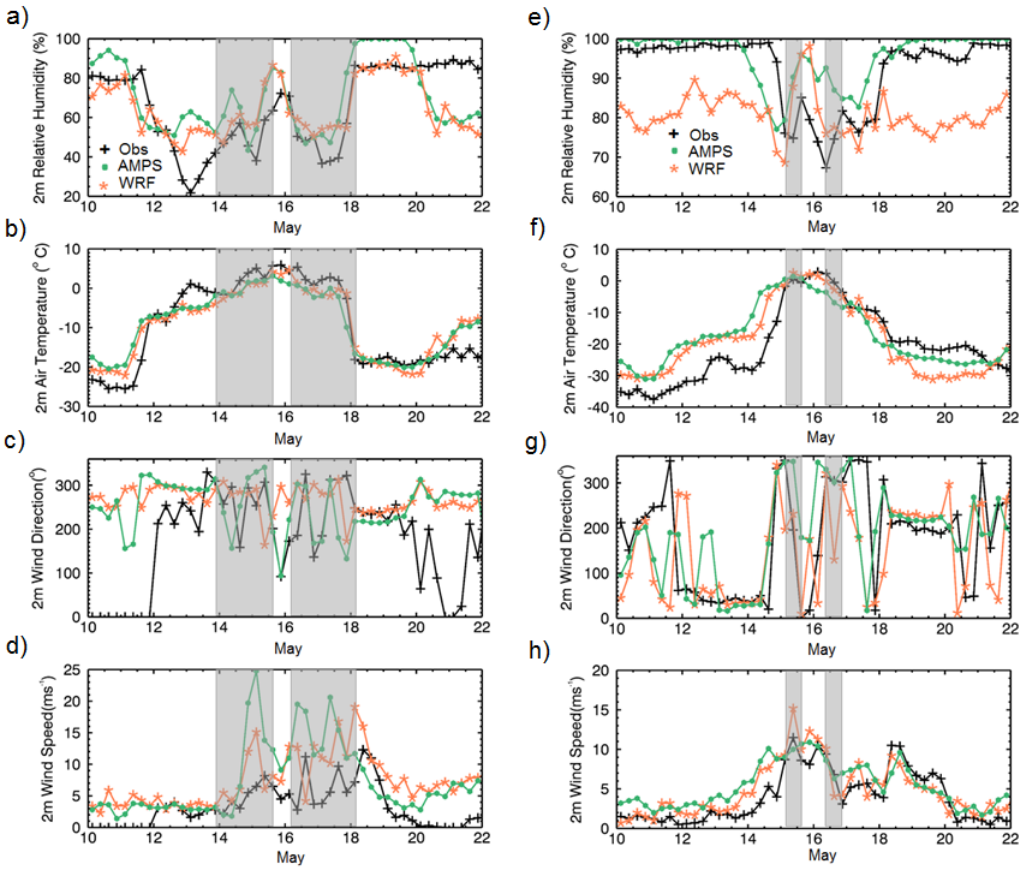

Figure 6.15: Timeseries of observational data from Cole Peninsula (a-d) and AWS2 (e-h) during the Autumn case study (10-22nd of May 2011). The 2m relative humidity (a,e), 2m air temperature (b,f), 2m wind speed (c,g) and wind direction (d,h). AWS observational data are black crosses, data from the 5km AMPS output are green dots and 1.5km WRF data are coral asterisks. Periods defined as föhn events are highlighted by grey boxes.

Table 6.6: The mean bias and Root Mean Square Error (RMSE) between the two models and the observations for each near-surface variable assessed at Cole Peninsula, for the Autumn case study period 10th- 22nd May 2011.

Variable	AMPS-AWS Mean Bias	AMPS-AWS RMSE	WRF-AWS Mean Bias	WRF-AWS RMSE
Relative Humidity (%)	4.8	18.6	-1.4	16.9
Air Temperature (°C)	0.5	4.6	0.4	4.3
Wind Speed (ms^{-1})	4.1	6.6	4.0	5.4

Both AMPS and WRF resolved the overall patterns of changing relative humidity at Cole Peninsula (Figure 6.15). During both föhn events, the timing of the relative humidity change was accurate. The magnitude of change was less well resolved. Both models overestimated the relative humidity during föhn conditions, leading to a simulated föhn flow that was more moist than observed. There was a large discrepancy between the observations and the model outputs on May 13th, when a föhn event was observed by the AWS, but it was not detected by the AMPS algorithm. Both models simulated a decrease in relative humidity on the 11th and 12th of May, but the very dry observed conditions on the 13th were not captured. At 00UTC on the 13th of May, when a minimum relative humidity of 21.7% was observed, the simulated relative humidity in AMPS and WRF had begun increasing, and overestimated the value by 41.2% (AMPS) and 31.7% (WRF). It appears that both models captured the timing of the near-surface signal, but failed to capture the very dry conditions which were subsequently detected by the AWS algorithm.

During the two föhn events identified at Cole Peninsula, the wind direction was more accurately simulated than prior to the first föhn event and after the second. The large difference between the observed wind and modelled wind from the 10th to 12th May, and on the 21st May was due to instrument error (Figure 6.15); the observed wind direction was 0°, and the wind speed was $0ms^{-1}$. During the föhn events, the wind direction changed rapidly between southwesterly (181°) to northwesterly (359°), which both models resolved well. During the break in föhn conditions on the 16th May, the wind direction shift was accurately resolved by the AMPS output, but not by the WRF model. Overall, the wind direction was simulated with a greater accuracy by the

AMPS run than the WRF run.

The wind speed was poorly simulated during föhn conditions. There was an overestimation in wind speed by both models, but it was slightly larger in the AMPS output (mean bias of 4.1ms^{-1}). During the first föhn event (14th to 15th of May) there was a positive bias of 18.3ms^{-1} by the AMPS output. The timing of the observed peaks in wind speed were replicated by the model runs, but the magnitude was overestimated.

From assessing the four variables discussed above, both models resolved conditions during föhn conditions relatively well at Cole Peninsula. WRF was slightly more accurate than AMPS for three of the variables. However, at other locations (such as at AWS2 which is addressed below) the situation was quite different. The WRF model struggled to simulate the relative humidity and air temperature as accurately, whilst both models had significantly less overestimation of the wind speed.

The relative humidity values estimated by WRF were largely underestimated at AWS1, AWS2, AWS3 and AWS6 throughout the case study, but more considerably during non-föhn periods (Figure 6.15). As an average over all locations except Cole Peninsula, the relative humidity during non-föhn conditions in WRF was 82.2%, whereas in observations it was 94.7%. During the föhn conditions, the relative humidity output from WRF was more accurate, however this may be due to the observed decrease in relative humidity, rather than an improvement in the model representation.

The following section focuses on the validation of WRF and AMPS at the AWS2 location. The timing of the decrease (increase) in humidity at the start (end) of the föhn events was simulated well by WRF. However, the magnitude of the humidity change during the first föhn event was too large. The relative humidity values during non-föhn conditions and the timing of föhn onset were well represented by AMPS. However, AMPS performed relatively badly during föhn conditions, by underestimating the magnitude of change in relative humidity, especially during the föhn event on the 16th of May 2011.

Table 6.7: The mean bias and Root Mean Square Error (RMSE) between the two model runs and the observations for each near-surface variable assessed at AWS2.

Variable	AMPS-AWS Mean Bias	AMPS-AWS RMSE	WRF-AWS Mean Bias	WRF-AWS RMSE
Relative Humidity (%)	6.0	9.8	-11.4	15.1
Air Temperature (°C)	3.1	7.2	1.7	7.3
Wind Speed (ms^{-1})	1.3	2.5	0.9	2.0

The general trend of increasing temperature between the 10th and 16th of May, and decreasing temperature after the 17th May was well captured by both models. However, prior to föhn onset (10th to 15th of May), the models overestimated the air temperature (warm bias), and after the föhn events (18th to 22nd of May) the models underestimated the air temperature (cold bias). This lead to relatively small mean biases, as they almost cancelled each other out (Table 6.7), however the offset between the models and observations was as large as 14.8°C (AMPS) at one time (06UTC 14th May). During the föhn events, the agreement between the observations and both models was much better, although this was only for a short period (Figure 6.15). The timing and amplitude of the temperature decrease after the second föhn event were well resolved in WRF. WRF estimated a maximum temperature of 2.6°C, whilst the AMPS model simulated a maximum temperature of 1.4°C.

Both the wind direction and wind speed were better resolved at AWS2 (and other locations) than at Cole Peninsula. The regime shift from northeasterlies prior to onset (12th-15th of May) to highly variable wind direction during the two föhn events was well captured by both model runs, although slightly better by WRF. The rapid change from northwesterly to northeasterly and back again during the break in föhn events was well resolved by WRF (Figure 6.15). At AWS2, the wind speed throughout the case study was well resolved by both models. The timing and magnitude of changes were captured.

6.5.4 Autumn Simulation Results

Both the observations and simulated near-surface conditions suggest that there were two separate föhn events at Cole Peninsula and AWS2. The break in föhn conditions was likely due to a change in the near-surface wind direction, as observed and simulated. However, the AMPS model continued to simulate föhn conditions during the break. Assessing the spatial distribution of the föhn air in WRF has provided more information into this disagreement between the AWS and AMPS algorithms.

The föhn event on the 12th to 14th of May was longer, and started earlier at Cole Peninsula than elsewhere. At Cole Peninsula the air temperature rise was sudden on the 12th of May, and the temperature remained above or close to freezing for approximately six days, whereas at AWS2 (and other locations), the large temperature rise was not observed until the 14th of May. After that, the air temperature over the ice shelf remained above freezing for just two days. Similarly, the relative humidity of the air was much lower at Cole Peninsula than at AWS2. WRF suggests that a cold, stable boundary layer over the ice shelf delayed the propagation of the föhn air to the surface of the ice shelf.

Figure 6.16 displays the 2m air temperature from WRF at the start of the föhn event identified at Cole Peninsula (18UTC 13th of May 2011) and at every six hours after that until it was identified at AWS2 (00UTC 15th of May 2011). The 30-hour gap between identification at Cole Peninsula and at AWS2 was due to the presence of a cold, stable boundary layer over the ice shelf. The cold pool prevented the föhn air from immediately penetrating to the surface and propagating across the LCIS. The föhn air descended down the leeside of the AP, and was identified immediately at Cole Peninsula due to its close proximity to the AP and its relatively higher elevation. For the föhn air to propagate across the ice shelf, it had to erode the stable cold air, or 'push' the air away. The stability began to break down to the north and east of the ice shelf first (Figure 6.16c) due to the strong northwesterly winds over Scar Inlet. The warm, föhn air eroded the cold air pool over a period of 30 hours, and propagated southwards across the ice shelf.

Some of the characteristics identified during this föhn event mimic features known to be present during linear flow regimes, as described over the LCIS by Elvidge *et al.* (2016) (see Chapter 1). Under linear flow, the erosion of the cold pool by the föhn air takes longer, as the downslope flow is weaker and less turbulent than non-linear flow. Subsequently, detection of the föhn effect near the surface can be delayed . Once the cold pool has been pushed away or eroded, the föhn air can propagate freely leading to a widespread, but relatively weak, föhn effect (Elvidge *et al.*, 2016). This process is only possible under relatively long and persistent föhn events. Calculating the Froude number from the upstream conditions in WRF reveals that the airflow was linear (Fr = 1.1) during the first föhn event. Therefore the slow erosion of the cold pool may be attributed to the linear föhn flow.

The resolution of the WRF model allows fine-scale spatial features to be identified. For example in Figure 6.16e, the cold air that has been pushed southwards by the föhn air appears to stagnate and pool on the south of the ice shelf due to blocking by Kenyon Peninsula. There were no observations at AWS5 during this case study, however, WRF suggests that near-surface föhn conditions would have been identified at roughly the same time as at AWS2 due to the southeastwards direction of the föhn propagation.

In between the two föhn events, the air temperature across most of the ice shelf remained above freezing, while the relative humidity increased for a short period of time (6-12 hours), before it decreased again, thereby separating the two föhn events. The AMPS algorithm did not indicate a break in föhn conditions. It is possible that the coarse temporal resolution of AMPS was unable to capture rapid, perhaps unexpected changes. However it may also suggest that the mechanism driving the föhn development (isentropic drawdown) was still operating at the AP ridge, whilst the near-surface conditions changed. Observations and near-surface conditions output by both model runs suggested a change in wind direction and an increase in relative humidity at the near-surface level. When assessing the wind direction with height simulated by WRF at the AWS2 location for 00UTC 15th May, it becomes clear that the low level winds, below 500m, were from a north-easterly direction (not shown). From approximately 500m to 2000m, the wind direction became northwesterly. Therefore at the AP ridge,

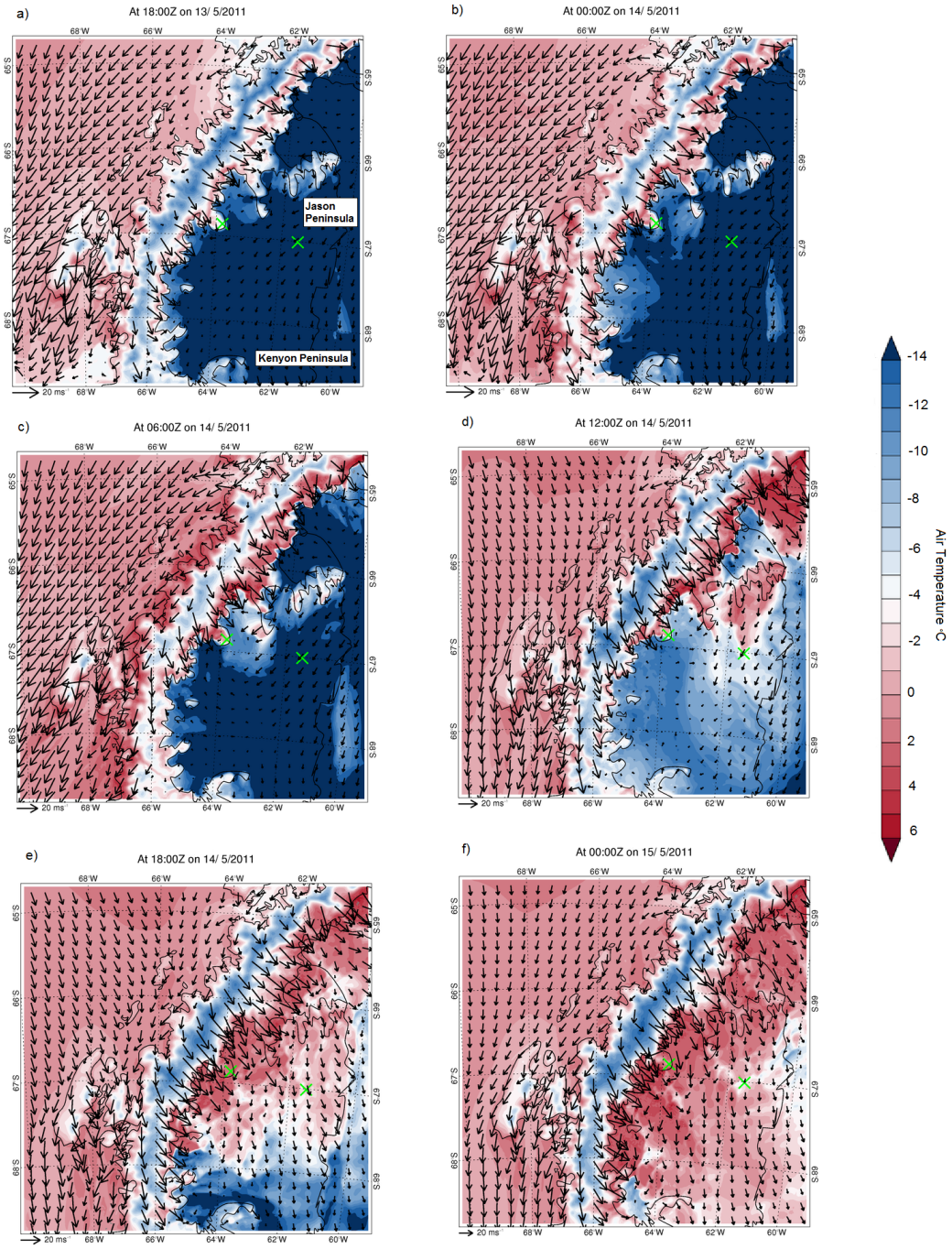

Figure 6.16: The 2m air temperature field over the LCIS simulated by WRF at the start of the first föhn event (18UTC on the 13th of May 2011) at Cole Peninsula (a) and at every six hours until the identification of the föhn event at AWS2 (f) 30 hours later (00UTC on the 15th of May 2011). The green crosses are located at Cole Peninsula and AWS2 locations.

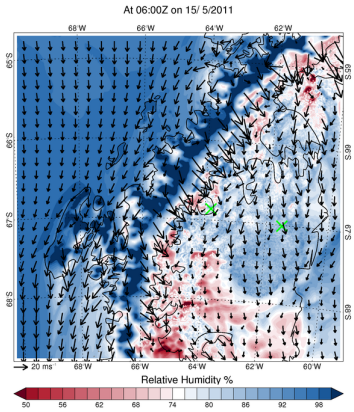

Figure 6.17: The 2m-relative humidity simulated by WRF at 06UTC on the 15th of May 2011. Moist air moved southwards over the ice shelf during an 18 hour period. This, combined with the northeasterly wind direction, terminated the first föhn event (12UTC on the 15th of May 2011) at AWS2 and Cole Peninsula (green crosses).

the winds had a westerly component, which would have initiated the isentropic draw-down that was subsequently identified by the AMPS algorithm, despite a northeasterly near-surface wind direction.

From approximately 06UTC on the 15th of May, more moist air moved onto the ice shelf from the north. The moist air mixed with the föhn air as it moved southwards over Larsen C. The mixing of air masses is visible in the WRF output. The speckled pattern of lighter and darker colours in Figure 6.17 displays the small-scale mixing of the two air masses as it moved south. This level of detail was not visible in the AMPS output (not shown).

At 00UTC on the 16th of May the second föhn event of the Autumn case study was identified at Cole Peninsula and AWS1. Six hours later it was identified at AWS2 and twelve hours later at AWS3 and AWS6. The earlier onset of föhn conditions at Cole Peninsula and AWS1 was a consequence of a localised föhn effect very close to the foot of the AP prior to eastwards propagation of the föhn air. Within 12 hours, the dry, warm air had spread over most of the ice shelf. This was the only föhn event to be identified as far south as AWS6.

During the second föhn event, warm, dry air propagated across the ice shelf quicker than during the first. The cold, stable boundary layer which was present over the ice shelf at the start of the case study, had already been removed by the first föhn event. The warm air that remained over the ice shelf in between the two events, prevented the formation of another cold pool. Therefore, there was relatively little resistance to the propagation of föhn air during the second event.

The second föhn event was characterised by non-linear features such as the presence of a 'hydraulic jump'. When the airflow towards the mountain is weakly subcritical (see Chapter 1) and it interacts with a mountain, the flow accelerates as the air ascends the upwind slope. Once above the mountain, the flow regime shifts to supercritical and the flow continues to accelerate as it descends down the lee slope, generating a downslope windstorm. The flow then abruptly readjusts to ambient conditions in the lee of the slope, by the formation of a hydraulic jump. This is visible in Figure 6.18 during the second föhn event. The two isentropic drawdown signatures in the lee of the AP were interrupted by a cooler updraft. Simultaneously the airflow was directed upwards.

Downslope windstorms often coincide with hydraulic jumps in the lee of steep mountain ranges. They are very strong downward winds which reach their peak windspeed at the foot of the leeside slope, and diminish rapidly downstream (Sun, 2013). The increased windspeed and the negative (downward) vertical velocity along the leeside of the AP, displayed in Figure 6.18, provides evidence for the downslope windstorm.

The hydraulic jump was poorly resolved by the AMPS model in comparison to the WRF run (Figure 6.19). There was no defined hydraulic jump, and the two isentropic drawdown features simulated by WRF were absent in the AMPS output. Instead, a broad region of drawdown was simulated. The poor representation in AMPS was likely due to a combination of the coarser horizontal and vertical resolution, and the lower-resolution topography, which is evident when comparing the WRF and AMPS cross sections (Figure 6.19).

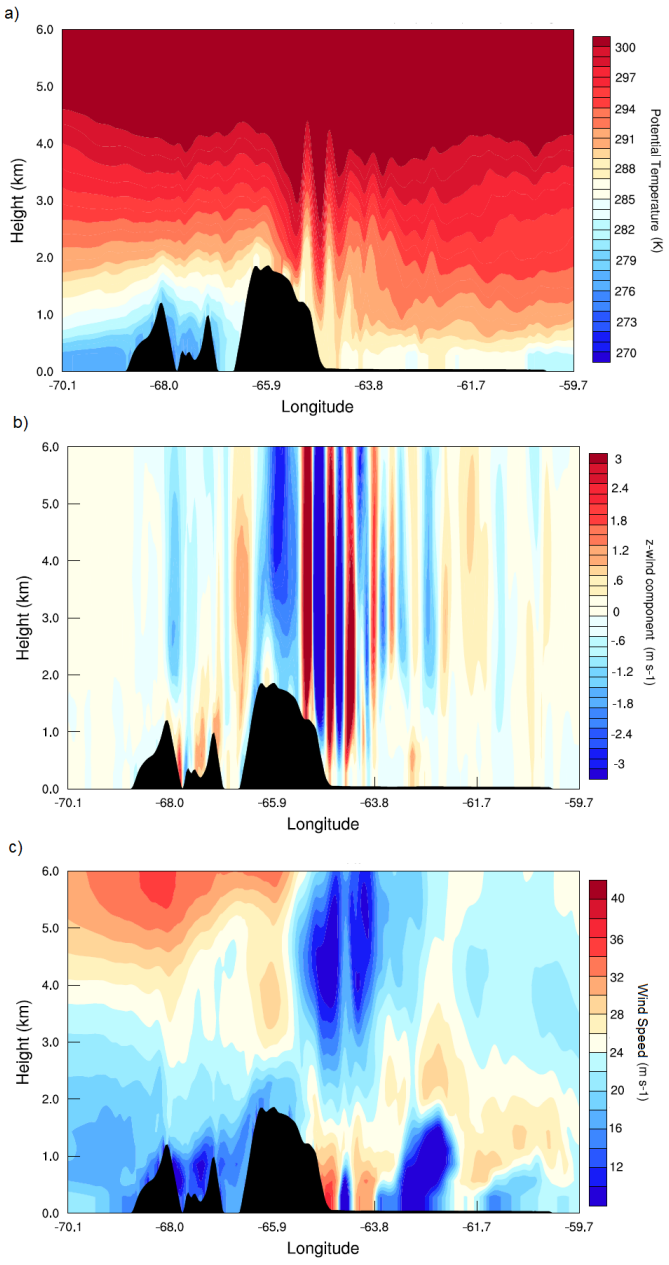

Figure 6.18: A cross section along 67.0°S (AWS2 latitude) of the potential temperature (a), vertical velocity (b) and the wind speed (c) at 00UTC on the 16th of May 2011. The hydraulic jump is well defined in the potential temperature and vertical velocity fields. A downslope windstorm is also visible in the wind speed field.

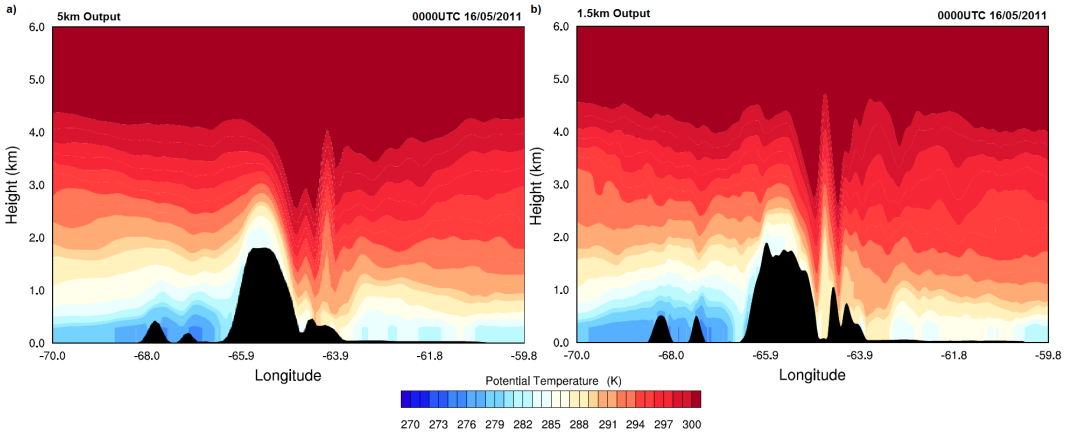

Figure 6.19: Cross sections through 66.8°S (Cole Peninsula latitude) of the AP, of modelled potential temperature from AMPS (a) and WRF (b). The double-isentropic drawdown and hydraulic jump was simulated well by the WRF model (b). AMPS simulated a broader area of isentropic drawdown and the absence of a hydraulic jump (a). Figure form Turton *et al.*.

Föhn jets are another common feature under non-linear flow. These were first described over the LCIS by Elvidge *et al.* (2015, 2016). WRF simulated föhn jets over the LCIS during the second föhn event (Figure 6.20). Föhn jets are a type of gap flow created by the flow of air through lower-elevation passes on a mountain range. They are more moist and cooler than the surrounding föhn flow because the air does not ascend and descend the full height of the mountain, and therefore adiabatic warming is reduced. (See Chapter 1 for a discussion of the processes responsible for föhn jets). The Froude number, calculated from upstream conditions simulated by WRF, reveal that the air flow was non-linear (Fr = 0.83) during the second föhn event. Therefore, the presence of a hydraulic jump and föhn jets over the LCIS are likely due to the non-linear flow over the AP.

The bands of relatively cool, moist jet air intersected the general föhn flow. The föhn jets are visible in the relative humidity and air temperature fields simulated by WRF (Figure 6.20). The jets are more defined in the relative humidity field as elongated bands of more moist air, emanating from the gaps in the AP topography. The

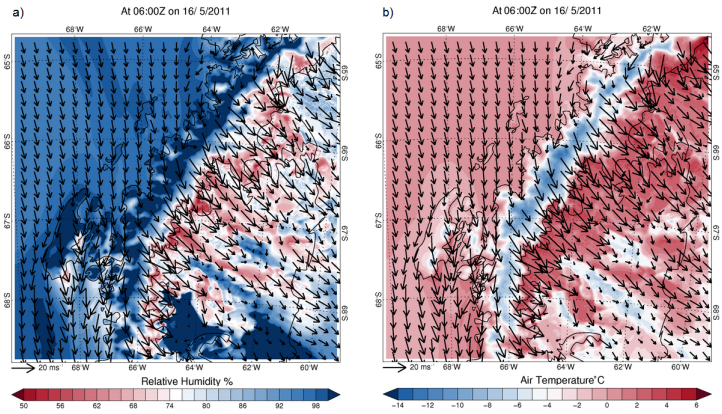

Figure 6.20: a) The 2m relative humidity and b) air temperature fields simulated by WRF at 06UTC on the 16th of May 2011. The bands of alternating warm, dry air and cold, moist jets are föhn jets. In the relative humidity field, they emanate from gaps in the AP topography, whereas in the air temperature field they start further east. Figure from Turton *et al.*.

jets appear to be 'attached' to the mountains where they had formed. The jets were also visible from assessing the air temperature field, but were less distinguishable from the ambient flow. The jets appear to be detached from the AP mountains, and are visible $\sim$ 20km east of the AP.

The föhn jets were less defined in the AMPS simulation. The shape of the föhn jets (elongated, thin bands) were not resolved by AMPS. Instead, larger patches of cooler air were simulated over the southern part of the ice shelf (Figure 6.21). The cooler air was more extensive in AMPS, which may lead to an underestimation of the impact of the föhn winds over the ice shelf. The coarser topographic, horizontal and vertical resolution in AMPS lead to poor representation of the föhn jets.

At AWS2 the föhn event on the 16th of May lasted only twelve hours. The breakdown of the föhn effect was linked to a change in wind direction. The warm air initially propagated across the whole ice shelf quickly. However after 12UTC on the 16th of May, the föhn air retreated back towards the AP. The wind direction at the ice shelf edge became northeasterly, which pushed relatively cool, moist air over the AWS2 location.

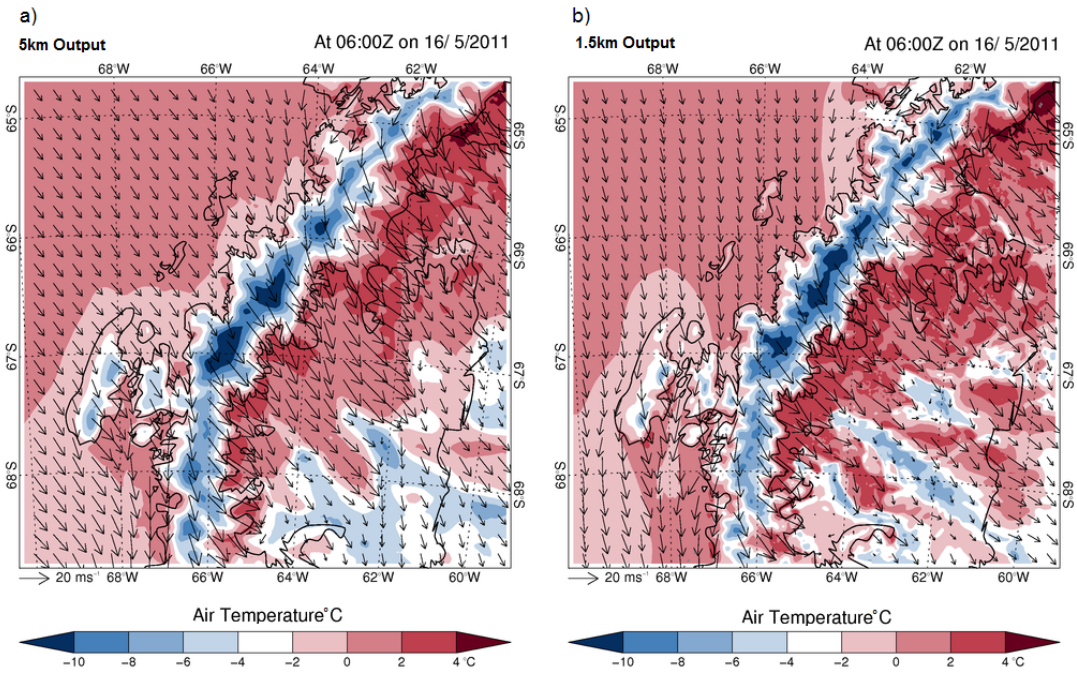

Figure 6.21: The 2m air temperature field simulated by AMPS (a) and WRF (b) at 06UTC on the 16th May 2011. The well defined, elongated jets of cooler air were clearly simulated by WRF (b), but were poorly resolved by AMPS (a).

The föhn event at Cole Peninsula lasted 12 hours longer than elsewhere. Gradually, the northeast wind pushed the colder, more moist air to the foot of the AP, and eroded the föhn air. Unlike the cessation of the first föhn event which was relatively abrupt and uniform in its timing across the ice shelf, this second föhn event was prolonged at the foot of the mountains, but short-lived elsewhere.

Without the high-resolution simulations, the level of detail of the spatial distribution of the föhn air, and the vertical structure would not have been known. AMPS failed to capture the shape and detail of the föhn jets, and the hydraulic jump, during the second föhn event.

6.5.5 Autumn Discussion

The case study period selected for Autumn was initially chosen to investigate the propagation of föhn air over the ice shelf, as the föhn event on May of 16th was identified at all locations. A further aim was to identify which processes were responsible for reducing or interrupting the near-surface föhn signal. The AMPS algorithm identified one continuous föhn event, whereas the near-surface signal was interrupted, leading to an intermittent föhn signal from the AWS algorithm.

Upon analysing the WRF output, the two föhn events had quite different characteristics. The first föhn event strongly resembled the 'linear' föhn flow regime, whilst the second föhn event resembled the 'non-linear' föhn flow regime, originally defined and presented by Elvidge *et al.* (2016). Under a linear flow regime, the dominant föhn mechanism is usually the thermodynamic processes. The non-linear flow regime is often determined by the isentropic drawdown mechanism for föhn heating.

The linear and non-linear classification does not simply relate to the mechanism responsible for the föhn winds, but also to the characteristics of the flow on the leeside of the AP and over the LCIS. Under non-linear flow, features such as hydraulic jumps, flow reversal, wave breaking and increased turbulence above the AP are present during föhn events (Elvidge *et al.*, 2016). The föhn effect is strongest (warmer and drier air) close to the foot of the AP Mountains, and the signal diminishes rapidly downwind

of the AP, creating a considerable horizontal west-east temperature gradient (Elvidge *et al.*, 2016). Under a linear flow regime the föhn flow is more characteristic of a laminar flow, and the non-linear features are absent. The föhn effect is more widespread under linear flow, affecting the near-surface conditions up to 200km from the AP, although it often has a reduced strength compared to the non-linear flow induced föhn (Elvidge *et al.*, 2016).

Characteristics which are present during both linear and non-linear flows are föhn jets. These are an extension of gap jets, and are cooler and more moist than the surrounding föhn air due to either the sourcing of lower-elevation (potentially cooler and less dry) upwind air, or due to reduced adiabatic ascent and descent as the air flows through lower-elevation passes in the AP crest (Elvidge *et al.*, 2015). Although cooler and more moist than the surrounding föhn air, they were still drier and warmer than the upwind airflow. In the case studies analysed by Elvidge *et al.* (2015), föhn jets during non-linear flow were clearly defined due to the weak surrounding air flow. Under the linear flow, the föhn jets were less distinctive due to more homogeneous windspeed of the leeside flow (Elvidge *et al.*, 2016).

In the present case study, the first assessed föhn event resembled a linear flow regime, but föhn jets were absent. The föhn event was identified at Cole Peninsula 36 hours before any other location. The lack of föhn propagation was caused by the presence of a stable boundary layer over the ice shelf. Cold (< 270K), stable air up to approximately 500m was located over the whole ice shelf including Scar Inlet. Cold pools have been frequently observed over Larsen B ice shelf, especially during the extended winter months (Scambos, 2016, personal communication). Cold pools in Alpine valleys are known to interrupt and terminate föhn air at near-surface levels (Drobinski *et al.*, 2007). Only the strongest föhn events are observed at the ground level when a persistent cold pool is present in the Alps (Drobinski *et al.*, 2007). The breakup of a cold pool and the penetration of the föhn air to the surface is likely governed by numerous mechanisms. Some of the suggested mechanisms include; diurnal heating by solar radiation during the daytime; turbulent mixing and heating at the top of the cold pool; convection of heating from underneath if the lateral boundary of the cold pool allows some entrainment of föhn air; and dynamical displacement or 'pushing' of the cold pool

away from the region (Drobinski *et al.*, 2007; Richner & Gutermann, 2007; Richner & Hächler, 2013). Whilst the pushing of cold pools away from the region is less prevalent within the Alps (due to the complex shape and direction of the valleys preventing the flushing of cold air), over the LCIS this mechanism has greater potential. The wide, flat surface of the ice shelf allows the föhn air to push the cold air towards the coast.

The spatial analysis of the near-surface temperature, wind and humidity fields from the WRF simulation suggests that the cold pool was pushed southwards by the encroaching northwesterly föhn winds. At the start of the föhn event (18UTC on the 13th of May) the cold air was widespread over the whole ice shelf. Eighteen hours later, the cold air was present over the southern portion of the ice shelf only, and the northern section of the ice shelf was characterised by considerably warmer and drier conditions (Figure 6.16). After a further 18 hours, the cold pool was completely removed from the ice shelf, and föhn conditions were observed over the majority of the ice shelf.

The widespread föhn warming experienced towards the end of this föhn event (15th of May) was characteristic of a linear-flow regime. The relatively slow erosion of the cold pool is also characteristic of laminar flow, as there is reduced turbulence and mixing at the edge of the cold pool (Elvidge *et al.*, 2016). The föhn warming was extensive, but slightly weaker in strength (lower temperatures and higher relative humidities) than during the second föhn event (non-linear flow regime). From calculating the Froude number, the up-barrier flow was linear (Fr= 1.2), and therefore this föhn event was characterised by linear flow features.

Once the cold pool was removed, the ice shelf remained close to, or above, freezing in between the two föhn events. The AMPS algorithm suggested that there was no break in föhn conditions, and that one continuous föhn event was present at the AP crest. This is because the wind direction remained northwesterly at the top of the AP. However, at the near-surface level, the relative humidity increased for a short period of time due to a change in the low-level wind direction from westerly to northeasterly. A similar situation was identified in the spring case study, where the AWS and AMPS algorithms disagreed. In the spring case study however, the AWS algorithm

identified near-surface föhn conditions, whilst the AMPS algorithm did not identify a corresponding upper-air signal. This again brings into question whether combining the two algorithms was a useful strategy in identifying föhn conditions. As the AMPS algorithm overestimated the number of föhn conditions in comparison to the AWS algorithm (see Chapter 3), it may be possible that the low-level winds are departing from the upper-level northwesterly airflow (predominant at the AP crest) relatively often.

The air from the second föhn event propagated quickly across the ice shelf, and was identified at multiple locations. The short time between the two föhn events and the warm air remaining on the ice shelf prohibited the formation of a second cold pool. Therefore, there was no resistance to the warm and dry föhn air propagating across the ice shelf. In the second föhn event, numerous non-linear flow features were evident, including föhn jets and a hydraulic jump.

The föhn jets were visible in both the relative humidity and temperature fields simulated by the WRF model (Figure 6.20). In the temperature field however, they were wider and detached from the foot of the AP. The detachment of the cool jets from the AP was potentially due to turbulent mixing of the jet air with the föhn air, prompted by the hydraulic jump in the lee. The increased turbulence from the hydraulic jump and the downslope windstorm, and the additional warming from the second isentropic drawdown may have mixed with the cooler jet air and masked the signal close to the mountains. Further east however, where the turbulence and the warming was reduced, the cooler near-surface air from the jets was visible in the air temperature field.

The hydraulic jump and downslope windstorm were evident in the vertical cross-section plots of vertical velocity, wind speed and potential temperature (Figure 6.18). The hydraulic jump advects the warm, dry air away from the surface. The föhn air then re-descends further downwind of the AP where it dissipates. This initial upward momentum reduces the föhn strength further downwind, leading to a larger horizontal temperature gradient than that observed during linear flow regimes (Elvidge *et al.*, 2015). The föhn jets are able to reach further downwind than the föhn air. From the simulated conditions presented in Figure 6.20, two of the jets appear to have distributed the cooler, moist air to the eastern edge of the ice shelf, whilst the surrounding föhn

air dissipated on the southern section of the LCIS.

The termination of the föhn event at AWS2 was a consequence of the dissipated föhn signal. The föhn signal weakened due to the movement of a föhn jet over the location and a localised, low-level change in the wind direction. The föhn jets originate from the lower elevation passes on the AP. Once they reach the ice shelf, they are not bounded by the topography, and they begin to move laterally, determined by small changes in the wind direction over the ice shelf. At Cole Peninsula, the föhn event continued for a further 30 hours before ending abruptly, marked by a large increase in relative humidity and a decrease in air temperature (Figure 6.15). The wind became southeasterly, bringing cold continental air onto the ice shelf.

The spatial distribution of the föhn air during this case study was largely controlled by the presence of a cold, stable boundary layer at the start, and its interaction with the air flow. This is quite different to the föhn events during the spring case study, which were largely controlled by the wind direction. The WRF model was capable of simulating a deep, cold, stable boundary layer, a hydraulic jump and föhn jets. However, it struggled to simulate the near-surface conditions accurately, due to a dry bias. AMPS was less successful at simulating the non-linear flow features. The hydraulic jump and flow jets were poorly defined, which is likely due to its coarser horizontal and vertical resolution.

6.6 Winter Case Study

The winter case study focuses on föhn events identified from the 5th to 10th of August 2011. Againt 48 hours prior to the case study was used for spin-up. Fewer observations were available during winter, due to a number of stations requiring solar radiation for energy. The frequency and spatial distribution of the föhn winds will have been underestimated during winter. The main aim of simulating this case study was to investigate whether the limited spatial coverage by observations during winter has led to an underestimation of the spatial distribution and impact of föhn winds in this season. Relatively strong westerly winds were present over the AP and LCIS during the case

study. The perpendicular interaction of strong westerlies and the AP is often seen as the 'textbook' föhn mechanism. However, föhn conditions were only identified at three locations. The second aim of the case study was to assess whether this limited spatial distribution of föhn air was due to the limited operational AWSs or due to the ambient conditions on the ice shelf.

6.6.1 Synoptic Situation

In the week prior to föhn onset the wind direction was largely dominated by southerly flow. From the 29th July to 4th of August, the mean sea level pressure of the AP was controlled by high pressure stretching from a large high pressure system centred on East Antarctica (Figure 6.22). This high pressure system was spread across much of the continent, with a week-average central pressure of 1048 hPa. Relatively low pressure systems were located near West Antarctica and east of the AP. The airflow over much of the AP region was from the south, and was stronger on the eastern side.

The high pressure centre over East Antarctica remained in place throughout the following week, however it did weaken. The high pressure system over the AP separated from the East Antarctic on the 5th August, although high pressure still dominated the conditions over the AP. The airflow was cross-ridge, flowing westerly across the AP and onto the LCIS (Figure 6.22). The westerly airflow across the LCIS is often seen as the 'textbook' way to generate föhn winds over the eastern ice shelves of the AP (see Chapter 1). Both the 850hPa and 10m wind directions were predominantly westerly over the AP.

On the 10th of August the wind direction remained westerly across the LCIS. By the 11th of August the airflow became predominantly southerly, and the wind direction was controlled by the presence of a low pressure centre to the east of the AP. The southerly winds were strongest on the east coast of the AP and over the LCIS. The development of this low pressure system likely terminated the development of föhn winds by controlling the wind direction.

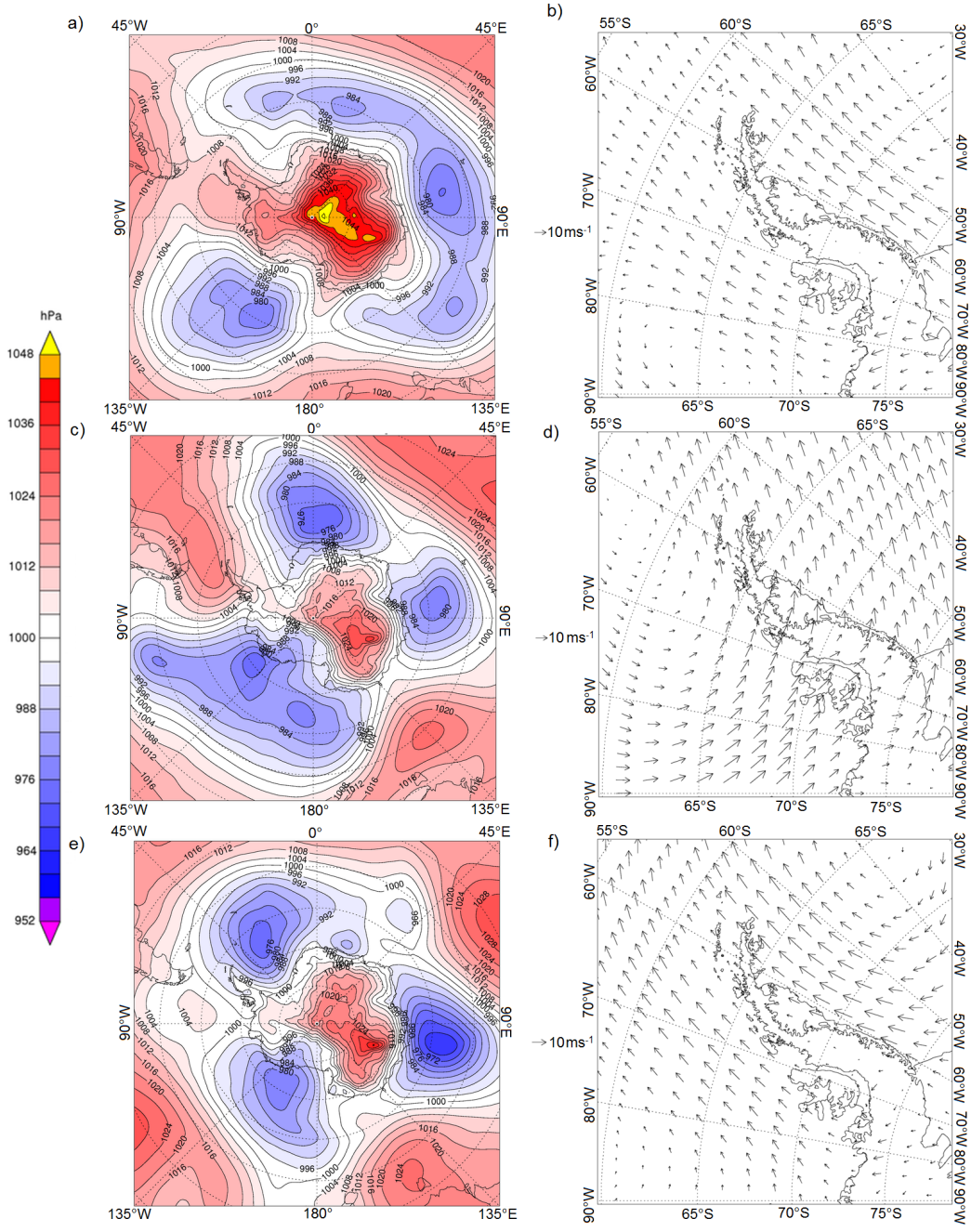

Figure 6.22: The mean sea level pressure (MSLP)for the Southern Ocean (left panels: a, c, e) and mean 850hPa wind vectors over the AP region (right panels: b, d, f) before, during and after the föhn events. a) and b)cover the period from 29th of July to 4th of August, the week prior to the föhn events. c) and d) are during the föhn days (5th to 10th of August). e) and f) display the synoptic situation for four days after the föhn events (11th to 15th of August).

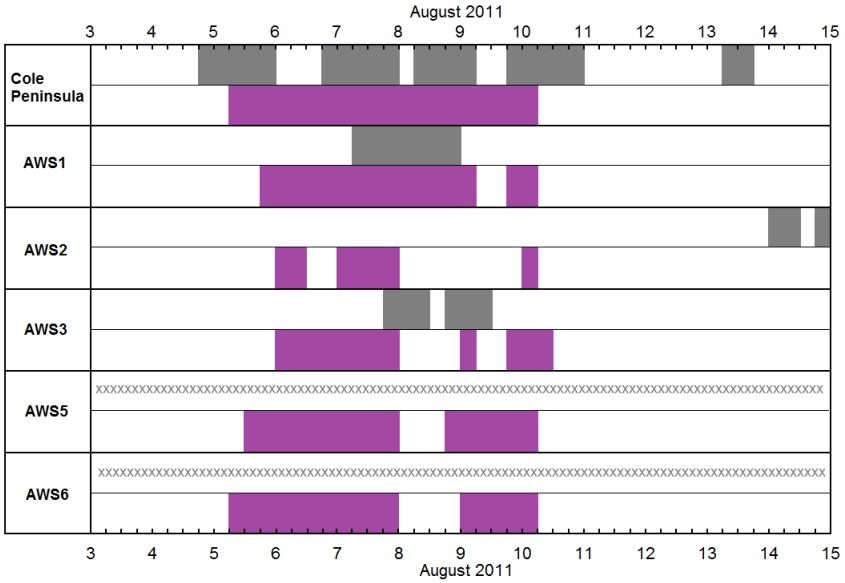

Figure 6.23: The timing of föhn events at each location during the winter case study. The grey bars are times when föhn conditions were identified by the AWS algorithm. Purple bars are times when föhn conditions were identified by the AMPS algorithm. When they overlap, and föhn conditions were identified by both algorithms, and these periods were analysed and are presented in Chapter 4.

6.6.2 Identified Föhn Events

Only three locations experienced föhn events during this case study period. Four individual föhn events were identified at Cole Peninula. One long föhn event was identified at AWS1 and two were identified at AWS3. Figure 6.23 presents the time and dates of these.

The föhn event at AWS1 was a continuous 42-hour long event. The AMPS algorithm suggested that the event could have been 84-hours long, however, there was no near-surface detection for the first 36 hours, and the near-surface signal subsided six hours earlier than AMPS suggested. At Cole Peninsula the AMPS algorithm also identified one continuous event from 06UTC 5th to 06UTC 10th of August. However, the AWS algorithm suggested multiple shorter föhn events.

6.6.3 Model Validation

Validation of the WRF and AMPS model for this case study will focus on the Cole Peninsula and AWS1 locations. Firstly, validation at Cole Peninsula will be addressed. Similar to the other case studies presented in this chapter, the near-surface air temperature values were well simulated by both models when compared to observations at Cole Peninsula (Figure 6.24). The timing of the temperature rise starting on the 4th of August and the large temperature decrease on the 11th of August observed at Cole Peninsula was captured by both models. However, the relatively small and short-lived increase in temperature on the 10th August was not captured by either model. The amplitude of the large increase and decrease in temperature on the 4th and 11th of August (respectively) was well modelled, leading to small mean biases and RMSE (Table 6.8).

The mean bias and RMSE of the relative humidity between the models and the observations were relatively small (Table 6.8). However, both the WRF run, and the AMPS run had difficulty with capturing a number of the relative humidity changes. The magnitude of the humidity decrease into the first föhn event (06UTC, 5th of August) was captured by WRF, as was the minimum value (31.4% in observations, 34.9% in WRF) (Figure 6.24). However, the WRF model simulated a more gradual humidity decrease than was observed. The low relative humidity values during the third Cole Peninsula föhn event (06UTC on the 8th of August) were not captured by either model run. The observed minimum relative humidity of 35.1% coincided with a WRF value of 61.5%, and an AMPS value of 60.8%. The timing of the large rise in relative humidity at the end of the final (fourth) föhn event (12UTC on the 10th of August) was well resolved by the WRF model, although the magnitude of the rise was underestimated. Both runs did manage to simulate relative humidity conditions as dry as those observed ($\sim$ 30%), which was not the case in the Autumn case study.

At Cole Peninsula, the models suggested that predominantly northwesterly to westerly winds were present on the LCIS throughout the majority of the case study, mimicking the ERA-Interim wind direction discussed in the synoptic section of the chapter. In observations, the wind direction was more variable, and switched between southeasterly and southwesterly. Towards the end of the case study, AMPS simulated the

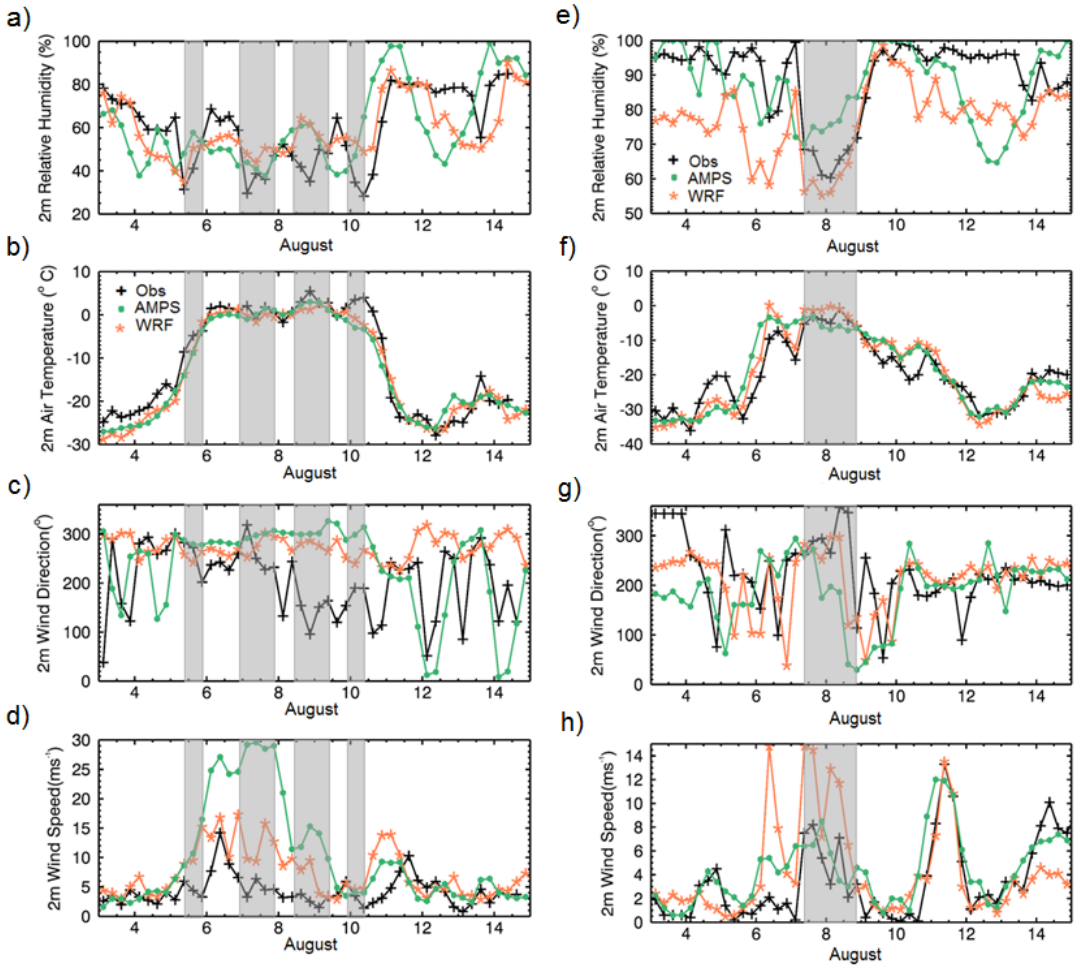

Figure 6.24: Timeseries of observational data from Cole Peninsula (a-d) and AWS1 (e-h) during the Winter case study (3rd to 15th of August 2011). The 2m relative humidity (a,e), 2m air temperature (b,f), 2m wind speed (c,g) and wind direction (d,h). AWS observational data are black crosses, data from the 5km AMPS output are green dots and 1.5km WRF data are coral asterisks. Periods defined as föhn events are highlighted by grey boxes.

Table 6.8: The mean bias and Root Mean Square Error (RMSE) between the two model runs and the observations for each near-surface variable assessed at Cole Peninsula.

Variable	AMPS-AWS Mean Bias	AMPS-AWS RMSE	WRF-AWS Mean Bias	WRF-AWS RMSE
Relative Humidity (%)	-2.2	16.5	-1.9	13.3
Air Temperature (°C)	-1.4	3.3	-1.5	3.1
Wind Speed (ms^{-1})	5.8	9.9	3.2	4.9

variability of the wind direction better than WRF (Figure 6.24).

As presented in the other case studies, the wind speed was vastly overestimated by AMPS, and slightly overestimated by WRF (Table 6.8). During the second föhn event at Cole Peninsula (7th of August), the AWS observed an average wind speed of $5.1ms^{-1}$, the WRF model simulated an average of $12.6ms^{-1}$ and the AMPS run suggested an average of $28.2ms^{-1}$. Wind speeds were resolved much better during non-föhn periods than during the föhn events (Figure 6.24).

The validation of both model runs for the AWS1 location will be presented now. At AWS1, the air temperature timeseries throughout the case study was well captured by both model runs (Figure 6.24). The timing and amplitude of the temperature change throughout the case study, including the föhn event were simulated well, and had small mean biases and RMSEs (Table 6.9). Six hours before the onset of the föhn event at AWS1, on the 7th of August, the observed temperature rose rapidly from -15.7°C to -5.3°C. A similar magnitude of increase was simulated by the WRF model, and the timing was accurately modelled, however the AMPS run did not resolve this short-lived but marked change.

As experienced in other case studies, the relative humidity was underestimated by the WRF model at all locations other than at Cole Peninsula. Regardless of the dry bias the WRF run simulated the timing and amplitude of the humidity changes relatively well. The AMPS model did capture the timing of some of the humidity changes, but it also simulated a considerable decrease in relative humidity towards the end of the case study (13th of August), that was not observed by AWS1 (Figure 6.24). The

Table 6.9: The mean bias and Root Mean Square Error (RMSE) between the two model runs and the observations for each near-surface variable assessed at AWS1.

Variable	AMPS-AWS Mean Bias	AMPS-AWS RMSE	WRF-AWS Mean Bias	WRF-AWS RMSE
Relative Humidity (%)	-1.0	13.1	-13.1	15.6
Air Temperature (°C)	-0.2	5.1	-0.5	4.7
Wind Speed (ms^{-1})	1.0	2.2	0.8	3.5

WRF run had a larger mean bias and RMSE for relative humidity than the AMPS run (Table 6.9), however this was largely caused by the WRF dry bias.

The WRF run simulated much higher wind speeds prior to and during the föhn event than were observed at AWS1 (Figure 6.24). The WRF model also simulated peaks in windspeed which were not observed even at smaller magnitudes, such as at 18UTC on the 5th of August, when the WRF model overestimated wind speed by 11.9ms^{-1}. Both the AMPS and WRF model simulated the observed large peak in wind speed on the 13th of August. Overall, both AMPS and WRF had similarly small mean biases and RMSEs (Table 6.9), which appear to hide the large peaks in simulated windspeed. The wind directions throughout the case study were also relatively well captured by both runs.

The performance of the two models varied depending on which location and which variable was analysed. In general, the WRF model performed better at simulating the observed near-surface characteristics at Cole Peninsula. At AWS1, the picture was more varied, and AMPS performed better at reproducing the relative humidity and wind speed. The WRF model resolved the timing and magnitude of changes well associated with the föhn events.

6.6.4 Winter Simulation Results

The föhn events at Cole Peninsula were shorter than at AWS1, but there were more of them, and therefore more föhn days. At Cole Peninsula there were four föhn events

over six föhn days. At AWS1, there was one föhn event, spanning over two föhn days.

The first föhn event at Cole Peninsula was 12-hours long. The föhn effect remained fairly localised to the foot of the AP. Very cold, stable air was present over the ice shelf prior to föhn onset, which likely halted the propagation of the warmer föhn air. In the Autumn case study, the presence of a cold, stable boundary layer prevented the föhn air from reaching the surface at some locations. However, once the föhn air had eroded the stable surface layer, the föhn event was observed across much of the ice shelf. That was not the case here, as the föhn air was not observed further east.

Prior to running the WRF simulation, it was theorised that the intermittent occurrence of the föhn events at Cole Peninsula was due to a strengthening or development of the cold pool over the ice shelf. Cold pool development during the austral winter is frequent due to the lack of solar radiation and the draining of cold air off the continent under southerly winds. However, from assessing the output from WRF, this does not explain the intermittent föhn signal. The air temperature increased during the first föhn event and remained high (at or near to freezing) until the cessation of the fourth föhn event. Consequently, no redevelopment of the cold pool was simulated by WRF.

The WRF model accurately simulated the relative humidity at Cole Peninsula, however it underestimated the relative humidity over most of the ice shelf (as presented in Figure 6.25). At Scar Inlet (AWS1), the model simulated humidity as low as 40%, suggesting that föhn air may be present on the 5th and 6th August, although the observed humidity was over 90% and therefore no föhn event was observed (Figure 6.25). The air temperature signal was a better indicator of föhn air than the relative humidity, due to the widespread dry bias in WRF. From assessing the air temperature fields, the warm föhn air was localised to the foot of the AP and to the southwest of the ice shelf (Figure 6.25). There were no observations at AWS5 or AWS6, however, the spatial distribution of the warm air from the WRF model suggested that the föhn effect may have influenced the near-surface conditions at both of these locations towards the end of the föhn event (6th of August).

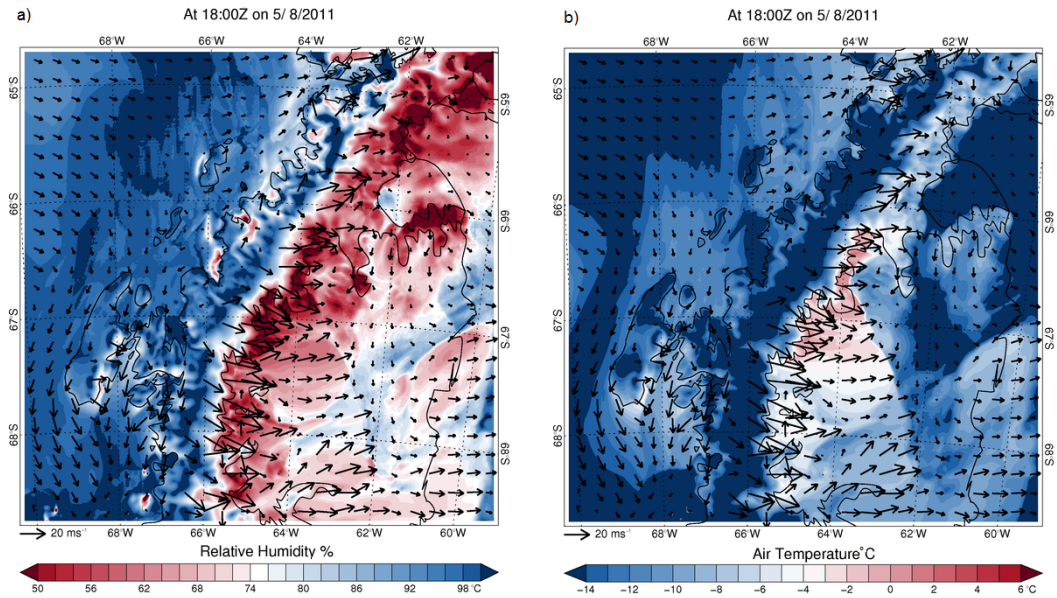

Figure 6.25: a) The 2m relative humidity and b) 2m air temperature simulated by WRF at 18UTC on the 5th of August 2011. The dry air spreads over much of the ice shelf, however this is an overestimation of the spatial extent and strength of the föhn signal. No observations revealed a föhn effect at any location except for Cole Peninsula. The air temperature output (b) provides a more accurate representation of the spread of the föhn effect during this particular event.

The second föhn event started at 18UTC on the 6th of August at Cole Peninsula, at 06UTC on the 7th of August at AWS1, and at 18UTC on the 7th August at AWS3. No föhn conditions were identified at AWS2, despite them being identified to the north and south of this location. Simulating this föhn event with the WRF model provided some explanation for this interesting spatial pattern.

A relatively warm and dry band of föhn air stretched from the AP to the ice shelf edge, approximately along the same latitude as the AWS3 location at 0600UTC on the 7th of August (Figure 6.26). Just north of this region, where AWS2 was located, the air was much cooler and more humid, which explains the lack of föhn identification at AWS2. This small patch of non-föhn air was relatively localised, as the majority of the ice shelf experienced warm and dry conditions. Had the AWS2 location been slightly south or west of its actual location, then föhn conditions would likely have been observed. If this small patch of relatively cool and moist air developed relatively often, it may explain the reduced frequency of föhn events at this location compared to elsewhere on the ice shelf.

The AMPS run was not able to simulate the spatial distribution of the föhn air. The band of warm, dry föhn air which was located over AWS3 was not visible in the relative humidity or temperature fields simulated by AMPS (Figure 6.26). The ice shelf was cooler and more humid in AMPS than in WRF. The two model runs suggest differing spatial distributions of the föhn air. From the WRF run, föhn conditions would likely have been identified at AWS5 and AWS6 if the instruments were operational. However, from assessing the AMPS output, the air surrounding AWS5 and AWS6 would have been too cool and moist to be detected as föhn. AMPS also simulated a lack of föhn air over the AWS3 location, despite the observations proving that a föhn event was detected. This highlights the benefit of using high-resolution models for simulating the spatial distribution of föhn events. The only location on the ice shelf without (WRF simulated) near-surface föhn conditions was AWS2.

The band of warm, dry föhn air which was observed at AWS3, was present over the ice shelf for approximately 18 hours before being displaced by cooler, more humid air advected from the northeast. The föhn event continued at AWS1 for 12 hours longer

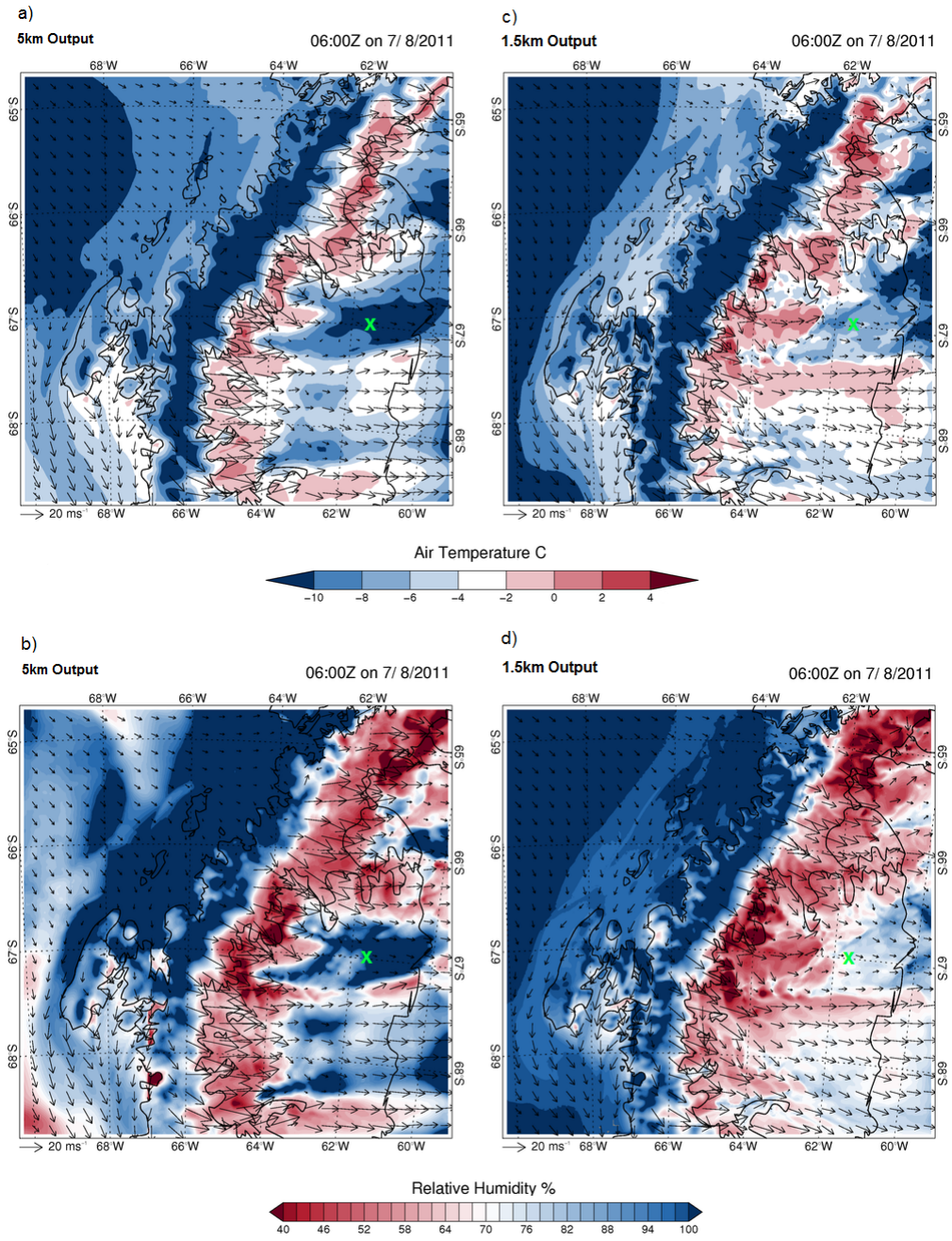

Figure 6.26: Left panels (a and b): near-surface air temperature (a) and relative humidity (b) from the AMPS run at 06UTC on the 7th of August 2011. Right panels (c and d): near-surface air temperature (c) and relative humidity (d) simulated by WRF during the same time period. The warm band of föhn air was more defined in the WRF model.

than at Cole Peninsula.

The WRF simulation suggested that at Cole Peninsula, the second föhn event did not terminate at 18UTC 7th of August, but continued for the next few days. This suggests that the three föhn events from the 7th to 10 of August were actually one, long event. This mimics the AMPS algorithm, which suggested one long föhn event. The periods in between the föhn events were not identified as 'föhn' by the AWS algorithm as the relative humidity was higher (more moist) than the thresholds used for detection. At Cole Peninsula, föhn conditions were detected when the relative humidity was below 51.8% or below 58.5% when accompanied by a 3K temperature rise. The average relative humidity value from the non-föhn periods in between the föhn events was 62.7% and therefore was relatively close to the thresholds. Therefore, it is possible that there was one long event from the 7th to 10th of August, that had slightly weaker near-surface conditions. Case studies such as this are useful for validating and assessing the algorithm used to identify föhn conditions.

Despite the relatively strong westerly winds suggested by the ERA-Interim data, the föhn events observed and simulated here do not stand out as 'textbook' föhn events. The föhn air from the second event was relatively widespread, however there were no enhanced föhn conditions at the foot of the mountains. It is possible that the föhn air from the first event would have propagated across the ice shelf if the cold, stable boundary layer had not been present, however there is no evidence of this. The textbook examples of föhn events with perpendicular winds approaching an idealised barrier, and föhn wind development along the full length of the barrier, are not observed regularly in reality. The topography of the AP is complicated and there are many gaps and valleys that direct the flow. The shape and length of the AP also reduces the idealised development of föhn winds. The AP is over 1300km long and is curved in places. Therefore, the winds do not always meet the Peninsula perpendicularly, leading to föhn event development along a section of the AP, rather than along the full length. Furthermore, ambient conditions over the ice shelf, and the low-level wind direction can interrupt, erode or terminate föhn conditions at the near-surface.

6.6.5 Winter Discussion

During winter, no observations were made at AWS5 or AWS6 due to the dependence of the instruments on solar radiation for energy. From approximately late May, through to the start of September, no measurements are taken south of -67.57° (AWS3). Therefore the analysis of the frequency of föhn events, and their spatial distribution, is likely to be underestimated. Investigating the spatial distribution of föhn air in winter was the aim of this case study, to address whether the gap in observation was an issue.

The propagation of the first föhn event was halted by a cold, stable boundary layer over the ice shelf. This was significantly deeper and colder than the cold pool simulated in the Autumn case study, as expected due to the lower average temperatures and lack of solar radiation during winter. As a consequence of this, föhn conditions were limited to the foot of the AP, and were only identified at Cole Peninsula. Towards the end of this föhn event, the föhn air on the south of the ice shelf was able to extend a little further. It would likely have been observed at AWS5, and possibly at AWS6, if observations were available. The interaction between the föhn air and cold pools is discussed in the autumn case study.

The interruption of the three föhn events succeeding this first one was not due to the redevelopment of the cold pool. During winter, cold pool development is frequent, and they can often persist for long periods of time (King *et al.*, 2008). However, as presented in the results (Figure 6.24), the temperature does not decrease between the events, and a cold pool does not form. Instead, it is suggested that there may have been one continuous föhn event from the 7th to 10th of August, instead of three shorter ones.

The thresholds used in the AWS algorithm were selected based on assessment of the climatology or average (four years of data only) of relative humidity and temperature values. The thresholds did not take into account the seasonal variability of the conditions. The three latter föhn events identified at Cole Peninsula were below the relative humidity and temperature thresholds, and were therefore categorised as föhn conditions. However, the periods in between the events were categorised as non-föhn, even though their relative humidities were only 1% or 2% above the threshold. The wind direction remained westerly to northwesterly and the air temperature remained

above freezing in between the föhn events, which further leads to the conclusion that there may have been only one föhn event.

The second föhn event identified at Cole Peninsula (7th of August) was spatially more expansive than the first. The spatial distribution was interesting, as the föhn air was not observed at AWS2, but was observed further north and south. This was attributed to a patch of cooler, more moist air surrounding the AWS2 location. An elongated band of warm and dry air stretched across the ice shelf and prompted the identification of föhn conditions at AWS3. As with the first föhn event, had the AWS5 and AWS6 instruments been operational, föhn conditions would likely have been identified.

6.7 Discussion of High-Resolution Simulations

Simulating föhn events in this manner puts the observations into a wider perspective. From the observations, we can only tell what the conditions are like at specific points, and this limits the spatial analysis. From the WRF simulations the localised features such as the band of warm air, and the patch of cool air provide more information on the distribution of the air across the ice shelf. The WRF simulations are also useful for filling short-lived observation gaps, such as investigating near-surface conditions during winter when AWS5 and AWS6 were unavailable. However, the conditions simulated by the model should be used cautiously. In all of the case studies presented here, the model sometimes struggles to represent the near-surface conditions, especially the relative humidity.

In all of the case studies, and at all of the locations except for Cole Peninsula, there was a dry bias in WRF. The WRF model underestimated relative humidity during non-föhn conditions too. The underestimation of relative humidity by WRF was also discovered by Wille *et al.* (2016) over the Ross Ice Shelf. Wille *et al.* (2016) found that in all seasons a dry bias was present at the near-surface and 30m level, and during March to August the dry bias was greatest. This may also be the case in the current case studies, as the dry biases during Autumn (May) and Winter (August) were larger

than those in Spring (October). Diagnosing the cause(s) of the dry bias in WRF is ongoing. The Wille *et al.* (2016) study suggested that the MYJ boundary layer scheme used in AMPS and WRF is unable to parameterise the sublimation of blowing snow. However, in the current study, the AMPS runs did not show a considerable dry bias, and the dry bias was largest during periods of low wind speed.

The poor representation of the relative humidity at most locations may be attributed to increasing the horizontal and vertical resolution of the model domain in WRF, and the increased resolution of the ingested topography. Increasing the vertical resolution does little to improve the near-surface forecasts, but does improve the synoptic and mesoscale weather situation (Zhang *et al.*, 2013). This finding may go some way to explain the improved representation of many of the mesocale föhn features (föhn jets, föhn propagation and dissipation across the LCIS), whilst the simulation of the near-surface variables was similar to, or worse than the coarser-resolution run. This suggests that the issues in representation of near-surface conditions is likely due to the boundary layer used.

The relative humidity was most accurate at Cole Peninsula. This is potentially due to the drier ambient conditions at this location, which the model accidentally resolves well due to the dry bias. However, it may also be due to the altitude of Cole Peninsula. Regional models often struggle to resolve the near-surface conditions. There are many interactions between the parameterisations for the boundary layer, surface layer, land surface model, radiation and turbulent fluxes, and the complex topography (Zhang *et al.*, 2013). Therefore, with Cole Peninsula being $\sim$ 400m a.s.l, some of the errors arising from modelling the near-surface processes may be reduced.

Both the AMPS and WRF runs regularly overestimated peak wind speed during the föhn events. On some occasions, the WRF model performed worse (e.g at AWS1 during Winter), on other occasions, the AMPS model performed worse (e.g at AWS5 in Spring). The overestimation of wind speed by WRF when the MYJ boundary layer scheme is used is well documented (e.g Bromwich *et al.* 2013; Hines & Bromwich 2008; Valkonen *et al.* 2014; Wille *et al.* 2016). As the positive bias was simulated by both the AMPS and WRF runs during these case studies, the MYJ scheme is likely the cause of

this issue.

Both the AMPS and WRF runs estimated similar near-surface temperature values. Prior to the föhn events, both runs overestimated air temperature (positive bias), however after the föhn events, the temperature was slightly better represented, although with a small negative bias. One direct impact of the föhn effect is the 'cloud-clearing' effect over the LCIS (Elvidge *et al.*, 2015). During föhn events the representation of the temperature was more accurate. However, prior to, and after the föhn events, when more clouds would likely have been present over the ice shelf, the largest biases were present. After the föhn events, the simulated air temperatures at most locations improved. Due to the relatively short case study periods, it is unknown whether the warm bias in air temperatures resumed a while after the cessation of the föhn events, when cloud cover increased again.

The air temperature biases and diurnal temperature fluctuations were larger in WRF than AMPS, especially during the nighttime. Many of the errors arising from the WRF runs are linked to the poor representation of clouds in the model, which influences the radiation fluxes, surface temperature and near-surface variables. The poor representation of clouds in WRF are most evident during the summer case study (Figure 6.27). The cloud fraction is a parameter output by WRF, and it was observationally-derived in 30-minute intervals by the AWS2 SEB model. Observationally-derived values of cloud fraction were only available during the summer case study. WRF unrealistically simulates a large swing in cloud fraction from 0 to 1 diurnally. Whereas, the observationally-derived values show a cloud fraction of over 0.6 throughout most of the case study. The simulated periods with no cloud cover (a cloud fraction of 0) correlate to the periods of (overestimated) high shortwave incoming radiation shown in Figure 6.6 in Section 6.3.5. Cloud cover in WRF was only realistically simulated during the föhn period, when the observationally-derived cloud fraction dropped to 0.03 due to the cloud clearing effect. The erroneous cloud cover simulation by WRF leads to poor representation of the radiation fluxes, and therefore the surface and air temperatures throughout the case study.

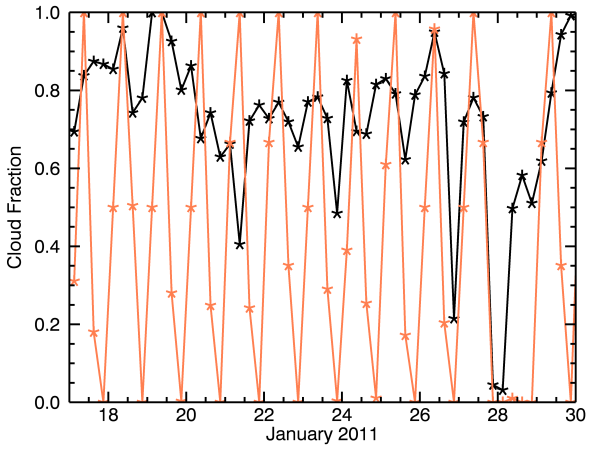

Figure 6.27: The cloud fraction (between 0 for clear skies, and 1 for full cloud cover) simulated by WRF (orange) and observationally-derived at AWS2 (black) during the summer case study from the 17th to 31st of January 2011.

Despite the clear errors in the simulation of cloud cover in WRF, there are advantages to using high-resolution simulations to analyse the spatial distribution of the föhn flow. Notably more information was gathered on the spatial distribution of the föhn flow over the LCIS when using WRF rather than AMPS. The small-scale spatial patterns, föhn jets, non-linear flow features (hydraulic jump and downslope winds) and localised föhn-enhancements were all more defined in the WRF simulation than in AMPS. Using the WRF simulations could provide a more accurate estimate of the impact of föhn winds on surface melt.

In the spring case study, the AMPS algorithm did not identify föhn despite a near-surface identification. In the winter case, the AMPS algorithm suggested a long föhn event, but the AWS algorithm did not. As the two algorithms do not use the same procedure to identify föhn, the two algorithms will not always agree on whether föhn conditions are present or not. There was a relatively good agreement between the two algorithms. Over 80% of the time, the two algorithms agreed on either 'föhn' or 'non-föhn' conditions. However, it may be useful to assess the föhn conditions identified from each method separately. This way, the impact of the föhn air on the surface could

be assessed with the AWS algorithm, and the dynamics and mechanisms responsible for the föhn development could be assessed with the AMPS algorithm. This will be discussed more in the 'Future Work' section of the Synopsis chapter.

6.8 Conclusions

The use of high-resolution simulations using the WRF model provides further understanding of the spatial distribution of föhn winds over the LCIS. A number of features were evident in the high-resolution simulations, which were absent or poorly resolved in AMPS and the observations. These include föhn jets, a localised föhn effect over Jason Peninsula and the interaction between föhn winds and cold pools on the ice surface. The relatively sparse observational network is able to capture the ice shelf-scale föhn propagation and the horizontal gradient in föhn strength, however it is unable to capture the small-scale and transient features.

The increased vertical resolution of the WRF simulations compared to AMPS provided information on the vertical structure of föhn winds and on the presence of a hydraulic jump during the Autumn case study. More work is needed in this area to assess the influence of the surface layer stability and the flow regime on föhn air distribution. This research was able to provide an insight into the interaction between strong surface stability and föhn winds, however it is unknown whether föhn air acts to erode or dynamically push cold air away from the LCIS surface.

The poor representation of cloud cover and SEB components in WRF leads to relatively large mean biases in the near-surface temperature, especially during the summer case study. The overestimated diurnal air temperature cycle was prompted by the large magnitude of change in the cloud cover and shortwave incoming radiation. This characteristic was evident in both the spring and summer case studies, when shortwave incoming radiation was highest. Assessing the impact of föhn winds on the surface of the LCIS through modelling is not ideal until the representation of clouds is improved.

High-resolution simulations of föhn events through case studies have been conducted before. In the current study, they have been used as a tool for validating the föhn identification algorithms and to gain an understanding of what influences the propagation of föhn air over the LCIS. Therefore, this work is novel, as features such as cold pools and localised föhn effects were identified from the simulations which were previously unexplored. More work is required to fully assess the validity of the föhn identification algorithms and to quantify the impacts of föhn winds on the ice shelf surface, as outlined in Chapter 7.

Chapter 7

Synthesis and Conclusions

7.1 Introduction

This is the final chapter of the thesis. Its purpose is to synthesise the main findings of the project, and discuss the wider context of the results. The research in this thesis was motivated by the 'föhn hypothesis'. This suggests that increased frequency of föhn winds over the AP has led to near-surface warming which may have contributed to the destabilisation of Larsen A and B ice shelves in 1995 and 2002 respectively (Marshall *et al.*, 2006). The current frequency of föhn winds over the LCIS was previously unknown, and therefore any increase in frequency could not be estimated. The spatial extent of föhn winds over Larsen C was also largely unknown. Previous studies of föhn winds in the region were limited to a handful of case studies, aircraft observations, or near-surface observations at only one or two locations. Therefore, one main aim of this research was to investigate the spatial and temporal distribution of föhn winds over LCIS. The second aim was to assess the impact that the föhn winds have on the ice shelf.

In order to address the main aims, a number of research questions were suggested. This research aimed to address the following:

- ***Develop and employ a föhn detection algorithm for both near-surface observations and archived model output.***
- ***What is the spatial distribution of föhn conditions across the LCIS?***
- ***How frequent are föhn events over the LCIS?***

- ***What is the impact of föhn conditions on the ice shelf, and in particular do föhn winds initiate surface melting?***
- ***Can high-resolution modelling of individual föhn events reveal additional information about the horizontal and vertical structure of the föhn winds?***

In order to investigate the frequency and spatial distribution of föhn winds, a novel detection algorithm had to be developed and applied to the observational data. An adaptation of a relatively new methodology for identifying föhn conditions from model data was also employed. This was presented in Chapter 3. The number of föhn conditions identified from the two algorithms were presented in Chapter 4, along with their near-surface characteristics and spatial patterns. The impact of the föhn conditions on the ice shelf surface was presented in Chapter 5, with an additional emphasis on the potential for föhn winds to initiate surface ice melting. The spatial distribution of individual föhn events, and their interaction with the boundary layer were assessed by high-resolution modelling from the WRF model. Three case studies of the high-resolution simulations were presented and discussed in Chapter 6.

A summary of the main findings is now presented in the current chapter, and the research aims outlined in Chapter 1 are reassessed. The chapter then outlines the possible future research avenues prompted by this research, before concluding with final remarks, and setting the findings into the wider context.

7.2 The Main Findings

7.2.1 Chapter 3: The Föhn Identification Algorithms

In order to investigate the impact of föhn winds on the surface of the LCIS, a method had to be developed to identify föhn conditions. Previous to this project, föhn winds were largely analysed on a case-by-case basis, when detection of the föhn conditions was unnecessary. No algorithm existed to detect föhn conditions from over the LCIS prior to this project. A novel semi-automatic algorithm has been developed to identify

föhn conditions from near-surface observations.

Data from six AWS were used from 2009 to 2012. This was one of the largest networks of AWSs in the Antarctic. This is also the only study to use a spatially extensive network of AWSs to identify föhn conditions over the LCIS. In combination with the AWS data, archived model output from AMPS was also used to identify föhn conditions.

The AWS algorithm is a novel method for identifying föhn winds from near-surface observations, specifically developed for the data and location of this research. It was necessary to develop a unique algorithm as opposed to applying one used in previous research (e.g Speirs *et al.* 2010, 2013), as the characteristics of föhn onset are specific to each location, and often specific to individual valleys (Vergeiner, 2004). The AWS algorithm uses a number of thresholds and criteria to detect near-surface changes to the wind direction, air temperature and relative humidity as the föhn air flows across the surface.

As the LCIS has a relatively large surface area for the föhn air to propagate over, the characteristics of the föhn air differ by location. It was essential that the AWS algorithm was able to identify the föhn characteristics at each location. Therefore, as opposed to numerous individual algorithms, which only identified föhn conditions at a specific location, the algorithm was developed so that only one algorithm was able to be easily adapted to take account of the localised conditions. Therefore, the thresholds within the algorithm are based on statistics (e.g the 10th percentile of relative humidity values), and the absolute values are determined by the localised conditions (e.g the 10th percentile at Cole Peninsula was 51.84% whereas at AWS2 it was 72.63%).

The algorithm used to detect föhn conditions from the AMPS output was originally used for detecting föhn winds over South Georgia by Bannister & King (2015), and it was adapted for use over the AP. As this algorithm detects the föhn development from the interaction between the airflow and the mountain, it can be applied to many mountainous regions. This was the first use of this relatively new algorithm over the AP and LCIS. Similar to the AWS algorithm, it was crucial that this algorithm could be adapted to take into account localised conditions. For example, the height of the AP

varies along its length, and this needed to be accounted for when setting the thresholds for each location.

The AMPS algorithm did overestimate the number of föhn conditions relative to the number identified using the AWS algorithm. To reduce the overestimation, and to ensure that only föhn air was identified near the surface, the two algorithms were combined. Therefore, for any time point to be categorised as a föhn period, it must have displayed both near-surface conditions to meet the AWS algorithm, and the upper-air characteristics to meet the AMPS algorithm. The föhn conditions analysed throughout the thesis refer to only those times which satisfied both the AWS and AMPS algorithms. The algorithms agreed on either föhn, or non-föhn conditions over 80% of the time.

As the algorithms were combined, both AWS and AMPS data must have been available to identify föhn conditions. In the absence of observational data, AMPS can not be used to accurately determine the number and location of föhn events. As the AMPS algorithm overestimated the number of föhn conditions, and there are errors within the model such as the timing and location of synoptic systems, the AMPS model alone can not be trusted to investigate the spatial and temporal distribution of the föhn winds over the LCIS.

The algorithms presented in Chapter 3 were developed and implemented to identify föhn conditions for six locations over the LCIS. Föhn conditions were identified at all locations, and during the four-year period. Therefore, the first aim (***Develop and employ a föhn detection algorithm for both near-surface observations and archived model output***) was successfully met.

7.2.2 Chapter 4: The Spatial and Temporal Distribution of Föhn Winds and Their Near-Surface Characteristics

From the algorithms, 878 föhn conditions were identified from 2009-2012, which equates to 15% of the four-year period. The least number of föhn conditions were identified in 2009, and the most were identified in 2011. In 2011, the Cole Peninsula AWS was

active, and over 190 föhn conditions were identified at this location in just one year. This skewed the data and made it appear as though more föhn conditions were identified in 2011 than in any other year. However, when assessing only the locations which had active AWSs for all four years (AWS2, AWS3, AWS6), it was revealed that fewer föhn conditions were identified in 2011 than in other years. Including Cole Peninsula data was beneficial to investigate the propagation of föhn air from the very foot of the mountains to the eastern edge of the LCIS, however it did skew the data in 2011.

The main finding from assessing the temporal characteristics of the föhn conditions is that the highest number of föhn events were identified in spring (SON). In 2010, this was particularly prevalent, as over 65% of the identified föhn conditions were during spring. On average one in every three days experienced a föhn event in spring. This finding was particularly interesting due to the heightened impact of spring föhn conditions compared to other seasons. The impact of spring föhn conditions was assessed in Chapter 5, and is summarised in Section 7.2.3.

Föhn events over the LCIS were shorter than identified elsewhere on the AP and South Georgia. This may be due to the differing algorithms used. It may also be due to the combination of algorithms in the current study. Longer föhn events were detected when only those periods identified by the AWS or AMPS algorithms were assessed separately. However, combining the algorithms lead to a shortening of some föhn events as the two algorithms did not always agree on whether a period did or did not display föhn characteristics. The average duration of föhn events was 12.5 hours.

Despite the relatively short duration of them, the föhn events often occurred within quick succession of one another, leading to multiple föhn days in a row. When assessing the density of föhn events within a moving week-long period, there were over 200 occurrences with a cumulative total of three days of föhn conditions within a week. On two occasions, there were over 23 föhn conditions in one week, which was equivalent to 5.75 days worth of föhn events occurring in just seven days. Therefore the combined effect of numerous föhn conditions can have implications of the ice shelf surface.

Another important finding from this project is that föhn conditions were identified over the whole ice shelf. This included frequent föhn identification at AWS6, the most southerly location on the AP to record föhn conditions. Near-surface observations of föhn winds this far south on the AP was a novel finding, as it was previously assumed that föhn conditions were more frequent and stronger on the north of the ice shelf. However, the average föhn temperature at AWS6 was similar to other locations over the LCIS, and föhn conditions were identified over 130km from the foot of the AP, and over 260km in the north-south direction.

Two interesting spatial patterns were identified in the observational data. Firstly, a west to east propagation of the föhn air led to stronger (lower relative humidity) föhn conditions closer to the AP (west), and a weakening of the föhn signal with distance from the AP (east). This generated a west to east gradient in decreasing föhn strength. This was not unexpected, as previous studies of individual föhn events had seen this spatial pattern in model simulations (e.g Elvidge *et al.* 2016).

The second spatial pattern was a north to south gradient in decreasing föhn strength. The relative humidities were lower, and the air temperatures were higher further north. This signal was not as clear as the west to east gradient in the observations. As the locations were not all equidistant from the AP, the effect of the föhn propagation influenced the spatial pattern.

The near-surface conditions during all föhn events simulated by AMPS revealed that the dominant spatial pattern over the LCIS was a northwest to southeast gradient in decreasing föhn strength. This appears to be a combination of the two spatial patterns observed by the AWSs. This signal is influenced by the propagation of föhn air across the ice shelf under the northwesterly winds which dominated the wind direction during föhn conditions. Due to the relatively sparse network of observations, the AMPS output is useful at providing more information on the spatial distribution of the föhn air. On an individual basis, the propagation of föhn air across the ice shelf was influenced by a number of factors including the prevailing wind direction at the height of the AP, low level wind direction and the presence of a cold pool on the ice shelf. This was investigated on a case-by-case basis using high-resolution simulations

with the WRF model, which is summarised in Section 7.2.4 below.

The results outlined in Chapter 4 answer both ***'What is the spatial distribution of föhn conditions across the LCIS?'*** and ***'How frequent are föhn events over the LCIS?'***.

7.2.3 Chapter 5: The Impact of Föhn Winds on the Surface Energy Balance and Surface Melting

The föhn winds influenced a number of components of the SEB. Some components became more positive (increased net shortwave radiation and increased sensible heat flux), and some components became more negative (decreased latent heat flux, negative net longwave radiation) under föhn conditions. In some cases, the components balanced each other out, and there was only a limited amount of residual energy available for melting. However, in other cases, the sensible heat flux and increased shortwave radiation outweighed the negative responses, and there was a large amount of residual energy available for melt. Similar results were also found by Elvidge *et al.* (2015); Kuipers Munneke *et al.* (2012) when assessing the impact of individual föhn conditions on the ice shelf.

The average or climatological response to föhn conditions was an increased amount of energy available for melt. The average daily energy available for melt during non-föhn periods was 1.6Wm^{-2}, whereas during föhn conditions it was 7.6Wm^{-2} on average. This lead to five times more melt during föhn conditions than during non-föhn conditions. Due to the uneven distribution of föhn conditions throughout the year, this value could be skewed, if for example, all föhn conditions happened to occur in summer, when sensible heat flux and shortwave incoming radiation were already higher than in other seasons.

To combat this, the seasonal effect of föhn conditions was also assessed, and it was found that in spring and summer, föhn conditions caused a significant increase in the energy available for melt, and daily melt amount, but that during autumn and winter,

föhn conditions had relatively little impact on the surface. Föhn conditions create additional melting on the surface of the ice shelf. The impact of föhn-induced melting on the ice shelf was evident over 130km from the foot of the AP.

Under non-föhn conditions during spring, the amount of melt was on average less than 0.2mm w.e day^{-1}. During föhn conditions in spring, the average amount of melt was approximately 1.75mm w.e day^{-1}, more than the average amount of melt in summer. During summer, the picture was similar. Even though there was already a large amount of melt energy and melt amount during summer (compared to other seasons), föhn-induced melting lead to an average of 3.5mm w.e day^{-1} melting. Therefore, the föhn events can extend the melt season, by prompting surface melt during spring and they can significantly increase the amount of melt in both spring and summer.

Prior to this study, the impact of föhn conditions on surface melt had been assessed on a case-by-case basis by Elvidge *et al.* (2016) and Kuipers Munneke *et al.* (2012). Recently, King *et al.* assessed the impact of a number of föhn conditions on the seasonal melt. King *et al.* found that whilst individual föhn events had a large impact on the surface melt, the combined effect of the föhn conditions was not significant when assessed over the whole season. This result contradicts the findings here. In the current study, the impact of the föhn conditions in spring and summer was significant on the seasonal scale. The current study assessed the impact of many more föhn conditions than the King *et al.*, which may explain the differing results. Until now, the average response of the SEB to föhn conditions over the LCIS was unknown. This research has allowed ***'What is the impact of föhn conditions on the ice shelf, and in particular do föhn winds initiate surface melting?'*** to be answered.

7.2.4 Chapter 6: High-Resolution WRF Modelling of Föhn Case Studies

The observation network used here is one of the densest networks in the Antarctic, however it is still relatively sparse. It is comparable to having just six observational sites in Wales. As discussed in Chapter 4, the föhn conditions were observed over the

whole ice shelf, but the near-surface characteristics were quite variable. To gain a better understanding of the spatial distribution of the föhn air, and the features which can control it on the local scale, a number of föhn events were simulated using the WRF model at high-resolution (1.5km horizontal resolution, 70 vertical levels).

A number of spatial features were identified from the simulations including the interaction between the föhn air and föhn jets, which had previously been identified by Elvidge *et al.* (2015) in a number of case studies, but which were absent from the near-surface composites in AMPS. The föhn jets were absent in the AMPS composite figures (Chapter 4) because of the poorly resolved topography in AMPS. It is also possible that föhn jets only occurred during a handful of föhn events, and that they were not a dominant spatial pattern. If this is the case, the föhn jets may modulate föhn conditions only occasionally, and the warm, dry föhn air may be having a greater effect on the surface. The föhn jets emanate from various gaps, depending on the wind direction and speed and up-barrier blocking, and therefore they did not have the same spatial pattern each time.

The WRF model simulations were better at representing the interaction between ambient air flow and the föhn air. Föhn jets were simulated by the WRF model during the föhn event on the 16th May 2011, which was assessed as part of the Autumn case study. The simulation of föhn jets in the WRF case studies, and in high-resolution modelling by Elvidge *et al.* (2015), suggests that a horizontal resolution of 1.5km is required to accurately resolve the jets. The jets were cooler and moister than the surrounding föhn flow, however they were not as well defined in the WRF output as in the MetUM output used by Elvidge *et al.* (2015).

Both the Spring and Autumn case studies provided examples of the variability in the interaction between cold, ambient air and the warm föhn air. In the Spring case study, the föhn air was restricted to the northern section of the ice shelf on the 9th October 2011, as the cold air further south prevented the propagation across more of the ice shelf. In the Autumn case study, föhn air from an event on the 13th - 15th May 2011 was able to erode a cold pool and propagate across the ice shelf, allowing the föhn signal to be detected by all six AWSs. The föhn event was identified at AWS1 and Cole

Peninsula first, and was identified 36 hours later at AWS6 after moving southwards. The WRF model provided more accurate simulations of the wind direction, mixing of the two air masses and propagation of the föhn air than the AMPS model.

The WRF model also gave an insight into periods when the AWS and AMPS algorithms did not agree on whether a period displayed föhn characteristics. During the Spring case study, föhn conditions were identified by the AWS algorithm at AWS2 on the 9th October 2011, however there was no corresponding AMPS algorithm detection. Assessment of the WRF output revealed that the interaction between the northwesterly föhn air and southeasterly airflow created a localised 'curl' of the wind. The föhn air was able to propagate to AWS2, but did not spread any further west to AWS5, or further south to AWS3. As this was a near-surface, localised pattern, there was no corresponding flow of air over the AP, which meant that no föhn conditions were detected by the AMPS algorithm.

Assessing the disagreement between the two algorithms was not the main aim of conducting the case studies, however it does give an example of the many advantages of using high-resolution models. The WRF case studies also provided additional information on the vertical structure and dynamics of föhn winds. A hydraulic jump was present during one of the föhn events simulated as part of the Autumn case study. The associated downslope windstorm and two areas of isentropic drawdown were present in the WRF simulation, but were absent, or less well defined by AMPS. Hydraulic jumps are known to occur during downslope windstorms and föhn winds over LCIS under non-linear flow regimes (Elvidge *et al.*, 2016). The definition of the hydraulic jump was poorer in the AMPS simulations, largely attributed to the lower number of vertical levels.

There were some disadvantages of using WRF, including the underestimation of the relative humidity (typically too dry), and enhanced diurnal cycle. These features have been identified in previous simulations with WRF (although not over the LCIS or during föhn conditions) (Deb *et al.*, 2016; Wille *et al.*, 2016; Zhang *et al.*, 2013). It was not within the aims of this research to investigate the main issues within WRF or attempt to combat them. However, as shown in Chapter 6, a number of the issues

cast doubt on the use of WRF as a tool for investigating the impact of föhn winds on the surface of the LCIS. The major issues involved the representation of clouds, the exaggerated diurnal air temperature bias and the cold bias during the night. The poor simulation of cloud cover influences the SEB components and the surface fluxes, which contributed to the near-surface meteorology issues. However, the surface and boundary layer schemes used within the model will also have influenced the air temperature. The schemes used in WRF were the same as in AMPS, as only the increased horizontal resolution was being assessed. However, previous studies have shown that changing the boundary layer scheme can influence the turbulent fluxes and near-surface variables in WRF (Deb *et al.*, 2016). Simulating the boundary layer accurately is crucial for investigating the near-surface conditions, especially under statically stable conditions which dominate in the Antarctic. Unrealistically high outgoing turbulent fluxes can lead to a cooling of the surface and therefore a cold bias in the near-surface air temperatures.

From simulating only three case studies, a lot of information about the spatial distribution and vertical structure of föhn winds has been gained. Regional modelling of föhn winds contributes additional information to the point-location data, and may be the best way to investigate individual föhn events. However, on the longer time scale, using observations and coarser archived model output was the best way to investigate the frequency and longer-term spatial distribution of the föhn air. Therefore the results from this chapter show that the research question: ***Can high-resolution modelling of individual föhn events reveal additional information about the horizontal and vertical structure of the föhn winds?*** has been successfully answered.

7.3 Future Work

The research aims set out at the start of the research project were all successfully met. However, a number of other questions were raised whilst undertaking the research, which were not answered, and these will prompt future work.

Is the frequency of föhn conditions increasing over time? This was the first study to assess the frequency of föhn winds over the LCIS. The föhn hypothesis

suggests that there has been an increase in the frequency of föhn winds over the last half century due to the links with the Southern Annular Mode (SAM). As only four years of data were used in this study (and some locations only had one year of available data), changes in the frequency of föhn conditions over time was not possible. Therefore, the first, and possibly largest research question which emanates from the current research is whether the frequency of föhn conditions has changed over time.

A number of the AWSs remain active to this day. AWS2 and AWS3 have been near-continuously recording since 2009, and are still active today. Similarly, AWS1 remains active after its deployment in 2011. Therefore, this study could now be extended to identify föhn conditions from these three locations for up to eight years. A study of this approximate length was conducted by Bannister & King (2015), who found that over South Georgia, the frequency of föhn events had not changed significantly in nine years. The year to year variability in the number of föhn conditions was quite large, therefore extending the period of study would also be useful to identify any trends in the frequency. Further north on the AP, Cape *et al.* (2015) used data from 1962 to 2010 from one AWS, and discovered that the most notable years for föhn events were 1999, 2000 and 2001, and that a positive trend in monthly föhn frequency was evident during summer. Given the urgency in understanding the longer-term trends in föhn frequency, it might be useful to use a number of data sources to extend the study period. For example, it might be useful to use methods which can asses the frequency of föhn winds using the large-scale flow or longer modelling studies.

A longer observational period would also be useful to provide confidence in the spatial distribution of föhn winds found in the current study, to ensure that the patterns seen over four years are indicative of the longer-term average.

Was it useful to combine the AWS and AMPS algorithm, or should the identified föhn conditions have been assessed separately? The analysis of the frequency and spatial distribution of föhn winds over the LCIS relied on the decision to combine the algorithms. The major advantage of this was that it ensured that föhn conditions were detected at the near-surface and upper-level, and that mis-categorisation of föhn due to advection of warmer air near the surface was not a problem. It also

reduced the overestimation of föhn conditions from the AMPS algorithm, which was a known problem in AMPS (Speirs *et al.*, 2010; Steinhoff *et al.*, 2013). However, there were a number of times which were likely mis-classified as non-föhn, due to a disagreement between the two algorithms.

In future, it may be useful to allow a time lag of six to 12 hours between the two algorithms, as was allowed by Bannister (2015). This would reduce the times when the two models disagreed, and more föhn conditions would have been identified. Another adaptation of the method would be to analyse the spatial and temporal distributions of the föhn events identified from the AWS algorithm and AMPS algorithm separately. If the same temporal and spatial characteristics are found from analysing the föhn events in this way, it would ensure that the findings from the current study are robust. If different spatial patterns are identified, it may reveal that combining the algorithms influenced the patterns found, and that this may not have been the best decision.

What is the relationship between cold pools and the föhn air distribution? Cold pools are known to prevent föhn air from reaching the surface in some valleys in the Alps (Drobinski *et al.*, 2007; Zängl *et al.*, 2004). Only limited research has investigated the interaction between föhn air and cold pools over the Antarctic. The research presented here, and by Elvidge *et al.* (2016) has touched on this interaction. However the observational data available for the current project were not able to provide enough information to thoroughly investigate how the two phenomenon are related.

Assessing the identified föhn events from each algorithm separately may reveal more information about the dynamics of the föhn winds, and the interaction with the boundary layer. If föhn conditions were identified by the AMPS algorithm, but there was no associated near-surface conditions, it may be due to the presence of a statically stable cold pool on the ice shelf. Similarly, observations taken over multiple levels may provide more information, such as that from a meteorological tower.

This is an emerging area of research at the moment. Over the Alps, a project has just been funded to assess the penetration and interruption of föhn winds due to the development of cold pools (Gohm A., personal communication, February 2017). That

research will include data from a Doppler wind lidar, which will take vertical and horizontal observations during föhn events. Similarly, research using observations from a 30m tall meteorological tower has been suggested, to assess the relationship between the boundary layer stability and downslope winds on the Ross ice shelf (John Cassano, personal communication, February 2017). Cold pools can be persistent in some areas of the Antarctic, which could make it an ideal location to assess these interactions.

Cold pools may have a modulating influence over the impact of the föhn winds. If cold pools are able to weaken the föhn signal, reduce the duration of the föhn event or completely stop the interaction with the surface, they may reduce the impact of the warm, dry air on the surface. Therefore, to fully assess the future stability of Larsen C (and other) ice shelves, it may be necessary to conduct this research.

What impact are föhn events having on the glaciers feeding into Larsen C ice shelf? It has been found that the föhn effect was strongest closer to the AP, and that föhn-induced surface melting has been observed at the foot of the mountains (Luckman *et al.*, 2014). Therefore the impact of the föhn air is greatest where the land ice meets the ice shelves. Sea level rise is an indirect impact of ice shelf disintegration, due to the accelerated loss of glaciers which fed into the ice shelves. Is it possible that the föhn effect is responsible for direct sea level rise due to melting of glaciers on the leeside of the AP? Glaciers and land ice cover over 80% of the AP along almost its full length. Over South Georgia, föhn winds are at least partly responsible for the asymmetric loss of glaciers on the leeside of the island (Bannister & King, 2015).

This research could be conducted through high-resolution numerical modelling, such as used in the Bannister & King (2015) study. This would require very high-resolution topography data and model resolution to fully represent the slope, land surface type and localised topography. The model would require some validation. Therefore, near-surface observations of meteorological variables and SEB components from AWSs and snow pits may be required from numerous glaciers. Clearly, this is a large undertaking, and would require a lot of new deployments.

Other possible data sets include assessing the glaciers from satellite images to monitor the size and shape of the glaciers. This may be more easily accessible than a range of field campaigns to deploy AWSs or SEB instruments. However, the satellite images would only be available during daylight hours, which would significantly hamper the winter time monitoring of the glaciers, and the data may be limited to only a few years.

If it is found that föhn winds are responsible for glacier melt, they may have a larger impact on the region than previously thought. Not only would they be partly responsible for the surface melting on Larsen A and B which likely aided in their destabilisation, but they may also be responsible for ongoing melting and sea level rise in these areas. Clearly, this would be a large research question to address, and would not be possible solely with the data available in this project.

What are the links between large-scale (upstream) flow and föhn-induced surface melt? A previous study by Elvidge *et al.* (2016) assessed the impact of three individual föhn winds on the surface of the LCIS under linear and non-linear flow. King *et al.* studied the impact of a succession of föhn events during November 2010 over the LCIS. The current study has investigated the overall or combined impact of föhn winds from 2009 to 2012. All three studies concur that föhn winds can initiate surface melt, influence the duration of melting and extend the melt season in this region. It is now necessary to combine the studies to quantify surface melt due to the combined impact of föhn winds under non-linear flow regime and that of föhn winds under linear regime. If the non-linear regime is dominant in this region, then the melt ponds observed near the foot of the AP (Luckman *et al.*, 2014) may be due to this localised but enhanced föhn effect. Conversely, if the linear flow regime dominates during föhn events, then surface melt may extend up to the easterly edge of the ice shelf, but not be sufficient enough to cause prolonged effects.

The current study has shown that there is inter-annual variability in the frequency of föhn events, and in the impacts of föhn winds. In 2010, it was evident that a large number of föhn events in spring and summer led to an increased amount of melt. It may be possible that a particular flow regime was dominant during this year which

further influenced the magnitude of the föhn-induced melting. The links between upstream flow and föh-induced melting could be assessed using AMPS and the SEB model at AWS2, as both have been used for SEB studies related to föhn events in both the current study and in King *et al.*. Although atmospheric models may not simulate the SEB and melt details completely right (as shown in Chapter 6), it is hoped that the upstream profile would be simulated with greater accuracy. However, it may also be necessary to include other data such as vertical profiles, and increase the number of SEB observation locations. The SEB model at AWS2 provided significant insight into föhn induced melting, despite being located at a distance of over 130km from the AP. It may be beneficial to implement the SEB model and observations at locations closer to the AP.

7.4 Föhn winds and the Larsen C Ice Shelf

With the completion of this project, our understanding of föhn winds over the LCIS has expanded. Prior to this project, föhn winds were observed and investigated over the LCIS by Elvidge *et al.* (2015, 2016). Those projects uncovered the dynamics of föhn flow over the LCIS, the near-surface conditions during individual föhn events and some interesting spatial features including föhn jets. Prior to the Elvidge *et al.* studies, our knowledge of föhn winds over the LCIS was sparse, as no other study had focused on föhn winds in this area.

Further north on the AP, Cape *et al.* (2015) has investigated the link between föhn winds and larger scale circulation such as the SAM and the Amundsen Sea Low (ASL), and found a significant relationship between föhn frequency and the location and strength of the ASL. These circulation patterns were also found to influence the air temperatures associated with the föhn events in a study over the northern section of the AP by Clem *et al.* (2016). The relationship between föhn events and their associated warming over the AP is now largely understood.

Prior to the current study, the frequency of föhn winds over the LCIS and the spatial distribution of the föhn air was largely unknown, and estimates were made from

individual case studies of föhn events. From this study, the temporal patterns of föhn frequency, the duration of föhn events, and their spatial extent are now known, along with the climatological or average impacts of the föhn air on the surface of the LCIS. The current project also touched upon small-scale interactions between the boundary layer and föhn air, however only a very brief analysis was possible.

Therefore, in terms of föhn winds over the LCIS, a wealth of information is now available on the drivers of föhn events and the large scale controls over their frequency. Information has now been gathered on the dynamics of the föhn winds (Elvidge *et al.*, 2016) and their spatial and temporal distribution. However, there is still little knowledge on the small-scale interactions between the föhn air and surface layer or boundary layer, but this is an emerging research area, as mentioned above.

The AP and Larsen C ice shelf will likely remain areas of significant ongoing research over the coming decade. Currently, the future stability of the ice shelf is uncertain due to the propagation of a crack on the ice shelf edge, which will likely lead to a calving of 10% of the ice volume in the next few years (Jansen *et al.*, 2015). The recent discovery of the hiatus in regional warming (Turner *et al.*, 2016) has also lead to more research in understanding the interactions between larger-scale and regional-scale climatology surrounding the area. Furthermore, longer-term global warming will likely cause changes to the climate of the region. The most recent Intergovernmental Panel on Climate Change findings suggest that with global warming, the polar westerlies will continue to strengthen over the next century, and this will likely lead to increased frequency or intensity of föhn winds over the AP (Kirtman *et al.*, 2013).

It was crucial to understand the current temporal and spatial extent of föhn winds over the LCIS before making assumptions on the impact of the föhn winds and any changes over time. While this project did not make inferences about changes over the long term, the impact of föhn winds on the surface of the ice shelf was addressed. This project has also laid some groundwork into understanding the small-scale meteorological processes and features which may further influence the föhn-induced surface melting. This, and the impact of regional climate change, are likely to dominate research in this field over the upcoming years. Due to the possible instabilities of Larsen

C, it may now be more crucial than ever to fully assess the influence of föhn winds on the surface of ice shelves.

References

Abram, N.J., Mulvaney, R., Wolff, E.W., Triest, J., Kipfstuhl, S., Trusel, L.D., Vimeux, F., Fleet, L. & Arrowsmith, C. (2013). Acceleration of snow melt in an Antarctic Peninsula ice core during the twentieth century. *Nature Geoscience*, **6**, 404–411.

Anderson, P.S. (1994). A Method for Rescaling Humidity Sensors at Temperatures Well below Freezing. *Journal of Atmospheric and Oceanic Technology*, **11**, 1388–1391.

Bannister, D. (2015). *Foehn winds on South Georgia and their impact on regional climate*. Ph.D. thesis, University of East Anglia.

Bannister, D. & King, J. (2015). Foehn winds on South Georgia and their impact on regional climate. *Weather*, **70**, 324–329.

Barrett, J.E., Virginia, R.A., Wall, D.H., Doran, P.T., Fountain, A.G., Welch, K.A. & Lyons, W.B. (2008). Persistent effects of a discrete warming event on a polar desert ecosystem. *Global Change Biology*, **14**, 2249–2261.

Bracegirdle, T.J. (2013). Climatology and recent increase of westerly winds over the Amundsen Sea derived from six reanalyses. *International Journal of Climatology*, **33**, 843–851.

Bracegirdle, T.J. & Marshall, G.J. (2012). The Reliability of Antarctic Tropospheric Pressure and Temperature in the Latest Global Reanalyses. *Journal of Climate*, **25**, 7138–7146.

Brandt, R.E. & Warren, S.G. (1993). Solar-heating rates and temperature profiles in Antarctic snow and ice. *Journal of Glaciology*, **39**, 99–110.

Braun, M., Saurer, H., Vogt, S., Simões, J.C. & Gossmann, H. (2001). The influence of large-scale atmospheric circulation on the surface energy balance of the King George Island ice cap. *International Journal of Climatology*, **21**, 21–36.

Brinkmann, W.A.R. (1971). What is a foehn? *Weather*, **26**, 230–240.

Bromley, A. (1985). *Weather observations Wright Valley, Antarctica*. New Zealand Meteorological Service.

Bromwich, D. (1991). Mesoscale cyclogenesis over the southwestern Ross Sea linked to strong katabatic winds. *Monthly weather review*, **119**, 1736–1752.

Bromwich, D.H., Monaghan, A.J., Manning, K.W., Powers, J.G., Bromwich, D.H., Monaghan, A.J., Manning, K.W. & Powers, J.G. (2005). Real-Time Forecasting for the Antarctic: An Evaluation of the Antarctic Mesoscale Prediction System (AMPS)*. *Monthly Weather Review*, **133**, 579–603.

Bromwich, D.H., Hines, K.M. & Bai, L. (2009). Development and testing of Polar Weather Research and Forecasting model: 2. Arctic Ocean. *Journal of Geophysical Research*, **114**, D08122.

Bromwich, D.H., Otieno, F.O., Hines, K.M., Manning, K.W. & Shilo, E. (2013). Comprehensive evaluation of polar weather research and forecasting model performance in the Antarctic. *Journal of Geophysical Research: Atmospheres*, **118**, 274–292.

Cape, M.R., Vernet, M., Skvarca, P., Marinsek, S., Scambos, T. & Domack, E. (2015). Foehn winds link climate-driven warming to ice shelf evolution in Antarctica. *Journal of Geophysical Research: Atmospheres*, **120**, 11,037–11,057.

Carrasco, J.F. (2013). Decadal Changes in the Near-Surface Air Temperature in the Western Side of the Antarctic Peninsula. *Atmospheric and Climate Sciences*, **3**, 275–281.

Chen, F. & Dudhia, J. (2001). Coupling an Advanced Land SurfaceHydrology Model with the Penn StateNCAR MM5 Modeling System. Part I: Model Implementation and Sensitivity. *Monthly Weather Review*, **129**, 569–585.

Clem, K.R. & Fogt, R.L. (2013). Varying roles of ENSO and SAM on the Antarctic Peninsula climate in austral spring. *Journal of Geophysical Research: Atmospheres*, **118**, 11,481–11,492.

Clem, K.R., Renwick, J.A., McGregor, J. & Fogt, R.L. (2016). The relative influence of ENSO and SAM on Antarctic Peninsula climate. *Journal of Geophysical Research: Atmospheres*, **121**, 9324–9341.

Clow, G.D., McKay, C.P., Simmons, G.M. & Wharton, R.A. (1988). Climatological Observations and Predicted Sublimation Rates at Lake Hoare, Antarctica. *Journal of Climate*, **1**, 715–728.

Cohen, A.E., Cavallo, S.M., Coniglio, M.C. & Brooks, H.E. (2015). A Review of Planetary Boundary Layer Parameterization Schemes and Their Sensitivity in Simulating Southeastern U.S. Cold Season Severe Weather Environments. *Weather and Forecasting*, **30**, 591–612.

Cook, A.J. & Vaughan, D.G. (2010). Overview of areal changes of the ice shelves on the Antarctic Peninsula over the past 50 years. *The Cryosphere*, **4**, 77–98.

Cuffey, K.M.K.M. & Paterson, W.S.B. (2010). *The physics of glaciers*. Elsevier Science.

De Angelis, H. & Skvarca, P. (2003). Glacier surge after ice shelf collapse. *Science*, **299**, 1560–2.

Deb, P., Orr, A., Hosking, J.S., Phillips, T., Turner, J., Bannister, D., Pope, J.O. & Colwell, S. (2016). An assessment of the Polar Weather Research and Forecasting (WRF) model representation of near-surface meteorological variables over West Antarctica. *Journal of Geophysical Research: Atmospheres*, **121**, 1532–1548.

Dee, D.P., Uppala, S.M., Simmons, A.J., Berrisford, P., Poli, P., Kobayashi, S., Andrae, U., Balmaseda, M.A., Balsamo, G., Bauer, P., Bechtold, P., Beljaars, A.C.M., van de Berg, L., Bidlot, J., Bormann, N., Delsol, C., Dragani, R., Fuentes, M., Geer, A.J., Haimberger, L., Healy, S.B.,

Hersbach, H., Hólm, E.V., Isaksen, L., Kållberg, P., Köhler, M., Matricardi, M., McNally, A.P., Monge-Sanz, B.M., Morcrette, J.J., Park, B.K., Peubey, C., de Rosnay, P., Tavolato, C., Thépaut, J.N. & Vitart, F. (2011). The ERA-Interim reanalysis: configuration and performance of the data assimilation system. *Quarterly Journal of the Royal Meteorological Society*, **137**, 553–597.

Ding, Q. & Steig, E.J. (2013). Temperature change on the Antarctic Peninsula linked to the tropical Pacific. *Journal of Climate*, **26**, 7570–7585.

Drechsel, S. & Mayr, G.J. (2008). Objective Forecasting of Foehn Winds for a Subgrid-Scale Alpine Valley. *Weather and Forecasting*, **23**, 205–218.

Drobinski, P., Steinacker, R., Richner, H., Baumann-Stanzer, K., Beffrey, G., Benech, B., Berger, H., Chimani, B., Dabas, A., Dorninger, M., Dürr, B., Flamant, C., Frioud, M., Furger, M., Gröhn, I., Gubser, S., Gutermann, T., Häberli, C., Häller-Scharnhost, E., Jaubert, E., Lothon, M., Mitev, V., Pechinger, U., Piringer, M., Ratheiser, M., Ruffieux, D., Seiz, G., Spatzierer, M., Tschannett, S., Vogt, S., Werner, R. & Zängl, G. (2007). Föhn in the Rhine Valley during MAP: A review of its multiscale dynamics in complex valley geometry. *Quarterly Journal of the Royal Meteorological Society*, **133**, 897–916.

Dürr, B. (2003). Automatisiertes Verfahren zur Bestimmung von Föhn in Alpentälern. Tech. Rep. 223, Meteoschweiz, Meteoschweiz, Zurich.

Durran, D. (1990). Mountain waves and downslope winds. *Atmospheric processes over complex terrain. Meteorological Monographs.*, **23**.

Dyer, A.J. (1967). The turbulent transport of heat and water vapour in an unstable atmosphere. *Quarterly Journal of the Royal Meteorological Society*, **93**, 501–508.

Dyer, A.J. & Hicks, B.B. (1970). Flux-gradient relationships in the constant flux layer. *Quarterly Journal of the Royal Meteorological Society*, **96**, 715–721.

Elvidge, A.D. & Renfrew, I.A. (2016). The Causes of Foehn Warming in the Lee of Mountains. *Bulletin of the American Meteorological Society*, **97**, 455–466.

Elvidge, A.D., Renfrew, I.A., King, J.C., Orr, A., Lachlan-Cope, T.A., Weeks, M. & Gray, S.L. (2015). Foehn jets over the Larsen C Ice Shelf, Antarctica. *Quarterly Journal of the Royal Meteorological Society*, **141**, 698–713.

Elvidge, A.D., Renfrew, I.A., King, J.C., Orr, A. & Lachlan-Cope, T.A. (2016). Foehn warming distributions in nonlinear and linear flow regimes: a focus on the Antarctic Peninsula. *Quarterly Journal of the Royal Meteorological Society*, **142**, 618–631.

Ficker, H. (1920). Der Einfluß der Alpen auf Fallgebiete des Luftdruckes und die Entstehung von Depressionen über dem Mittelmeer. *Meteorologische Zeitschrift*, **37**, 50–63.

Fretwell, P., Pritchard, H.D., Vaughan, D.G., Bamber, J.L., Barrand, N.E., Bell, R., Bianchi, C., Bingham, R.G., Blankenship, D.D., Casassa, G., Catania, G., Callens, D., Conway, H., Cook, A.J., Corr, H.F.J., Damaske, D., Damm, V., Ferraccioli, F., Forsberg, R., Fujita, S., Gim, Y., Gogineni, P., Griggs, J.A., Hindmarsh, R.C.A., Holmlund, P., Holt, J.W., Jacobel, R.W., Jenkins, A., Jokat, W., Jordan, T., King, E.C., Kohler, J., Krabill, W., Riger-Kusk, M., Langley, K.A., Leitchenkov, G., Leuschen, C., Luyendyk, B.P., Matsuoka, K., Mouginot, J., Nitsche, F.O., Nogi, Y., Nost, O.A., Popov, S.V., Rignot, E., Rippin, D.M., Rivera, A., Roberts, J., Ross, N., Siegert, M.J., Smith, A.M., Steinhage, D., Studinger, M., Sun, B., Tinto, B.K., Welch, B.C., Wilson, D., Young, D.A., Xiangbin, C. & Zirizzotti, A. (2013). Bedmap2: improved ice bed, surface and thickness datasets for Antarctica. *The Cryosphere*, **7**, 375–393.

Gaffin, D.M. (2007). Foehn Winds That Produced Large Temperature Differences near the Southern Appalachian Mountains. *Weather and Forecasting*, **22**, 145–159.

Gill, A.E. (1982). *Atmosphere-ocean dynamics*. Academic Press.

Glasser, N.F., Kulessa, B., Luckman, A., Jansen, D., King, E.C., Sammonds, P.R., Scambos, T.A. & Jezek, K.C. (2009). Surface structure and stability of the Larsen C ice shelf, Antarctic Peninsula. *Journal of Glaciology*, **55**, 400–410.

Golding, D. (1978). Calculated snowpack evaporation during chinooks along the Eastern slopes of the Rocky Mountains in Alberta. *Journal of Applied Meteorology*, **17**, 1647–1651.

Grace, B. (1990). Some observations on the effect of chinooks on field microclimates and soil moisture status in Southern Alberta. *Climatological Bulletin*, **24**, 67–83.

Grosvenor, D., Choularton, T., King, J. & Lachlan-Cope, T. (2014). Downslope Fohn winds over the Antarctic Peninsula and their effect on the Larsen Ice Shelves. *Atmos.Chem.Phys.Discuss.*, **14**, 9481–9509.

Grosvenor, D.P., Choularton, T.W., Lachlan-Cope, T., Gallagher, M.W., Crosier, J., Bower, K.N., Ladkin, R.S. & Dorsey, J.R. (2012). In-situ aircraft observations of ice concentrations within clouds over the Antarctic Peninsula and Larsen Ice Shelf. *Atmospheric Chemistry and Physics*, **12**, 11275–11294.

Gutermann, T. (1970). Vergleichende Untersuchungen zur Föhnhäufigkeit im Rheintal zwischen Chur und Bodensee. *Scientific Reports*, **18**.

Haid, V. (2013). *Coastal polynyas in the southwestern Weddell sea: Surface fluxes, sea ice production and water mass modification*. Ph.D. thesis, Universitaet Bremen.

Hann, J. (1866). Zur Frage über den Ursprung des Föhn. *Zeitschrift der österreichischen Gesellschaft für Meteorologie*, **1**, 257–263.

Hayashi, M., Hirota, T., Iwata, Y. & Takayabu, I. (2005). Snowmelt Energy Balance and Its Relation to Foehn Events in Tokachi, Japan. *Journal of Meteorological Society of Japan.*, **83**, 783–798.

Hines, K.M. & Bromwich, D.H. (2008). Development and Testing of Polar Weather Research and Forecasting (WRF) Model. Part I: Greenland Ice Sheet Meteorology. *Monthly Weather Review*, **136**, 1971–1989.

Hines, K.M., Bromwich, D.H., Bai, L.S., Barlage, M. & Slater, A.G. (2011). Development and testing of polar WRF. Part III: Arctic land. *Journal of Climate*, **24**, 26–48.

Hines, K.M., Bromwich, D.H., Bai, L., Bitz, C., Powers, J.G. & Manning, K.W. (2015). Sea Ice Enhancements to Polar WRF. *Monthly Weather Review*, **143**, 2363–2385.

Hock, R. (2003). Temperature index melt modelling in mountain areas. *Journal of Hydrology*, **282**, 104–115.

Hodgson, D.A., Bentley, M.J., Roberts, S.J., Smith, J.A., Sugden, D.E. & Domack, E.W. (2006). Examining Holocene stability of Antarctic Peninsula ice shelves. *Eos, Transactions American Geophysical Union*, **87**, 305.

Högström, U. (1988). Non-dimensional wind and temperature profiles in the atmospheric surface layer: A re-evaluation. *Boundary-Layer Meteorology*, **42**, 55–78.

Hoinka, K. (1985). What is a Foehn Clearance? *Bulletin American Meteorological Society*, **66**, 1123–1132.

Holland, P.R., Corr, H.F.J., Pritchard, H.D., Vaughan, D.G., Arthern, R.J., Jenkins, A. & Tedesco, M. (2011). The air content of Larsen ice shelf. *Geophysical Research Letters*, **38**, L10503.

Holton, J.R. (2004). Chapter 5 - The Planetary Boundary Layer. In *An Introduction to Dynamic Meteorology*, vol. 88, 115–138, Elsevier Academic Press, Burlington, MA, 4th edn.

Hong, S.Y., Dudhia, J. & Chen, S.H. (2004). A Revised Approach to Ice Microphysical Processes for the Bulk Parameterization of Clouds and Precipitation. *Monthly Weather Review*, **132**, 103–120.

Hood, E., Williams, M. & Cline, D. (1999). Sublimation from a seasonal snowpack at a continental, mid-latitude alpine site. *Hydrological Processes*, **13**, 1781–1797.

Hosking, J.S., Orr, A., Marshall, G.J., Turner, J. & Phillips, T. (2013). The Influence of the AmundsenBellingshausen Seas Low on the Climate of West Antarctica and Its Representation in Coupled Climate Model Simulations. *Journal of Climate*, **26**, 6633–6648.

Jansen, D., Kulessa, B., Sammonds, P., Luckman, A., King, E. & Glasser, N. (2010). Present stability of the Larsen C ice shelf, Antarctic Peninsula. *Journal of Glaciology*, **56**, 593–600.

Jansen, D., Luckman, A.J., Cook, A., Bevan, S., Kulessa, B., Hubbard, B. & Holland, P.R. (2015). Brief Communication: Newly developing rift in Larsen C Ice Shelf presents significant risk to stability. *The Cryosphere*, **9**, 1223–1227.

Jaubert, G. & Stein, J. (2003). Multiscale and unsteady aspects of a deep fohn event during MAP. *Quarterly Journal of the Royal Meteorological Society*, **129**, 755–776.

Jones, J. (2012). Climate science: Tree rings and storm tracks. *Nature Geoscience*, **5**, 764–765.

King, J., Kirchgaessner, A., Orr, A., Luckman, A., Bevan, S., Elvidge, A., Renfrew, I. & Kuipers Munneke, P. (????). The Impact of Foehn Winds on Surface Energy Balance during the 2010-2011 Melt Season over Larsen C Ice Shelf, Antarctica.

King, J.C. (1990). Some measurements of turbulence over an antarctic ice shelf. *Quarterly Journal of the Royal Meteorological Society*, **116**, 379–400.

King, J.C. (1994). Recent climate variability in the vicinity of the antarctic peninsula. *International Journal of Climatology*, **14**, 357–369.

King, J.C. & Anderson, P.S. (1994). Heat and water vapour fluxes and scalar roughness lengths over an Antarctic ice shelf. *Boundary-Layer Meteorology*, **69**, 101–121.

King, J.C., Anderson, P.S., Smith, M.C. & Mobbs, S.D. (1996). The surface energy and mass balance at Halley, Antarctica during winter. *Journal of Geophysical Research: Atmospheres*, **101**, 19119–19128.

King, J.C., Anderson, P.S. & Mann, G. (2001). The seasonal cycle of sublimation at Halley, Antarctica. *Journal of Gla*, **47**, 1–8.

King, J.C., Lachlan-Cope, T.A., Ladkin, R.S. & Weiss, A. (2008). Airborne Measurements in the Stable Boundary Layer over the Larsen Ice Shelf, Antarctica. *Boundary-Layer Meteorology*, **127**, 413–428.

King, J.C., Gadian, A., Kirchgaessner, A., Kuipers Munneke, P., Lachlan-Cope, T.A., Orr, A., Reijmer, C., van den Broeke, M.R., van Wessem, J.M. & Weeks, M. (2015). Validation of the summertime surface energy budget of Larsen C Ice Shelf (Antarctica) as represented in three high-resolution atmospheric models. *Journal of Geophysical Research: Atmospheres*, **120**, 1335–1347.

Kirtman, B., Power, S.B., Adedoyin, J., Boer, G.J., Bojariu, R., Camillion, L., Doblas-Reyes, F., Fiore, A.M., Kimoto, M., Meehl, G.A., Prather, M., Sarr, A., Schaer, C., Sutton, R., van Oldenborgh, G., Vecchi, G. & Wang, H. (2013). Climate Change 2013: The Physical Science Basis. Contribution of Working Group 1 to the Fifth Assessment Report of the Intergovernmental Panel on Climate Change. Tech. rep., IPCC 2013.

Kleczek, M.A., Steeneveld, G.J. & Holtslag, A.A.M. (2014). Evaluation of the Weather Research and Forecasting Mesoscale Model for GABLS3: Impact of Boundary-Layer Schemes, Boundary Conditions and Spin-Up. *Boundary-Layer Meteorology*, **152**, 213–243.

Kuipers Munneke, P., van den Broeke, M.R., Reijmer, C.H., Helsen, M.M., Boot, W., Schneebeli, M. & Steffen, K. (2009). The role of radiation penetration in the energy budget of the snowpack at Summit, Greenland. *The Cryosphere*, **3**, 155–165.

Kuipers Munneke, P., van den Broeke, M., King, J.C., Gray, T. & Reijmer, C. (2012). Near-surface climate and surface energy budget of Larsen C ice shelf, Antarctic Peninsula. *The Cryosphere*, **6**, 353–363.

Kuipers Munneke, P., Ligtenberg, S.R., Van Den Broeke, M.R. & Vaughan, D.G. (2014). Firn air depletion as a precursor of Antarctic ice-shelf collapse. *Journal of Glaciology*, **60**, 205–214.

Lachlan-Cope, T. (2010). Antarctic clouds. *Polar Research*, **29**, 150–158.

Luckman, A., Elvidge, A., Jansen, D., Kulessa, B., Kuipers Munneke, P., King, J. & Barrand, N.E. (2014). Surface melt and ponding on Larsen C Ice Shelf and the impact of föhn winds. *Antarctic Science*, **26**, 625–635.

Makkonen, L. & Laakso, T. (2005). Humidity Measurements in Cold and Humid Environments. *Boundary-Layer Meteorology*, **116**, 131–147.

Maria, O. (2010). Responses of Antarctic Tundra Ecosystem to Climate Change and Human Activity. *Papers on Global Change IGBP*, **17**, 43–52.

Marshall, G. & National Center for Atmospheric Research (2016). Climate Data Guide.

Marshall, G.J. (2003). Trends in the Southern Annular Mode from Observations and Reanalyses. *Journal of Climate*, **16**, 4134–4143.

Marshall, G.J., Orr, A., van Lipzig, N.P.M. & King, J.C. (2006). The Impact of a Changing Southern Hemisphere Annular Mode on Antarctic Peninsula Summer Temperatures. *Journal of Climate*, **19**, 5388–5404.

Milovac, J., Warrach-Sagi, K., Behrendt, A., Späth, F., Ingwersen, J. & Wulfmeyer, V. (2016). Investigation of PBL schemes combining the WRF model simulations with scanning water vapor differential absorption lidar measurements. *Journal of Geophysical Research: Atmospheres*, **121**, 624–649.

Monaghan, A.J., Bromwich, D.H., Powers, J.G. & Manning, K.W. (2005). The Climate of the McMurdo, Antarctica, Region as Represented by One Year of Forecasts from the Antarctic Mesoscale Prediction System*. *Journal of Climate*, **18**, 1174–1189.

Monaghan, A.J., Bromwich, D.H., Fogt, R.L., Wang, S.H., Mayewski, P.A., Dixon, D.A., Ekaykin, A., Frezzotti, M., Goodwin, I., Isaksson, E., Kaspari, S.D., Morgan, V.I., Oerter, H., Van Ommen, T.D., Van der Veen, C.J. & Wen, J. (2006). Insignificant change in Antarctic snowfall since the International Geophysical Year. *Science (New York, N.Y.)*, **313**, 827–31.

Morris, E. & Vaughan, D. (2003). Spatial and Temporal Variation of Surface Temperature on the Antarctic Peninsula and the Limit of Variability of Ice Shelves. In *Antarctic Peninsula Climate Variability: Historical and Paleoenvironmental Perspective*, vol. 79, 61–68, American Geophysical Union.

National Center for Atmospheric Research (2014). Weather Research and Forecasting ARW Version 3 Modeling System Users' Guide. Tech. rep., National Center for Atmospheric Research.

Nylen, T., Fountain, A. & Doran, P. (2004). Climatology of katabatic winds in the McMurdo dry valleys, southern Victoria Land, Antarctica. *Journal of Geophysical Research*, **109**, D03114.

Ohmura, A. & Ohmura, A. (2001). Physical Basis for the Temperature-Based Melt-Index Method. *Journal of Applied Meteorology*, **40**, 753–761.

Okogbue, E.C., Adedokun, J.A. & Holmgren, B. (2009). Hourly and daily clearness index and diffuse fraction at a tropical station, Ile-Ife, Nigeria. *International Journal of Climatology*, **29**, 1035–1047.

Orr, A., Cresswell, D., Marshall, G.J., Hunt, J.C.R., Sommeria, J., Wang, C.G. & Light, M. (2004). A 'low-level' explanation for the recent large warming trend over the western Antarctic Peninsula involving blocked winds and changes in zonal circulation. *Geophysical Research Letters*, **31**, L06204.

Orr, A., Marshall, G., Hunt, J., Sommeria, J., Wang, C.G., Van Lipzig, N., Cresswell, D. & King, J. (2008). Characteristics of Summer Airflow over the Antarctic Peninsula in Response to Recent Strengthening of Westerly Circumpolar Winds. *Journal of the Atmospheric sciences*, **65**, 1396–1413.

Parish, T.R. (1983). The influence of the Antarctic Peninsula on the wind field over the western Weddell Sea. *Journal of Geophysical Research*, **88**, 2684.

Plavcan, D., Mayr, G.J. & Zeileis, A. (2014). Automatic and Probabilistic Foehn Diagnosis with a Statistical Mixture Model. *Journal of Applied Meteorology and Climatology*, **53**, 652–659.

Powers, J.G. (2007). Numerical Prediction of an Antarctic Severe Wind Event with the Weather Research and Forecasting (WRF) Model. *Monthly Weather Review*, **135**, 3134–3157.

Pradier, S., Chong, M. & Roux, F. (2002). Radar Observations and Numerical Modeling of a Precipitating Line during MAP IOP 5. *Monthly Weather Review*, **130**, 2533–2553.

Pritchard, H.D., Ligtenberg, S.R.M., Fricker, H.A., Vaughan, D.G., van den Broeke, M.R. & Padman, L. (2012). Antarctic ice-sheet loss driven by basal melting of ice shelves. *Nature*, **484**, 502–5.

Raphael, M.N., Marshall, G.J., Turner, J., Fogt, R.L., Schneider, D., Dixon, D.A., Hosking, J.S., Jones, J.M. & Hobbs, W.R. (2016). The Amundsen Sea Low: Variability, Change, and Impact on Antarctic Climate. *Bulletin of the American Meteorological Society*, **97**, 111–121.

Renfrew, I.A. (2004). The dynamics of idealized katabatic flow over a moderate slope and ice shelf. *Quarterly Journal of the Royal Meteorological Society*, **130**, 1023–1045.

Richner, H. & Gutermann, T. (2007). Statistical analysis of foehn in Altdorf, Switzerland. In *Extended abstracts, Volume 2, International Conference on Alpine Meteorology, June 4 to 8, 2007.*, 457–460.

Richner, H. & Hächler, P. (2013). Understanding and Forecasting Alpine Foehn. In *Mountain weather research and forecasting: recent progress and current challenges*, 219–260, Springer Netherlands.

Richner, H., Baumann-Stanzer, K., Benech, B., Berger, H., Chimani, B., Dorninger, M., Drobinski, P., Furger, M., Gubser, S., Gutermann, T., Häberli, C., Häller, E., Lothon, M., Mitev, V., Ruffieux, D., Seiz, G., Steinacker, R., Tschannett, S., Vogt, S. & Werner, R. (2005). Unstationary aspects of foehn in a large valley part I: operational setup, scientific objectives and analysis of the cases during the special observing period of the MAP subprogramme FORM. *Meteorology and Atmospheric Physics*, **92**, 255–284.

Robertson, R., Visbeck, M., Gordon, A. & Fahrbach, E. (2002). Long-term temperature trends in the deep waters of the Weddell Sea. *Deep Sea Research Part II*, **49**, 4791–4806.

Rott, H., Skvarca, P. & Nagler, T. (1996). Rapid Collapse of Northern Larsen Ice Shelf, Antarctica. *Science*, **271**, 788–792.

Scambos, T., Hulbe, C. & Fahnestock, M. (2003). Climate-induced ice shelf disintegration in the Antarctic Peninsula. *Antarctic Research Series*, **79**, 79–92.

Scambos, T., Fricker, H.A., Liu, C.C., Bohlander, J., Fastook, J., Sargent, A., Massom, R., Wu, A.M. & Carlson, R.W. (2009). Ice shelf disintegration by plate bending and hydro-fracture: Satellite observations and model results of the 2008 Wilkins ice shelf break-ups. *Earth and Planetary Science Letters*, **280**, 51–60.

Scambos, T.A. (2004). Glacier acceleration and thinning after ice shelf collapse in the Larsen B embayment, Antarctica. *Geophysical Research Letters*, **31**, L18402.

Scambos, T.A., Hulbe, C., Fahnestock, M. & Bohlander, J. (2000). The link between climate warming and break-up of ice shelves in the Antarctic Peninsula. *Journal of Glaciology*, **46**, 516–530.

Schneider, L. (1930). GREENLAND WEST-COAST FOEHNS: A DISCUSSION BASED ON THE FOEHNS OF JANUARY, 1929. *Monthly Weather Review*, **58**, 135–138.

Schwerdtfeger, W. (1975). The effect of the Antarctic Peninsula on the temperature regime of the Weddell Sea. *Monthly weather review*, **103**, 45–51.

Scorer, R. (1978). *Environmental Aerodynamics*. Wiley and Sons.

Seibert, P. (2005). Hann's thermodynamic foehn theory and its presentation in meteorological textbooks in the course of time. *From Beaufort to Bjerknes and Beyond, Algorismus*, **52**, 169–180.

Sergienko, O. & Macayeal, D.R. (2005). Surface melting on Larsen Ice Shelf, Antarctica. *Annals of Glaciology*, **40**, 215–218.

Sheshadri, A., Plumb, A. & Domeisen, D. (2014). Can the delay in Antarctic polar vortex breakup explain recent trends in surface Westerlies? *Journal of the Atmospheric Sciences*, **71**, 566–573.

Sicart, J.E., Litt, M., Helgason, W., Tahar, V.B. & Chaperon, T. (2014). A study of the atmospheric surface layer and roughness lengths on the high-altitude tropical Zongo glacier, Bolivia. *Journal of Geophysical Research: Atmospheres*, **119**, 3793–3808.

Skamarock, W.C. & Klemp, J.B. (2008). A time-split nonhydrostatic atmospheric model for weather research and forecasting applications. *Journal of Computational Physics*, **227**, 3465–3485.

Skansi, M., King, J., Lazzara, M., Cervent, R., Stella, J., Solomon, S., Jones, P., Bromwich, D., Renwick, J., Burt, C., Peterson, T., Brunet, M., Driouech, Vose, R. & Krahenbuhl, D. (2017). Evaluating highest-temperature extremes in the Antarctic. *Earth and Space Science News*, **98**.

Speirs, J.C., Steinhoff, D.F., McGowan, H.A., Bromwich, D.H. & Monaghan, A.J. (2010). Foehn Winds in the McMurdo Dry Valleys, Antarctica: The Origin of Extreme Warming Events. *Journal of Climate*, **23**, 3577–3598.

Speirs, J.C., McGowan, H.A., Steinhoff, D.F. & Bromwich, D.H. (2013). Regional climate variability driven by foehn winds in the McMurdo Dry Valleys, Antarctica. *International Journal of Climatology*, **33**, 945–958.

Steele, C.J., Dorling, S.R., von Glasow, R. & Bacon, J. (2013). Idealized WRF model sensitivity simulations of sea breeze types and their effects on offshore windfields. *Atmospheric Chemistry and Physics*, **13**, 443–461.

Steig, E.J., Schneider, D.P., Rutherford, S.D., Mann, M.E., Comiso, J.C. & Shindell, D.T. (2009). Warming of the Antarctic ice-sheet surface since the 1957 International Geophysical Year. *Nature*, **457**, 459–462.

Steinhoff, D.F., Bromwich, D.H., Lambertson, M., Knuth, S.L. & Lazzara, M.A. (2008). A Dynamical Investigation of the May 2004 McMurdo Antarctica Severe Wind Event Using AMPS. *Monthly Weather Review*, **136**, 7–26.

Steinhoff, D.F., Bromwich, D.H. & Monaghan, A. (2013). Dynamics of the Foehn Mechanism in the McMurdo Dry Valleys of Antarctica from Polar WRF. *Quarterly Journal of the Royal Meteorological Society*, **139**, 1615–1631.

Steinhoff, D.F., Bromwich, D.H., Speirs, J.C., McGowan, H.A. & Monaghan, A.J. (2014). Austral summer foehn winds over the McMurdo dry valleys of Antarctica from Polar WRF. *Quarterly Journal of the Royal Meteorological Society*, **140**, 1825–1837.

Sterk, H.A.M., Steeneveld, G.J., Vihma, T., Anderson, P.S., Bosveld, F.C. & Holtslag, A.A.M. (2015). Clear-sky stable boundary layers with low winds over snow-covered surfaces. Part 1: WRF model evaluation. *Quarterly Journal of the Royal Meteorological Society*, **141**, 2165–2184.

Sun, W.Y. (2013). Numerical study of severe downslope windstorm. *Weather and Climate Extremes*, **2**, 22–30.

Thompson, D.W.J. & Solomon, S. (2002). Interpretation of recent Southern Hemisphere climate change. *Science (New York, N.Y.)*, **296**, 895–9.

Trusel, L.D., Frey, K.E., Das, S.B., Karnauskas, K.B., Kuipers Munneke, P., van Meijgaard, E. & van den Broeke, M.R. (2015). Divergent trajectories of Antarctic surface melt under two twenty-first-century climate scenarios. *Nature Geoscience*, **8**, 927–932.

Turner, J., Lachlan-Cope, T.A., Marshall, G.J., Morris, E.M., Mulvaney, R. & Winter, W. (2002). Spatial variability of Antarctic Peninsula net surface mass balance. *Journal of geophysical research*, **107**, 4173.

Turner, J., Lachlan-Cope, T., Colwell, S. & Marshall, G.J. (2005). A positive trend in western Antarctic Peninsula precipitation over the last 50 years reflecting regional and Antarctic-wide atmospheric circulation changes. *Annals of Glaciology*, **41**, 85–91.

Turner, J., Phillips, T., Hosking, J.S., Marshall, G.J. & Orr, A. (2013). The Amundsen Sea low. *International Journal of Climatology*, **33**, 1818–1829.

Turner, J., Lu, H., White, I., King, J.C., Phillips, T., Hosking, J.S., Bracegirdle, T.J., Marshall, G.J., Mulvaney, R. & Deb, P. (2016). Absence of 21st century warming on Antarctic Peninsula consistent with natural variability. *Nature*, **535**, 411–415.

Turner, R. (1966). Pincher Creek. *Weather*, **21**, 412–413.

Turton, J., Kirchgaessner, A., King, J. & Ross, A. (????). Does high-resolution modelling improve the spatial analysis of foehn flow over the Larsen C ice shelf? *Weather*.

Välisuo, I., Vihma, T. & King, J.C. (2014). Surface energy budget on Larsen and Wilkins ice shelves in the Antarctic Peninsula: results based on reanalyses in 19892010. *The Cryosphere*, **8**, 1519–1538.

Valkonen, T., Vihma, T., Johansson, M.M. & Launiainen, J. (2014). Atmosphere-sea ice interaction in early summer in the Antarctic: evaluation and challenges of a regional atmospheric model. *Quarterly Journal of the Royal Meteorological Society*, **140**, 1536–1551.

Van As, D., Reijmer, C. & De Wal, R. (2005). The summer surface energy balance of the high Antarctic Plateau. *Boundary-Layer Meteorology*, **115**, 289–317.

Van Den Broeke, M. (2005). Strong surface melting preceded collapse of Antarctic Peninsula ice shelf. *Geophysical Research Letters*, **32**.

van den Broeke, M., Smeets, P., Ettema, J., van der Veen, C., van de Wal, R. & Oerlemans, J. (2008). Partitioning of melt energy and meltwater fluxes in the ablation zone of the west Greenland ice sheet. *The Cryosphere*, **2**, 179–189.

van Wessem, J.M., Ligtenberg, S.R.M., Reijmer, C.H., van de Berg, W.J., van den Broeke, M.R., Barrand, N.E., Thomas, E.R., Turner, J., Wuite, J., Scambos, T.A. & van Meijgaard, E. (2016). The modelled surface mass balance of the Antarctic Peninsula at 5.5 km horizontal resolution. *The Cryosphere*, **10**, 271–285.

Vaughan, D.G. (2006). Recent trends in melting conditions on the Antarctic Peninsula and their implications for ice-sheet mass balance and sea level. *Arctic Antarctic and Alpine Research*, **38**, 147–152.

Vaughan, D.G., Marshall, G.J., Connolley, W.M., Parkinson, C., Mulvaney, R., Hodgson, D.A., King, J.C., Pudsey, C.J. & Turner, J. (2003). Recent Rapid Regional Climate Warming on the Antarctic Peninsula. *Climatic Change*, **60**, 243–274.

Vergeiner, J. (2004). *South foehn studies and a new foehn classification scheme in the Wipp and Inn valley*. Ph.D. thesis, University of Innsbruck, Austria.

Wille, J.D., Bromwich, D.H., Nigro, M.A., Cassano, J.J., Mateling, M., Lazzara, M.A. & Wang, S.H. (2016). Evaluation of the AMPS Boundary Layer Simulations on the Ross Ice Shelf with Tower Observations. *Journal of Applied Meteorology and Climatology*, **55**, 2349–2367.

Wilson, A.B., Bromwich, D.H. & Hines, K.M. (2011). Evaluation of Polar WRF forecasts on the Arctic System Reanalysis domain: Surface and upper air analysis. *Journal of Geophysical Research*, **116**, D11112.

Wilson, A.B., Bromwich, D.H. & Hines, K.M. (2012). Evaluation of Polar WRF forecasts on the Arctic System Reanalysis Domain: 2. Atmospheric hydrologic cycle. *Journal of Geophysical Research*, **117**, D04107.

Wyszogrodzki, A., Liu, Y., Jacobs, N., Childs, P., Zhang, Y., Roux, G. & Warner, T, T. (2013). Analysis of the surface temperature and wind forecast errors on NCAR-AirDat operational CONUS 4-km WRF forecst system. *Meterol Atmos Phys*, **122**, 125–143.

Zängl, G. (2002). Idealized numerical simulations of shallow foehn. *Quarterly Journal of the Royal Meteorological Society*, **128**, 431–450.

Zängl, G., Chimani, B. & Häberli, C. (2004). Numerical Simulations of the Foehn in the Rhine Valley on 24 October 1999 (MAP IOP 10). *Monthly Weather Review*, **132**, 368–389.

Zawar-Reza, P., Katurji, M., Soltanzadeh, I., Dallafior, T., Zhong, S., Steinhoff, D., Storey, B. & Cary, S.C. (2013). Pseudovertical Temperature Profiles Give Insight into Winter Evolution of the Atmospheric Boundary Layer over the McMurdo Dry Valleys of Antarctica. *Journal of Applied Meteorology and Climatology*, **52**.

Zhang, H., Pu, Z. & Zhang, X. (2013). Examination of Errors in Near-Surface Temperature and Wind from WRF Numerical Simulations in Regions of Complex Terrain. *Weather and Forecasting*, **28**, 893–914.